

JPL D-99657



Next-Generation Radioisotope Thermoelectric Generator Study Final Report

David F. Woerner, Study Team Lead

National Aeronautics and
Space Administration

Jet Propulsion Laboratory
California Institute of Technology
Pasadena, California

June 2017

The research described in this publication was partially carried out at the Jet Propulsion Laboratory, California Institute of Technology, under a contract with the National Aeronautics and Space Administration.

Reference herein to any specific commercial product, process, or service by trade name, trademark, manufacturer, or otherwise, does not constitute or imply its endorsement by the United States Government or the Jet Propulsion Laboratory, California Institute of Technology.

© 2017. All rights reserved.

Foreword

For more than four decades, NASA missions have used radioisotope power systems (RPS) to provide electricity for spaceflight missions. Currently, the Multi-Mission Radioisotope Thermoelectric Generator (MMRTG) is the only spaceflight-qualified RTG, and it relies on technology derived for the NASA Pioneer and Viking missions of the 1970s. The MMRTG's predecessor, the General Purpose Heat Source (GPHS)-RTG, first flew on the Voyager missions launched in 1977, and went out of production shortly after the turn of the 21st century. While reactivating manufacturing of GPHS-RTGs is theoretically possible, there have been many improvements in thermoelectric materials, and these advances warrant a clear-eyed review. Further, it is worth exploring alternative architectures for newly designed RTGs that might result from the requirements that would enable challenging science missions at more remote and less accessible destinations across the solar system.

This Next-Generation RTG Study was initiated in July 2016 after discussions with NASA's RPS Program. The completion of the Nuclear Power Assessment Study in February 2015 set the stage for the Next-Generation RTG Study. NASA requested a thorough review of potential RTG concepts that were within reach and could serve the Agency from the late 2020s into the foreseeable future.

The following objective was set for the Next-Generation RTG Study:

“The objective of this study is to determine the characteristics of the next RTG that would ‘best’ fulfill Planetary Science Division (PSD) mission needs. This study is limited to systems that convert heat to electricity using thermocouples (thermoelectric couples). In this study, ‘best’ is defined as a confluence of the following factors:

- An RTG that would be useful across the solar system
- An RTG that maximizes the types of missions: flyby, orbit, land, rove, boats, submersibles, balloons
- An RTG that has reasonable development risks and timeline
- An RTG that the value (importance, worth and usefulness) returned to the PSD for investment is warranted, as compared with retaining existing baseline systems.”

The objective tied the scope of this study to a very broad range of topics.

Cost estimates were deliberately not included in this study to maintain a strict focus on the projected applicability of different RPS options.

Acknowledgements

The Next-Generation RTG Study Team gratefully acknowledges the skilled help of the many people who have contributed to the successful execution of this study and compilation of this report. In particular, the efforts of Young Lee and the NASA Jet Propulsion Laboratory (JPL) Mission Study Team, along with the Mission Design Centers at NASA Goddard Space Flight Center (GSFC), Johns Hopkins University (JHU) Applied Physics Laboratory (APL), and NASA Glenn Research Center (GRC). Many staff members at JPL, GSFC, APL, and GRC, independent of the Study Team, provided useful insights regarding the currently available MMRTG and the potential enhanced MMRTG for future deep space missions. Similarly, the various NASA and Department of Energy (DOE) facilities that provided support via their Collaborative Engineering Centers and support for the many technical interchange meetings are gratefully acknowledged. We owe a debt of gratitude to Roger Carlson, Samantha Ozyildirim, Mary Young, Barry Coleman, and other members of the editorial staff at the NASA Jet Propulsion Laboratory, California Institute of Technology, in producing this study report. We finally thank June F. Zakrajsek of the NASA RPS Program, for sponsoring, coordinating, and supporting all of the study efforts.

Study Team

The members of the Next-Generation RTG Study Team and their affiliations follow.

Study Team Lead

David Woerner, NASA Jet Propulsion Laboratory

Next-Generation RTG Study Team Members

NASA Jet Propulsion Laboratory, California Institute of Technology

Nitin Arora	John Elliot	David Neff
Dan Berisford	Jean-Pierre Fleurial	Knut Oxnevad, <i>Database</i>
Pradeep Bhandari	Terry Hendricks	<i>Development</i>
Chester Borden	Insoo Jun	Martin Ratliff
Sevan Chanakain	Damon Landau	Timothy Shirey
Alan Didion	Hari Nayar	Kevin Yu
Fivos Drymiotis		

Chadwick Barklay, University of Dayton Research Institute

Ken Hibbard, John Hopkins University, Applied Physics Laboratory

Anthony Nicoletti, NASA Goddard Space Flight Center

Paul Ostdiek, John Hopkins University, Applied Physics Laboratory

June Zakrajsek, NASA Glenn Research Center

RPS Program Mission Analysis Team

NASA Jet Propulsion Laboratory, California Institute of Technology

Young Lee, *Lead* Brian Bairstow

Johns Hopkins University, Applied Physics Laboratory — Mission Analysts

Chris Hersman Ken Hibbard Paul Ostdiek Dennis Woodfork

NASA Glenn Research Center — Compass Members

Steve Oleson, <i>Lead</i>	Ralph Lorenz (JHU, APL)	Evan Roelke (GT)
Amee Bogner	Mike Martini	Paul Schmitz
Tony Colozza	Steve McCarty	Elizabeth Turnbull
James Fittje	Paul Michael (ARL)	Justin Walsh (ARL)
John Gyekenyesi	Tom Packard	Jeff Woytach
Robert Jones	Tom Parkey	

NASA Goddard Space Flight Center — Mission Design Lab

James Sturm, <i>Lead</i>	Jacob Englander	Blake Lorenz
David Batchelor	Matthew Garrison	Paul Mason
Bob Beaman	John Godfrey	Dave Palace
Porfy Beltran	Kyle Hughes	Daniel Ramspacher
Kim Brown	Frank Kirchman	David Robinson
Jacob Burke	Jeremy Knittel	Terry Smith

Consultants

Mike Amato, NASA Goddard Space Flight Center

Dirk Cairns-Gallimore, Department of Energy

Steve Johnson, Department of Energy Idaho National Laboratory

Anthony Nicoletti, NASA Goddard Space Flight Center

Louise Procktor, John Hopkins University, Applied Physics Laboratory

Cheryl Reed, John Hopkins University, Applied Physics Laboratory

Kim Reh, NASA Jet Propulsion Laboratory, California Institute of Technology

Tom Spilker, Independent Consultant

Table of Contents

Foreword.....	iii
Acknowledgements.....	iii
Study Team.....	iv
Table of Contents.....	vi
1 Executive Summary	1-1
1.1 Objective and Approach	1-1
1.2 Key Findings	1-1
1.3 Thermoelectric Couple Selection	1-1
1.4 Summary of RTG Concepts	1-2
2 Mission Analysis.....	2-1
2.1 Targets and Destinations	2-1
2.1.1 Introduction	2-1
2.1.2 Ocean Worlds	2-1
2.1.3 The Gas Giants: Jupiter and Saturn	2-4
2.1.4 The Ice Giants: Uranus and Neptune.....	2-4
2.1.5 Venus.....	2-5
2.1.6 Destination-Specific Observations	2-5
2.2 Mission Types	2-7
2.2.1 Introduction	2-7
2.2.2 Flyby.....	2-8
2.2.3 Orbiter	2-8
2.2.4 Atmospheric Probe	2-9
2.2.5 Aerial	2-9
2.2.6 Surface.....	2-11
2.2.7 Lander.....	2-12
2.2.8 Subsurface	2-13
2.2.9 Sample Return	2-15
2.3 Prioritized Missions.....	2-15
2.3.1 Prioritized Missions and NASA’s Mission Classes	2-17
2.3.2 Observations on Prioritized Missions.....	2-19
2.4 Summary of Mission Analyses.....	2-20
2.4.1 Introduction	2-20
2.4.2 Mission Analyses for RPS.....	2-22
2.4.3 Summary	2-26
2.5 Mission-Specific Requirements.....	2-26
2.5.1 Power.....	2-26
2.5.2 Mission Length.....	2-26
2.5.3 Vacuum vs. Atmosphere	2-26
2.6 Requirements.....	2-26
2.6.1 Introduction	2-26
2.6.2 Approach	2-27
2.6.3 GPHS-RTG- and MMRTG-Derived Requirements	2-27
2.6.4 Launch Vehicle Environment Characteristics	2-27
2.6.5 Destination- and Mission-Specific Derived Requirements	2-28
2.6.6 Requirement Tables.....	2-29
2.7 References	2-34

3	Thermoelectric Materials: Technologies and Risk Assessment.....	3-1
3.1	Objective.....	3-1
3.2	Background.....	3-1
3.3	Thermoelectric Material Efficiency.....	3-2
3.4	Thermoelectric Materials Considered.....	3-2
3.5	Screening Criteria and Results	3-3
3.6	Performance Analysis of Couple Architectures	3-4
3.7	Segmentation	3-4
3.8	Couple Configurations.....	3-8
3.9	Configuration Stability Evaluation.....	3-10
3.10	Discussion.....	3-13
3.11	Recommendations	3-13
3.12	Research & Development.....	3-14
3.13	Summary.....	3-15
3.14	References	3-15
4	Next-Generation RTG Concepts	4-1
4.1	Introduction	4-1
4.1.1	A Brief Introduction to RTG Designs	4-2
4.2	A Framework for Development of RTG Concepts.....	4-3
4.2.1	Architectural Trades and Design Constraints	4-4
4.2.2	Details of the Architectural Trades.....	4-5
4.3	Next-Generation RTG Concepts	4-7
4.3.1	Segmented RTG (SRTG)	4-8
4.3.2	Segmented-Modular RTG (SMRTG).....	4-8
4.3.3	Cold-Segmented RTG (CSRTG).....	4-12
4.3.4	Cold-Segmented-Modular RTG (CSMRTG).....	4-13
4.3.5	Hybrid-Segmented-Modular RTGs (HSMRTG).....	4-13
4.3.6	Cold-Hybrid-Segmented-Modular RTGs (CHSMRTGs).....	4-15
4.3.7	Summary of Findings and Observations for Next-Generation RTGs Concepts.....	4-15
4.4	References	4-18
5	Mission Concepts by GSFC and GRC as Independent Assessment of Selected Concepts.....	5-1
5.1	Introduction	5-1
5.2	The Chiron Explorer Mission Concept.....	5-1
5.2.1	Chiron Design Study Assumptions.....	5-2
5.2.2	ChirEx Mission Concept Phases.....	5-3
5.2.3	Spacecraft Design.....	5-4
5.2.4	ChirEx Resources	5-6
5.2.5	System Trades	5-6
5.2.6	Flight Dynamics Parametric Studies	5-7
5.3	The Titan Turtle Mission Concept.....	5-9
5.3.1	Initial Design Concept.....	5-10
5.3.2	Switching to a CHMSRTG-8	5-11
5.4	References	5-11
6	Conclusions	6-1

Appendices

A	Science Mission Concepts Analyzed for RTG Requirements.....	A-1
B	Aerial Missions	B-1
C	Melt Probes	C-1
D	Landers, Rovers, Boats, and Submarines	D-1
E	Probing Subsurfaces of Icy Bodies	E-1
F	Temperatures across the Solar System and RTG Thermal Analyses	F-1
G	Radiation Environments for Space Missions with RTGs.....	G-1
H	Planetary Protection: Requirements, Compliance, and Considerations for Missions Integrating Next-Generation RTG Technologies	H-1
I	Micrometeoroids	I-1
J	Launch Vehicles and Mission Analyses.....	J-1
K	Thermoelectric Technology Risk Assessment Details	K-1
L	Intensity Matrix	L-1
M	Destination Table	M-1
N	Reference RTGs: The GPHS-RTG, MMRTG, and eMMRTG.....	N-1
O	Calculating RTG Fin Size and Mass	O-1
P	Modeling Results for RTG Concepts	P-1
Q	Factors of Safety – GPHS-RTG and MMRTG	Q-1
R	Next-Generation RTG: Factors of Safety, Acoustics, and Random Vibrations.....	R-1

1 Executive Summary

Knut I. Oxnevad

NASA Jet Propulsion Laboratory, 4800 Oak Grove Drive, Pasadena, CA 91109

1.1 Objective and Approach

The overall objective of this study was to “determine the characteristics of the next radioisotope thermoelectric generator (RTG) that would ‘best’ fulfill Planetary Science Division (PSD) mission needs.” The study team utilized a top-down and a bottom-up approach in parallel to identify materials and requirements and determine the recommended characteristics of a “Next-Generation RTG.” The top-down approach was used to derive requirements for a Next-Generation RTG from previously flown RTGs (the General Purpose Heat Source [GPHS]-RTG and the Multi-Mission RTG [MMRTG]). This involved the study of spacecraft and associated missions, potential destinations within the solar system, and potential launch vehicles for future spacecraft that could use the Next-Generation RTG. The bottom-up approach was used to propose the most suitable thermoelectric materials and couple configurations for a Next-Generation RTG.

1.2 Key Findings

Two key findings emerged from this study:

1. The bottom-up approach found eight candidate thermoelectric couple (TEC) configurations that have minimal risk and enough efficiency to warrant developing RTG concepts around them.
2. Six Next-Generation RTG concepts were developed in the top-down approach using the requirements from missions flown, mission concepts studied, and concepts prioritized in the National Research Council’s most recent Decadal Surveys. Three concepts were ultimately judged to be non-compliant; three others were found to be compliant, and they form the three recommended candidates for a Next-Generation RTGs that would best fulfill future PSD needs.

1.3 Thermoelectric Couple Selection

Table 1-1 lists the eight candidate TEC configurations selected by the study team. Configurations 1, 2, 3, 4, 14, and 21 include “low-temperature” segments made from a bismuth-telluride (BiTe) compound. The team ultimately discarded the BiTe segments from the proposed configurations and used only the segments labeled as “mid” and “high” temperatures in developing the Next-Generation RTG concepts in this report.

1. Selection of the eight TECs started with an evaluation of 38 n-type, and 29 p-type materials sourced from scientific literature and from test results from NASA/JPL. All of these were screened to detect materials that individually or in combination with other materials could potentially achieve:
 - a. $ZT_{max} > 1$ (ZT is a figure of merit)
 - b. A stable Seebeck coefficient over time
 - c. Efficient operation over a large temperature gradient $> 700^{\circ}\text{C}$, and
 - d. Low risk from a technology maturation perspective.
2. Next, the resultant p- and n-type thermoelectric materials were modeled in couple configurations; 22 TEC configurations were conceived and modeled.
3. Finally, of the 22 configurations, the eight TECs with the lowest risk were selected. The selected configurations were also characterized by:
 - a. Fairly high predicted efficiencies that ranged from 11 to 17%

- b. Flexibility of operating in a vacuum or argon cover gas environments
- c. Highly desirable sublimation rates $\leq 10^{-6}$ g/cm²/hr
- d. Minimal (anticipated) development effort (<1 year), with low risk to develop the process required for hot side metallization, and
- e. Less than a 10% mismatch in coefficient of thermal expansion between the individual segmented materials (except configurations 3 and 4).

Table 1-1. Thermoelectric couple configuration that were found to be candidates for further study. The table shows materials and temperature ranges for each segment of the p- and n-type legs of the conceived couples. Temperatures are in Kelvins (K). Ultimately, the “low-temperature,” or BiSeTe segments were discarded from the Next-Generation RTG concepts.

Configuration	n-type			p-type		
	Low (300–473 K)	Mid (473–873 K)	High (873–1273 K)	Low (300–473 K)	Mid (473–873 K)	High (873–1273 K)
1	BiSeTe	Mg ₃₊₆ Sb ₂	Nano Ni 15% La ₃ Te ₄	BiSbTe	Ca ₉ Zn _{4.6} Sb ₉	Yb ₁₄ MgSb ₁₁
2	BiSeTe	Mg ₃₊₆ Sb ₂	ATEC 2014 LaTe	BiSbTe	Ca ₉ Zn _{4.6} Sb ₉	Yb ₁₄ MgSb ₁₁
3	BiSeTe	SKD-CoSb ₃	Nano Ni 15% La ₃ Te ₄	BiSbTe	SKD-CeFe ₄ Sb ₁₂	Yb ₁₄ MgSb ₁₁
4	BiSeTe	SKD-CoSb ₃	ATEC 2014 LaTe	BiSbTe	SKD-CeFe ₄ Sb ₁₂	Yb ₁₄ MgSb ₁₁
10	—	Nano Ni 15% La ₃ Te ₄		—	Yb ₁₄ MgSb ₁₁	
11	—	ATEC 2014 LaTe		—	Yb ₁₄ MgSb ₁₁	
14	BiSeTe	Nano Ni 15% La ₃ Te ₄		BiSbTe	Yb ₁₄ MgSb ₁₁	
21	BiSeTe	ATEC 2014 LaTe		BiSbTe	Yb ₁₄ MgSb ₁₁	

1.4 Summary of RTG Concepts

The derived requirements for a Next-Generation RTG, combined with the candidate thermoelectric couples identified, resulted in six RTG concepts for analysis. After further study, the six candidates were winnowed to three candidates: a Segmented¹ RTG (SRTG), a Segmented-Modular² RTG (SMRTG), and a Hybrid³-Segmented Modular RTG (HSMRTG). The other three candidate concepts failed to meet critical requirements. The study prioritized the selected concepts, from high to low, as SMRTG, SRTG, and HSMRTG. An analysis of the reviewed spacecraft and mission concept studies amplified this prioritization. It showed that about 80% of these notional spacecraft would operate in vacuum-only environments. Hence, 80% of the mission concepts studied could benefit significantly from an SRTG or SMRTG power systems.

A summary of key findings includes:

1. The SRTG and SMRTG would operate in vacuum-only environments. The HSMRTG would be able to operate in both the vacuum of space and in an atmosphere (e.g., Titan), and is thus regarded as a more complex system and hence riskier to develop than the SRTG or SMRTG.
2. RTGs using the selected eight TECs have the potential to deliver the same amount of power as a GPHS-RTG using just 44% of the radioisotope fuel.
3. The concepts include a series-parallel electrical wiring approach operating at 22–34 V to mate with a common spacecraft power bus.

¹ “Segmented” refers to RTG concepts employing thermoelectric couples composed of segments.

² “Modular” refers to RTG concepts that scale with the number of GPHS. In this study, the smallest concept was an RTG fueled by 2 GPHSs. Variants of a concept could therefore be fueled with 2, 4, 6, 8, 10, 12, 14, or 16 GPHS

³ “Hybrid” refers to RTG concepts using sealed housings so that they could operate in both vacuum and atmospheres (e.g., Titan).

4. Power generated by SMRTGs or HSMRTGs, both modular generators, using the selected TECs, is estimated to fall within an envelope of 50 W_e and 600 W_e , using between 2 and 16 GPHS for the smallest and largest variants, respectively. Such a range could make it possible for a Next-Generation RTG to support the power needs of both small and large spacecraft, covering the entire range of NASA planetary science mission concepts: Discovery class, New Frontiers class, and Flagship class.
 - a. Spacecraft requiring ~2 kW of power could use four Next-Generation RTGs. This is more than enough power to adequately power a large Cassini-like spacecraft or a radioisotope electric propulsion system.
5. Power generated by an SRTG using the identified TECs is estimated to be fall within an envelope of 400 W_e and 600 W_e , as this generator is envisioned as being available in only one size.

Notional requirements for specialized RTG concepts were also identified as part of this study. These requirements stem from very challenging mission scenarios; such requirements would burden most other NASA missions likely to fly in the next two to three decades. For example, exploration of the ice sheets and likely oceans of the ocean worlds (such as Europa or Enceladus) or the surface of Venus would require a pressure vessel to protect the RTG from hydrostatic and dynamic pressure levels. Such a vessel could add tens to hundreds of kilograms to the mass of an RTG, making this type of RTG unusable for most other spacecraft and associated missions. On the other hand, a pressure vessel could enable as-of-yet unattempted missions.

2 Mission Analysis

Brian Bairstow, Young H. Lee, and Knut I. Oxnevad

NASA Jet Propulsion Laboratory. 4800 Oak Grove Drive, Pasadena, 91109

The scope of this study was to identify requirements for Next-Generation RTG concepts. This section largely captures and documents the top-down processes and findings to establish a reasonable set of requirements for a Next-Generation RTG. Sections 2.1 and 2.2 are references and provide some of the bases for Next-Generation RTG concepts. Section 2.1 describes potential mission destinations, including their physical data and environments, with a focus on the solar system's ocean worlds, gas giants, ice giants, and Venus. Section 2.2 defines mission concept types as used in this study. Section 2.3 introduces prioritized mission concepts as defined in the Planetary Science Decadal Surveys [1, 2]. A summary of the mission analyses performed is in Section 2.4, with mission-specific and general requirements on Next-Generation RTGs in Sections 2.5 and 2.6, respectively.

To perform the required analyses, and to combine data and present the results in a unique way, an extensive relational database was developed. The database includes detailed data for 63 targets, 6 generic potential destinations (comet, Trojan, Centaur, etc.), 143 spacecraft concepts (65 launched and 78 studied), 249 missions associated with these spacecraft concepts, and 309 RTG concepts (existing and new). A discussion on the RTG concepts is in Section 4. A number of spacecraft are associated with a number of mission types/subtypes at different destinations, thus, in this report, a mission is defined as a unique vector of spacecraft, mission type (e.g., lander) /subtype (e.g., rover), and target. For example, Cassini did flybys of Enceladus and the asteroid 2685 Masursky, and is still conducting science orbits around Saturn, which is considered three missions under this definition. Furthermore, there are two categories of spacecraft concepts: launched missions (e.g., Cassini, Mars Science Laboratory [MSL], etc.) and missions studied for possible future targets.

This study was conducted at the Applied Physics Laboratory (APL), NASA Glenn Research Center (GRC), NASA Goddard Space Flight Center (GSFC), and NASA Jet Propulsion Laboratory (JPL).

2.1 Targets and Destinations

2.1.1 Introduction

For the study, the team selected 63 specific targets based on visits/approaches by launched missions or suggestions in the Decadal Surveys, with a few exceptions. The targets are located at distances measured in astronomical units (AU) from the Sun, ranging from Mercury (0.39 AU) to the Kuiper Belt (44 AU), a distance spanning more than two orders of magnitude. The 63 targets include 8 planets, 23 moons, 3 minor planets, 4 dwarf planets, 5 Centaurs, 10 asteroids (including one of Jupiter's Trojans), Earth-Sun L1, and 9 comets. This section provides a discussion of many of these targets, focusing on the solar system's ocean worlds, gas giants, ice giants, and Venus.

Relevant physical data for these targets and destinations used in this study are in Appendix M, Destination Tables.

2.1.2 Ocean Worlds

Triton and Pluto/Charon/Kuiper Belt objects (KBOs) are classified together with Ceres and Mimas as possible ocean worlds [3]. This designation is based on limited science data from the Dawn (Ceres), Cassini (Mimas), New Horizons (Pluto/Charon/KBO), and Voyager (Triton) missions. The Roadmaps to Ocean Worlds (ROW) Team, chartered by the NASA Outer Planets Assessment Group (OPAG), has further identified the Saturnian icy satellites Tethys, Dione, Rhea, and Iapetus, based on Cassini data, and the Uranian icy satellites Miranda, Ariel, Umbriel, Titania, and Oberon, based on Voyager data, as possible ocean worlds [3].

NASA classified Europa, Ganymede, Callisto, Enceladus, and Titan as ocean worlds based on a solid foundation of science data provided by the Galileo (Europa, Ganymede, and Callisto) and Cassini (Enceladus and Titan) missions.

Flyby, orbiting, and landed mission concepts are possible at these worlds using launch vehicles available in the near-term. Table 2-1 lists the delivered mass for these three mission types. The delivered masses listed are the best cases over the period from 2020 to 2040. These estimates make no assumptions on margin reserves or the mass fraction of any supporting structure. The Atlas V 551 is presently available, the Delta V Heavy is being phased out, and the Space Launch System (SLS) 70 is in development.

Table 2-1. Estimates of delivered mass to ocean worlds given a few of the foreseeable launch vehicles provided by U.S. industry. See also Appendix J.

Destination	Atlas V (551) (kg)			Delta IV Heavy (kg)			SLS (70) (kg)		
	Flyby	Orbit. insert.	Landed	Flyby	Orbit. insert.	Landed	Flyby	Orbit. insert.	Landed
Ceres	2700	500	400	5000	925	820	10000	1800	1600
Europa	3000	2400	1400	5300	4200	2400	11000	8800	4100
Ganymede	3000	2200	1100	5300	3800	1900	11000	8000	4000
Callisto	3000	2900	1500	5300	5100	2500	11000	10000	5000
Mimas	4000	3000	2800	7000	5300	5000	16000	12000	11000
Enceladus	4000	3000	2750	7000	5300	4800	16000	12000	10500
Titan	4000	3000	2000	7000	6000	3500	16000	13000	8000
Triton	1300	1200	600	2350	2100	1000	4750	4500	1750
Pluto	2200	0	0	3750	0	0	7500	0	0
Charon	2200	0	0	3750	0	0	7500	0	0

For Europa (a moon of Jupiter) and Enceladus (a moon of Saturn), the oceans are hypothesized to extend beneath a protective layer of water ice down to a rocky ocean floor that might contain minerals and thermally vented energy sufficient to support life. Water from these oceans may be reaching the ice's surface through fissures. Geysers on the south pole of Enceladus observed by the Cassini spacecraft suggest such processes; Europa is expected to have similar processes. Neither of these destinations has an atmosphere defined by its pressure as $P_{\text{surf}} > 10^{-4}$ Pa. Temperatures on the surface of Europa and Enceladus are approximated at 100 K and 75 K, respectively. The worst-case predicted radiation on Europa is ~ 9.0 Mrad/day [4, 5], enough to cause severe damage to unshielded electronics, instruments, solar panels, and even RTGs.

Ice thickness on Europa may be as much as 30 km and its ocean may be as deep as 110 km from the bottom of the ice sheet to ocean floor. By comparison, Earth's Mariana Trench is 11 km deep. The pressure at a depth of 15 km in the European ice is approximately 1.8×10^7 Pa and equal to the pressure on Earth at 2 km of ocean depth. To survive these high-pressure environments, electronics, instruments, and power systems would need to be protected inside a pressure vessel. The estimated, but not optimized, mass for a Titanium alloy—in this example a Ti-6Al-4V pressure vessel, with a 0.4-m diameter and 0.8-m length, sized for 30-km ice depth—would be ~ 173 kg. A similar pressure vessel for maximum ocean depth would have a mass of 334 kg (see Table 2-2 for mass estimates).

Nine mission concepts (flyby, orbiter, and lander) have been studied for Europa and 16 (flyby, orbiter, lander, and sample return missions) for Enceladus; no deep-penetrating subsurface ice or ocean missions have been studied for either.

Table 2-2. Estimated masses of pressure vessels (PVs) for max ice thickness and ocean depths. Al 6061-T6 is from the 6000 series of aluminum alloys with a T6 temper. Ti-6Al-4V is a titanium alloy featuring high strength and low weight ratio. Inconel 625 is a nickel-based superalloy. All of these materials are corrosion resistant. These masses are for the PV only.

Destination	PV Mass (kg) for max expected ice thickness				PV Mass (kg) for max expected ocean depth			
	Al 6061-T6	Ti-6Al-4V	Inconel 625	Silicon Carbide	Al 6061-T6	Ti-6Al-4V	Inconel 625	Silicon Carbide
Ceres	102	136	210	61	0	0	0	0
Europa	130	173	264	77	260	334	496	140
Ganymede	275	352	522	147	800	920	1251	330
Callisto	261	336	499	141	386	482	698	193
Mimas	64	86	134	39	0	0	0	0
Enceladus	56	76	118	35	69	93	145	43
Titan	224	291	435	124	394	491	710	197
Triton	240	310	462	131	337	426	622	174
Pluto	244	315	469	133	288	368	544	153

Titan, a moon of Saturn, contains surface liquid ethane, methane, and propane, nested in a water ice sheet, potentially covering a water ocean. According to Cassini mission data, this ocean is expected to have a content of minerals (salt) similar to the level in the Dead Sea, and be wedged between the outer ice sheet and high-pressure ice at the bottom. Titan has an atmosphere, consisting of 98% nitrogen and 1.4% methane, extending to 600 km with an expected pressure at the surface of 1.47×10^5 Pa (Earth is 1.01×10^5). Surface temperature is around 94 K.

For Titan, the anticipated landed masses are 2,000 kg for the Atlas V (551) case, 3,500 kg for the Delta IV Heavy, and 8,000 kg for the SLS70. Quasi-static loads during entry, descent, and landing (EDL) at Titan would be expected to be less than for Mars. Expected maximum ice thickness is 100 km, and expected maximum ocean depth is 200 km. The corresponding estimated masses for ice and ocean pressure vessels are 291 and 491 kg.

Twenty-five (25) Titan mission concepts—including flybys, orbiters, an aerial balloon, a fixed-wing aircraft, landers, a rover, boats, and a submarine—have been studied; no deep penetrating subsurface ice or ocean mission concepts have been studied for Titan. For further details on these studies, see Section 2.4 and Appendix L, Intensity Matrix.

Pluto and its satellite Charon are the most-studied KBOs. Pluto's surface is composed of more than 98% nitrogen ice and its mountains are made of water ice. Radioactive elements may be heating interior water ices, leaving a subsurface ocean more than 100 km thick nested between an outer ice sheet and a rocky core. Pluto has a tenuous atmosphere consisting of nitrogen, methane, and carbon monoxide. Traces of atmospheric gases have been observed at heights of 1,670 km. Surface pressure likely varies with Pluto's distance from the Sun and were estimated at 1 Pa after the Pluto New Horizons encounter. Surface temperature was approximately 44 K. The estimated maximum ice thickness for Pluto is 260 km, and maximum ocean depth is 105 km.

Charon is a moon of Pluto. Water ices dominate the surface materials. Images from the New Horizons spacecraft suggest Charon once had an ocean that has long since frozen and expanded, causing massive surface cracks. Surface temperature is 53 K. Charon has no atmosphere. More observations are required before the ice thickness of Charon can be determined.

For Pluto and Charon, the anticipated flyby masses are 2,200 kg for the Atlas V (551) case, 3,750 kg for the Delta IV Heavy, and 7,500 kg for the SLS50. None of these launch vehicles can deliver orbiting or landed masses with chemical propulsion. A high-powered radioisotope electric propulsion (REP) system would be able to deliver an orbiter or a lander.

For additional information about possible ocean worlds, see Appendices L and M.

2.1.3 *The Gas Giants: Jupiter and Saturn*

Jupiter is primarily composed of hydrogen (~75%) and helium (~24%). It may also have a rocky core surrounded by metallic hydrogen that extends to approximately 78% of its radius. Outside of that radius, the hydrogen turns into liquid and farther out, gas. The gaseous hydrogen is expected to extend 1,000 km up to the cloud layer. The total span of Jupiter’s atmosphere is 5,000 km from its surface to deep space, where the surface is defined as the point in its atmosphere where the pressure is 100–200 kPa and the temperature is 165 K.

Fifteen mission concepts targeting Jupiter have been studied, including flybys, orbiters, atmospheric probes, and fixed-wing aerial, as well as a potential high-atmosphere sample return.

Table 2-3 provides flyby and orbiter delivered masses for Jupiter.

Saturn is like Jupiter, primarily composed of hydrogen (~75%) and helium (~24%) and may also have a rocky core surrounded by metallic hydrogen. Winds in the atmosphere can reach speeds as high 500 m/s. The atmosphere’s temperature is 134 K where pressure reaches 100–200 kPa. This temperature is slightly lower than Jupiter. Additional physical data are provided in Appendix M.

Twenty mission concepts targeting Saturn have been studied, including flybys, orbiters, and atmospheric probes. There is also a potential for fixed-wing missions; however, high winds could pose a challenge for such missions. See also Appendix L.

Table 2-3 provides flyby and orbiter delivered masses for Saturn.

Table 2-3. Estimates of delivered mass to Jupiter and Saturn in the best cases over the period from 2020 to 2040.

Destination	Atlas V (551) (kg)			Delta IV Heavy (kg)			SLS (70) (kg)		
	Flyby	Orbit. insert.	Landed	Flyby	Orbit. insert.	Landed	Flyby	Orbit. insert.	Landed
Jupiter	3500	3000		6500	5300	0	13000	11000	0
Saturn	4200	4000		7100	7000	0	16500	16000	0

2.1.4 *The Ice Giants: Uranus and Neptune*

Uranus and Neptune have a three-layer composition: a rocky core, an icy mantle, and an outer gaseous atmosphere. Uranus’s atmosphere is 83% hydrogen and 15% helium. Neptune’s atmosphere is 80% hydrogen and 19% helium. The ice mantle consists of a hot and dense fluid consisting of water, ammonia, and other volatiles, sometimes called a water-ammonia ocean. Wind speeds in the atmosphere can reach as high as 250 m/s (Uranus) and 580 m/s (Neptune). At 100 kPa pressure, the temperature is ~76 K for Uranus and ~72 K for Neptune.

Ten mission concepts targeting Neptune have been studied, including flybys, orbiters, and atmospheric probes. There is also a potential for fixed-wing missions; however, high wind speeds could pose a challenge.

Delivered masses for Uranus and Neptune are provided in Table 2-4.

Table 2-4. Estimates of delivered mass to Uranus and Neptune in the best cases over the period from 2020 to 2040.

Destination	Atlas V (551) (kg)			Delta IV Heavy (kg)			SLS (70) (kg)		
	Flyby	Orbit. insert.	Landed	Flyby	Orbit. insert.	Landed	Flyby	Orbit. insert.	Landed
Uranus	3500	2700		6100	5000	0	13500	10500	0
Neptune	3000	1300		5400	2350	0	11000	4750	0

2.1.5 Venus

The Venus atmosphere consists of 96.5% carbon dioxide, 3.5% nitrogen, and other gases, including sulphur dioxide. Surface temperature reaches more than 737 K (hotter than Mercury). Atmospheric pressure is 9.3 MPa and atmospheric density is 65 kg/m³, 50 times that of Earth's atmosphere at sea level. Thus, quasi-static loads during EDL for flown NASA missions have been in the range of 276 to 487 g's [6]. The upper bound of this range is more than 10 times that of a Mars EDL. A new EDL approach under development by NASA, the Adaptive Deployable Entry and Placement Technology (ADEPT), aims to reduce these g-loads to 20–30 g's [7], which would be in line with Mars numbers. There is speculation that life could exist in the acidic environment of the cloud layers at 50 km up from the surface, with temperatures between 303 and 353 K [8, 9, 10]. Additional physical data are provided in Appendix M.

Twelve mission concepts targeting Venus have been studied, including flybys, orbiters, atmospheric probes, aerial balloons, and surface rovers. There is also potential for fixed-wing, helicopter, subsurface, and sample return missions. See also Appendix L.

Delivered masses for Venus are provided in Table 2-5.

Table 2-5. Estimates of delivered mass to Venus in the best cases over the period from 2020 to 2040.

Destination	Atlas V (551) (kg)			Delta IV Heavy (kg)			SLS (70) (kg)		
	Flyby	Orbit. insert.	Landed	Flyby	Orbit. insert.	Landed	Flyby	Orbit. insert.	Landed
Venus	4800	1750	2400	8100	3000	4050	22000	8100	11000

2.1.6 Destination-Specific Observations

This section highlights key destination-specific facts used in this report to form the bases of requirements documented in Section 2.6.

2.1.6.1 Atmospheric Pressure

Venus, Mars, Jupiter, Saturn, Titan, Uranus, Neptune, Triton, Pluto, and Makemake have, based on our current data, surface atmospheric pressure, P_{surf} , greater than 10^{-4} Pa. Any power system used for atmospheric, surface, or subsurface exploration of these worlds would have to be able to operate in the atmospheres noted in Table 2-6.

The two mission concepts studied for Venus, nine of the 21 missions studied for Titan, one of the 15 missions studied for Saturn, four of the nine missions studied for Uranus, and three of the nine missions studied for Neptune would be operating under atmospheric conditions. The atmospheric missions to Saturn, Uranus, and Neptune would be in the form of short-term atmospheric probes. For Triton and Pluto, only flyby and orbiter missions have been studied.

Table 2-6. Destinations with an atmosphere: surface temperature, pressure, and atmospheric composition. See also Appendix M.

Destination	Surface pressure (Pa)	Temp at surface (K)	Atmosphere
Venus	9.20E+06	737	96.5% CO ₂ , 3.5% N ₂ , SO ₂ (150 ppm)
Jupiter	2.00E+05	165	75% H ₂ , 24% He
Saturn	2.00E+05	134	75% H ₂ , 24% He
Titan	1.47E+05	94	98% N ₂ , 1.4 % CH ₄
Uranus	1.00E+05	76	83% H ₂ , 15% He
Neptune	1.00E+05	72	80% H ₂ , 19% He
Triton	1.65E+00	38	N ₂
Pluto	1.00E+00	44	>99% N ₂ , 0.25 % CH ₄

2.1.6.2 Temperatures

Missions to bodies within the solar system must traverse deep space and potentially be exposed to its 4 K thermal sink. A Next-Generation RTG would need to operate in the 4 K thermal sink of deep space during cruise to any of the destinations analyzed in this report. The temperature of an RTG's housing could also be exposed to a range of temperatures depending upon the environment at a destination. For example, on Mars, at the equator at noon on a hot summer day, the MMRTG's fin-root temperature has reached as high as 465 K. This condition can be approximated with a 270 K thermal sink surrounding the MMRTG. The fin-root temperatures of any RTGs placed in a dense atmosphere will follow the atmosphere's temperatures. On Titan, this would mean an RTG's fins would drop to ~94 K if the device was left unprotected. Extreme high and low environmental temperatures will likely have to be addressed by spacecraft design rather than RTG design, as those temperatures would need to be counteracted by the use of exotic materials and design techniques that would likely make an RTG unacceptable for the vast majority of foreseeable mission concepts.

2.1.6.3 Atmospheric Composition

The atmosphere of Venus contains 150 ppm of sulfur dioxide, which forms highly corrosive sulfuric acid (H_2SO_4). External surfaces of a RTG for Venus would have to be made of materials that can withstand the corrosive effects of this atmosphere. The atmospheres of the other destinations are regarded as noncorrosive (see Table 2-7).

2.1.6.4 Radiation

On the surface of Europa, radiation can be as high as ~9.0 Mrad/day accumulated at an average rate of 100 rad/s [4, 5]. With a 2.54-mm Al shield, this value would drop to ~0.090 Mrad/day and an average accumulation rate of 1 rad/s [11]. Even in orbit around Europa, radiation levels behind a 2.54-mm of Al shield can reach 3 Mrad of total ionizing dose (TID) over 3 years [11]. The radiation on Io is estimated to be higher. For other destinations, the radiation levels are less. Hence, only power systems for surface missions to Europa and Io need to withstand extreme radiation levels throughout the duration of the mission.

2.1.6.5 EDL

Quasi-static deceleration loads imposed during hypersonic atmospheric entry for NASA missions flown at Venus saw peaks between 276 and 487 g [6]. This is ten times that of a Mars EDL. However, NASA's ADEPT system (currently under development) could reduce this to 20–30 g [7], similar to atmospheric deceleration loads at Mars. Therefore, for Venus missions utilizing the ADEPT architecture, their power systems need only be designed to meet the EDL quasi-static load requirements of a Mars mission. However, for other approaches, power systems for Venus would have to survive EDL quasi-static load requirements of 276 to 487 g.

2.1.6.6 Subsurface Exploration

For ocean worlds, ice thicknesses are expected to range from 30 km to 260 km, and ocean depths range from 30 km to more than 700 km. In some places, ice thickness may be less. For Enceladus, ice thickness for the south pole has been estimated to be about 6 km [12]. In comparison, the thickest ice sheet in Antarctica, near the Dome Summit, is 4.7 km deep. Vertical exploration of these worlds could be done either through systems connected to the surface via a tether or through tether-less systems [13]. Either system would have to be integrated into a pressure vessel to withstand the significant pressures at depths on icy bodies. A tether-less system would need a power system that provides stable power for long-lived missions, is integrated into the pressure vessel at launch, and has a thermal management system that can keep within a required temperature band during launch, cruise, and landing and into subsurface operations. These power systems would be required for subsurface ice and/or ocean missions

to the 22 destinations listed as ocean worlds and possible ocean worlds, including Europa, Enceladus, Titan, Pluto, and Charon. Only one subsurface mission has been studied, a submarine for the surface lakes of Titan.

2.2 Mission Types

2.2.1 Introduction

A review of mission concept studies and flown missions included 249 missions that visited many of the 63 targets discussed in Section 2.1.1. This review allowed the opportunity to find additional bases for requirements. These missions were categorized into seven mission types, with three types having subclasses as ordered in Table 2-7. Figure 2-1 displays the breadth of the missions reviewed and their targets. The mission types are discussed and defined in this section. The discussion includes only specific differences between the mission types. Each of the mission types relied upon spacecraft equipped with a science package, power system, navigation and control system, communication system, and command and data handling (CD&H) system, and more. To capture the intent, richness, and coverage of the missions, this report follows the terminology used by each mission.

Table 2-7. Types of missions.

Class	Flyby	Orbiter	Atmospheric Probe	Aerial			Surface				Subsurface			Sample Return
				Balloon	Fixed Wing	Helicopter	Impact	Lander	Rover	Boat	Liquid	Soil & Regolith	Ice	
Sub-class														

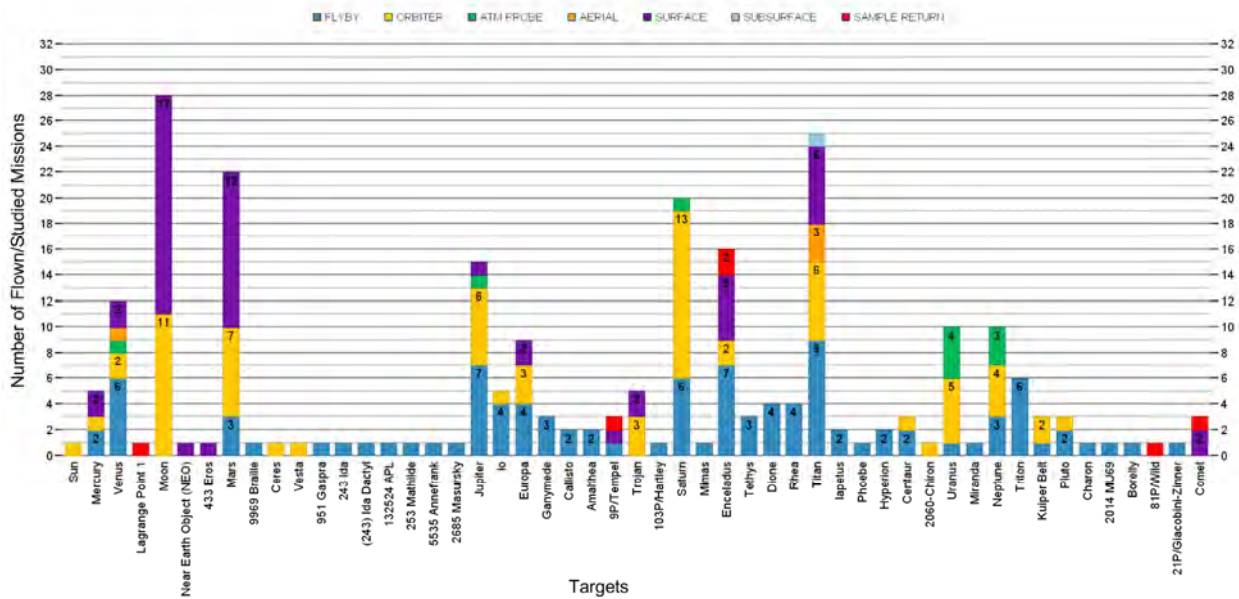


Fig. 2-1. Mission types per targets.

2.2.2 *Flyby*

There is no specific definition of a flyby. The strictest interpretation of a flyby comes from the trajectory design community: a “flyby” is a mission that delivers a spacecraft to a hyperbolic trajectory at the target body, with a closest approach to the target measured from the surface or atmosphere. In most cases, this close approach is a few hundred kilometers above the surface or atmosphere (with ringed planets, this is adjusted appropriately). No attempt is made to insert into an orbit about the target, and the spacecraft proceeds to escape the target after its flyby. This definition is used when discussing delivered flyby mass to a given destination.

Launched missions used a wider understanding of the term and could define a flyby as taking place even though the distance to the destination could be millions of km. For example, the Pioneer 11 mission lists a directed pass by Phoebe at a distance of 13.7 million km as a flyby. Of the 249 missions depicted in Fig. 2-1, 102 are defined as flybys. An example of a flyby spacecraft study is shown in Fig. 2-2.

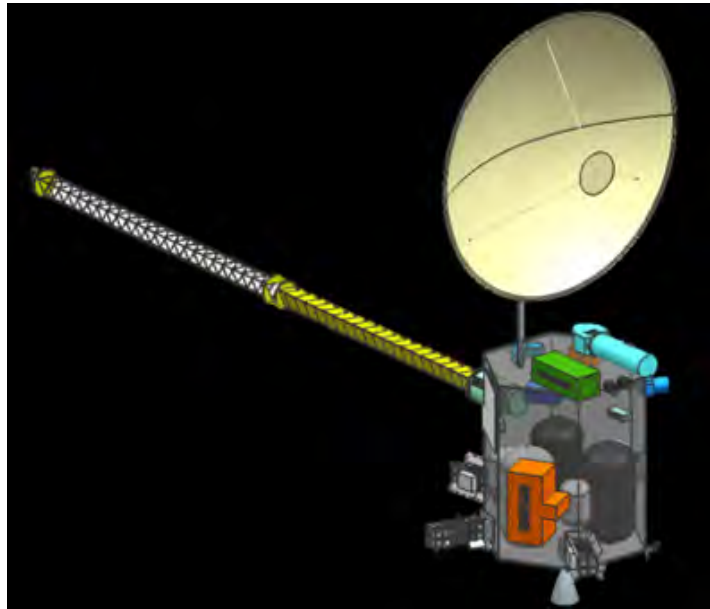


Fig. 2-2. An example from a mission concept study of a Triton flyby spacecraft dubbed TRIDENT [14].

2.2.3 *Orbiter*

From the trajectory design community: an “orbiter” approaches on the same hyperbolic trajectory as a “flyby” spacecraft, but at periapsis, executes an impulsive maneuver to reduce the orbit to an ellipse. The maneuver serves to capture the spacecraft and prevent escape from the target system. This definition is used when discussing delivered orbited mass to a given destination.

Of the 249 missions listed, 72 are defined as orbiters. An example of a flyby spacecraft study is shown in Fig. 2-3.

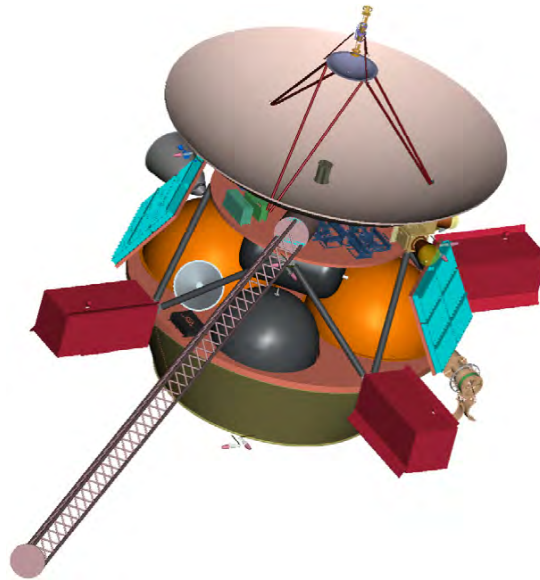


Fig. 2-3. Example of a Uranus orbiter mission concept.

2.2.4 *Atmospheric Probe*

If a destination has an atmosphere, the first order of in situ exploration has been to fly a probe into its atmosphere. An atmospheric probe is defined as a probe that is sent into the atmosphere of a destination to perform in situ analyses as it descends, suspended by a parachute and pulled downward by gravity, towards its surface or center.

Of the 249 missions listed, 10 are defined as atmospheric probes. An example of atmospheric probe mission study is shown in Fig. 2-4 [15].

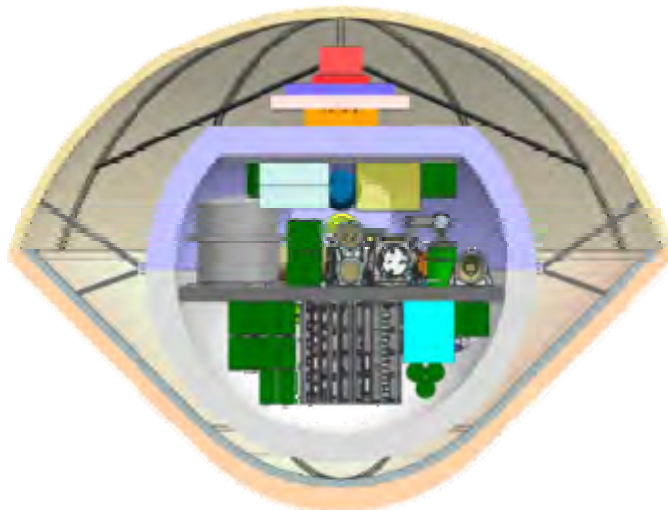


Fig. 2-4. Cutaway drawing of a concept for atmospheric probes of Uranus or Neptune.

2.2.5 *Aerial*

Aerial probes are active systems that use lift to actively move up and down and around in an atmosphere, and include balloon, fixed-wing, and helicopter subclasses. They may be able to perform multiple landings and takeoffs, and may be deployed during the EDL phase or from a lander on the surface. For more information on aerial vehicles, see Appendix B.

2.2.5.1 Balloon

Balloons would passively make vertical and horizontal excursions following atmospheric flows. There are two balloon categories: a hot air balloon (often called a Montgolfier) and a helium-filled balloon. Hot air balloon concepts seem to be preferred for Mars and Titan. For Titan, helium balloons have also been considered. For Venus, due to the high temperature, helium balloons seem to be the preferred choice. Balloons in the atmospheres of Jupiter, Saturn, Uranus, and Neptune, due to their hydrogen-rich atmospheres, would require sizes that would make them impractical.

Hot air balloons can actively control altitude through release of easily replaceable hot gasses. Helium balloons are typically meant to stay at one altitude through their lifetime. Control of altitude through the release of helium is possible but would reduce mission life.

Of the 249 missions reviewed, four are defined as balloons. An example of a balloon mission is shown in Fig. 2-5.



Fig. 2-5. A Titan Montgolfière mission concept [16].

2.2.5.2 Fixed-Wing

Fixed-wing aircraft use an airfoil(s) and speed to stay airborne. They can be passive, gliders, or active, with onboard propulsion. Both control horizontal and vertical movements by actively using elevators (vertical), a rudder (horizontal), and possibly ailerons. Other control surfaces may also be applied. Fixed-wing aircraft have been considered for Mars and Titan.

Of the 249 missions listed, one is defined as a fixed-wing aircraft. An example of a fixed-wing mission concept is shown in Fig. 2-6.



Fig. 2-6. An aerial vehicle for the in situ and Airborne Titan Reconnaissance (AVIATR) concept [17].

2.2.5.3 Helicopter

A helicopter is a rotary-winged craft. Lift and thrust are supplied by rotating lifting surfaces. This allows the helicopter to take off and land vertically, to hover, and to fly forward, backward, and laterally. A helicopter scout has been proposed for inclusion in the Mars 2020 mission.

Of the 249 missions listed, zero helicopters are included in this study. An example of a helicopter mission concept is shown in Fig. 2-7.



Fig. 2-7. Mars 2020 helicopter concept.

2.2.6 Surface

These are missions that would land on and explore a surface (i.e., liquid, ice, or soil). Four surface mission subclasses were defined: impact, lander, rover, and boat.

2.2.6.1 Impact

An impact mission is one designed to crash a spacecraft into a target to observe and analyze ejecta during impact or penetrate the surface for analysis (Deep Space 1; failed impact). Instruments are typically not expected to survive the impact.

Of the 249 missions reviewed, 10 are defined as surface-impact missions. An example of an impact spacecraft is depicted in Fig. 2-8.

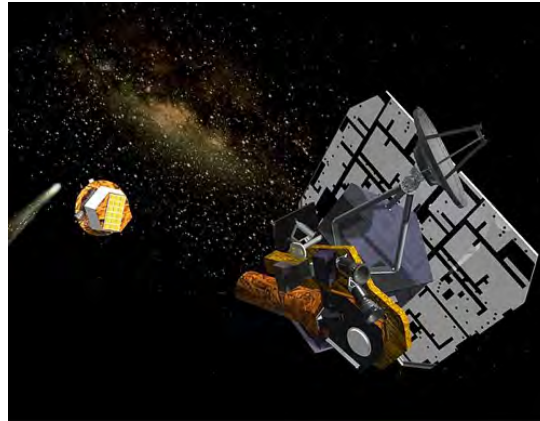


Fig. 2-8. A representation of the NASA Deep Impact spacecraft and its impactor.

2.2.7 Lander

Lander missions perform landings on the surface of a target, with the intention of operating and performing analyses for a period of time. Full functionality is expected after landing. A lander mission, as defined in this report, is stationary at the position where it landed unless moved by propulsive force. It does not include any surface mobility capabilities. Landers that can perform multiple landings and takeoffs are sometimes referred to as hoppers. A Mars hopper and a comet hopper were part of the mission set considered for this study.

Of the 249 missions listed, 31 are defined as surface-lander missions. An example of a lander mission concept is shown in Fig. 2-9.

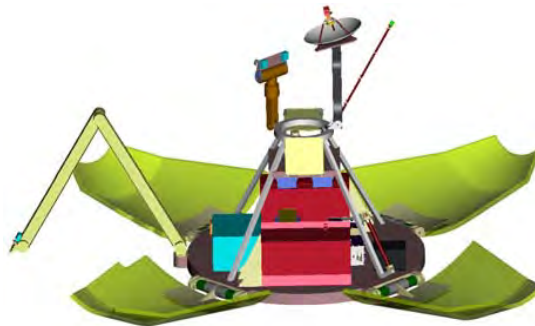


Fig. 2-9. A Titan Explorer/Lander concept [18].

2.2.7.1 Rover

Rover missions are made for surface exploration using mobility. They are self-propelled, using wheels, belts, ‘walking’, climbing, crawling, or slithering for motion.

Of the 249 missions listed, 10 are defined as surface-rover missions. An example of a rover mission concept is shown in Fig. 2-10.

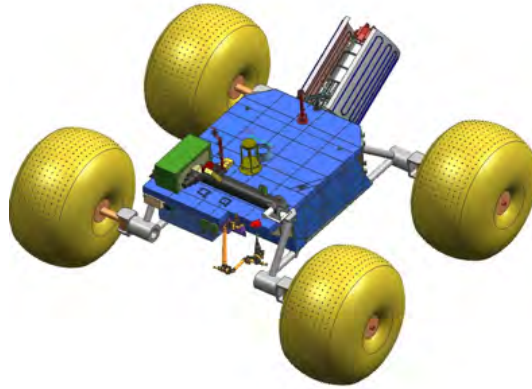


Fig. 2-10. A Titan Rover concept [19].

2.2.7.2 Boat

A separate surface mission type was defined to distinguish robots for liquid bodies from robots for solid surface exploration. A boat can passively explore lakes/oceans by riding currents. It may also be self-propelled using propellers, paddles, other types of actuators to actively explore regions or the entirety of a lake/ocean. Actuated sails may also be an option.

Of the 249 missions listed, three are defined as surface-boat missions. An example of a boat mission concept is shown in Fig. 2-11.



Fig. 2-11. A Titan lake boat concept [20].

2.2.8 Subsurface

Subsurface missions explore regions below the surface of a target. Exploring soil, liquid, and ice pose very different challenges, thus, three subsurface-mission types were defined: liquid, soil, and ice. Subsurface exploration is considered by many as essential to humankind's quest for life elsewhere.

2.2.8.1 Liquid

Subsurface exploration in liquid bodies is possible in the exposed Mare/lakes on Titan and in the ice-capped oceans expected to be found on Europa, Enceladus, and other ocean worlds (see Section 2.1).

A submarine could perform such exploration. A submarine is a pressure vessel designed to protect instruments, avionics, and other pressure-sensitive items from the high pressures found below the surface

of a liquid body. Submarines designed for Europa and Enceladus could stay submerged or move between the surface and selected depths. Submarines might have to resurface to communicate.

Of the 249 missions listed, one is defined as a subsurface-liquid mission. An example subsurface-liquid mission concept is shown in Fig. 2-12.

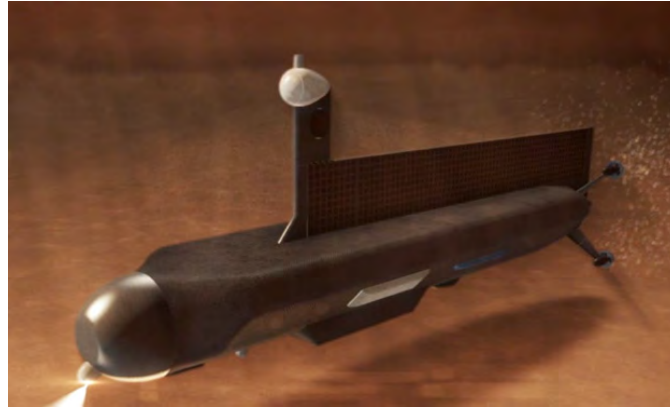


Fig. 2-12. A Titan submarine concept [21].

2.2.8.2 Soil and Regolith

Soil is comprised of minerals and organic matter. Regolith does not contain organic matter. Subsurface soil and regolith missions would be conceived to explore beneath a body's surface. This type of mission would include a separately landed drill, a drill on a lander or a rover, or a mole (tethered or untethered) that would drill itself into the surface. Shallow drills deployed by a robotic arm on a lander or rover are not considered separate missions. Current drills depths can be measured in centimeters. NASA and others are evaluating a great many drill systems to find an optimal technique, including rotary, percussive, rotary-percussive, piezoelectric, and ultrasonic. None of the reviewed missions are categorized as subsurface soil and regolith missions

2.2.8.3 Ice

Subsurface-ice missions are focused on penetrating and exploring ice layers, and potentially, the subsurface-liquid bodies on ocean worlds. These spacecraft would be exposed to very high pressures once maneuvering in an ice sheet and would have to be built, as submarines, within a pressure vessel. These spacecraft could be tethered or untethered, and could deploy drill technologies used for soil and regolith penetration or alternatives. Penetration is possible by melting the ice, which might be enhanced when combined with water jets [22]. A tethered system would not need an internal power system, and would use the tether to communicate with surface communication systems. None of the reviewed missions are categorized as a subsurface-ice mission. An example of a melt-probe spacecraft concept is shown in Fig. 2-13. More information on melt probes can be found in Appendix C.

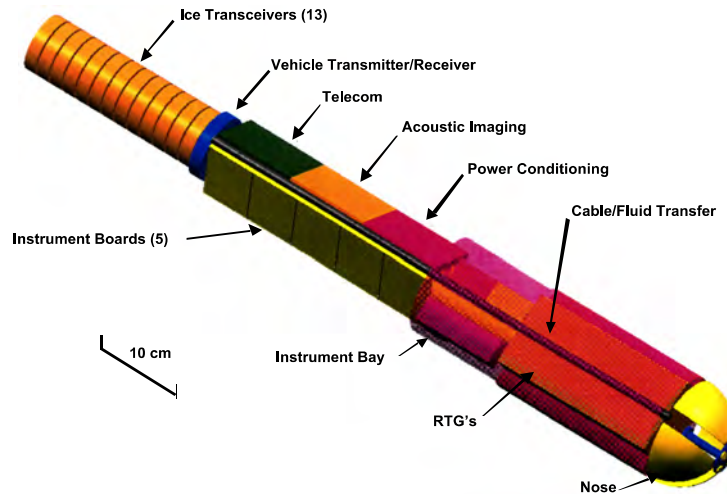


Fig. 2-13. The Cryo-Hydro Integrated Robotic Penetrator System (CHIRPS) mole concept [22].

2.2.9 Sample Return

A sample return mission is defined as a mission with the capability of returning a sample from a target to Earth. Of the 249 missions reviewed, six are designated sample return missions. An example of a sample return mission concept is shown in Fig. 2-14.

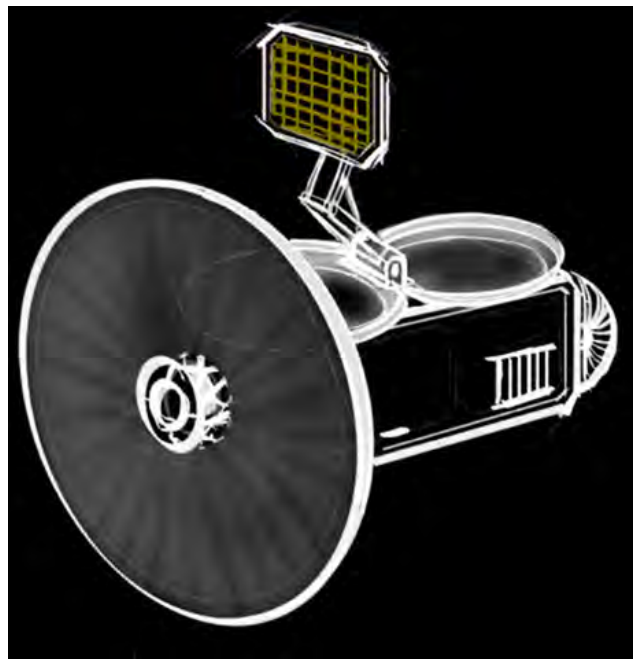


Fig. 2-14. An Enceladus sample return spacecraft concept, a sketch of the Life Investigation for Enceladus (LIFE) spacecraft [23].

2.3 Prioritized Missions

Prioritized missions, as defined in this report, are those ranked by scientists and recommended to NASA. The most respected references used in the last two decades for capturing recommended and prioritized science investigations are the National Research Council's Planetary Science Decadal Surveys [1, 2], sometimes shortened to PSDS.

NASA has launched several missions with the scope of the most recent PSDS, and is studying mission concepts to a number of targets. The PSDS prioritizes science investigations, affecting the recommended distribution of mission classes, since limited resources generally prevent them from being conducted simultaneously. The synthesis of requirements for a Next-Generation RTG concept must stem from a multitude of destinations within the solar system, from flown and studied missions, and from recently prioritized missions.

Members of the RPS Program Mission Analysis Team evaluated and assessed existing NASA PSD mission concepts to various targets across the solar system. The team relied upon priorities provided by NASA and the National Research Council. This aided the Next-Generation RTG Study Team to understand mission “pull” that is crucial to identify requirements for the next generation of RTGs. Two sources were examined: the Science Mission Directorate’s (SMD) Science Plan [24] and the 2011 PSDS.

This study uses the NASA mission class categories: Discovery, New Frontiers, and Flagship. Other NASA mission classes, such as Cubesat and SmallSat, are beyond the scope of this study.

The rightmost column of Table 2-8 lists the references to targets in the two PSDSs. The references are further categorized to indicate the source of the information and the class of mission recommended.

Table 2-8. Targets identified in PSDSs. (Atm Probe stands for atmospheric probe.)

Target	Location	Body	Decadal References
Mercury	Mercury	Planet	D1fd
Venus	Venus	Planet	D1nf, D1fd, D2nf, nf4, nf5, D2f
Moon	Earth	Moon	D1nf, D1nfd, D2nf, nf4, nf5
Mars	Mars	Planet	D1f, D2f
Asteroid	Main Asteroid Belt	Asteroid	D1nfd
Jupiter	Jupiter	Planet	D1nf, D2f
Io	Jupiter	Moon	D2nf, D1nfd, nf5
Europa	Jupiter	Moon	D1f, D1fd, D2f
Ganymede	Jupiter	Moon	D1nfd
Trojan	Jupiter Trojan	Asteroid	D1nfd, D2nf, nf4, nf5
Saturn	Saturn	Planet	D1fd, D2nf, nf4, nf5
Enceladus	Saturn	Moon	nf4, nf5, D2f
Titan	Saturn	Moon	D1fd, nf4, nf5
Centaur	Centaur (Jupiter - Neptune)	Centaur	D1nfd
Uranus	Uranus	Planet	D1fd, D2f
Neptune	Neptune	Planet	D1fd
Triton	Neptune	Moon	D1fd
Kuiper Belt			D1nf
Pluto	Kuiper Belt	Dwarf Planet	D1nf
Charon	Kuiper Belt	Moon	D1nf
Comet	Periodic Comet	Comet	D1nf, D1fd, D2nf, nf4, nf5
	Ocean World	Gas Giant	
	Possible Ocean World	Icy Giant	

Nomenclature:

- D1f: Destination selected in Decadal 1 for Flagship (f) mission
- D1nf: Destination selected in Decadal 1 for New Frontiers (nf) mission
- D1nfd: Destination selected in Decadal 1, but deferred (d) to Decadal 2, for New Frontiers (nf) mission
- D1di: Destination selected in Decadal 1 for Discovery (di) mission
- D2f: Destination selected in Decadal 2 for Flagship (f) mission
- D2nf: Destination selected in Decadal 2 for New Frontiers (nf) mission

2.3.1 *Prioritized Missions and NASA’s Mission Classes*

2.3.1.1 Science Mission Directorate Science Plan

In 2014, NASA SMD developed its newest Science Plan [24] that lays out a number of science goals in response to NASA’s Strategic Plan [25] for conducting planetary science. NASA’s Strategic Plan lists one of the objectives as, “Ascertain the content, origin, and evolution of the solar system and the potential for life elsewhere.” Table 2-9 shows science goals resulting from one of NASA’s strategic objectives and the Decadal Survey [2] priorities that follow suit. The priorities ultimately affect the recommended distribution of investigations by NASA mission class.

Table 2-9. An excerpt of SMD’s science objectives mapped to PSDS [24].

NASA Strategic Objective	Science Goals	Decadal Survey Priority
Ascertain the content, origin, and evolution of the solar system and the potential for life elsewhere.	1. Explore and observe the objects in the solar system to understand how they formed and evolve.	a. Building New Worlds—advance the understanding of solar system beginnings (1, 2)
	2. Advance the understanding of how the chemical and physical processes in our solar system operate, interact and evolve.	b. Planetary Habitats—search for the requirements for life (3, 4)
	3. Explore and find locations where life could have existed or could exist today.	c. Workings of Solar Systems—reveal planetary processes through time (1, 2, 5)
	4. Improve our understanding of the origin and evolution of life on Earth to guide our search for life elsewhere.	
	5. Identify and characterize objects in the solar system that pose threats to Earth, or offer resources for human exploration.	

2.3.1.2 Planetary Science Decadal Surveys

The PSDSs prioritize and recommend a significant number of scientific investigations [1, 2] and are used as a roadmap by NASA. Next-Generation RTG concepts should respond to the needs of the latest PSDS.

The mission concepts studied by the PSDSs and NASA fall into three categories of ambition and cost. At the high end (near \$2–2.5 billion), are the Flagship-class missions that would use highly capable spacecraft for exploration and a broad array of science investigations. These missions include the Curiosity Mars rover and its sibling, the Mars 2020 rover.

At the low end (near \$600 million), are the Discovery-class missions that conduct highly focused investigations. Teams are free to propose missions to study any solar system body except the Sun and Earth (which are studied through other programs at NASA). Ten of these planetary missions have flown successfully, including the MESSENGER spacecraft that orbited Mercury and the Dawn spacecraft that currently orbits the asteroid Ceres.

At a total cost of somewhere around \$1 billion, the New Frontiers-class missions fit between these two programs in ambition and cost. These missions are designed to address focused high-priority science questions. The scientific community selects candidate themes through the Decadal Surveys, during which a long list of scientist-proposed ideas are vetted and prioritized.

2.3.1.2.1 *Flagship-Class Missions*

Flagship-class missions are characterized as ‘large’ missions—the largest of the variety NASA’s PSD flies. These missions are typically assigned by NASA to specific flight centers.

The latest PSDS was written to cover the decade 2013 to 2022, but also identified two candidate missions for the following decade, 2023 to 2032. Flagship-class missions from that PSDS are listed in Table 2-10; four mission concepts that might rely upon an RPS are highlighted in bold text.

Table 2-10. Prioritized Flagship missions from the most recent PSDS.

Priority	Name	Power Source	Power Level (We)
1	Mars 2018 MAX-C Rover	Solar	~600
2	Jupiter Europa Orbiter	Solar	~500
3	Uranus Orbiter and Probe	RPS	~375
4	Enceladus Orbiter	RPS	~480
5	Venus Climate Orbiter	Solar	?
Missions for Next Decade			
-	Titan Saturn System Mission	RPS	~750
-	Neptune System Orbiter and Probe	RPS	~750

2.3.1.2.2 *New Frontiers–Class Missions*

The New Frontiers Program was established in 2003. The missions in the program tackle specific solar system exploration goals identified as top priorities by consensus of the planetary science community. Total cost for the development of the spacecraft, the instruments, and analysis of the returned data cannot exceed \$850 million, in fiscal year 2015 dollars (FY15\$). NASA pays separately for the mission’s launch and operation costs. Proposed mission concepts must address high-priority investigations identified within a PSDS. Figure 2-15 shows the investigations requested of proposers in the New Frontiers #4 Announcement of Opportunity and the additional investigations likely to be requested of proposers for New Frontiers #5.

Of those investigations, several have been studied with mission concepts using RPS power:

- Trojan Tour. The PSDS study developed three mission concepts: one relied upon chemical propulsion and solar power, the second on chemical propulsion and an RPS, and the third on REP and RPS. The chemical-RPS mission provided 224 W_e at the end of an 11-year mission. The 9-year REP mission provided 810 W_e at the end of its mission.
- Saturn Probe. The PSDS study traded between solar and RPS power and chose RPS. The 7-year mission provided 264 W_e at end of mission (EOM).
- Lunar Geophysical Network. The PSDS study initially had only an RPS option; however, a subsequent mission concept study demonstrated the feasibility of a solar option. The 6-year mission provided 56 W_e per lander at EOM.
- Io Observer. The PSDS study evaluated one RPS and three solar-powered options with various instrument payloads. The 9-year mission had 258 W_e at EOM.



Fig. 2-15. Candidate mission concepts from the New Frontiers #4 Announcement of Opportunity and New Frontiers #5 options [26].

2.3.1.2.3 *Discovery-Class Missions*

The Discovery Program was established in 1992, targeting smaller missions using fewer resources and shorter development times. The current cost cap is \$450M (FY15\$) per mission excluding launch vehicle and operations-phase costs. Each opportunity is an open competition for investigations at any solar system destination, except for the Earth and Sun.

There is no priority specified for Discovery-class missions in the Decadal Survey. Note that the low-cost cap can make RPS-powered mission concepts for Discovery very challenging [27].

2.3.2 *Observations on Prioritized Missions*

On today's interplanetary spacecraft, roughly between 300 W_e and 1.0 kW_e of power is required to supply power to all the computers, radio transmitters, receivers, motors, valves, data storage devices, instruments, sensors, and other devices [28].

Utilizing more power would increase the cost of the power subsystem and would likely be indicative of more instruments or more powerful instruments. With current mission cost caps, projected power

requirements for an individual spacecraft are unlikely to exceed $\sim 600 W_e$ [27]. If there were to be significant budget increases for any of the discussed mission classes, then missions requiring more power would be more likely to fly.

Note that many of the RPS-based and prioritized mission concepts discussed have been designed to the constraints of available RTGs. It is important to note that if new RTGs become available, mission designers would likely find ways to use them. For the mission concepts examined, powers have ranged from $100 W_e$ up to $1,000 W_e$, with instrument suites limited by available power. It is likely that new missions might be envisioned and enabled if a set of RTGs was available to produce power across that or an even broader range.

2.4 Summary of Mission Analyses

2.4.1 Introduction

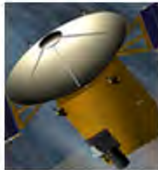
The Mission Analysis Team gathered information on past RPS mission studies by various organizations in the United States to support the Next-Generation RTG Study and crystallize an understanding of mission pull that is crucial to requirements for a next generation of RTGs. Together with the Next-Generation RTG Study Team, the RPS Program Mission Analysis Team developed and harnessed a set of RPS-based mission concepts for a database developed during this study.

The data on missions and RPS related information was collected from several sources (see Appendix A for more details):

- Studies performed for the PSDS published in 2011 [2] (The studies were performed by design centers at GRC, GSFC, JHU/APL, JPL, and MSFC.)
- Studies performed by the RPS Program Mission Analysis Team
- The non-advocate studies solicited by NASA for the Discovery mission analyses entitled the 2007 Discovery and Scout Mission Capabilities Expansion (DSMCE)
- The 2014 Nuclear Power Assessment Study (NPAS) Study [27]
- A summary of GRC COMPASS Team studies
- A summary of GSFC Mission Design Lab studies
- Other publically available mission studies conducted for NASA

In total, 77 RPS-powered spacecraft and associated mission studies were evaluated and assessed for the Next-Generation RTG Study. A synopsis of a mission report used in this study can be seen in Fig. 2-16 as a snapshot of the report output of the Next-Generation RTG Study's database; this snapshot lists a subset of useful fields from the one of the mission analyses provided for this study by the RPS Mission Analysis Team.

Io
Io Observer





Science Goals

- Test and revise models for active volcanic processes on Io.
- Determine the state (melt fraction) of Io's mantle.
- Test and revise models of tidal heating mechanisms.

Characteristics

<u>Mission Type</u>	Flyby
<u>Mission Class</u>	New Frontiers
<u>EOM Power (W_e)</u>	370
<u>Power Source</u>	ASRG
<u># Units</u>	2
<u>Status</u>	Studied
<u>Launch Date</u>	6/1/2021
<u>Launch Vehicle</u>	Atlas V 401
<u>Mission Life (y)</u>	8.5
<u>Science Duration (y)</u>	2.0
<u>Vehicle Dry Mass (kg)</u>	821
<u>Payload Mass (kg)</u>	49
<u>Propulsion System</u>	Chemical

Destination(s)

-  Jupiter
-  Io

Payload

- NAC
- Ion and Neutral Mass Spectrometer
- Thermal Mapper
- Fluxgate Magnetometers

Data Source PSDS Study Study Date 5/1/2010 Study CML 4 Organization JPL 27

The technical data in this document is controlled under the U.S. Export Regulations. Release to foreign persons may require an export authorization.

Fig. 2-16. An example of a mission concept study snapshot from the Next-Generation RTG Study database.

These 77 RPS mission studies are a subset of the 249 total missions included in the study, going to 63 targets. A summary of the statistics of the data analyzed can be found in Table 2-11.

Table 2-11. Mission Analysis Summary. The 249 mission studies reviewed were aimed at 63 targets. The table breaks down the 249 studies two ways: (1) flown missions plus RPS mission studies, and (2) mission type.

Number of Analyzed Targets	63
Total missions used in this study	249
Flown missions reviewed in the study	124
Studied mission concepts in the study	125
Total missions used in this study	249
Flyby missions (flown and studied)	102
Orbiter missions (flown and studied)	72
Atmospheric probe missions (flown and studied)	10
Aerial missions (flown and studied)	4
Surface missions (flown and studied)	54
Subsurface missions (flown and studied)	1
Sample return missions (flown and studied)	6

2.4.2 Mission Analyses for RPS

The RPS-based mission studies examined for this report cover a range of targets and power levels (Fig. 2-17). Note that the Titan missions are broken out from the other Saturn system missions, due to the unique environment at Titan and high interest displayed by several mission study teams. Altogether, 30 Saturn system mission studies were reviewed, far more than the next most common target, the Jupiter system with eight.

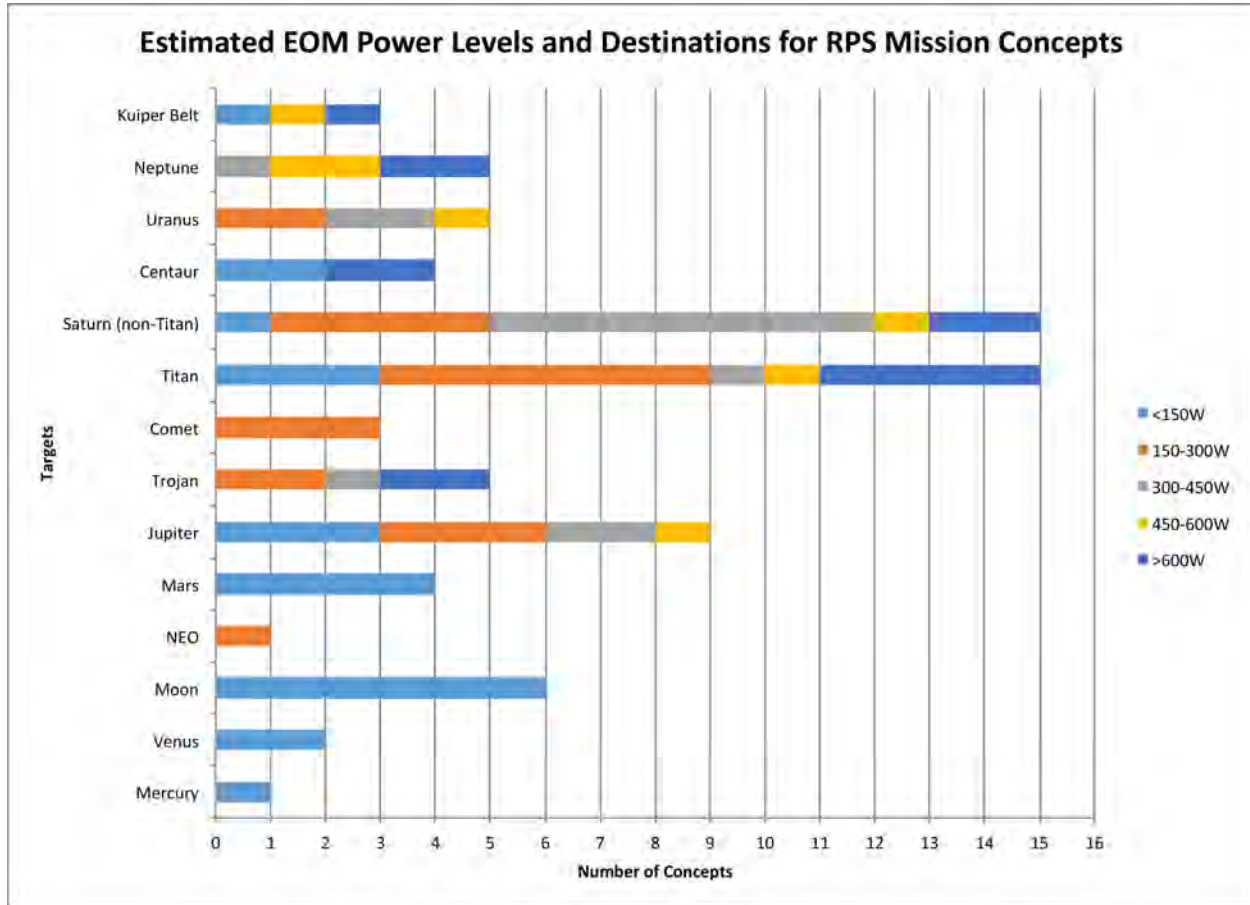


Fig. 2-17. The RPS mission studies sorted by targets and EOM power level.

The preponderance of Saturn system missions should not be surprising. Missions to targets closer than Saturn can often be accomplished using solar power, and would be less likely to be studied with RPS options. However, targets farther than Saturn are more difficult to reach, due to challenges including constrained launch masses, limited data return, need for large delta-Vs, and long travel times causing degradation in power output. These challenges are especially significant for cost-constrained missions, thus, missions to targets beyond Saturn may be less frequently studied.

Note that mission analysts have, in general, not conceived missions that use RPS outside of the ones available to them. For example, missions using 50 W_e RTGs are not to be found in this analysis as no one has proposed to develop such an RTG nor shared a concept for such an RTG with the mission analyst and scientific communities.

To illustrate a different perspective, the data used in Figure 2-17 can also be sorted by mission class, as shown in Fig. 2-18.

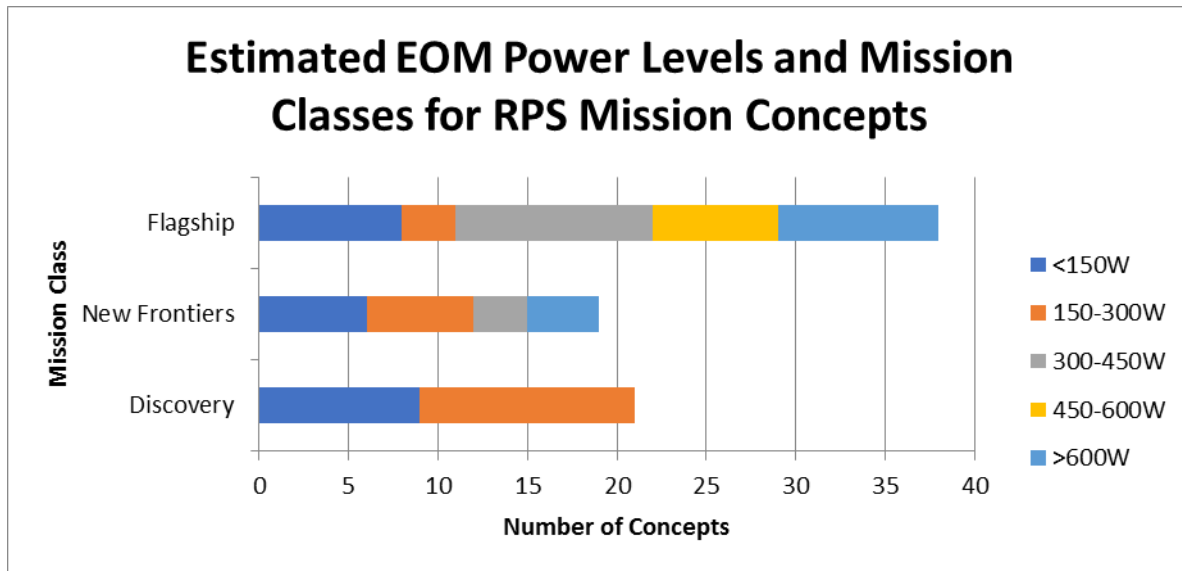


Fig. 2-18. The RPS mission concept studies sorted by mission class and EOM power level.

Discovery-class missions are extremely resource-constrained, making them especially sensitive to mass and power generation values for RPS units. The power needs in the mission studies used here are in line with the Discovery-class missions from the DSMCE studies, which were in range from 130 W_e to 325 W_e EOM.

New Frontiers-class missions are also resource-constrained, though not so much as Discovery-class missions. The power needs for the New Frontiers-class concepts used here are in line with those from the PSDS studies, in range from 170 W_e to 750 W_e EOM.

Flagship-class missions generally need more power to operate ambitious investigations with large payloads and high data return requirements. Most proposed mission power needs are in range from 150 W_e to 1,000 W_e EOM.

Altogether, it is unsurprising that nearly half of the mission concepts that could require RPS are in the Flagship class, due to the challenges in accommodating RPS.

Fig. 2-19 shows the data sorted by power level, target, and mission class in a single plot. From Fig. 2-19 it can be seen that Discovery-class RPS mission concept have not made it past 12 AU (a Centaur SmallSat study), and generally tend towards lower Sun-spacecraft distances. The New Frontier RPS mission concepts do not make it past 19 AU (Uranus), while the Flagship missions cover the breadth with the highest power levels and the farthest targets. Three missions requiring more than 1,000 W_e power, a KBO orbiter with REP, a Neptune orbiter with REP, and a Saturn ring observer, have not been included in Fig. 2-19 as outliers so as to focus on the majority of missions. Their powers ranged from 2,476 W_e to 4,105 W_e EOM.

Slicing the data slightly differently shows that the number of studied missions (only counting primary targets) that have power needs <300 W_e EOM is 47 out of 77 or 60%. Likewise, the number of missions with power needs <550 W_e EOM is 66 out of 77 or 77% and for those with power needs <820 W_e EOM, the numbers are 71 or 92%.

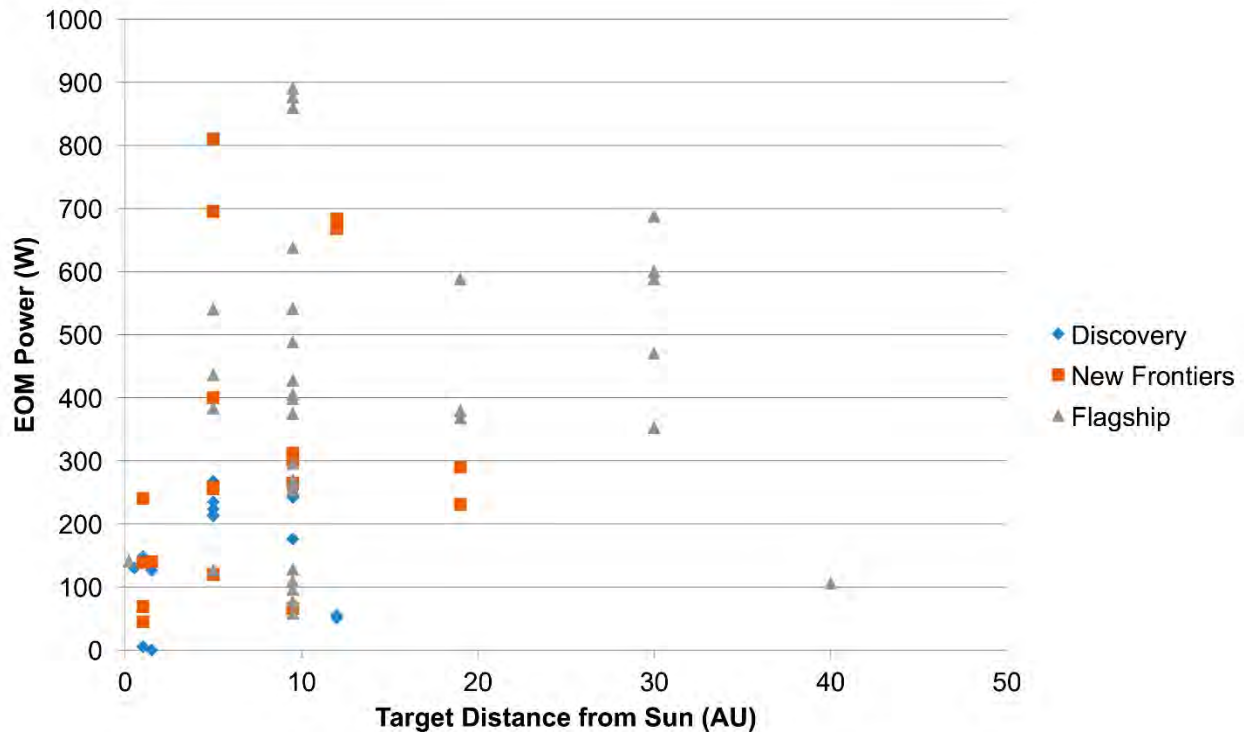


Fig. 2-19. RPS mission concept studies sorted by EOM power level, their target’s distance from Sun, and mission class. Note that 1.5 AU roughly corresponds to the distance between the Sun and Mars, 5.2 AU corresponds to Jupiter, 9.6 AU corresponds to Saturn, 19 AU corresponds to Uranus, 30 AU corresponds to Neptune, and 40 AU corresponds to Pluto.

Another item of interest for a power system is mission length. Fig. 2-20 shows mission length vs. distance to the Sun measured in AU for Flagship, New Frontiers, and Discovery missions. Mission lengths for studied missions to Mars, Venus, and the Moon are 1–11 years, to Jupiter at 5 AU is 2.5–17 years, to Saturn at 10 AU is 7–19.3 years, to Uranus at 20 AU is 13–14 years, and for Neptune at 30 AU is 13.5–18 years (Fig. 2-20). The few missions to KBOs at 40–44 AU are ~17 years.

Fig. 2-20 shows that the minimum mission length nearly doubles, 7 to 13 years, when comparing Saturn mission studies with Uranus mission studies. Mission length stays in the same range for studies of missions to Uranus and Neptune. Mission length then increases again from 13.5 to 16.5 years when going to the Kuiper Belt. The figure shows the maximum mission length for the studied RPS missions by class are: 14 years for Discovery, 17 years for New Frontiers, and 19.3 years for Flagship.

The mission studies are sorted by target and colored by mission type as a stacked bar chart in Fig. 2-21. For example, there were seven Europa missions among those analyzed: two flyby missions, three orbiter missions, and two surface missions. The surface mission type includes impact, lander, rover, and boat missions. Aerial includes balloon, fixed-wing craft, and helicopter missions. The complete list of mission types and their subclasses are in Section 2.2. This visualization includes secondary targets as well as primary targets, so a Saturn (primary target) orbiter may also perform a Dione (secondary target) flyby and be counted as both in the chart, or a Neptune (primary target) flyby might carry an atmospheric probe (secondary target).

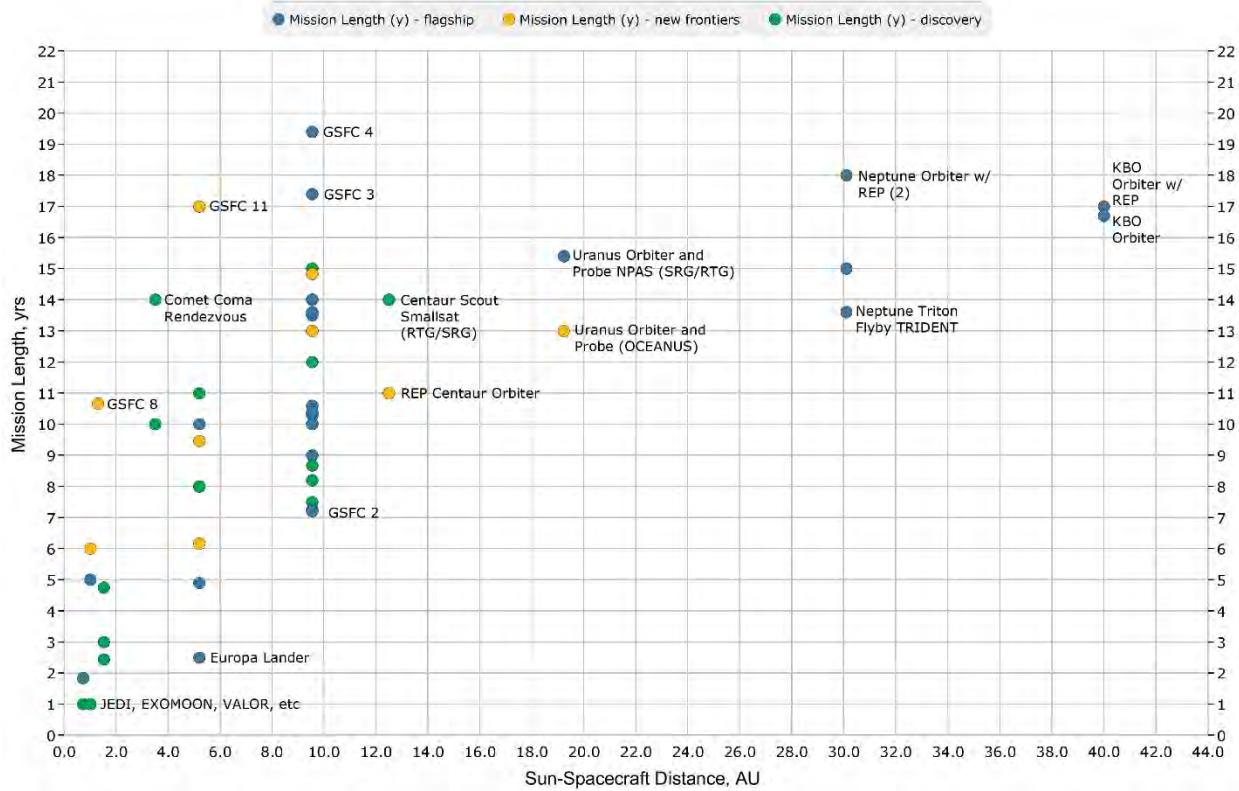


Fig. 2-20. Mission concept length plotted against distance from the Sun, measured in AU.

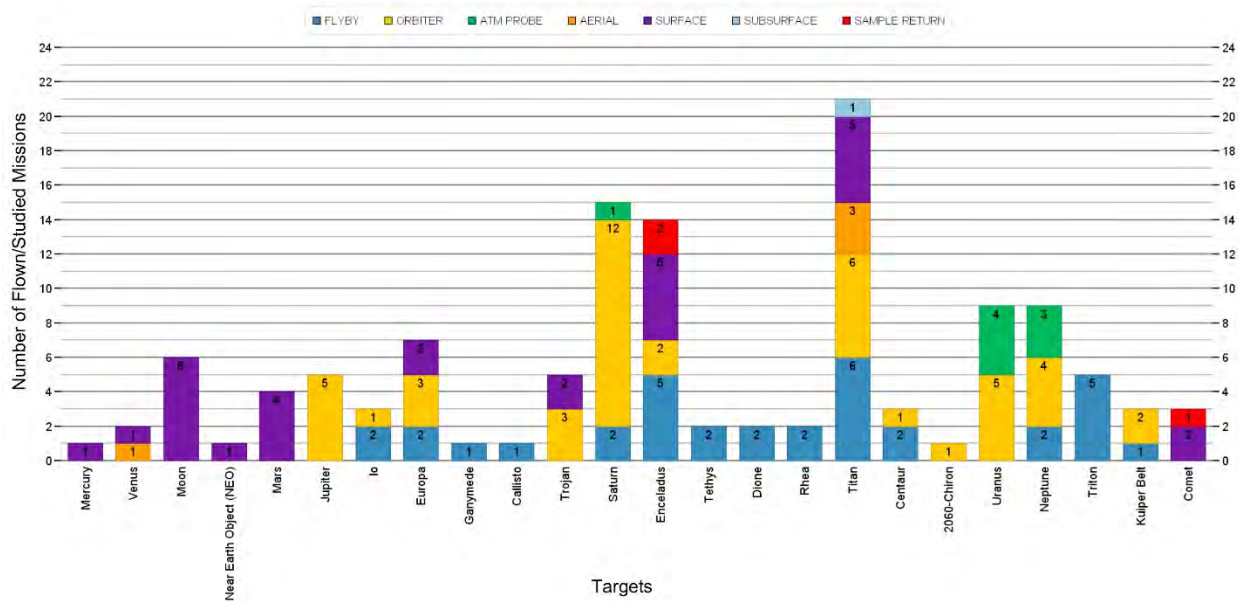


Fig. 2-21. RPS-mission concept study count by targets showing mission classes.

As might be expected, there are very few orbiter/flyby mission concepts using RPS for destinations closer than 5 AU to the Sun, as solar power is plentiful in this region. However, there are still several surface mission concepts using RPS for targets closer than 5 AU to the Sun, as solar power may be

unavailable on a body due to shadowed regions, atmospheric conditions, or long night times or where carrying solar arrays may make a mission impractical.

There is also significant interest in Enceladus and Titan lander missions. Titan stands out in general, with interest in flybys, orbiters, and in situ missions exploring Titan's atmosphere, surface, and lakes.

2.4.3 Summary

The RPS Program Mission Analysis Team gathered 77 mission concepts that would use RPS, including many with design parameters of interest to a broad community. These mission concepts were used to determine which potential RTG concepts would be applicable to many future missions, using the missions' power levels as inputs for the analysis. In addition, this analysis lent credence to the requirements documented for a Next-Generation RTG.

2.5 Mission-Specific Requirements

2.5.1 Power

Power needs for the studied spacecraft and associated missions range from less than 10 W_e to more than 1000 W_e at EOM. Sixty percent (60%) of the missions have power needs below 300 W_e at EOM, 77% below 550 W_e at EOM, and 92% below 820 W_e at EOM. This indicates that a single Next-Generation RTG, or some small number of RTGs, would have to produce 820 W_e total at EOM to meet the power demands of 92% of the studied missions; a "small number of RTGs" was used to qualify the quantity to reflect the difficulty of integrating more than four RTGs just before launch. However, with dimension and mass restrictions, a generator producing 820 W_e at EOM would in reality only be used for a mission with power demands near 820 W_e EOM. It is very unlikely missions needing only 100 W_e would fly an 820 W_e RTG. Therefore, a much more optimal solution would be to develop a modular RTG that could be procured in sizes more closely matched to the power needs of the greatest number of missions.

2.5.2 Mission Length

The MMRTG has a requirement to operate for 17 years once fueled. With an expected storage period of three years before liftoff, this translates into a flight life of 14 years. Of the mission concepts studied, 71.4% have a flight lifetime less than this. However, to meet the demands of all the studied missions, the flight lifetime requirement would have to be expanded to 19.4 years (see GSFC mission 4, an Enceladus lander in Fig. 2-20). Since mission flight durations are expanding, Next-Generation RTGs should consider total predicted lifetimes of 20–24 years.

2.5.3 Vacuum vs. Atmosphere

Of 77 studied RPS-powered mission concepts (using their primary mission type), 40 are flybys and orbiters, requiring a power source that only needs to operate in the vacuum of space. Thirty-seven (37) are aerial, surface, subsurface, and sample return mission types; 16 of those are to targets with an atmosphere and 21 are to targets without one. This means that nearly 80% (61/77) of the missions studied only need a power source that can operate in the vacuum of space, suggesting a Next-Generation RTG should be very similar to a GPHS-RTG in this matter.

2.6 Requirements

2.6.1 Introduction

In this section, the destination- and mission-specific requirements (derived in Sections 2.1 and 2.3), together with launch and other environment characteristics and MMRTG and GPHS-RTG requirements, are analyzed to recommend a set of requirements for Next-Generation RTG concepts.

2.6.2 Approach

Requirements were extracted from selected GPHS-RTG and MMRTG documents and aligned with launch vehicle environment characteristics and destination- and mission-specific requirements. This ensures Next-Generation RTG concepts could be launched on relevant launch vehicles and utilized on missions (Section 2.3) of different types (e.g., flyby, surface, subsurface, etc.) and subtypes (e.g., lander, rover, boat, etc.) to the targets in the reviewed studies and the destinations discussed in Section 2.1.

The resulting requirements are shown in Tables 2-13 (Performance), 2-14 (Physical and Structural), and 2-15 (Environment).

2.6.3 GPHS-RTG- and MMRTG-Derived Requirements

The Next-Generation RTG concepts could either operate in only the vacuum space or in vacuum and atmospheres. Requirements for RTGs developed for operation in either environment, the GPHS-RTG (vacuum) and the MMRTG (atmospheres), were therefore considered. This also provided a solid foundation based upon qualified and proven designs from which to consider new and novel requirements for a next generation of RTGs.

Initially, some 20 GPHS-RTG and MMRTG requirements documents and related articles were reviewed to get a comprehensive understanding of which documents were the most appropriate to use. From those 20, six specific requirements documents were selected for an in-depth review to capture key requirements. These were structured into a table as a starting point and formed the basis of the requirements in Section 2.6.6, Requirements Tables.

2.6.4 Launch Vehicle Environment Characteristics

Actual and predicted launch environments were considered for the Next-Generation RTG concepts when adequate information was available. The Cassini spacecraft is powered by three GPHS-RTGs and was launched on a Titan IV (401)B/Centaur, and MSL is powered by one MMRTG and was launched on an Atlas V (541). The Titan family of rockets was retired in 2005. The Atlas V family of rockets is therefore the only existing launch vehicle that has flown an RTG at this time.

Next-Generation RTGs could be launched on an Atlas V [29], Delta IV Heavy [30], or the SLS70 (Block 1A or B) [31] rockets, as well as on comparable, but currently ill-defined launch vehicles such as the Vulcan [32]. Next-Generation RTGs could be flown on a number of different types of spacecraft. At this point, the mounting geometries of any RTG concept and how they would be integrated before launch are unknowns. Only a very early first order analysis can therefore be done at this time. For this analysis, it was decided to focus on the quasi-static load factors, acoustics (launch fairing internal overall sound pressure level [OASPL]), and shock levels (Table 2-12).

Table 2-12. Potential requirements on Next-Generation RTG concepts vs. launch vehicle specification. Quasi-static load factors are unit-less, OASPL is in dB, and shock is in g's.

	Next-Generation RTG Requirements	Atlas V (500 Series) [25]	Delta IV H [26]	SLS70 (1B) (Goal)
Quasi Static Load Factors	25	Lat: -2 to 2; Axi: -2 to 6	Lat: -2 to 2; Axi: -2 to 6	NA
Acoustics – internal (OASPL)	143	138.1	143.1	141.3 / 144.7 [27]
Shock	6000 g	1500–10,000 Hz, 4500 G	1400–10,000 Hz, 5000 G	800–8000 Hz; 3000 G; 10,000 Hz; 4000 G

The OASPL for the Delta IV Heavy and SLS70 [31] are similar and the Atlas V has a lower OASPL (Table 2-12). The numbers for the SLS70 are goals and estimates at this point—NASA has made no formal release of the SLS launch environments; therefore, these numbers are expected to change. None of the launch vehicles have quasi-static loads near the 25 quasi-static load requirement. The same goes for

the 6,000 g shock value. The Titan IV A rocket had similar values: OASPL 139.1, max shock values of 2,000 g at 5,000 Hz [33]. The Titan IV (401)B/Centaur combination had a 25% increase in thrust capability compared to the Titan IV A version. This should place the launch environments of the Titan IV B very close to the Atlas V (541) [29], Delta IV Heavy [30], or the SLS70 (Blocks 1A and B) [31].

2.6.5 Destination- and Mission-Specific Derived Requirements

2.6.5.1 Atmospheric Pressures

Venus, Mars, Jupiter, Saturn, Titan, Uranus, Neptune, Triton, Pluto, and Makemake have surface atmospheric pressures of $P_{\text{surf}} > 10^{-4}$ Pa. Ergo, any power system used for exploring these worlds would have to be able to operate in these atmospheres. Twenty of the missions studied would be operating in an atmosphere using $> 10^{-4}$ Pa as the definition of an atmosphere.

2.6.5.2 Temperatures

No new or novel temperature requirements were identified for Next-Generation RTG concepts. However, modifications to a Next-Generation RTG concept would be required for it to operate in an atmosphere with a ~ 94 K temperature, as on Titan. This could include thin insulation on the outside of the RTG housing after its fins have been removed. Next-Generation RTGs should consider a requirement to finless and finned generators to enable unforeseen mission concepts.

2.6.5.3 Radiation

The MMRTG requirements specify a maximum MMRTG TID of 4 Mrad. After evaluating the radiation environments across the solar system, it was decided to keep the TID requirement of 4 Mrad. Based on cursory estimates, a Next-Generation RTG concept should be able to operate on the surface of Europa behind 2.5 mm of Al for 45 days assuming the radiation susceptibility of an MMRTG; it is likely a Next-Generation RTG could be designed to eliminate the weaknesses of the MMRTG under an extreme radiation environment. Under 1 m of ice, a generator's operational lifetime could exceed its design lifetime. Such a capability would be welcome for a multiyear subsurface mission [4, 5, 6]. A Next-Generation RTG developed to the same radiation requirements as the MMRTG should be able to operate for four years in orbit around Europa.

2.6.5.4 EDL

The quasi-static load requirement for the MMRTG was changed in 2007 from 40 g's to 25 g's [7]. The MMRTG can support these high-values because of its internal design, which effectively supports the thermoelectric couples in high-g environments. It was decided to use the lower number for the Next-Generation RTG concepts, but it should be noted that concepts that do not structurally support the TECs as the MMRTG may be suspect. This requirement would make it possible the Next-Generation RTG to go through EDL for Mars and Titan, and for Venus, if an ADEPT-type EDL system is used [7]. A specialized RTG would be needed for a 'traditional' Venus EDL of 276–487 g [6].

2.6.5.5 Subsurface Exploration

Penetrating ice sheets of the ocean worlds or other icy bodies will likely require a power system integrated into a pressure vessel, and the lower the diameter of the vessel, the more quickly such a vehicle could descend through the ice. To minimize frontal area, a Next-Generation RTG for these missions should be integrated into a finless pressure vessel. This would require a thermal management system external to the RTG to keep the RTG within the required temperature bounds through ground operations, launch, cruise, and landing. Once landed and deployed, presumably, any additional temperature control system could be jettisoned. A specialized Next-Generation RTG would need to be developed to meet these requirements.

2.6.5.6 Power

Converting EOM power estimates to BOM power estimates ($P_{\text{BOM}} = P_{\text{EOM}} * e^{rtm}$) for mission concepts with very similar EOM needs shows that 60% of the studied missions can be covered by a set of Next-Generation RTGs producing up to 421 W_e at BOM (300 W_e at EOM), 77% by a set producing up to 733 W_e at BOM (550 W_e at EOM), and 92% by a set producing systems up to 961 W_e at BOM (820 W_e at EOM). Having modular RTGs would be of great benefit to the user community based upon this breakdown.

2.6.5.7 Mission Length

The MMRTG has the requirement to operate for 17 years once fueled. With a storage period of three years before liftoff, this translates into a flight life of 14 years. Of the missions studied, 71.4% have a flight lifetime less than this. However, to meet the demands of all the studied missions, the flight lifetime requirement would have to be expanded to 19.4 years (see GSFC mission 4, an Enceladus lander in Fig. 2-20). Since mission flight durations are expanding, Next-Generation RTGs concepts should consider total lifetimes of 20–24 years.

2.6.6 Requirement Tables

The draft requirements for Next-Generation RTG concepts are shown in the Tables 2-13 to 2-15.

Table 2-13. Draft performance requirements for Next-Generation RTG concepts. The columns labeled GPHS-RTG, MMRTG, and eMMRTG contain information available from specifications and reports. The columns for the Next-Generation RTG concepts contain draft requirements.

Parameter	GPHS-RTG	MMRTG	eMMRTG	SMRTG	CSMRTG	HSMRTG	CHSMRTG	SRTG	CSRTG	References
P_0 - BOL (We) ⁽¹⁾	291	110	148	See Appendix P, Modeling Results for RTG Concepts						GPHS-RTG [35,36] MMRTG [37]
Efficiency - $P_e/Q_0 \cdot 100$ (%)	6.60%	5.50%	7.40%	See Appendix P, Modeling Results for RTG Concepts						Calculated
Specific Power - P_e/m_{th} (We/Kg)	5.11	2.44	3.29	See Appendix P, Modeling Results for RTG Concepts						Calculated
Q_0 - BOL (Wth) ^(4, 5)	4410	2000	2000	See Appendix P, Modeling Results for RTG Concepts						GPHS-RTG [35,36] MMRTG [37]
Average annual power degradation, r (%/yr)	1.85	4.8	2.5 ⁽²⁾	1.9 ⁽²⁾	1.9 ⁽²⁾	1.9 ⁽²⁾	1.9 ⁽²⁾	1.9 ⁽²⁾	1.9 ⁽²⁾	GPHS-RTG [35,36] MMRTG [37]
$P_{BOM} = P = P_0 \cdot e^{-rt}$ (We)	NA	110	NA	See Appendix P, Modeling Results for RTG Concepts						Calculated
Fueled storage life, t_s (years)	2	3	3	3	3	3	3	3	3	GPHS-RTG [35] MMRTG [37]
$P_{EODL} = P = P_0 \cdot e^{-rt}$ (We)	NA	NA	80	See Appendix P, Modeling Results for RTG Concepts						Calculated
Design Life, t_d (Years)	16	17	17	17	17	17	17	17	17	GPHS-RTG [35,36] MMRTG [37]
Allowable Flight Voltage Envelope (V)	22-36	22-36	22-34	22-34	22-34	22-34	22-34	22-34	22-34	GPHS-RTG [35,36] MMRTG [37]
Allowable Flight Finroot Temperature Envelope (°C)	<260	50-200	50-200	50-200 ⁽³⁾	50-150 ⁽³⁾	50-200 ⁽³⁾	50-150 ⁽³⁾	50-200 ⁽³⁾	50-150 ⁽²⁾	GPHS-RTG [35,36] MMRTG [37]
Open Circuit Time (min)	<3	<4	<4	<4	<4	<4	<4	<4	<4	GPHS-RTG [38] MMRTG [34]
Vacuum of Space (Y/N)	Y	Y	Y	Y	Y	Y	Y	Y	Y	GPHS-RTG [35,36] MMRTG [37]
Planetary Atmospheres (Y/N)	N	Y	Y	N	N	Y	Y	N	N	GPHS-RTG [35,36] MMRTG [37]

Notes (Tables 2-13 to 2-15)

⁽¹⁾ P_0 was calculated based on Q_0 at $T_{fr} = 157^\circ\text{C}$ and $T_{fr} = 55^\circ\text{C}$

⁽²⁾ Design goal

⁽³⁾ These fin-root temperature envelopes are for flight and allow operation in a 4 K thermal sink in vacuum and a 270 K thermal sink as estimated for Mars on a hot, sunny day at the equator

⁽⁴⁾ Measured at 1 meter

Table 2-14. Draft physical and structural requirements for Next-Generation RTG concepts. The columns labeled GPHS-RTG, MMRTG, and eMMRTG contain information available from specifications and reports. The columns for the Next-Generation RTG concepts contain draft requirements.

Parameter	GPHS-RTG	MMRTG	eMMRTG	SMRTG	CSMRTG	HSMRTG	CHSMRTG	SRTG	CSRTG	References
TEC Redundancy Approach	Series-parallel	Series-parallel	Series-parallel	Series-parallel	Series-parallel	Series-parallel	Series-parallel	Series-parallel	Series-parallel	GPHS-RTG [35,36] MMRTG [37]
Mass - m (kg)	57	45	45	See Appendix P, Modeling Results for RTG Concepts						GPHS-RTG [35,36] MMRTG [37]
Dimensions, d x l (m)	0.422 x 1.14	0.65 x 0.69	0.65 x 0.69							GPHS-RTG [35,36] MMRTG [37]
Mission-to-Mission Interchangeability	Y	Y	Y	Y	Y	Y	Y	Y	Y	GPHS-RTG [38] MMRTG [34]
Thermal Control	Fluid Loops (Water/28 ± 2% ethyl alcohol)	Fluid Loops (CFC11/Freon)	Fluid Loops (CFC11/Freon)	Fluid Loops (CFC11/Freon)	Fluid Loops (CFC11/Freon)	Fluid Loops (CFC11/Freon)	Fluid Loops (CFC11/Freon)	Fluid Loops (CFC11/Freon)	Fluid Loops (CFC11/Freon)	GPHS-RTG [35,36] MMRTG [37]
Cover Gas for Ground Ops, Vented at Launch (Y/N)	Y	N	N	Y	Y	N	Y	Y	N	GPHS-RTG [38] MMRTG [34]
Factors of Safety	See Appendix Q, Factors of Safety – GPHS-RTG and MMRTG	See Appendix Q, Factors of Safety – GPHS-RTG and MMRTG	See Appendix Q, Factors of Safety – GPHS-RTG and MMRTG	See Appendix R, Next-Generation RTG: Factors of Safety, Acoustics, and Random Vibrations	See Appendix R, Next-Generation RTG: Factors of Safety, Acoustics, and Random Vibrations	See Appendix R, Next-Generation RTG: Factors of Safety, Acoustics, and Random Vibrations	See Appendix R, Next-Generation RTG: Factors of Safety, Acoustics, and Random Vibrations	See Appendix R, Next-Generation RTG: Factors of Safety, Acoustics, and Random Vibrations	See Appendix R, Next-Generation RTG: Factors of Safety, Acoustics, and Random Vibrations	[39]
Primary Modal Frequency (Hz)	NA	> 50	> 50	> 50	> 50	> 50	> 50	> 50	> 50	GPHS-RTG [38] MMRTG [34]

Notes (Tables 2-13 to 2-15)

(1) P_0 was calculated based on Q_0 at $T_{fr} = 157^\circ\text{C}$ and $T_{fr} = 55^\circ\text{C}$

(2) Design goal

(3) These fin-root temperature envelopes are for flight and allow operation in a 4 K thermal sink in vacuum and a 270 K thermal sink as estimated for Mars on a hot, sunny day at the equator

(4) Measured at 1 meter

Table 2-15. Draft environmental requirements for Next-Generation RTG concepts. The columns labeled GPHS-RTG, MMRTG, and eMMRTG contain information available from specifications and reports. The columns for the Next-Generation RTG concepts contain draft requirements.

Parameter	GPHS-RTG	MMRTG	eMMRTG	SMRTG	CSMRTG	HSMRTG	CHSMRTG	SRTG	CSRTG	References
Quasi-static acceleration (g) (Q/FA)	NA/40	NA/25	NA/25	NA/25	NA/25	NA/25	NA/25	NA/25	NA/25	GPHS-RTG [29] MMRTG [34]
Random Vibration - GRMS (g) (Q/FA)	7.44/4.79	10.54/7.45	10.54/7.45	7.44/4.79	7.44/4.79	7.44/4.79	7.44/4.79	7.44/4.79	7.44/4.79	GPHS-RTG [35,36] MMRTG [37]
Acoustic Sound Pressure (Overall) (db) (Q/FA)	147/143	146.1/143.1	146.1/143.1	147/143	147/143	147/143	147/143	147/143	149/145	GPHS-RTG [35,36] MMRTG [37]
Pyrotechnic shock load (g) (Q/FA)	NA/4000	6000/NR	6000/NR	6000/NR	6000/NR	6000/NR	6000/NR	6000/NR	6000/NR	GPHS-RTG [35,36] MMRTG [37]
Magnetic Field Emissions (nT) ⁽¹⁾	<78	<25	<25	Scaled by module relative to the GPHS-RTG (18 module) value of 78 nT						GPHS-RTG [38] MMRTG [34]
Neutron emission rate (#n/s/g-PuO2)	<7000	<8000	<8000	<8000	<8000	<8000	<8000	<8000	<8000	GPHS-RTG [35,36] MMRTG [37]
Gamma emission rate (#s/g-PuO2)	NA	<5E+10	<5E+10	<5E+10	<5E+10	<5E+10	<5E+10	<5E+10	<5E+10	GPHS-RTG [35,36] MMRTG [37]
Max External Total Ionizing Dose (TID) (Mrad)	NA	4	4	4	4	4	4	4	4	GPHS-RTG [35,36] MMRTG [37]
Radiation Design Factor (RDF)	NA	2	2	2	2	2	2	2	2	GPHS-RTG [38] MMRTG [34]
Sterilization Temperature (°C) (Min/Finroot Max)	NA	110/191	110/191	110/191	110/191	110/191	110/191	110/191	110/191	GPHS-RTG [38] MMRTG [34]
Venus Gravity Assist (VGA)	Thermal shield reqd	Multiple	Multiple	Multiple	Thermal shield reqd	Multiple	Thermal shield reqd	Multiple	Thermal shield reqd	GPHS-RTG [35,36] MMRTG [37]

Notes (Tables 2-13 to 2-15)

⁽¹⁾ P₀ was calculated based on Q₀ at T_{fr} = 157°C and T_{fr} = 55°C

⁽²⁾ Design goal

⁽³⁾ These fin-root temperature envelopes are for flight and allow operation in a 4 K thermal sink in vacuum and a 270 K thermal sink as estimated for Mars on a hot, sunny day at the equator

⁽⁴⁾ Measured at 1 meter

2.6.6.1 Requirements Explained

P_0 – Power at BOL (We):	Calculation is explained in Appendix P, Modeling Results for RTG Concepts
Efficiency - P_0/Q_0*100 (%):	Calculation is explained in Appendix P, Modeling Results for RTG Concepts
Specific Power - P_0/m (We/Kg):	Calculation is explained in Appendix P, Modeling Results for RTG Concepts
Q_0 – Thermal Inventory at BOL (Wth):	Calculation is explained in Appendix P, Modeling Results for RTG Concepts
Average Annual Power Degradation, r (%/yr):	The degradation rate was set to the actual value for the Cassini spacecraft GPHS-RTGs, 1.85 % and then rounded to 1.9%.
$P_{BOM} - P=P_0*e^{-rt_s}$ (We):	Calculation is explained in Appendix P, Modeling Results for RTG Concepts
Fueled Storage Life, t_s (years):	Time from when an RTG is fueled to launch. The requirement was set to three years based upon the MMRTG requirement. Fueled storage life for a GPHS-RTG was two years.
$P_{EODL} - P=P_0*e^{-rt_{ll}}$ (We):	Calculation is explained in Appendix P, Modeling Results for RTG Concepts
Design Life, t_l (Years):	Set to 17 years, derived from both the GPHS-RTG and MMRTG requirements. Both have mission lifetime requirements of 14 years. These requirements were aligned with the mission lifetimes and found acceptable. See also Section 2.5.5.7.
Allowable Flight Voltage Envelope (V):	Set to 22–34 V DC as derived from the MMRTG requirements
Allowable Flight Fin-root Temperature Envelope:	Set to 50–200°C as derived from the MMRTG
Open Circuit Time (min):	Set to <4 minutes as derived from the MMRTG requirements
Vacuum of Space (Y/N):	All Next-Generation RTG concepts, as well as the GPHS-RTG and the MMRTG, are to be able to operate in the vacuum of deep space.
Planetary Atmospheres (Y/N):	Some types of Next-Generation RTGs will be required to operate under atmospheric conditions.
TEC Redundancy Approach:	Derived from the MMRTG design, series-parallel wiring of TECs
Mass (kg):	See Appendix P, Modeling Results for RTG Concepts
Dimensions (m):	See Appendix P, Modeling Results for RTG Concepts
Mission-to-Mission Interchangeability:	This has been a requirement since the GPHS-RTG; one RTG must be interchangeable with the next of the same design.
Thermal Control:	Fluid loops derived from the MMRTG requirements

Cover Gas for Ground Ops, Vented at Launch (Y/N):	For Next-Generation RTG concepts that operate as vacuum-only, cover gas needs to be vented at launch, derived from the GPHS-RTG. For concepts that will operate in an atmosphere, such venting will not be required.
Factors of Safety:	See Appendices Q and R
Primary Modal Frequency (Hz):	Set to >50 Hz as derived from the MMRTG requirements
Quasi-static Acceleration (g):	Set to 25 g for qualification as derived from the MMRTG requirements. The number was aligned with the EDL requirements for destinations such as Mars, Titan, and with special treatment at Venus, and found acceptable.
Random Vibration - G_{RMS} (g):	G_{RMS} was set to 7.44 for qualification (Q) and 4.79 g for Flight Acceptance (FA), derived from the GPHS-RTG requirements. See also Appendix R.
Acoustic Sound Pressure (Overall) (dB):	Set to 147/143 dB for qualification and Flight Acceptance respectively as derived from the GPHS-RTG requirements. See also Appendix R.
Pyrotechnic Shock Load (g):	Set to 6,000 g's for qualification
Magnetic Field Emissions (nT):	Scaled by generator size and derived from the GPHS-RTG requirements
Neutron Emission Rate (#n/s/g-PuO ₂):	Set at <8,000 as derived from the MMRTG estimates
Gamma Emission Rate (#/s/g-PuO ₂):	Set at $<5 \times 10^{10}$ as derived from the MMRTG estimates
Total Ionizing Dose (TID) (Mrad):	Set at 4 as derived from the MMRTG requirements
Radiation Design Factor (RDF):	Set to 2 as derived from MMRTG requirements
Sterilization Temperature (°C) (Min/Fin-root Max):	Set to 110/191 as derived from MMRTG requirements
Venus Gravity Assist (VGA):	Next-Generation RTG concepts designed to an operating point of $T_{fr}=55^{\circ}\text{C}$ would require a thermal shield and would be required to maintain the low T_{fr} temperature during the VGA maneuver. Next-Generation RTG concepts operating at $T_{fr}=157^{\circ}\text{C}$ do not need such a shield, and multiple VGAs could be performed. These requirements are derived from the GPHS-RTG ($T_{fr}=55^{\circ}\text{C}$) and the MMRTG ($T_{fr}=55^{\circ}\text{C}$) requirements.

2.7 References

- [1] National Research Council of the National Academies. 2003. *New Frontiers in the Solar System: An Integrated Exploration Strategy*. Washington, DC: The National Academies Press. doi: 10.17226/10432.

- [2] National Research Council of the National Academies. 2011. *Vision and Voyages for Planetary Science in the Decade 2013–2022*. Washington, DC: The National Academies Press. doi: 10.17226/13117.
- [3] Hendrix, A. and T. Hurford. February 2017. Roadmaps to Ocean Worlds: OPAG Update. Atlanta, GA.
- [4] Paranicas, C., J.F. Cooper, H.B. Garrett, R.E. Johnson, and S.J. Sturmer. 2009. “Europa’s Radiation Environment and Its Effects on the Surface,” *Geophys Res Lett*, 539. doi: 10.1029/2007GL030834.
- [5] Paranicas, C., J.M. Ratliff, B.H. Mauk, C. Cohen, and R.E. Johnson. 2002. “The Ion Environment of Europa and its Role in Surface Energetics,” *Geophys Res Lett.*, 29. doi: 10.1029/2001GL014127.
- [6] Dutta, S., B. Smith, D. Prabhu, and E. Venkatapathy. 2012. “Mission Sizing and Trade Studies for Low Ballistic Coefficient Entry Systems to Venus,” IEEEAC 1343, 2, IEEE Aerospace Conference, Big Sky, MT, March 2012.
- [7] Venkatapathy, E., L. Glaze, D. Prabhu, B. Smith, B. Yount, A. Makino, et al. 2012. “A Game Changing Approach to Venus In-Situ Science Missions Using Adaptive Deployable Entry and Placement Technology (ADEPT),” International Planetary Probe Workshop, Toulouse, France, June 19, 2012.
- [8] Mullen, L. 2002. “Venusian Cloud Colonies,” *Astrobiology Magazine*, November 13, 2002.
- [9] Landis, G.A. 2003. “Astrobiology: The Case for Venus,” *Journal of the British Interplanetary Society*, 56 (7–8): 250–254, July 2003. Bibcode:2003JBIS...56..250L. NASA/TM—2003-212310.
- [10] Cockell, C.S. 1999. “Life on Venus,” *Planetary and Space Science*, 47 (12): 1487–1501. Bibcode:1999P&SS...47.1487C. doi:10.1016/S0032-0633(99)00036-7, 12/1999.
- [11] Pich, M. S-S. de, H.B. Garrett, R.W. Evans, I. Jun., W. Kim, and C. Paranicas. 2016. “The GIRE2 Model and Its Application to the Europa Mission,” 4, IEEE Conference, Big Sky, March 5–12, 2016. doi: 10.1109/AERO.2016.7500516.
- [12] Olgin, J.G., B.R. Smith-Konter, and R.T. Pappalardo. 2011. “Limits of Enceladus’ Ice Shell Thickness from Tidally Driven Tiger Stripe Shear Failure,” *Geophysical Research Letters*, 1–3, 38.2.
- [13] Zimmerman, W., R. Bonitz and J. Feldman. 2001. “Cryobot: An Ice Penetrating Robotic Vehicle for Mars and Europa,” IEEE. doi: 10.1109/AERO.2001.931722.
- [14] Budney, C. et al. 2014. “TRIDENT: Taking Remote and In-situ Data to Explore Neptune and Triton,” Planetary Science Summer Seminar.
- [15] Hofstadter, M. and K. Reh, K., 2017. Ice Giants, Pre-Decadal Study Summary, ESA Headquarters, January 31, 2017.
- [16] NASA. 2009. Titan Saturn System Mission Final Report, Task Order #NM0710851.
- [17] Barnes, J. et al. 2012. “AVIATR—Aerial Vehicle for In-situ and Airborne Titan Reconnaissance,” *Exp. Astron.*
- [18] John Hopkins University, Applied Physics Laboratory. January 2008. Titan Explorer Flagship Mission Study.
- [19] Jet Propulsion Laboratory. November 2005. Extending Exploration with Advanced Radioisotope Power Systems, JPL D-28903.
- [20] Jet Propulsion Laboratory. April 2010. Team X Titan Lake Probe Study Final Report.
- [21] Oleson, S., R. Lorenz and M. Paul. 2015. “Titan Submarine: Exploring the Depths of Kraken Mare,” AIAA SPACE 2015 Conference and Exposition.

- [22] Zimmerman, W., S. Bryant, J. Zitzelberger, and B. Nesmith. 2001. “Radioisotope Powered Cryobot for Penetrating the European Ice Shell,” *American Institute of Physics, Conf. Proc.* 552, 707.
- [23] Tsou, P. et al. 2013. “Low Cost Enceladus Sample Return Mission Concept,” LCPM-10.
- [24] NASA, Science Mission Directorate. 2014. NASA 2014 Science Plan.
- [25] NASA. 2014. NASA Strategic Plan 2014, NP-2014-01-964-HQ.
https://www.nasa.gov/sites/default/files/files/FY2014_NASA_SP_508c.pdf
- [26] Green, J. 2015. Planetary Science Division Status Report, Presentation at CAPS and Assessment Groups, March 31, 2015.
- [27] John Hopkins University, Applied Physics Laboratory. 2015. Nuclear Power Assessment Study, TSSD-23122. <http://solarsystem.nasa.gov/rps/npas.cfm>
- [28] Doody, D. 1995. *Basics of Space Flight*, Chapter 11: Typical Onboard Systems, Electrical Power Supply and Distribution Subsystems, MOPS0513-02-00, JPL D-9774, Rev. A.
- [29] United Launch Alliance. March 2010. Atlas V Launch Services User’s Guide.
- [30] United Launch Alliance. June 2013. Delta IV Launch Services User’s Guide.
- [31] Space Launch Systems. 2017. Mission Planner’s Guide, ESD30000, Initial Baseline, pp. 41–42, April 12, 2017.
- [32] DeRoy, R.S. and J.G. Reed. 2016. “Vulcan,” IEEEAC 1343, 2, AAS 16-052.
- [33] Mareta, M., Space Launch Systems, Astronautics Group. 1990. User’s Handbook Titan IV, Revision A, pp. 5-8-5-11.
- [34] Department of Energy. August 14, 2007. System Requirements Document for Multi-Mission Radioisotope Thermoelectric Generator (MMRTG), CP340R0001, Contract: DE-AC07-03SF22307, Prepared by Pratt & Whitney Rocketdyne, Inc., Canoga Park, CA, p. 11.
- [35] Lockheed Martin. 1996. Product Specification GPHS-RTG for Cassini, PS 23009148, Rev. F and Addendum I, 11,23.
- [36] Lockheed Martin. 1995–1996. Environmental Criteria and Test Requirements, 23009150 Revs. 9, 11, 12.
- [37] Department of Energy. October 2, 2007. Multi-Mission Radioisotope Thermoelectric Generator (MMRTG), MMRTG System Requirements Document, CDRL No: 24, Contract: DE-AC07-03SF22307, Prepared by Pratt & Whitney Rocketdyne, Inc., Canoga Park, CA, pp.15–17.
- [38] General Electric. May 4, 1989. Product Specifications for GPHS-RTG, Doc CP47A14639 Rev Q.
- [39] Jet Propulsion Laboratory, California Institute of Technology. May 27, 2011. Mars Science Laboratory, Multi-Mission Radioisotope Thermoelectric Generator (MMRTG) Interface Control Document, MSL-322-0107, JPL D-27138, Rev. A (internal document), p. 22.

3 Thermoelectric Materials: Technologies and Risk Assessment

Dr. Chadwick Barklay

University of Dayton Research Institute, 300 College Park, Dayton, Ohio 45469-0172

Dr. Jean-Pierre Fleurial and Dr. Terry Hendricks

NASA Jet Propulsion Laboratory, 4800 Oak Grove Drive, Pasadena, CA 91109

3.1 Objective

The objective of this assessment was to evaluate potential candidate thermoelectric materials that would be well suited for Next-Generation RTG concepts. These concepts are often also discussed in relation to the MMRTG, the presently available RTG, and the potential eMMRTG, which is an MMRTG that would use new, more powerful thermoelectric couples (see Appendix N for more details on these two generators). This evaluation considered a total of 38 n-type and 29 p-type materials. The pool of thermoelectric materials was generated predominantly from a broad spectrum of scientific publications that span the past decade. The exceptions to this are legacy materials or those currently undergoing some level of technology development by NASA, which were also included as candidate materials. Thus, the technology maturity of the potential candidate thermoelectric materials was inclusive from fundamental research level to flight proven. This assessment also examined some of the potential technical issues that could hinder the technology maturation of some of the candidate thermoelectric materials.

3.2 Background

Since the early 1960s, telluride-based thermoelectric materials have been used for energy conversion in RTGs for space applications.⁴ Telluride-based thermoelectric materials are limited to a maximum operating temperature range of 300–800 K. Due to the deleterious effects of oxygen on these materials and their high vapor pressure, these thermoelectric materials must be operated in a sealed RTG with an inert cover gas to retard sublimation and vapor phase transport of the sublimation products within the converter. Silicon-germanium (SiGe) alloys were later employed as thermoelectric materials in RTGs to increase the specific power. This was because devices made from SiGe-based thermoelectric materials have higher efficiencies than those made of telluride-based thermoelectric materials, when operated in a higher temperature range of 800–1300 K. Another advantage of SiGe-based thermoelectric materials is that they do not significantly sublime at temperatures below 1,300 K, thus can operate in a vacuum without a cover gas to retard sublimation. It is important to note that the higher hot-side temperature of a thermoelectric material translates into greater conversion efficiency, and the cold-side temperature dictates the radiator dimensions and specific power [1].

Research is ongoing within the United States and other countries to investigate novel thermoelectric materials that produce higher efficiencies and more stable performance over longer operating lifetimes. This research has led to the discovery, characterization, and laboratory demonstration of a new generation of thermoelectric materials, such as Zintl, skutterudites, half-Heusler, quantum well/superlattice, nanocomposites, and silicides. This new generation of thermoelectric materials, as well as legacy materials, were included in this study to ensure that a comprehensive suite of materials and couple configurations showing the most promise would be considered for inclusion in Next-Generation RTG concepts.

⁴ Bismuth telluride (BiTe) has not been used in a space RTG application.

3.3 Thermoelectric Material Efficiency

Thermoelectric materials allow for direct electricity generation through the Seebeck effect, where a temperature gradient applied to a circuit at the junction of two dissimilar conductors produces an electromotive force based on the following relation:

$$E_{emf} = -S\nabla T \quad (\text{Eq. 3-1})$$

where S is the Seebeck coefficient and ∇T is the gradient in temperature T . The efficiency of a thermoelectric material to convert heat into electricity is characterized by the dimensionless figure of merit ZT :

$$ZT = \frac{\sigma S^2 T}{\lambda} \quad (\text{Eq. 3-2})$$

where σ is the electrical conductivity, S is the Seebeck coefficient, T is the temperature, and λ is the thermal conductivity. Based on this figure of merit equation, it is easy to understand that lower electric resistance (i.e., higher electrical conductivity, σ) and higher temperature will result in greater efficiency.⁵ Thus, an ideal thermoelectric material will have electrical and thermal transport properties that are inversely proportional. The relationship between ZT and efficiency (η) for a thermoelectric element is expressed in the following:

$$\eta = \frac{T_h - T_c}{T_h} \cdot \frac{\sqrt{1 + Z\bar{T}} - 1}{\sqrt{1 + Z\bar{T}} + T_c / T_h} \quad (\text{Eq. 3-3})$$

where T_h and T_c are the temperatures of the hot-side and cold-side temperatures of the element, respectively, and \bar{T} is the average of T_h and T_c [2]. These equations are presented only to provide some foundation for the significance of the figure of merit, and how it and hot- and cold-side temperatures relate to efficiency. Thus, increasing the temperature gradient across the thermoelectric element, or increasing ZT , will result in a corresponding increase in efficiency. For example, for a material with a ZT of 1 that has a hot-side temperature of 500 K and a cold-side temperature of 300 K, an increase in the hot-side temperature to 1,000 K would correspond to an efficiency increase from 12 to 17%, for the simplest device architecture. By increasing the ZT of the same material from 1 to 2, but maintaining the original hot- and cold-side temperatures of 500 K and 300 K, respectively, the same efficiency increase from 12 to 17% would also be realized.

Legacy thermoelectric materials used in RTGs (PbTe, TAGS, and Si₇₈Ge₂₂) generally have low ZT values, which range from 0.51 to 0.99 depending on the material. When these materials were incorporated into legacy RTG designs, they have generally resulted in low system-level conversion efficiencies that range from approximately 3% to 6%, depending on the hot- and cold-side temperatures. Thus, new advanced thermoelectric materials must be employed to potentially attain higher levels of performance intended for the Next-Generation RTG concepts.

3.4 Thermoelectric Materials Considered

As previously noted, this evaluation considered a total of 38 n-type, and 29 p-type materials, which are presented in Appendix K.1. The pool of candidate thermoelectric materials was generated predominantly from a broad spectrum of scientific publications that span the last decade. The exceptions to this are legacy materials or those currently undergoing some level of technology development by

⁵ In general, materials with high electrical conductivity (σ) also tend to have high thermal conductivity (λ), which is consistent with the Wiedemann-Franz law. However, for thermoelectric materials the relationship between electrical and thermal conductivity is inversely proportional, which make them unique.

NASA, which were also included as candidate materials. The thermoelectric materials presented in Appendix K.1 are the result of a systematic approach, and compiling and holistically examining the state-of-the-art thermoelectric technologies, regardless of origin. It is important to note that of the 67 candidate thermoelectric materials considered, the only non-legacy materials that are capable of operating at temperatures greater than 1,200 K were developed by, or in collaboration with, JPL.

3.5 Screening Criteria and Results

The thermoelectric material technology to be baselined in a Next-Generation RTG should be an evolutionary step forward in performance that equates to improvements in conversion efficiency, reliability, and degradation rates. When incorporated into a Next-Generation RTG, these material properties would translate into higher RTG efficiency, a potential reduction of the amount of plutonium-238 (Pu-238) radioisotope fuel required, and higher EOM power for users. In simple terms, an evolutionary thermoelectric technology would possess the following attributes:

1. A reasonably high figure of merit ($ZT_{max} > 1$)
2. A stable Seebeck coefficient, electrical conductivity, and thermal conductivity over the operating lifetime of the device
3. Efficient operation ($\geq 12\%$) over a large temperature gradient ($\Delta T > 700$ K), and
4. Low programmatic risk from a technology maturation perspective.

The following criteria were used to screen which thermoelectric materials (presented in Appendix K.1), either individually or when incorporated with other materials, could potentially result in a thermoelectric technology that possesses the attributes listed above.

1. Technology Readiness Level (TRL): TRLs are a systematic, metrics-based approach to assess the maturity of, and the risk associated with, a particular technology under development. In practice, the maturity of a specific technology was evaluated against the parameters for each technology level and then assigned a corresponding TRL rating. For the purposes of this study, proposed TRL definitions were derived for RTG-specific thermoelectric material technologies. These definitions are presented in Appendix K.2. Once the compilation of potential candidate material technologies presented in Appendix K.1 was complete, each technology was individually assessed and assigned a TRL. Assigning a TRL to each of the candidate materials presented in Appendix K.1 required a unique level of subject matter expertise along with a thorough understanding of the TRL definitions. This allowed Dr. Jean-Pierre Fleurial, who has firsthand knowledge of the most recent advances in the technical performance and demonstration of the majority of material technologies evaluated, to accurately determine a corresponding TRL for each material technology in Appendix K.1.⁶ In order to ensure a reasonably low programmatic risk from a technology maturation perspective, thermoelectric materials with a $TRL < 2$ were not considered for inclusion in this study. Many of these low-TRL materials have a high potential to achieve predicted ZT values greater than 1, but have not matured toward a stage where couple-level proof-of-concept testing for performance and possible degradation mechanisms have been conducted. The remaining thermoelectric materials have achieved the next level of technical maturity that provides some level of confidence that devices made from these materials would exhibit stability and efficient long-term performance.
2. Material System: Over the past decade, there has been significant levels of research performed to develop novel thermoelectric materials and advanced techniques for fabricating them. These novel material systems range from Zintl, skutterudite, chalcogenide, and half-Heusler materials to

⁶ It is important to note that the most recent advances in the technical performance and demonstration of a given thermoelectric material technology often transcend information in the most recent scientific publications.

nanostructured materials, such as nanowires, quantum dots, quantum wells, and thin film superlattices. Unfortunately, many of these nanostructured materials are not practical from a fabrication perspective because they are fabricated by atomic layering processes, which are costly and limit the amount of material that can be produced.⁷ Thus, bismuth and lead telluride nanocomposites, nanowire, quantum well, and thin film superlattice systems were not considered.

3. **Country of Research Origin:** Experimental results cannot be fully established unless they can be independently reproduced. Data for many of the thermoelectric materials presented in Appendix K.1 has been either reviewed or independently verified by representatives from the Materials and Device Technologies group at JPL. In order to consider thermoelectric materials research data that has been generated solely by a foreign entity, and not independently verified by NASA, replication experiments would have to be performed to verify the reproducibility of the original results.⁸ The level of effort and funding required to conduct this level of verification was outside the scope of this study. Additionally, utilization of this type of unverified data as the foundation for a thermoelectric technology suitable for possible incorporation into Next-Generation RTG concepts represents an unacceptable risk. Thus, thermoelectric materials that were solely developed by a foreign entity were not considered.

Table 3-1 and Table 3-2 represent the n-type and p-type thermoelectric materials, respectively, that remain after completion of the screening process. Although many of the remaining thermoelectric materials possess attributes suitable for Next-Generation RTG concepts, an additional detailed material-specific analysis of the post-screened materials was conducted and will be discussed later.

The temperature dependent ZT for the n-type and p-type thermoelectric materials shown in Table 3-1 and Table 3-2 are presented in Fig. 3-1 and Fig. 3-2, respectively. For both the n-type and p-type thermoelectric materials, only the bismuth telluride ternary alloys are a good choice for low temperature applications. Whereas, for high temperature applications, lanthanum chalcogenides, 14-1-11 Zintl, and silicon-germanium materials are suitable. The intermediate range between these materials is covered by skutterudite, half-Heusler, lead telluride, tetrahedrite, Zintl, and TAGs-based thermoelectric materials. What becomes apparent in both Fig. 3-1 and Fig. 3-2 is that there is not any one material that is efficient in all temperature ranges.

3.6 Performance Analysis of Couple Architectures

The next step in the evaluation process involved modeling combinations of the screened p- and n-type thermoelectric materials shown in Table 3-1 and Table 3-2. The thermophysical properties of the materials were used to predict the conversion efficiency of devices made from these materials, within the relevant operating temperature range of the materials. Additionally, the modeling included both segmented and non-segmented couple-level architectures. Since modeling the segmented architectures was the most complex, this was done first. In total, 22 couple-level configurations were modeled using the JPL-developed Thermoelectric Efficiency Modeling (T-MOD) program, which included one-, two-, and three-segment architectures. The T-MOD program and the uncertainties associated with the calculated efficiencies for each configuration are discussed further in Appendix K.3.

3.7 Segmentation

One strategy to achieve an evolutionary step forward in efficiency is by segmenting the n- and p-legs of a device into several segments made of different materials. This results in an increase in the average

⁷ It should be noted that bulk nanostructured material is fabricated using bulk processes rather than a nanofabrication process, and thus could be produced in large quantities.

⁸ Reproducibility is the verification of the results by a different entity using the same measurement procedures, different measuring systems, under the same operating conditions.

thermoelectric figure of merit of each leg over a relatively large temperature gradient [3]. For the modeled configurations, the materials for each segment were selected based on the temperature range where their peak ZT occurred, which is denoted by the term ZT_{\max} . Thus, two- and three-segmented configurations were developed to optimize ZT over the entire thermal gradient. This results in a higher effective ZT for the thermoelectric configuration, and thus higher electrical generation efficiency.

Table 3-1. Screened n-type thermoelectric materials.

Thermoelectric Material	Material System	ZT_{\max}	Max. Continuous Operating Temp. (K)	Lattice Thermal Conductivity ($\text{W m}^{-1} \text{K}^{-1}$)	Linear Thermal Expansion (10^{-6}K^{-1})	Temp Range (Top: 1273–873; Mid: 873–473; Bottom: 473–300)	TRL	Country
BiTeSe (TESI)	Bismuth Telluride	0.9	500	1.04	17	Bottom	4	USA
$\text{K}_{0.95}\text{Pb}_{20}\text{Sb}_{1.2}\text{Te}_{22}$	PbTe-based nanocomposite	1.6	750	0.4	20	Mid	2.5	USA
$\text{Mg}_{2.20}\text{Si}_{0.49}\text{Sn}_{0.5}\text{Sb}_{0.01}$	n-silicide	1.2	800	–	15	N/A	3	China/USA
n-PbTe (MMRTG)	PbTe	0.99	825	–	20	Mid	9	USA
$\text{Ba}_{0.08}\text{La}_{0.05}\text{Yb}_{0.04}\text{Co}_4\text{Sb}_{12}$	Skutterudite	1.2	850	–	12	Mid	2.5	China/USA
$\text{Na}_{0.48}\text{Co}_4\text{Sb}_{12}$	Skutterudite	1.25	850	–	12	Mid	2.5	China/USA
(Hf,Zr)NiSn	n-half Heusler	1.2	875	1.3	11	Mid	3	China/USA
TM JPL CoSb_3 (eMMRTG)	Skutterudite	1.22	875	3.14	12	Mid	4	USA
$\text{LaTe}_{1.46}$	Lanthanum Chalcogenide	1.17	1273	1.4	18	Top	3.5	USA
$\text{LaTe}_{1.46}+\text{Ni}$ composite	Lanthanum Chalcogenide	1.33	1273	1.48	18	Top	3	USA
n- $\text{Si}_{80}\text{Ge}_{20}$ (MIT/JPL)	SiGe-based nanocomposite	1.3	1273	0.8	4.5	N/A	2.5	USA
n- $\text{Si}_{78}\text{Ge}_{22}$ (GPHS RTG)	SiGe	0.94	1300	2.75	4.4	N/A	9	USA

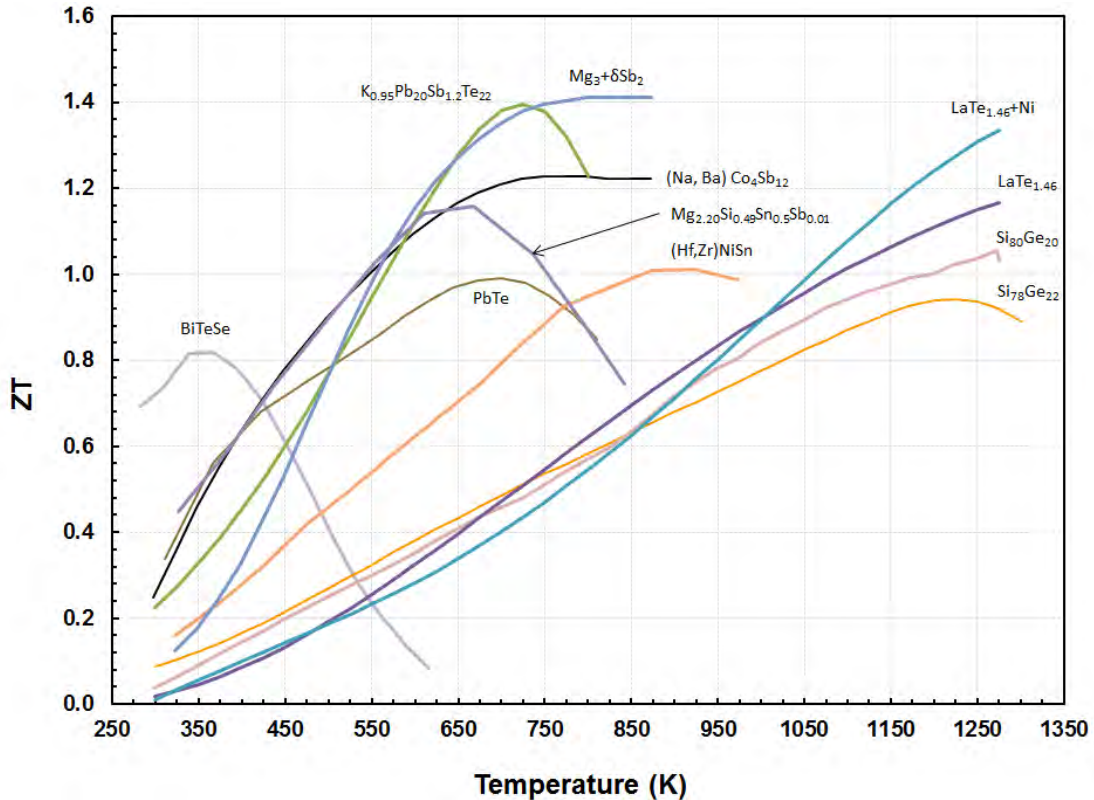


Fig. 3-1. Figure of merit (ZT) as a function of temperature of the n-type thermoelectric materials in Table 3-1.

Table 3-2. Screened p-type thermoelectric materials.

Thermoelectric Material	Material System	ZT_{max}	Max. Continuous Operating Temp. (K)	Lattice Thermal Conductivity ($W\ m^{-1}\ K^{-1}$)	Linear Thermal Expansion ($10^{-6}\ K^{-1}$)	Temp Range (Top: 1273–873; Mid: 873–473; Bottom: 473–300)	TRL	Country
BiSbTe (JPL)	Bismuth Telluride	1.23	500	1.04	17	Bottom	4	USA
p-TAGS-85 (MMRTG)	TAGS	0.78	675	–	15	Mid	9	USA
$Cu_{12}Sb_{4-x}Te_xS_{13}$ $x = 0.2-1.5$	Tetrahedrite	1	725	0.5	13.5	Mid	3	USA
p-(Pb,Sn)Te (MMRTG)	PbTe	0.63	825	–	20	Mid	9	USA
$Ce_{0.9}Fe_{3.5}Co_{0.5}Sb_{12}$ (eMMRTG)	Skutterudite	0.88	875	2.8	13.5	Mid	4	USA
$Ca_9Zn_{4.6}Sb_9$	9-4-9 Zintl	0.93	900	0.77	18	Mid	2.5	China/USA
(Hf,Zr)CoSn	p-half Heusler	1	975	–	11	Mid	3	China/USA
p-Si ₈₀ Ge ₂₀ (MIT/JPL)	SiGe nanocomposite	0.95	1173	0.95	4.5	N/A	2.5	USA
Yb ₁₄ MnSb ₁₁	14-1-11 Zintl	1.34	1273	0.81	17	Top	3.5	USA
p-Si ₇₈ Ge ₂₂ (GPHS RTG)	SiGe	0.51	1300	3.2	4.4	N/A	9	USA
p-Si ₇₈ Ge ₂₂ (GPHS RTG)	SiGe	0.51	1300	3.2	4.4	N/A	9	USA

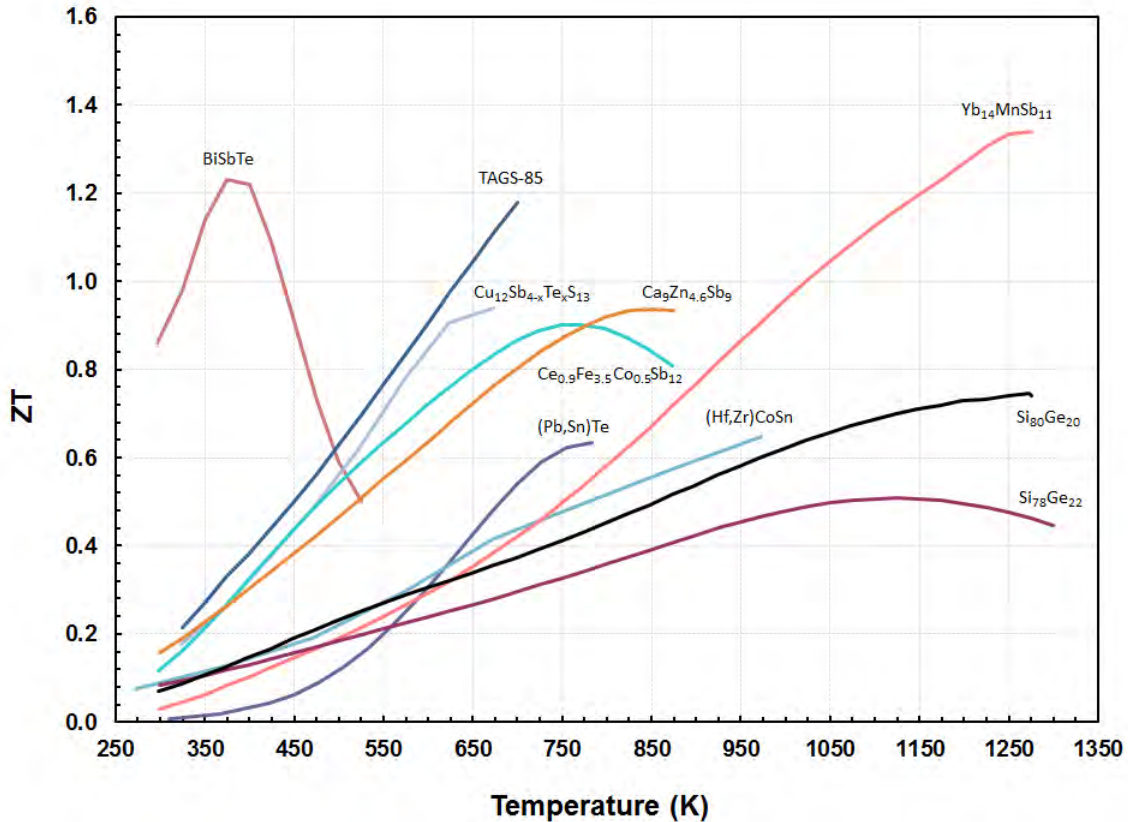


Fig. 3-2. Figure of merit (ZT) as a function of temperature of the p-type thermoelectric materials in Table 3-2.

The first step in developing the segmented configurations was to select n- and p-leg materials from Table 3-1 and Table 3-2, respectively, that have similar compatibility factors. Compatibility factor is defined by the following expression [4]:

$$s = \frac{\sqrt{1 + ZT} - 1}{ST} \quad (\text{Eq. 3-4})$$

where ZT is the dimensionless figure of merit, S is the Seebeck coefficient, and T is temperature at the segment interface [4]. The compatibility factor is a temperature dependent materials property derived from the temperature dependent materials properties of electrical conductivity (σ), Seebeck coefficient (S), and thermal conductivity (λ).

If the compatibility factors of two segmented thermoelectric materials differ by a factor of two or more, then resulting segmentation will not be efficient because a given relative current density would not be suitable for both segmented materials.⁹ Such is the case for silicon germanium, which (despite the high figure of merit) cannot be efficiently segmented with the other thermoelectric materials. It should be noted that the compatibility factor cannot be changed by varying the geometry of the thermoelectric couple, or the electrical or thermal currents [4]. Table 3-3 and Table 3-4 provide the compatibility factors for the screened n- and p-type materials shown in Table 3-1 and Table 3-2.

⁹ The relative current density (u) is the ratio of the electric current density to the heat flux by thermal conduction defined by the expression $u = J/\lambda \nabla T$, where J is the electric current density, λ is thermal conductivity, and T is temperature.

Table 3-3. Compatibility factors for the screened n-type thermoelectric materials.

Thermoelectric Material	Material System	ZT _{max}	Compatibility Factor	Relative Current Density (u) (A mm ⁻²)	Coefficient of Thermal Expansion (10 ⁻⁶ K ⁻¹)	Temp Range (Top: 1273–873; Mid: 873–473; Bottom: 473–300)
BiSeTe (JPL)	Bismuth Telluride	0.9	3.9	3.8	17	Bottom
K _{0.95} Pb ₂₀ Sb _{1.2} Te ₂₂	PbTe-based nanocomposite	1.6	4	-	20	Mid
Mg _{2.20} Si _{0.49} Sn _{0.5} Sb _{0.01}	n-silicide	1.2	2.8	-	15	N/A
n-PbTe (MMRTG)	PbTe	0.99	2.6	2.3	20	Mid
Ba _{0.08} La _{0.05} Yb _{0.04} Co ₄ Sb ₁₂	Skutterudite	1.2	3.5	3.1	12	Mid
Na _{0.48} Co ₄ Sb ₁₂	Skutterudite	1.25	3.5	3.1	12	Mid
(Hf,Zr)NiSn	n-half Heusler	1.2	2.5	-	11	Mid
TM JPL CoSb ₃ (eMMRTG)	Skutterudite	1.22	3.5	3.1	12	Mid
LaTe _{1.46}	Lanthanum Chalcogenide	1.17	1.8	2.4	18	Top
LaTe _{1.46} +Ni composite	Lanthanum Chalcogenide	1.33	3	-	18	Top
n-Si ₈₀ Ge ₂₀ (MIT/JPL)	SiGe-based nanocomposite	1.3	1.6	-	4.5	N/A
n-Si ₇₈ Ge ₂₂ (GPHS RTG)	SiGe	0.94	1.3	1.2	4.4	N/A

Table 3-4. Compatibility factors for the screened p-type thermoelectric materials.¹⁰

Thermoelectric Material	Material System	ZT _{max}	Compatibility Factor(s)	Relative Current Density (u) (A mm ⁻²)	Coefficient of Thermal Expansion (10 ⁻⁶ K ⁻¹)	Temp Range (Top: 1273–873; Mid: 873–473; Bottom: 473–300)
BiSbTe (JPL)	Bismuth Telluride	1.23	4.2	4.6	17	Bottom
p-TAGS-85 (MMRTG)	TAGS	0.78	3.9	3.7	15	Mid
Cu ₁₂ Sb _{4-x} Te _x S ₁₃ x=0.2-1.5	Tetrahedrite	1.00	3.3	-	13.5	Mid
p-(Pb,Sn)Te (MMRTG)	PbTe	0.63	2.2	2.7	20	Mid
Ce _{0.9} Fe _{3.5} Co _{0.5} Sb ₁₂ (eMMRTG)	Skutterudite	0.88	3.5	3.5	13.5	Mid
Ca ₉ Zn _{4.6} Sb ₉	9-4-9 Zintl	0.93	2.1	-	18	Mid
(Hf,Zr)CoSn	p-half Heusler	1.00	2	-	11	Mid
p-Si ₈₀ Ge ₂₀ (MIT/JPL)	SiGe nanocomposite	0.95	1.3	-	4.5	N/A
Yb ₁₄ MnSb ₁₁	14-1-11 Zintl	1.34	2	2	17	Top
p-Si ₇₈ Ge ₂₂ (GPHS RTG)	SiGe	0.51	1	1	4.4	N/A
MnSi _{1.73}	p-silicide	0.80	1.7	-	11	N/A

3.8 Couple Configurations

Table 3-5 presents the 22 couple-level configurations modeled, using the JPL-developed T-MOD program, to predict couple-level efficiencies. Of the 22 couple-level configurations, 18 were high-temperature configurations ($T_{HJ} = 1273K$), 1 mid-temperature configuration ($T_{HJ} = 873K$),¹¹ and 3 low-temperature configurations ($T_{HJ} = 473-873K$).¹² Within the n- and p-type categories in Table 3-5, each column represents the thermoelectric material for a given segment, and the approximate temperature range the material would be operating within the couple-level architecture. Table 3-6 provides a summary of the results of thermoelectric efficiency modeling for a subset of the thermoelectric couples in Table 3-5. Table 3-6 includes the efficiency and average ZT for a given set of cold and hot junction temperatures. The complete results are presented in Appendix K.4.

¹⁰ MnSi_{1.73} is a material that did not meet the previously discussed screening criteria, and thus is not included in Table 3-2. However, it was included in subsequent analyses because it was the only material suitable for a two-segment p-leg configuration architecture that also possesses a SiGe segment.

¹¹ Configuration 22 represents a configuration that is equivalent to the eMMRTG/SKD couple architecture, and was included solely to provide a relative baseline for comparison of efficiency and ZT values.

¹² It is important to note that early in the study there was interest in configurations that could be employed in a ‘cold’ RTG concept. These are represented by configurations 13, 15, and 16. Since this RTG concept is outside the scope of this study, these thermoelectric couple level configurations will not be discussed further.

Table 3-5. The 22 modeled thermoelectric couple-level configurations.

Configuration	n-type			p-type		
	Low (300–473 K)	Mid (473–873 K)	High (873–1273 K)	Low (300–473 K)	Mid (473–873 K)	High (873–1273 K)
1	BiSeTe	Mg _{3+δ} Sb ₂	Nano Ni 15% La ₃ Te ₄	BiSbTe	Ca ₉ Zn _{4.6} Sb ₉	Yb ₁₄ MgSb ₁₁
2	BiSeTe	Mg _{3+δ} Sb ₂	ATEC 2014 LaTe	BiSbTe	Ca ₉ Zn _{4.6} Sb ₉	Yb ₁₄ MgSb ₁₁
3	BiSeTe	SKD-CoSb ₃	Nano Ni 15% La ₃ Te ₄	BiSbTe	SKD-CeFe ₄ Sb ₁₂	Yb ₁₄ MgSb ₁₁
4	BiSeTe	SKD-CoSb ₃	ATEC 2014 LaTe	BiSbTe	SKD-CeFe ₄ Sb ₁₂	Yb ₁₄ MgSb ₁₁
5	BiSeTe	Mg ₂ SiSn	Nano Ni 15% La ₃ Te ₄	BiSbTe	Cu ₁₂ Sb _{4-x} Te _x S ₁₃	Yb ₁₄ MgSb ₁₁
6	BiSeTe	(Hf,Zr)NiSn	Nano Ni 15% La ₃ Te ₄	BiSbTe	(Hf,Zr)CoSn	Yb ₁₄ MgSb ₁₁
7	BiSeTe	PbTe	Nano Ni 15% La ₃ Te ₄	BiSbTe	TAGS	Yb ₁₄ MgSb ₁₁
8	BiSeTe	nano PbTe	Nano Ni 15% La ₃ Te ₄	BiSbTe	TAGS	Yb ₁₄ MgSb ₁₁
9	—	Mg ₂ SiSn	Nano SiGe	—	MnSi _{1.7} ¹³	nano SiGe
10	—	Nano Ni 15% La ₃ Te ₄		—	Yb ₁₄ MgSb ₁₁	
11	—	ATEC 2014 LaTe		—	Yb ₁₄ MgSb ₁₁	
12	—	Nano SiGe		—	nano SiGe	
13	BiSeTe	—	—	BiSbTe	—	—
14	BiSeTe	Nano Ni 15% La ₃ Te ₄		BiSbTe	Yb ₁₄ MgSb ₁₁	
15	BiSeTe	SKD-CoSb ₃	—	BiSbTe	SKD-CeFe ₄ Sb ₁₂	—
16	BiSeTe	PbTe	—	BiSbTe	TAGS	—
17	BiSeTe	Mg ₂ SiSn	ATEC 2014 LaTe	BiSbTe	Cu ₁₂ Sb _{4-x} Te _x S ₁₃	Yb ₁₄ MgSb ₁₁
18	BiSeTe	(Hf,Zr)NiSn	ATEC 2014 LaTe	BiSbTe	(Hf,Zr)CoSn	Yb ₁₄ MgSb ₁₁
19	BiSeTe	PbTe	ATEC 2014 LaTe	BiSbTe	TAGS	Yb ₁₄ MgSb ₁₁
20	BiSeTe	nano PbTe	ATEC 2014 LaTe	BiSbTe	TAGS	Yb ₁₄ MgSb ₁₁
21	BiSeTe	ATEC 2014 LaTe		BiSbTe	Yb ₁₄ MgSb ₁₁	
22	—	SKD-CoSb ₃	—	—	SKD-CeFe ₄ Sb ₁₂	—

Table 3-6. Summary results of thermoelectric efficiency modeling.

Configuration	Hot Junction Temperature (K)	Average ZT at 450 K Cold Junction	Efficiency at 450 K Cold Junction (%)	Configuration	Hot Junction Temperature (K)	Average ZT at 450 K Cold Junction	Efficiency at 450 K Cold Junction (%)
1	1275	1.15	16.5	11	1275	0.65	11.3
2	1275	1.01	15.3	12	1275	0.53	9.8
3	1275	1.06	15.8	14	1275	0.90	14.0
4	1275	0.91	14.3	17	1275	0.94	14.5
5	1275	1.10	16.1	18	1275	0.81	13.1
6	1275	0.91	14.3	19	1275	0.88	14.0
7	1275	1.05	15.6	20	1275	0.91	14.3
8	1275	1.05	15.6	21	1275	0.71	12.0
9	1275	0.69	11.8	22	875	0.93	9.96
10	1275	0.85	13.8				
Configuration	Hot Junction Temperature (K)	Average ZT at 350 K Cold Junction	Efficiency at 350 K Cold Junction (%)				
13	525	0.76	5.68				
15	875	0.95	13.25				
16	875	0.77	10.75				

¹³ MnSi_{1.73} is a material that did not meet the previously discussed screening criteria, and thus is not included in Table 3-2. However, it was included in the modeled couple-level architectures because it was the only material suitable for a two-segment p-leg configuration architecture that also possesses a SiGe segment.

3.9 Configuration Stability Evaluation

A first-order assessment of each derived configuration in Table 3-5 was conducted to gauge the potential stability of each configuration based on differences in the coefficient of thermal expansion (CTE) between segmented materials, and the likelihood that unintended or undesirable binary compounds could form at the segment interfaces. This assessment provided some insight into the mechanical and chemical stability of each derived configuration.

The CTE is a key design parameter for thermoelectric materials, and is critical for thermoelectric couples that have a segmented architecture. The stresses generated by a CTE mismatch between segmented materials, by thermal gradients and transients will scale with the CTE of the thermoelectric material. In general, CTE mismatches between segmented materials that are greater than an absolute value of 10% could be problematic during RTG fueling, assembly, and testing, and—depending on the mission profile—EDL, and diurnal cycling. However, the incorporation of an intermediate bonding layer(s) could potentially mitigate CTE mismatches, but the bonding layer(s) must have a CTE that is in between the segmented materials. However, this strategy can also lead to the formation of undesirable binary or other compounds, if not properly selected. Specific to the CTE mismatch between segmented materials, Table 3-7 provides a summary of the first-order assessment of each derived configuration.

The chemical compatibility of joined materials is often overlooked in the design phase of many applications. However, the joining of incompatible materials can result in the generation of binary or other compounds at segment interfaces, which can result in:

- Kirkendall voiding (Fig. 3-3),
- The formation of low temperature eutectics,
- CTE mismatches associated with the newly generated binary or other compounds,
- Crystallographic changes at the segment interfaces, and
- Electrical and contact resistance changes at the interfaces.

Table 3-7. The CTE mismatch between segments in the modeled thermoelectric couple-level configurations defined in Table 3-5.

Configuration	CTE Mismatch between Segments (%) n-type		Configuration	CTE Mismatch between Segments (%) p-type	
	Low (300–473 K) to Mid (473–873 K)	Mid (473–873 K) to High (873–1273 K)		Low (300–473 K) to Mid (473–873 K)	Mid (473–873 K) to High (873–1273 K)
1 / 2	-6.3%	11.1%	1 / 2	5.6%	-5.9%
3 / 4	-41.7%	33.3%	3 / 4	-25.9%	20.6%
5 / 17	-13.5%	16.7%	5 / 17	-25.9%	20.6%
6 / 18	-54.4%	38.9%	6 / 18	-54.5%	35.3%
7 / 19	15%	-11.1%	7 / 19	-13.3%	11.8%
8 / 20	15%	-11.1%	8 / 20	-13.3%	11.8%
9	-233.3%		9	-144.4%	
10	N/A - Unsegmented		10	N/A - Unsegmented	
11	N/A - Unsegmented		11	N/A - Unsegmented	
12	N/A - Unsegmented		12	N/A - Unsegmented	
13	N/A - Unsegmented		13	N/A - Unsegmented	
14 / 21	5.6%		14 / 21	0.0%	
15	-41.7%	N/A	15	-25.9%	N/A
16	15%	N/A	16	-13.3%	N/A
22	N/A - Unsegmented		22	N/A - Unsegmented	

*Negative % CTE = CTE of cooler segment > CTE hotter segment

Positive % CTE = CTE of cooler segment < CTE hotter segment

Specific to the chemical compatibility between segmented materials, Table 3-8 provides a listing of the potential binary compounds that could be generated at the interfaces of each derived configuration.¹⁴ As previously discussed, for the instances where the chemical compatibility of two segmented thermoelectric materials are not ideal, the application of a bonding layer can potentially mitigate these reactions. However, any potential bonding layer(s) would have to have a CTE that is within an absolute value of 10% of the segmented materials, and would be less chemically active than the original segmented interface. Although not presented in this study, potential bonding layer materials were identified for each of the configurations, but without any long-term compatibility data of how these materials would behave in a segmented thermoelectric architecture under operational conditions, it was impossible to predict the performance of any identified potential bonding layer. Additionally, this study did not thoroughly investigate the metallization layers between any of the derived configurations, nor any potential hot- and cold-shoe materials.

¹⁴ It should be noted that an extensive effort was made to identify as many potential binary compounds as possible; however, there are most likely additional binary compounds that were not identified because the binary phase diagrams either do not exist or could not be located within the time frame of this study. Additionally, no effort was made to identify any potential ternary or quaternary compounds.

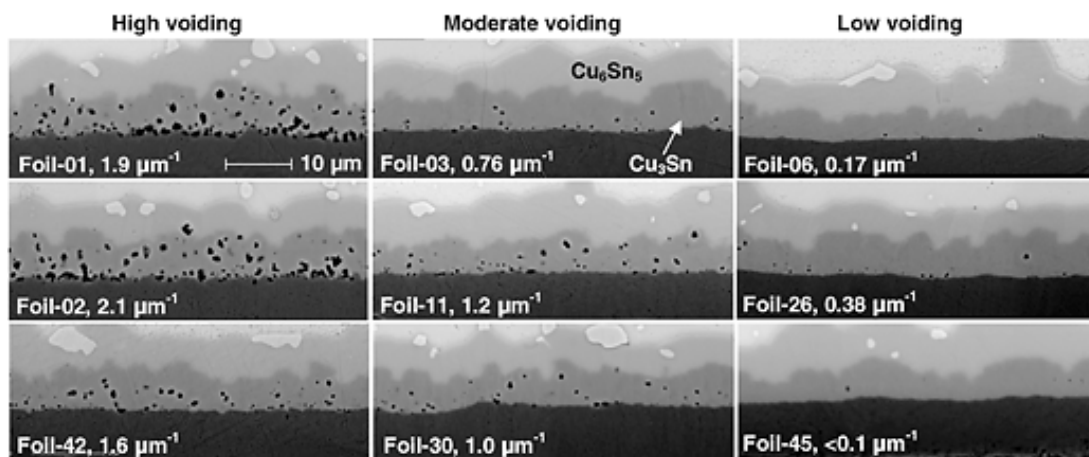


Fig. 3-3. An example of Kirkendall voiding in a nonthermoelectric material [5].

Table 3-8. Potential binary compounds that could be generated at the interfaces of each derived configuration.

Configuration	Potential Binary Compounds n-type		Configuration	Potential Binary Compounds p-type	
	Low Segment (300–473 K) to Mid Segment (473–873 K)	Mid Segment (473–873 K) to High Segment (873–1273 K)		Low Segment (300–473 K) to Mid Segment (473–873 K)	Mid Segment (473–873 K) to High Segment (873–1273 K)
1 / 2	Bi_2Mg_3 , Sb_2Se_3 , Sb_2Te_3	$\text{Mg}_{17}\text{La}_2$, MgLa , Mg_2La , Mg_3La , Mg_{12}La , Sb_2Te_3 ,	1 / 2	$\text{Ca}_{11}\text{Bi}_{10}$, Ca_5Bi_3	Mg_2Ca , CaSb_3 , Ca_5Sb_3 , $\text{Ca}_{11}\text{Sb}_{10}$, Mg_7Zn_3 , MgZn , Mg_2Zn_3 , MgZn_2 , $\text{Mg}_2\text{Zn}_{11}$, YbZn , YbZn_2 , Yb_3Zn , $\text{Yb}_{13}\text{Zn}_{58}$, $\text{Yb}_2\text{Zn}_{17}$, YbZn_{11}
3 / 4	Co_9Se_8 , CoSe_2 , Sb_2Se_3 , Sb_2Te_3	La_2Sb , La_3Sb_2 , LaSb_2 , LaSb , La_5Sb_3 , La_4Sb_3 , Sb_2Te_3 ,	3 / 4	Ce_2Bi , Ce_5Bi_3 , Ce_4Bi_3 , CeBi , CeBi_2	Mg_{12}Ce , Mg_3Ce , Mg_2Ce , MgCe
5 / 17	Bi_2Mg_3 , SeSn , Se_2Sn , Si_2Te_3 , SnTe	La_3Sn , La_5Sn_4 , $\text{La}_{11}\text{Sn}_{10}$, LaSn , La_2Sn_3 , La_3Sn_5 , LaSn_3 , $\text{Mg}_{17}\text{La}_2$, MgLa , Mg_2La , Mg_3La , Mg_{12}La , Si_2Te_3	5 / 17	Bi_2S_3	Cu_2Mg , CuMg_2
6 / 18	Bi_3Ni_2 , Ni_3Se_2 , Ni_{1-x}Se , NiSe_2 , $\text{NiTe}_{0.775}$, NiTe_{2-x} , SnTe	La_3Ni , La_7Ni_3 , LaNi , La_2Ni_3 , $\text{La}_7\text{Ni}_{16}$, LaNi_3 , La_2Ni_7 , LaNi_6 , La_3Sn , La_5Sn_4 , $\text{La}_{11}\text{Sn}_{10}$, LaSn , La_2Sn_3 , La_3Sn_5 , LaSn_3	6 / 18	None	MgCo_2 , Mg_2Sn , SnYb_3 , SnYb , Sn_4Yb_5 , Sn_3Yb_5 , SnYb_2
7 / 19	PbSe	La_5Pb_3 , La_4Pb_3 , La_5Pb_4 , La_3Pb_4 , LaPb_2 , LaPb_3	7 / 19	None	Ag_9Yb_2 , Ag_7Yb_2 , AgYb , Ag_2Yb_3 , Ag_3Yb_5 , Ag_3Mg , AgMg_4
8 / 20			8 / 20		
9	Mg_2Ge		9	Mn_3Ge_2	
10	N/A - Unsegmented		10	N/A - Unsegmented	
11	N/A - Unsegmented		11	N/A - Unsegmented	
12	N/A - Unsegmented		12	N/A - Unsegmented	
13	N/A - Unsegmented		13	N/A - Unsegmented	
14 / 21	Bi_2Mg_3 , Sb_2Se_3 , Sb_2Te_3		14 / 21	$\text{Ca}_{11}\text{Bi}_{10}$, Ca_5Bi_3	
15	Co_9Se_8 , CoSe_2 , Sb_2Se_3 , Sb_2Te_3	N/A	15	Ce_2Bi , Ce_5Bi_3 , Ce_4Bi_3 , CeBi , CeBi_2	N/A
16	PbSe	N/A	16	None	N/A
22	N/A - Unsegmented		22	N/A - Unsegmented	

3.10 Discussion

Although the thermoelectric materials employed in the 22 thermoelectric couple-level configurations shown in Table 3-5 have TRLs greater than 2, when combined into two- or three-segment architectures, the overall TRL of a given configuration is most likely less than 2. For the majority of the configurations there was little, if any, test data on materials compatibility issues related to direct bonding of segmented thermoelectric materials for most configurations, or on materials compatibility and CTE mismatch issues related to bonding layers between segmented thermoelectric materials. These technology gaps lead to tradeoffs between programmatic risk and the desire for relatively high potential system-level efficiencies. In an attempt to elucidate these tradeoffs, a scorecard for segmented and non-segmented thermoelectric configurations shown in Table 3-5 was developed and is presented in Appendix K.5.

What can be easily discerned from the scorecard is that single-segment architectures¹⁵ are low risk and offer incremental improvements in efficiency when compared to MMRTG and predicted eMMRTG performance levels. However, these configurations do not represent an evolutionary step forward in thermoelectric material technology due to either their calculated efficiencies or low TRL. Conversely, the two- and three-segment architectures¹⁶ have the potential for relatively high efficiencies by comparison, but present a spectrum of technology risks associated with bonding the individual thermoelectric material segments, depending on the configuration.

In general, these segmented configurations will have to demonstrate thermal, structural, and chemical stability, and be able to maintain nominal performance levels during vibration and thermal cycling conditions. These would be especially critical if the final Next-Generation RTG concepts resulting from this study employed a cantilevered couple design. Unfortunately, the long-term stability and performance of these segmented material combinations is an unknown, especially under vacuum conditions. As recently experienced during the NASA RPS Program's Skutterudite Technology Maturation Program (SKD Tech Mat), it is plausible that sophisticated bonding/metallization layers could be required to join the segment interfaces, and the segmented thermocouple legs to the cold- and hot-shoe materials. Additionally, coatings to suppress high-temperature material sublimation could also be required to ensure long-term stability.

Thus, there is an unquantifiable level of uncertainty associated with the level of technology development required to mature each of the modeled configurations from their current TRL to a TRL greater than 2. As previously discussed, the scorecard presented in Appendix K.5 quantifies the technology risk and performance for each configuration in an attempt to discern the top candidate configurations. Ideally, the top configurations would offer the option of evolutionary steps forward in performance when coupled with the capability for block improvements as the material technology would continue to mature.

3.11 Recommendations

The eight TEC configurations in Table 3-9 were determined to be the best candidates for further study based on the weighted and unweighted scores shown in the scorecard presented in Appendix K.5. These configurations offer:

1. Fairly high predicted efficiencies that range from 11.3 to 16.5%
2. Flexibility of operating in a vacuum or argon cover gas environments
3. Highly desirable sublimation rates at or near $\leq 10^{-6}$ g/cm²/hr

¹⁵ Configurations 10, 11, 12, and 22

¹⁶ Configurations 1-9, 13-21

4. Anticipated to require minimal development effort (<1 year) to develop the process required for hot side metallization, and
5. Possess less than a 10% mismatch in coefficient of thermal expansion between the individual segmented materials (except configurations 3 and 4).

Table 3-9. Top eight TECs.¹⁷

Configuration	n-type			p-type		
	Low (300–473 K)	Mid (473–873 K)	High (873–1273 K)	Low (300–473 K)	Mid (473–873 K)	High (873–1273 K)
1	BiSeTe	Mg _{3+δ} Sb ₂	Nano Ni 15% La ₃ Te ₄	BiSbTe	Ca ₉ Zn _{4.6} Sb ₉	Yb ₁₄ MgSb ₁₁
2	BiSeTe	Mg _{3+δ} Sb ₂	ATEC 2014 LaTe	BiSbTe	Ca ₉ Zn _{4.6} Sb ₉	Yb ₁₄ MgSb ₁₁
3	BiSeTe	SKD-CoSb ₃	Nano Ni 15% La ₃ Te ₄	BiSbTe	SKD-CeFe ₄ Sb ₁₂	Yb ₁₄ MgSb ₁₁
4	BiSeTe	SKD-CoSb ₃	ATEC 2014 LaTe	BiSbTe	SKD-CeFe ₄ Sb ₁₂	Yb ₁₄ MgSb ₁₁
10	—	Nano Ni 15% La ₃ Te ₄		—	Yb ₁₄ MgSb ₁₁	
11	—	ATEC 2014 LaTe		—	Yb ₁₄ MgSb ₁₁	
14	BiSeTe	Nano Ni 15% La ₃ Te ₄		BiSbTe	Yb ₁₄ MgSb ₁₁	
21	BiSeTe	ATEC 2014 LaTe		BiSbTe	Yb ₁₄ MgSb ₁₁	

Configuration 11 offers the most flexibility regarding the capability for block improvements as the material technology continues to mature with Nano Ni 15% La₃Te₄ or by segmentation with materials identified in configurations 1 through 4. However, the predicted performance of configuration 11 is not considered an evolutionary step forward. As previously noted, configurations 3 and 4 offer some technology development challenges because the CTE mismatch between lanthanum telluride and the skutterudite segments is greater than 30%. It is possible to develop a multilayer bonding approach to mitigate this high degree of CTE mismatch, but it offers some degree of additional programmatic risk.

3.12 Research & Development

Each of the eight configurations presented in Table 3-9 provides a significant level of improvement over the legacy TAGS-85/lead telluride thermoelectric technology employed in the MMRTG. However, near-term research and development is essential and recommended to further develop methods and materials to bond segmented materials, to mitigate material diffusion across the segmented interfaces, and to develop protective coatings to reduce sublimation. These bonding layers must be mechanically stable, thermal expansion matched, act as a diffusion barrier, and possess the appropriate thermal and electrical conductivity characteristics. Furthermore, it is recommended that these low-level R&D efforts should be investigated at universities that specialize in thermoelectric materials research, which could be funded through programs such as a NASA and/or Department of Energy (DOE) Small Business Innovation Research (SBIR) grant, or the DOE Nuclear Energy University Program (NEUP). The research and development efforts should be independent and exclude participation from federally funded research and development centers (FFRDC). Furthermore, these research and development efforts should be conducted on a number of configurations, be executed in parallel, and be closely coordinated, so that information could be shared between research entities. This will help to ensure that only the most viable of the eight configurations would advance into a technology maturation program designed to progress the configuration from TRL 3 to TRL 6.

¹⁷ Next Generation RTG concepts are baselined with a $T_{HJ} = 1273\text{K}$ and $T_{CJ} = 450\text{K}$. It should be noted that when configurations 1–4, 14, and 21 are utilized at $T_{CJ} = 450\text{K}$, there is only a negligible contribution to the overall efficiency of the configuration from the BiTe segments associated with both the n- and p-legs of the configuration. Thus, for this study, the BiTe segments can be eliminated from configurations 1–4, 14, and 21 without any negative impact to the modeled efficiency calculations.

3.13 Summary

There has been a significant level of global research performed over the last decade to develop novel advanced thermoelectric materials. These advanced thermoelectric materials range from Zintl, skutterudite, chalcogenide, and half-Heusler materials to nanostructured materials, such as nanowires, quantum dots, quantum wells, and thin film superlattices, combinatorial sputtered deposits, and many others. However, this study reinforces the understanding that many of these novel thermoelectric material systems are not suitable for incorporation into an RTG design intended for space applications. The efforts undertaken by JPL over the last few decades to identify novel thermoelectric materials potentially suitable for terrestrial and space RTGs are noteworthy. These efforts, coupled with their ability to conduct research to mature these potential materials to a higher level where they can be thoroughly assessed, enable NASA to have the ability to validate whether future investments should be made to further mature some of these novel thermoelectric materials to TRLs 2–3.

Furthermore, this study has shown that thermoelectric-couple efficiencies ranging from approximately 13–16% may be achievable by employing segmented thermoelectric couple architectures.¹⁸ Segmentation is one approach to improve the efficiency of thermoelectric devices by segmenting with different materials that have peak figure of merit (ZT) at different temperatures, thus effectively designing a thermoelectric leg to provide a large average figure of merit over a specific temperature range [5]. This was done in the construction of the TECs used in the MMRTG. However, such an evolutionary step forward in thermoelectric technology is not simple, and this study has identified many significant technical challenges that must be addressed before any of the segmented configurations could be baselined into Next-Generation RTG concepts.

Finally, this study has identified a strong need for a closely coordinated and parallel research and development effort focused on developing and validating methods and materials to bond the thermoelectric materials identified as segmented configurations, to mitigate material diffusion across the segmented interfaces, and to develop protective coatings to reduce sublimation. If the research and development (R&D) efforts are not conducted in parallel and in a coordinated manner, then by default, the most mature configuration will become the baseline technology in Next-Generation RTG concepts.

3.14 References

- [1] Abelson, R.D. 2006. Chapter 56, CRC, in *Thermoelectrics Handbook Macro to Nano*, ed. By D.M. Rowe, Boca Raton, FL.
- [2] Tritt, T.M. and M.A. Subramanian. 2011. “Thermoelectric Materials, Phenomena, and Applications: A Bird’s Eye View,” *MRS Bulletin*, 31 (3), p. 188. doi:10.1557/mrs2006.44, 2011.
- [3] Hadjistassou, C., E. Kyriakides, and J. Georgiou. 2013. “Designing High Efficiency Segmented Thermoelectric Generators,” *Energ Convers Manage.*, 66, pp. 165–172.
- [4] Snyder, G.J. and T.S. Ursell. 2003. “Thermoelectric Efficiency and Compatibility,” *Phys. Rev. Lett.*, 91 (14), 148301.
- [5] Yin, L. and P. Borgesen. 2011. “On the Root Cause of Kirkendall Voiding in Cu₃Sn,” *Journal of Materials Research*, 26 (3), pp. 455–66, 2011.

¹⁸ These projected efficiencies are based on a hot-side temperature to 1273 K and a cold-side temperature of 450 K.

4 Next-Generation RTG Concepts

David F. Woerner

NASA Jet Propulsion Laboratory, 4800 Oak Grove Drive, Pasadena, CA 91109

4.1 Introduction

Radioisotope thermoelectric generators appear to be simple devices. The conversion of heat into electricity using two different conductors in a thermal gradient summarizes the functional nature of the thermoelectric conversion process. There are no moving parts. An RTG produces DC electrical power. The electrical circuit uses a series-parallel network. These and other accurate observations about RTGs can make them appear as simple devices. However, they are not simple. From an RTG concept to its flight development, from heat source design, thermoelectric materials selection and thermoelectric couple design, to the pins in the electrical connector, none or few design trades are ignored in the typical decade-plus time it takes to deliver an RTG to flight. The development of an RTG is a multidisciplinary task. This report documents several similar trades for the Next-Generation RTG concepts that might be flown late in the next decade, and briefly introduces the outline of an RTG design; this report will briefly summarize a few of the key trades at hand.

Two distinct types of RTGs have been used since RTGs were first flown on NASA missions. The two can be labeled as “vacuum-only operation (VO)” and “vacuum and atmosphere operation (V&A).” RTGs for vacuum-only operation could not be used inside of planetary atmospheres; they required the vacuum of space to protect them from oxidation that would arise from dipping them into atmospheres on Mars, Titan, or other bodies. These RTGs were designed to leak at low rates, so any gas forming inside would likely leak to space. Hence, any gas surrounding one of these RTGs would likely leak into the housing and poison the thermoelectric couples. Orbiter missions and flyby missions have typically, but not always, relied upon these generators. Inversely, RTGs for vacuum and atmospheric operations were designed with hermetically sealed thermoelectric convertors/housings. Oxidizing molecules in planetary atmospheres were precluded from entering the convertor and damaging the thermoelectric couples. These generators are sometime referred to as “multi-mission,” as in the MMRTG being used by the Curiosity rover on Mars. Table 4-1 lists several NASA missions and the Operational Mode of the two types of RTGs.

In Table 4-1, “TE” is a descriptor for thermoelectric material system used to build the thermoelectric couples provided in the “RTG model.” “Power Level” records the total power at the beginning of a mission. “Operational Mode” lists each RTG as Vacuum and Atmosphere (V&A) operation or Vacuum-Only (VO). The table also makes clear that only two TE material systems have been used to create thermoelectric couples for these generators.

Another subtle feature in Table 4-1 is that the generators labeled for vacuum-only operation are also linked to the SiGe TE material system only, while vacuum and atmosphere operation relies upon PbTe. The SiGe TECs are typically operated with a hot-side temperature of 1,000°C while the PbTe systems are typically at 530°C or less. These temperatures were selected because of the performance and behavior of the materials; the PbTe TECs produce more power than the SiGe TECs at temperatures near 500°C while the SiGe produces more power near 1,000°C and does not sublime much when operated below 1,025°C. It is worth noting this historical record indicates it has been difficult or impossible to develop an RTG for vacuum and atmosphere operation while operating at 1,000°C on the hot side of the TECs.

Table 4-1. Past NASA RTG-powered missions and the type of RTGs each employed.

Mission	RTG Model (quantity flown)	TE	Destination	Launch Year	Mission Length, yr.	Power Level, W	Operational Mode
Apollo 12-14-17	SNAP-27 RTG (1)	PbTe	Lunar Surface	1969	8	~ 70	V&A
Pioneer 10	SNAP-19 RTG (4)	PbTe	Outer Planets	1972	34	~ 160	V&A
Pioneer 11	SNAP-19 RTG (4)	PbTe	Outer Planets	1973	35	~ 160	V&A
Viking 1	SNAP-19 RTG (2)	PbTe	Mars Surface	1975	> 6	~ 84	V&A
Viking 2	SNAP-19 RTG (2)	PbTe	Mars Surface	1975	> 4	~ 84	V&A
Voyager 1	MHW-RTG (3)	Si-Ge	Outer Planets	1977	40	~475	VO
Voyager 2	MHW-RTG (3)	Si-Ge	Outer Planets	1977	40	~475	VO
Galileo	GPHS-RTG (2)	Si-Ge	Outer Planets	1989	14	~ 574	VO
Ulysses	GPHS-RTG (1)	Si-Ge	Outer Planets/Sun	1990	18	~ 283	VO
Cassini	GPHS-RTG (3)	Si-Ge	Outer Planets	1997	20	~ 885	VO
New Horizons	GPHS-RTG (1)	Si-Ge	Outer Planets	2005	11	~ 246	VO
MSL	MMRTG (1)	PbTe	Mars Surface	2011	>5	~ 115	V&A
Mars 2020*	MMRTG (1 baselined)	PbTe	Mars Surface	2020	(5)	> 110	V&A

GPHS = general purpose heat source

PbTe = lead-telluride

SiGe = silicon-germanium

* To be launched

4.1.1 A Brief Introduction to RTG Designs

The efficiency (η) of RTGs is often approximated. Equation (4-1) is one means to estimate efficiency and it is used here to illustrate how efficiency varies.

$$\eta = \frac{\Delta T}{T_h} * \frac{\sqrt{1+ZT} - 1}{\sqrt{1+ZT} + T_c/T_h} \quad (\text{Eq. 4-1})$$

The equation is not a complete description of an RTG. Equation (4-1) does not account for system inefficiencies such as heat flow that is not through the TE couples, it averages certain values, and so on, but for this introduction, it serves the purposes of this study. T_h is the temperature of the hot junction of a TE couple, T_c the cold-junction temperature, and ZT (this is shorthand for ZT_{avg} in (Eq. 4-1) is the unit-less figure of merit of thermoelectric couples in a generator whose efficiency is being calculated. Hot-side and hot-junction are used interchangeably in this report as are cold-side and cold-junction, except where noted.

The equation points to two significant decisions that give RTG designers some control. The first is in the left-hand term: this term suggests delta-T should be maximized to maximize efficiency. T_h and T_c are design points of an RTG and designers can be very specific about their values. That is, there should be little uncertainty in the values of the design parameters T_h and T_c relative to the uncertainty imposed by not having selected a TEC and characterizing the TEC's performance. The second term points to the need to select thermoelectric materials that maximize that term as well, but there is much more uncertainty in the ZT of the couples when the couple design is unknown and materials for the couples have not been finalized. In such a case, maximizing delta-T is a low-risk/high-confidence choice to maximizing a generator's efficiency, ignoring the other ramifications of selecting those two temperatures; the other term in Equation 4-1 will remain uncertain for some time—maybe years—as a couple's design is perfected.

It is useful to put this equation into context grounded in experience. Three RTGs were used throughout this study as references, to compare mass and power estimates and other design features of new RTG concepts. They are described briefly in Table 4-2.

Table 4-2. Reference RTGs used in this study.

Acronym	Definition	Descriptions
GPHS-RTG	General-Purpose Heat Source RTG	This RTG was designed to operate in vacuum only. It was flown on PNH, Cassini, and other missions. Not a modular system.
MMRTG	Multi-Mission RTG	Operates in vacuum and atmosphere. Flown on the Curiosity rover. Not a modular system.
eMMRTG	enhanced Multi-Mission RTG	A potential enhanced version of the MMRTG. Designed to operate in vacuum and atmosphere. Not a modular system. While not yet approved for development, it is extremely well modeled and its system-level requirements are well understood.

General information about these RTGs can be found in Appendix N.

The GPHS-RTG had a T_h of $\sim 1,000^\circ\text{C}$ when fueled and the MMRTG has a T_h of $\sim 530^\circ\text{C}$; these two temperatures are a reflection of the fact that these two generators used very different TE materials. The GPHS-RTG TECs used SiGe; the MMRTG used PbTe TECs. SiGe thermoelectric couples can be operated at $1,000^\circ\text{C}$ while PbTe couples can be operated near 530°C . The GPHS-RTG TE couples can produce a delta-T of $\sim 800^\circ\text{C}$ while the MMRTG TECs can produce a delta-T of $\sim 330^\circ\text{C}$ for the same cold-side temperature. This results in:

	$T_h, ^\circ\text{C}$	$T_c, ^\circ\text{C}$	$\frac{\Delta T}{T_h}$
GPHS-RTG	1000	200	0.80
MMRTG	530	200	0.62

This clearly shows that choosing a large $\Delta T/T_h$ has a strong effect on RTG efficiency. Modeling the second term using a ZT_{avg} of 0.7 and 1.15, the range of ZT_{avg} for the eight couples identified during the TE materials review, while using the hot- and cold-side temperatures of the GPHS-RTG gives:

	$T_h, ^\circ\text{C}$	$T_c, ^\circ\text{C}$	$ZT=0.65$	$ZT=1.15$
GPHS-RTG	1000	200	0.17	0.28

Comparing the results from the two terms of equation (4-1) for these examples shows that the $\Delta T/T_h$ term is clearly the larger multiplier of the two. In the face of uncertainty in the choice of TE materials for a Next-Generation RTG, the first term can be used to maximize generator efficiency and diminish the uncertainty in estimated system efficiency incurred by carrying multiple couple designs and thereby multiple values of ZT_{avg} . T_h is a design parameter and can be dictated in the course of an RTG design effort. ZT , in this report, is dependent on a down-selection from the eight couple configurations available.

In addition, the MMRTG and eMMRTG set T_h at nearly identical values, 530°C and 600°C . This suggests some other T_h should be selected for the Next-Generation RTG concept, as selecting a temperature near 530 and 600°C temperature is likely to have little additional benefit over MMRTGs and eMMRTGs. As a test of this hypothesis, an RTG was conceived that relied upon the TE materials being developed for the eMMRTG. The results are shown in plots in later sections. The Next-Generation RTG concepts set T_h at or near $1,000^\circ\text{C}$.

4.2 A Framework for Development of RTG Concepts

Past experience, practical matters, and modern engineering techniques lead to a framework for focusing trades for RTG concepts on key first-order matters.

The concepts for a next-generation of RTGs resulted from a framework employing simultaneous top-down and bottom-up engineering. This framework was developed to bound the engineering trades. Requirements were developed at the highest levels and then ascribed to the Next-Generation RTG

concepts. Bottom-up engineering threw a “wide net” to identify and evaluate potential thermoelectric materials and potential couple configurations. The couple configurations were scored in multiple categories and then ranked. Architectural trades for the Next-Generation RTG concepts were performed as the requirements and the TE couple configurations were being developed. The RTG concepts described in the report were derived within this engineering framework.

4.2.1 Architectural Trades and Design Constraints

The architectural trades for the RTG concepts drew on the designs of the GPHS-RTG and MMRTG, and then went beyond those designs to consider trades emanating from the breadth of missions reviewed for this study and considered real-world constraints. Ultimately, the highest levels of architectural trades explored are documented in Table 4-3.

Table 4-3. Architectural trades used in this study.

Architectural Trades	Motivation
Couple Segmentation	Maximize couple performance
Cold Systems	Optimize for thermally sensitive environments
Modular Systems	Optimize radioisotope consumption, ease spacecraft integration, and closely match power available with power needs
Hybrid Systems	Maximize utility across the solar system

These trades were constrained by a pair of preexisting devices. All RTG concepts would have to meet the constraints in Table 4-4. The costs of replacing the Step-2 GPHS module and/or the DOE 9904 shipping cask were deemed too expensive, and so those options were removed from the trade space and instead used as constraints. Fig. 4-1 is a graphical representation of a GPHS both in an assembled form and an exploded view that depicts the proper relationship of the internal components.

Table 4-4. Constraints on RTG concepts.

Constraints	Comments
Use the Step-2 GPHS Module	The heat-source available specifically for RTGs
Fit within a DOE Shipping Cask	The only shipping container for RTGs

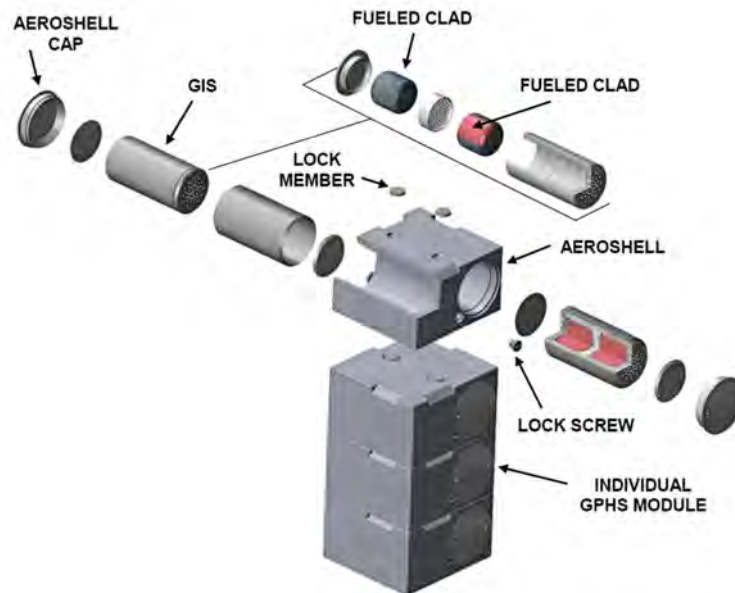


Fig. 4-1. This graphic depicts the internal hardware of a GPHS and its aeroshell. Fueled clads are housed in a graphite impact shell (GIS) that is ultimately slipped into a GPHS aeroshell. A stack of GPHS, four in this case, is constrained against lateral movement by the lock members placed between GPHS in a stack.

Fig. 4-2 is an image of one of the DOE's 9904 shipping containers [1]. It has usable internal dimensions of 81 cm in diameter and 135 cm in height.

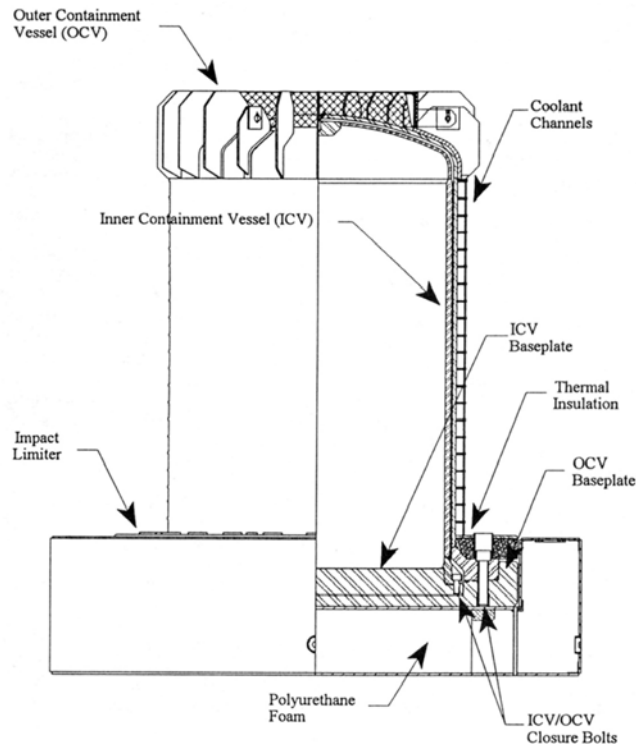


Fig. 4-2. 9904 shipping containers used to transport RTGs.

The framework and constraints noted in Table 4-3 and Table 4-4 can be mixed in a multitude of ways to produce a very large trade space.

4.2.2 Details of the Architectural Trades

Details underpinning each of the trades listed in Table 4-3 can be found below. Risks were identified for each of the trades and many are captured here.

4.2.2.1 Segmented TECs

The trade space here was bounded by the list of TECs (eight) identified in Section 3.0. Segmentation included one-, two-, and three-segmented couples. Most of the couples were configured to operate in a more typical temperature range of 1,000°C to 177°C, and a few were configured to operate in the broader (or “cold”) temperature range from 1,000°C to 77°C.

Risks for segmented TECs:

Risk increases with increasing segmentation.

Each segment will have two or more mechanical interfaces each with a potential for CTE mismatch, and by adding more segments, designers add more materials composed of different molecules whose segments multiple the risk of CTE mismatch. In addition, each segment will have its own degradation performance that will have to be engineered. These things make clear risk will increase with increasing segmentation. It was noted that no RTG manufacturer has ever flown a TEC composed of legs with three segments.

CTE mismatch between segments can rapidly increase couple design complexity.

The temperature range over which a couple and all of its internal interfaces must operate is from room temperature to ~1,000°C on the hot-side and then back to room temperature. This cycle will be repeated a handful or more times during ground operations before the RTG's couples are finally heated, one last time, to ~1,000°C. CTE mismatch can require relatively exotic solutions and it can be eliminated from the risk list by material selection.

4.2.2.2 Cold-Segmented TECs

Cold-segmented TECs were conceived that operated over the broadest possible temperature range. Several couples were engineered to operate with a hot-side of 1,000°C while the cold-side could operate at a temperature as low as 77°C (see Section 3). This allowed engineers the opportunity to explore operating couples at a fixed delta-T but various hot-side to cold-side temperatures. For example, a fixed delta-T of 800°C could be chosen and achieved using triple-segment TECs that were operated from 1,000°C to 200°C in one RTG or 900°C to 100°C in another RTG. The electrical performance of the two RTGs would be nearly identical, but the thermal design of the RTGs would be different.

Another option of these cold-segmented TECs was that delta-T could be set even higher than 800°C. Values of T_h and T_c could be set to 1,000°C and 55°C, respectively. This would set delta-T at 945°C and the cold-side operating temperature ~30°C above the couples' design limit at 27°C.

Risks for cold-segmented TECs:

Risk increases with increasing segmentation.

Each segment will have two or more mechanical interfaces each with a potential for CTE mismatch, and by adding more segments, designers add more materials composed of different molecules whose segments multiply the risk of CTE mismatch. In addition, each segment will have its own degradation performance that will have to be engineered. These things make clear risk will increase with increasing segmentation. It was noted that no RTG manufacturer has ever flown a TEC composed of legs with three segments.

CTE mismatch between segments can rapidly increase couple design complexity.

The temperature range over which a couple and all of its internal interfaces must operate is from room temperature to ~1,000°C on the hot-side and then back to room temperature. This cycle will be repeated a handful or more times during ground operations before the RTG's couples are finally heated, one last time. CTE mismatch can require relatively exotic solutions and it can be eliminated from the risk list by material selection.

4.2.2.3 Modular RTGs

The trade space for modular RTGs resulted from the question, “What is the benefit of modularizing the system over not doing so?” Modularization holds the promise of simpler, more precise spacecraft accommodation. Spacecraft designers would not be forced to use one size but could deliberately choose from a range of sizes that would fit a specific mission concept. In theory, this would also allow radioisotope fuel to be judiciously metered out.

The DOE, its contractors, and others have published papers on modularized designs [2] and the need to satisfy a broad range of NASA planetary spacecraft power needs [3]. Each of those designs was overcome by events: the need to deliver a working generator for flight, technical issues, or other similar events.

The trade study for modular RTGs in this report was tempered by these known risks, and resulted in a relatively simplified degree of modularization at the system level. Modular RTGs were conceived as each having a unique housing rather than being assembled from building blocks as in the fashion of LEGO™ blocks. Internal components would be packaged in a manner to support spacecraft accommodation electrically.

Modularization at the system level was driven by a desire to provide RTGs that would readily mate using a common spacecraft bus requirement, a voltage range of 22–34 volts. This and other factors limited the minimum RTG size to be based upon two GPHS. The height imposed by the DOE's shipping container internal dimensions limited the largest Next-Generation RTG concepts to ones using 16 GPHS. A modular RTG could then be available in eight different sizes or variants relying on 2, 4, 6, 8, 10, 12, 14, or 16 GPHSs. No further evaluation of the merit of three GPHS vs. four GPHS vs. more as the basis of RTG sizing was considered; that trade will be conducted later.

Risks for modular RTGs:

The degree of modularization at the system level can have a strong bearing on the risk of success or failure.

The more extensive modularization is, or the higher the degree of modularization, the more complex a generator’s design and the greater number of interfaces it will include. That is, a generator whose design of the housing is assembled from lower-level assemblies, whose circuit follows suit, and whose TECs are modularized, maximizes the design challenges and interfaces. More interfaces can typically be a measure of added risk. For example, if an RTG consisted of a single GPHS surrounded by TECs and each of those RTGs would have to be integrated to produce more powerful generators, the number of mating tasks would be multiplied and so to the opportunity for problems.

4.2.2.4 Hybrid RTGs

A hybrid RTG would combine the relatively low weight of a GPHS-RTG with the MMRTG’s capability to operate in atmospheres and vacuum.

The MMRTG design of using pistons and springs to hold TECs in place was quickly discarded, as it would be heavier than an RTG design that used cantilevered TECs, as in the GPHS-RTG. However, the mechanical mounting of cantilevered couples in the GPHS-RTG was done using holes in the RTG housing, holes that leaked intentionally. A hybrid RTG would have to use couples that mounted to the housing without penetrating the housing. The housing could then be hermetically sealed and evacuated.

Risks for hybrid RTGs:

Hybridization incurs risk by being responsive to too many functional requirements, that is, it risks failure while trying to satisfy all users.

Too many requirements can increase engineering focus on development of system-level solutions. This compounds the risk to an RTG system by increasing design and manufacturing challenges while potentially increasing risk in thermoelectric couple technologies for this variety of Next-Generation RTG concepts. As examples,

- Guaranteeing hermeticity for the life of an RTG is a challenge.
- Many of the components in an MMRTG-like design, a known design that works, must be discarded to provide a lightweight system requiring designers to create new system-level solutions. No such RTG exists for spaceflight.

4.3 Next-Generation RTG Concepts

Six distinct RTG concepts emerged from the trades performed in this study. Table 4-5 effectively maps the complexity as features were added to the concepts. Each RTG concept was then thermally and electrically modeled using the eight TEC configurations identified in Section 3; details on how the modeling was performed and the results from the models can be found in Appendices O and P while the bounding allowable flight temperatures along with the remainder of the draft requirements are in Section 2.5.

Table 4-5. Summary of the features of the conceptual Next-Generation RTGs.

RTG Type/Acronym	Segmented (TECs)	Modular (at the system-level)	Cold (lower cold-side temperature)	Hybrid (Operates in vacuum and atmospheres)
SRTG	X			
SMRTG	X	X		
CSRTG	X		X	
CSMRTG	X	X	X	
HSMRTG	X	X		X
CHSMRTG	X	X	X	X

The acronyms for the Next-Generation RTG concepts were created from prefixes in Table 4-6, which also provides a summary of the concepts.

Table 4-6. Next-Generation RTG concepts and their names.

Prefix	Definition	Description
S	Segmented	An SRTG concept would use segmented TECs to boost power and would be a single size, in this case one built around 16 GPHS. Operates only in vacuum. No system-level modularity. Optimized for specific power.
SM	Segmented-Modular	An SMRTG concept uses segmented TECs built into housings that could be procured in differing sizes and hence was modularized at the system level. The size of the variant conceived of in this study was based upon the smallest sized RTG using 2 GPHS. RTGs built around 2, 4, 6, 8, 10, 12, 14, and 16 GPHSs would be possible. Operates only in vacuum.
CS	Cold-Segmented	A CSRTG concept designed to the cold-side of the RTG operated at significantly colder temperatures than is typical. This single-sized RTG would be built around 16 GPHS. Operates only in vacuum. No system-level modularity. Optimized for specific power.
CSM	Cold-Segmented-Modular	This generator concept uses the same couples as the SMRTG except that BiTe segments have been added to boost power and lower the cold-side operating temperature. The size of the variant conceived of in this study was based upon the smallest sized RTG using 2 GPHS. RTGs built around 2, 4, 6, 8, 10, 12, 14, and 16 GPHSs would be possible.
HSM	Hybrid-Segmented Modular	This HSMRTG would use segmented TECs in a sealed and evacuated vessel and modularize the system. The size of the variant conceived of in this study was based upon the smallest sized RTG using 2 GPHS. RTGs built around 2, 4, 6, 8, 10, 12, 14, and 16 GPHSs would be possible. Operates in vacuum and atmospheres.
CHSM	Cold-Hybrid, Segmented-Modular	Combines the HSMRTG with a segmented TEC whose segments were designed to allow the generator to operate at significantly lower cold-side temperatures. Operates in vacuum and atmospheres. RTGs built around 2, 4, 6, 8, 10, 12, 14, and 16 GPHSs would be possible.

4.3.1 *Segmented RTG (SRTG)*

The Segmented RTG (SRTG or SRTG-16) concept had the closest external resemblance to a GPHS-RTG of all the RTG concepts described in this report. It would use a very similar housing, but be sized for 16 GPHS Step-2 heat sources rather than the 18 GPHS Step-0 heat sources used in the GPHS-RTG. This sizing should allow an SRTG to fit within the DOE's shipping container.

The primary distinction and advantage that segmented concepts had over other RTG concepts is maximized specific power; the SRTG-16 and SMRTG-16 concepts were estimated to have identical mass and power. The cold concepts produced lower specific power.

Table 4-7 displays a power estimate for an SRTG at beginning of life (BOL) using the TEC configuration TC-1. Other parameters are also shown.

Table 4-7. The SRTG-16 (TC-1) by the numbers.

Parameter	Value	Comments
P _{BOL} , W	590	Beginning of Life
Mass, kg	62	
Operating Voltage, V	32	
Operations	Vacuum-only	

4.3.2 *Segmented-Modular RTG (SMRTG)*

Modularization of an RTG has been proposed repeatedly in the past, and the idea still garners favor today. One of the reasons for its support is the oft-unstated goal of maximizing interchangeability at the system level. Interchangeability in the mechanical and electrical interfaces with a spacecraft—the same operating temperature range, the same operating voltage, the same optical properties, the same electrical connector, and more—improves a spacecraft designer's ability to mix and match RTGs. This adds value in several ways, including the less than obvious ability for NASA to manage their fuel inventory by not forcing users into one-size-fits-all RTGs. Modularity also eases the pathway for spacecraft designers to upgrade to the next larger size of RTG in the face of growth of spacecraft power demands, and the greater the number of variants to choose from, the more flexibility modularity adds. There are many things that

will not be interchangeable, such as thermal waste heat, but the value of modularity to NASA, as stated in the objectives of this study, peaks when interchangeability is maximized.

One approach considered at the system level would have been to develop a “building-block” module, which would require each module to be bolted to the next to get the next larger-sized SMRTG. These could be integrated electrically in parallel so that the output voltage of the smallest module would dictate the voltage of the largest generator. The operating temperature would be the same for all SMRTGs. This design would deliver the same mechanical interface to each spacecraft. A stack of RTG modules bolted together however runs the risk of resulting in a very leaky system housing, as each module bolted to the next would have a mechanical interface whose leak rate would not be predictable *a priori*, especially across large thermal excursions. This would be a very difficult engineering challenge to overcome. A leaky housing in flight would meet the requirement of vacuum-only operation, but a leaky housing would ensure the required protective cover gas in ground operations would bleed off at an unpredictable rate. This potential choice was disqualified due to that risk.

Instead, the Next-Generation SMRTG concept evolved to use a new housing for each SMRTG size or variant. This choice eliminated a great many potential leak paths, minimized the chance of damage and anomalies during assembly, and reduced the number of mechanical interfaces in the system.

The next choice for the SMRTG concept became, “What is the minimum size RTG practical to develop?” Initially, the SMRTG concept assumed using a single GPHS would lead to the smallest SMRTG. The operating temperature would be the same for all SMRTGs. This design would deliver the same mechanical interface to each spacecraft. These generators could be wired to produce a different operating voltage for each variant of the SMRTG or to produce the same voltage as the smallest SMRTG. Imposing a requirement to produce 22–34 V limited the smallest variant of an SMRTG to house two GPHS. Allowing the voltage to vary for each SMRTG variant was not studied; that choice has spacecraft-level impacts that need further scrutiny.

NASA spacecraft power busses have typically been designed to operate from 22 to 34 V or some very similar range. A means of increasing the number of TECs was considered rather than attempt to overturn this cultural practice. TECs electrically linked into a series circuit will produce a voltage that is dependent on the number of TECs in the circuit. Multicouples [4], short for “multiple couples in a single package,” allowed the study team to increase the density of TECs in the smallest SMRTG to achieve 34 V without jeopardizing the mechanical strength of the couples. Fig. 4-3 depicts a multicouple. This architecture was baselined for the SMRTG, and hence the SMRTG multicouples.

RTGs flown previously have used series-parallel circuits for improved reliability and fault tolerance; this study took advantage of that reliability improvement as well. The TECs in the multicouple package were configured in a series-parallel electrical circuit. This circuit design doubled the number of couples to be built into a generator. The volume available in the smallest RTG housing dictated the maximum number of TECs it could house and, hence, what voltage could be delivered. The TECs had to be built into multicouples in order to achieve the needed density. This calculus found the smallest modular RTG required TECs to be put into multicouples containing eight TECs each, and the output voltage could be delivered at ~34 V so long as the smallest sized housing for modular RTG concepts was limited to housing fitted with two GPHS.

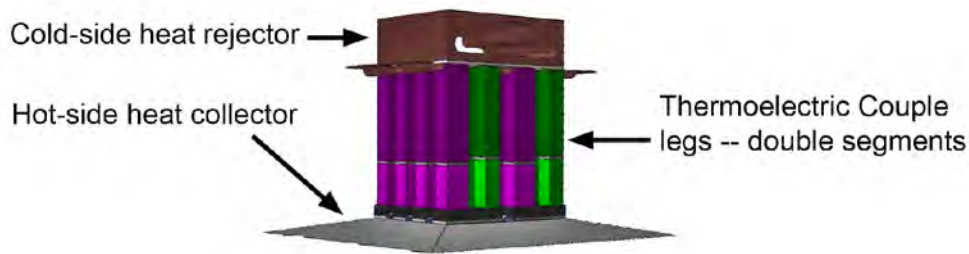


Fig. 4-3. A multicouple used in the SMRTG concepts and other modular system concepts. It contains eight TECs electrically wired in a series-parallel circuit. Heat would radiate from GPHS at the core of the generator into the hot-side heat collectors that would channel the heat into the TEC legs. The heat would leave the legs via the cold-side heat rejector mounted to the RTG housing.

Each multicouple would be wired in series to the next to form a ring of these arrays around the inside diameter of the smallest SMRTG, an SMRTG-2. Fig. 4-4 provides a graphic of this wiring and array layout.

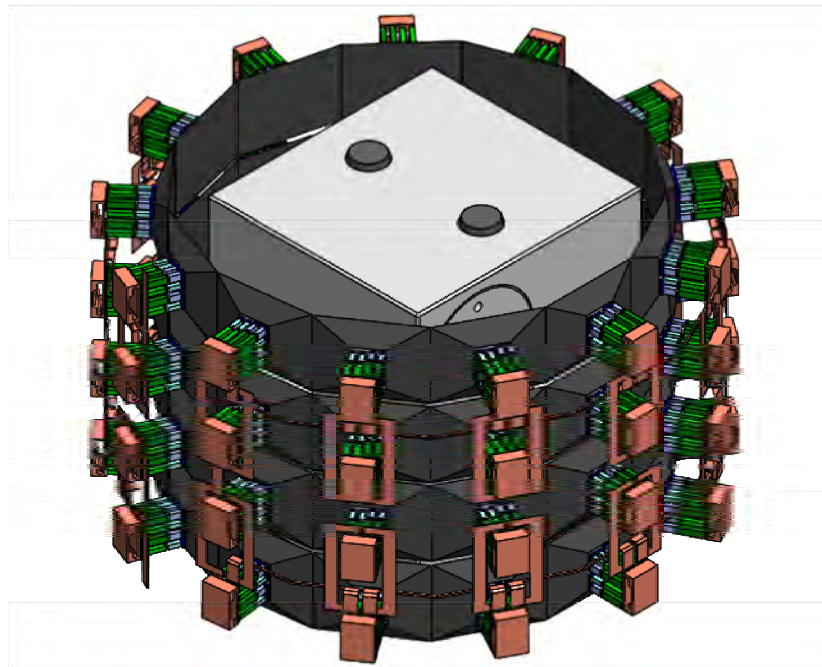


Fig. 4-4. Conceptual design of a ring of multicouples surrounding a stack of two heat sources. Fifty-two multicouples surround a pair of GPHS to produce 34 V. The hot-side heat collectors are the black and grey polygonal, surfaces surrounding the GPHS. The electrical interconnects between the multicouples are the copper-colored straps between the multicouples.

Physical models of the housing and multicouples were developed, and a 2-GPHS SMRTG concept can be seen in Fig. 4-5 without housing closeouts.

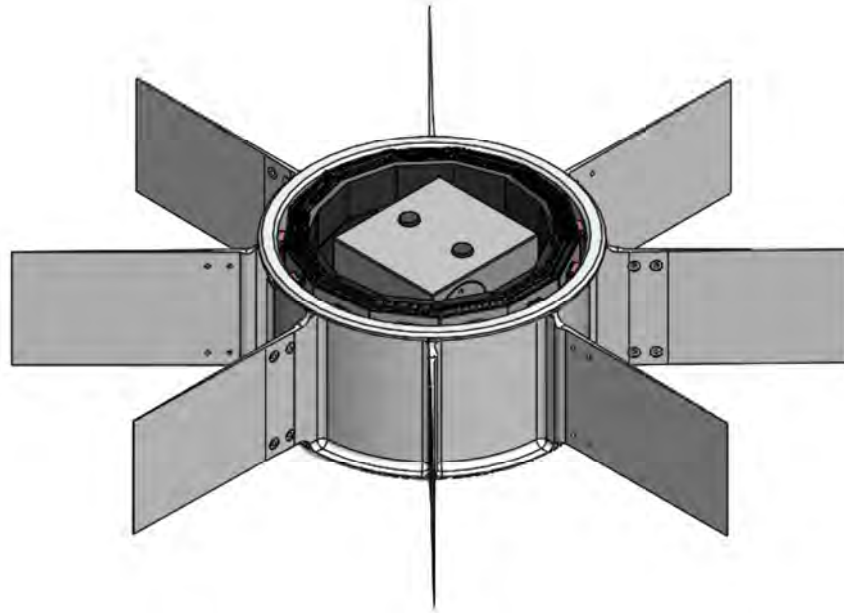


Fig. 4-5. SMRTG-2 concept without closeouts. This graphic is illustrative of an SMRTG design and does not represent actual hardware or a complete design.

The quantization of the minimum size of the SMRTG concept at two GPHS and the inside dimensions of the DOE shipping cask dictated the range of possible larger SMRTG sizes. Eight SMRTG sizes are possible utilizing 2, 4, 6, 8, 10, 12, 14, or 16 GPHS.

There are 64 possible variations of SMRTGs using the eight best candidate couples. Power, thermal, and mass models were developed for all 64 options plus eight more using the skutterudite couples in development for the eMMRTG, for a total of 72. The mass and power of the largest, most powerful SMRTG is shown in Table 4-8. Fig. 4-6 catalogs the power of the 72 SMRTGs and the reference RTGs. Fig. 4-7 catalogs the mass of each SMRTG and the reference RTGs.

Table 4-8. The SMRTG-16 (TC-1) in numbers.

Parameter	Value	Comments
P_{BOL} , W	590	Beginning of mission
Mass, kg	62	
Operating Voltage, V	32	
Operations	Vacuum-only	

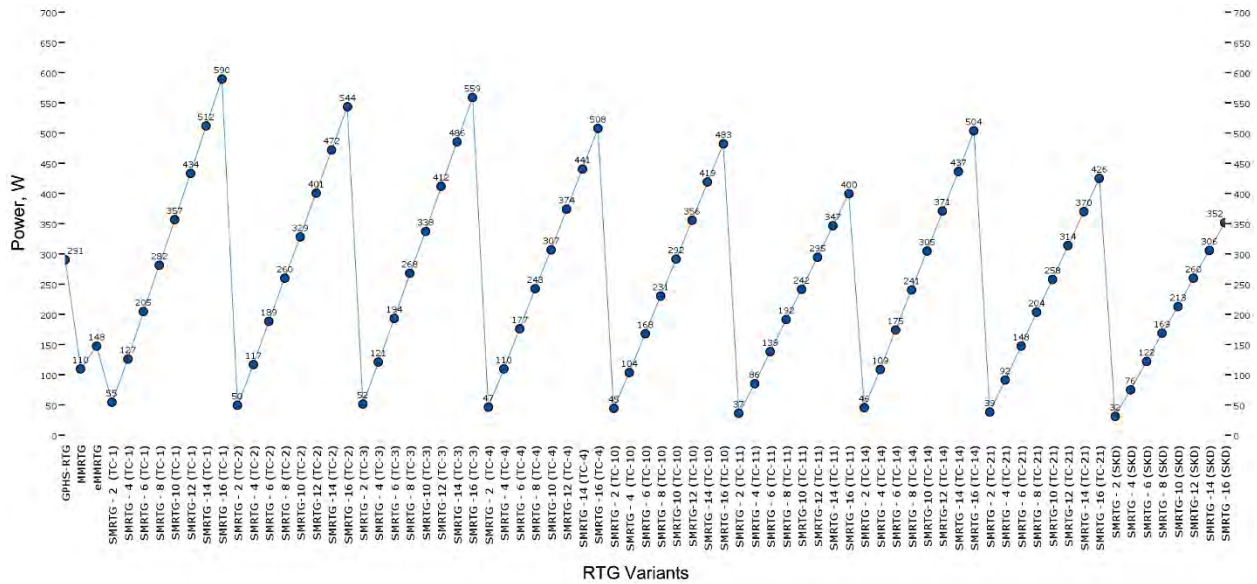


Fig. 4-6. Beginning of life power (P_{BOL}) for eight sizes of SMRTG concepts utilizing nine different couple configurations. Electrical power (W) is scaled on the y-axes. The SMRTG sizes range from “-2” GPHS to “-16” GPHS are displayed on the x-axis for each of the eight best candidate couples (TC-x) as well as couples crafted for the eMMRTG, the SKD couples. Electrical power for each of these generators is displayed next to the appropriate marker on the plot. For example, SMRTG-10 (TC-2) was estimated to produce 329 W.

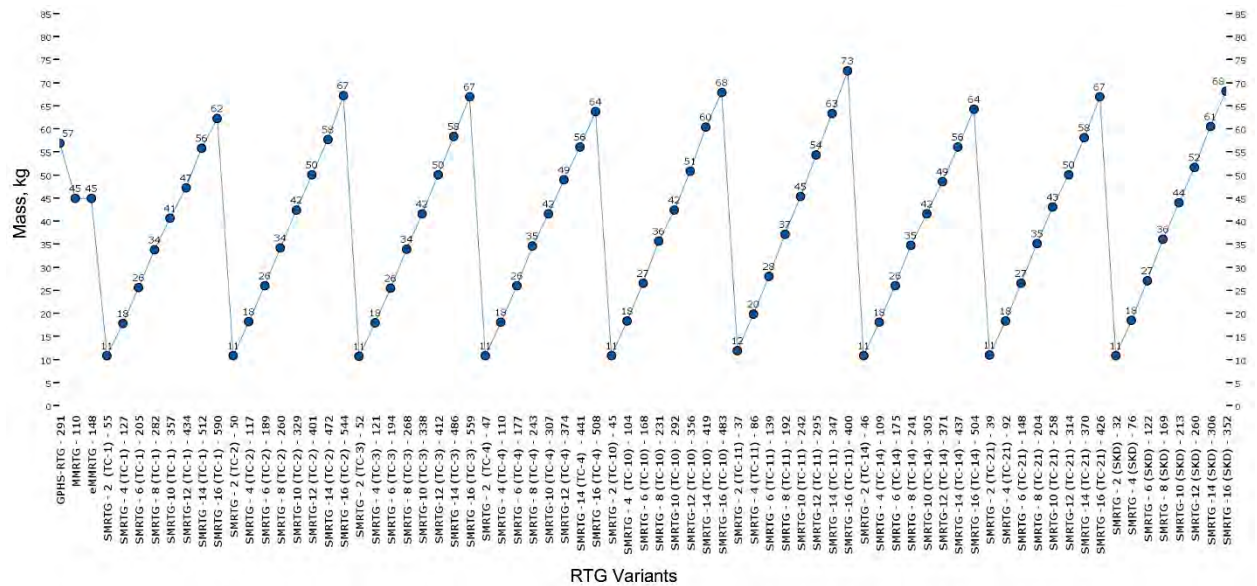


Fig. 4-7. Mass for each of eight sizes of SMRTGs utilizing nine different couple configurations. Mass (kg) is scaled on the y-axes. The mass for each of these generators is displayed next to the appropriate marker on the plot. For example, SMRTG-10 (TC-2) was estimated at 42 kg. The x-axis lists the variants of the SMRTG, their TECs, and their power estimates.

4.3.3 Cold-Segmented RTG (CSRTG)

The Cold-Segmented RTG (CSRTG or CSRTG-16) concept utilizes TECs designed to operate with a T_h of $\sim 1,000^\circ\text{C}$ and a T_c of $\sim 77^\circ\text{C}$. This design choice boosted delta-T and power significantly. The design of this generator appears largely as many of the other concepts in this study except that the fins

would be extremely large in order to drive T_c to a nominal value of $\sim 77^\circ\text{C}$. The thermal model of this concept required a generator diameter that spanned ~ 2 m from fin-tip to fin-tip. This detail made the CSRTG-16 unable to fit within the DOE’s shipping container. The size of the fins drove the CSRTG-16 mass estimate to 322 kg, and this also disqualified the CSRTG from further consideration. A summary of this concept is provided in Table 4-9.

Table 4-9. The CSRTG-16 (TC-1) in numbers.

Parameter	Value	Comments
P_{BOL} , W	672	Beginning of Mission
Mass, kg	322	
Operating Voltage, V	32	
Operations	Vacuum-only	

4.3.4 Cold-Segmented-Modular RTG (CSMRTG)

The Cold-Segmented-Modular RTG (CSMRTG) concept utilized TECs designed to operate with a T_h of $\sim 1,000^\circ\text{C}$ and a T_c of $\sim 77^\circ\text{C}$ and added the feature of system-level modularization. This “cold” design boosted delta-T significantly and power as well over equivalently sized RTGs in this study. The design of these generators relied upon fins that spanned from ~ 1 m to ~ 2 m from fin-tip to fin-tip. This prevented the generators with the highest numbers of GPHS from fitting in the DOE’s shipping container; to fit the CSMRTGs with fewer GPHS would require the fins be reshaped to take advantage of unused volume in the shipping container. Again, this made the masses appreciably higher than the other types of RTGs in this study. Fig. 4-8 makes clear the masses of CSMRTGs would exceed acceptable levels; it is highly improbable a mission would fly a single generator weighing so much, and the masses in the figure make clear this concept does not maximize utility. The notional CSMRTG masses far exceed the reference RTGs; only the CSMRTG-2 and CSMRTG-4 configurations do not.

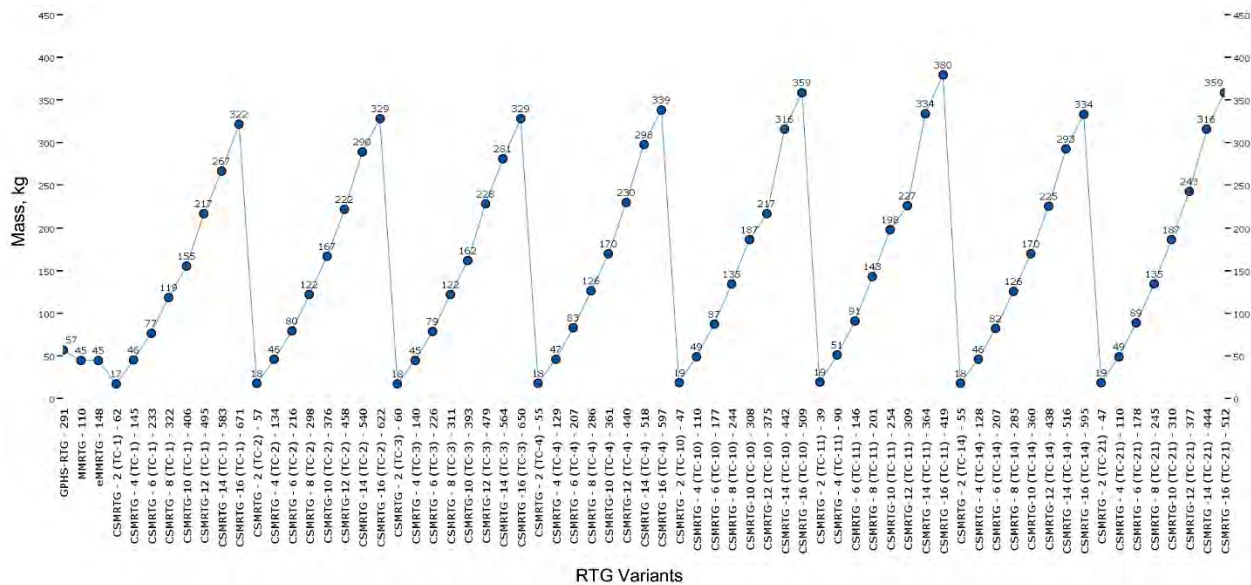


Fig. 4-8. The masses of the CSMRTG concepts are presented side-by-side with the mass of the three reference generators called out on the left-hand side of the plot. The mass (kg) scales are on the y-axes, and RTG configurations and their power estimates are listed on the x-axis.

4.3.5 Hybrid-Segmented-Modular RTGs (HSMRTG)

Adding hybridization to an SMRTG converted the concept generator from vacuum-only operations to one capable of operating in vacuum and atmospheres. As such, this architecture appeared to be the one architecture that fits all, this Next-Generation RTG concept minimized the number of concepts to pursue

as flight developments. It would be available in a variety of sizes all of which could be used in vacuum or on Mars or Titan.

The power estimates for the Hybrid SMRTG (HSMRTG) are identical to the SMRTG (see Fig. 4-9).

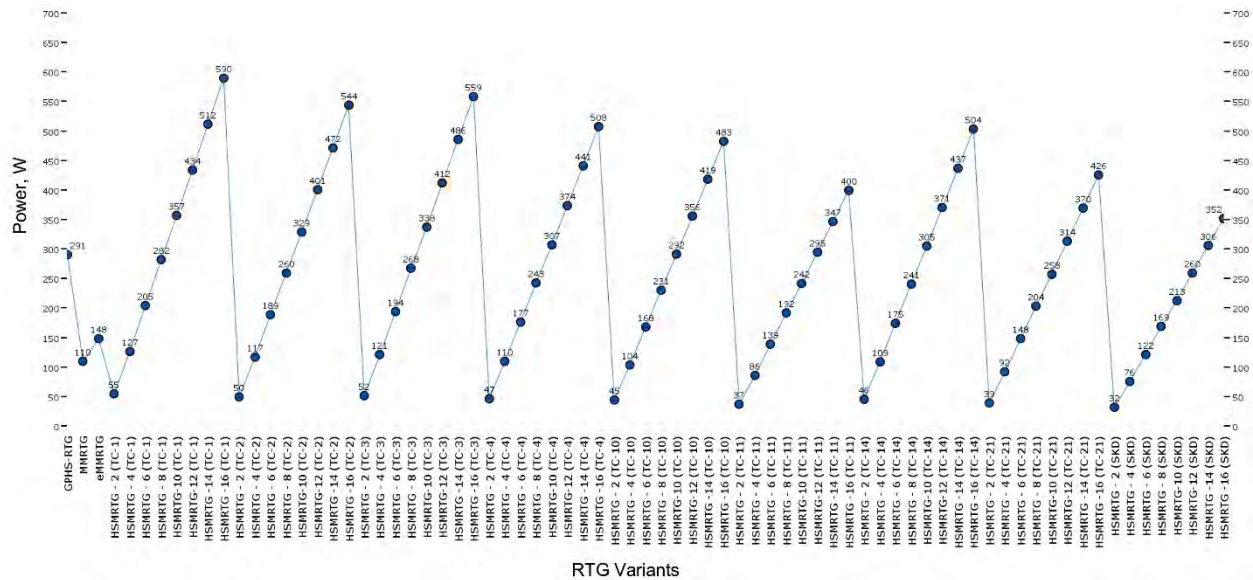


Fig. 4-9. The power estimates of the HSMRTG concept are plotted. The y-axes are the power (W) scales. The x-axis lists the HSMRTG configurations and the reference RTGs.

The HSMRTG concept incurred no mass penalty for hybridization at the fidelity of the models prepared in this study. This concept was found to increase risk over the SMRTG as the hermeticity is an added feature of the HSMRTG and must be preserved throughout the 17-year design life of the generator. Micrometeoroids have the potential to penetrate the housing of an HSMRTG and create a leak. However, a hybrid RTG destined for Titan, Venus, or Mars atmospheres was assumed to be inside of a protective shell or aerobody and hermeticity would be preserved during interplanetary cruise. The impact of micrometeoroids on the HSMRTG on vacuum-only missions was not evaluated and is a significant risk to this RTG concepts mass and specific power estimates.

Missions in the atmospheres of gas and ice giant planets were not considered credible. The tropospheres of the gas giants and the ice giants alike are mostly (81–89% by number mixing ratio) hydrogen, and most of the rest (10–18%) is helium. This makes their atmospheric average molecular mass very low, ~2.2–2.5 atomic mass unit (AMU). The only way to have a light-gas balloon in a mostly hydrogen atmosphere is to have pure hydrogen in the envelope, and that is only marginally lighter than the surrounding air, so the envelope volume must be huge and thus the envelope itself is massive. Hot air balloons fare no better—in most environments, they are power intensive too. To produce a significant mass density contrast from the envelope interior to the ambient air, the air in the envelope must be heated to a higher temperature than the ambient air. If one tries to keep the envelope small, the result is an unreasonably high temperature requirement inside the envelope, which yields unreasonable thermal losses through the envelope and thus unreasonable amounts of thermal power to make up for those losses.

Further, it was not deemed credible to fly an atmospheric probe mission using an RTG that descends into the atmospheres of a gas or ice giant. Such a mission might last for one or two hours making the use of an RTG over batteries extremely unlikely.

In addition, the fuel for RTGs produces helium (He) as the fuel decays. Any hybrid RTG has to be able to accommodate 17 years’ worth of He; a detailed analysis of this was not performed for this study.

4.3.6 Cold-Hybrid-Segmented-Modular RTGs (CHSMRTGs)

The concept of cold RTGs was proposed to minimize temperature-related issues for RTGs in cold environments, environments such as on an icy body or ocean world, and maximize power output. A lower cold-side temperature was thought to lower ice sublimation in the vicinity of landers on icy bodies and ease spacecraft thermal design.

These RTG concepts were envisioned to lower the housing temperature 100°C assumed for the other generators in this study. This increases the delta-T drop across the thermoelectric couples, $1,000^{\circ}\text{C} - 77^{\circ}\text{C} = 923^{\circ}\text{C}$.

4.3.7 Summary of Findings and Observations for Next-Generation RTGs Concepts

The GPHS-RTG, flown on the Cassini and Galileo missions; the MMRTG, flown on the Curiosity rover; and the potential eMMRTG, an enhancement of the MMRTG that is undergoing technology maturation, were all used for comparisons in this study. Those generators also provided rich sources of system requirements and concrete designs from which to evaluate Next-Generation RTG concepts.

Many of the advantages and disadvantages of the RTG concepts are documented above. The features that stem from the architectural trades in this study are coarsely captured in the acronyms for the Next-Generation RTG concepts: SRTG, SMRTG, HSMRTG, CHSMRTG, and all the other concepts in between. It should be clear—engineering risk grows with feature count.

The cold RTG concepts (CSRTG, CSMRTG, and CHSMRTG) were the first to be disqualified as violating the constraints and requirements for this study; specifically, these concepts grew to exceed the volume within the DOE shipping container for RTGs. This was accompanied by excessive mass growth. Figure 4-10 displays specific power for SMRTGs compared with CSMRTGs. The trend in specific power for each of the cold variants was inversely related to the number of GPHSs in the generator, while the opposite was true for the SMRTG.

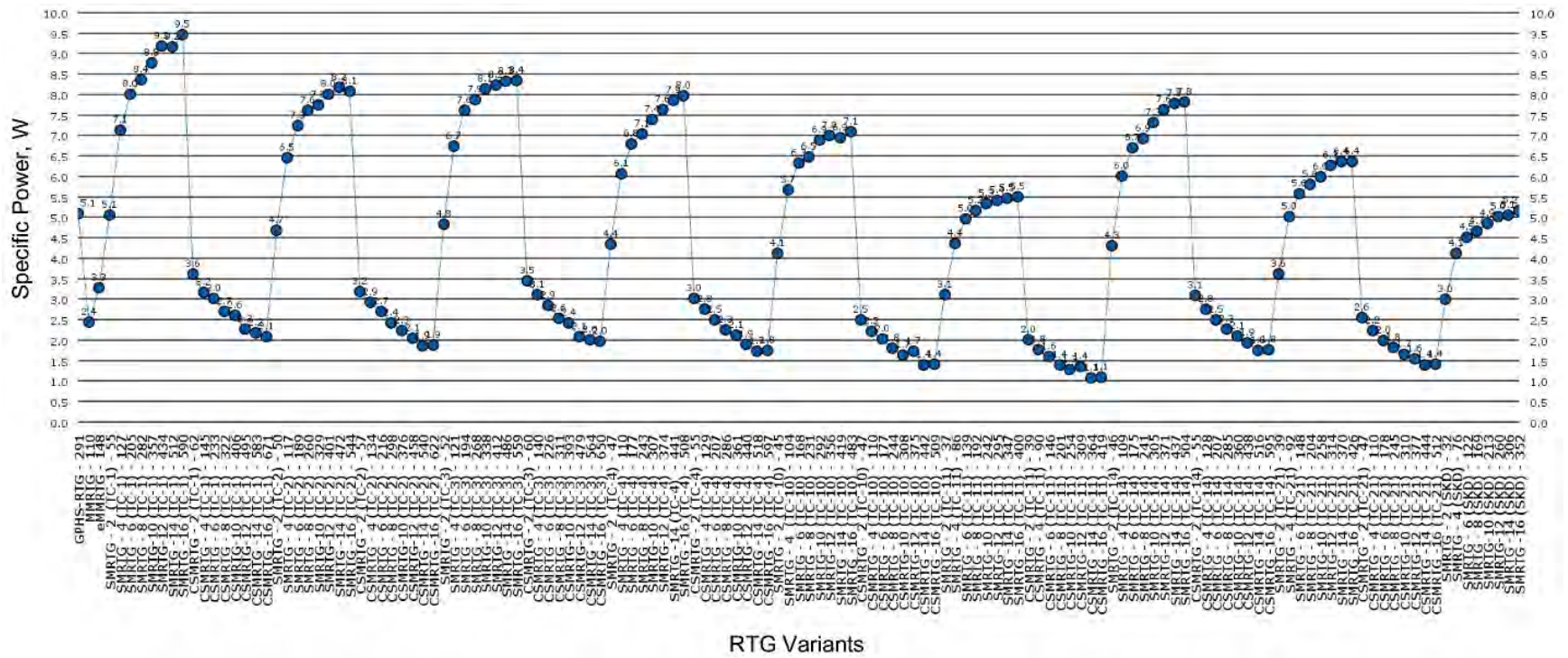


Fig. 4-10. Specific power for the CSMRTG and SMRTG variants is plotted. The y-axes are values of specific power, the x-axis lists CSMRTG and SMRTG variant along with the three reference generators used throughout this study. The CSMRTG curves demonstrate the behavior of all of the cold variants.

The study team found the SRTG, HSMRTG, and SMRTG to be the most compelling design concepts. Their top-level features are summarized in Table 4-10. Their power estimates range from 400–600W when fueled with 16 GPHS and using any of the eight TECs identified in Section 3 (see Table 4-11). Key parameters for all of the RTG concepts prepared for this study can be found in Appendix P.

Modestly detailed designs were prepared for these RTG concepts. Mechanical drawings were prepared (Figure 4-4) and used as assumptions, but thermal modeling of most of the components was not performed. Little internal structure was thermally modeled. Appendix O details how thermal modeling was performed. Both the mass and power estimates in Table 4-11 and all of the values in Appendix P are current best estimates (CBEs) and no error analysis was performed; the values in Table 4-11 and Appendix P should be reviewed with that in mind. For example, the GPHS-RTG had a mass of 57 kg, very close to the values below for the SMRTG-16 and SRTG-16, strongly suggesting that less than 60 kg is achievable with those two concepts. Electrical power estimates are of a similar fidelity. It is unlikely the three remaining RTG concepts each produce the exact same amount of power. More detailed designs will result in higher-fidelity power estimates likely to diverge slightly from the values in Table 4-11 and Appendix P.

Table 4-10. RTG concepts for a Next-Generation RTG: the singular SRTG-16 and the SMRTG and HSMRTG variants.

RTG Name	Segmented (TECs)	Modular (at the system-level)	Cold (lower cold-side temperature)	Hybrid (Operates in vacuum and atmospheres)
SRTG	X			
SMRTG	X	X		
HSMRTG	X	X		X

Table 4-11. Power and mass estimates for the SRTG-16, SMRTG-16, and HSMRTG-16 concepts, each modeled with the eight couple configurations identified in Section 3.

RTG Concept	BOL Power, W	Mass, kg
SRTG-16 (TC-1)	590	63
SRTG-16 (TC-2)	544	67
SRTG-16 (TC-3)	560	67
SRTG-16 (TC-4)	509	68
SRTG-16 (TC-10)	484	68
SRTG-16 (TC-11)	401	73
SRTG-16 (TC-14)	504	64
SRTG-16 (TC-21)	427	67
SMRTG-16 (TC-1)	590	62
SMRTG-16 (TC-2)	544	67
SMRTG-16 (TC-3)	560	67
SMRTG-16 (TC-4)	509	64
SMRTG-16 (TC-10)	484	68
SMRTG-16 (TC-11)	401	73
SMRTG-16 (TC-14)	504	64
SMRTG-16 (TC-21)	427	67
HSMRTG-16 (TC-1)	590	68
HSMRTG-16 (TC-2)	544	73
HSMRTG-16 (TC-3)	560	73
HSMRTG-16 (TC-4)	509	69
HSMRTG-16 (TC-10)	484	74
HSMRTG-16 (TC-11)	401	76
HSMRTG-16 (TC-14)	504	70
HSMRTG-16 (TC-21)	427	73

The value of modularity, along with its features supporting interchangeability, outweighed the perceived lower risk of a single-point design as embodied in the SRTG-16. The hybrid feature would add more development risk over the other two generator concepts, but is still a viable candidate. While none of these three were dropped from the study, they were prioritized as SMRTG, SRTG, and HSMRTG.

Finally, the MMRTG, and the potential eMMRTG, can provide effective radioisotope power for missions at Titan and Mars and balloon missions at Venus. This observation and the higher-level risk of the HSMRTG suggest one attractive strategy would be to sustain the MMRTG, complete the eMMRTG, and develop the SMRTG.

4.4 References

- [1] Ferrell, P.C. and D.A. Moody, D.A. 1996. "Radioisotope Thermoelectric Generator Transportation System Licensed Hardware Second Certification Test Series and Package Shock Mount System Test," AIP Conference Proceedings 361, 1469. doi: 10.1063/1.49858.
- [2] Hartman, R.F. 1995. "Modular RTG Technology," in *CRC Handbook of Thermoelectrics*, Valley Forge, PA: CRC Press, LLC, pp. 471–478.
- [3] Teledyne Energy Systems Inc. 1975. Low Cost High Performance Generator Technology Program: Mission Application Study, Vol. 4, Timonium, MD: TESI, Inc.
- [4] Fleurial, J-P., Chase, J., Gogna, P., Firdosy, S., Li, B.C-Y., Keyawa, N., Huang, C-K., Nakatsukasa, G., Nesmith, B., 2013, "1 kW Small Fission Heat Pipe-cooled Thermoelectric Power System Design Concept and Technology Maturation," 11th International Energy Conversion Engineering Conference, Joint Propulsion Conferences, San Jose, July, 14–17, 2013. doi: 10.2514/6.2013-3930.

5 Mission Concepts by GSFC and GRC as Independent Assessment of Selected Concepts

Anthony Nicoletti

NASA Goddard Spaceflight Center, 8800 Greenbelt Road, Greenbelt, MD 20771

5.1 Introduction

Two independent studies were conducted integrating Next-Generation RTGs into early planetary mission concepts to assess the general feasibility of these RTGs as a future power systems, as well as their ability to enable new planetary missions. The Mission Design Lab (MDL) at NASA GSFC developed a mission to study the Centaur small body 2060 Chiron. This study selected RTGs that best supported the mission, assessed how the RTGs drove the mission concept, and conducted trades and parametric studies to evaluate mission sensitivity to RTG design parameters.

The Compass Team at NASA GRC analyzed the impact of integrating a CHSMRTG-8 into an existing submarine mission, the Titan Turtle, which relied upon an eMMRTG for power to explore the methane lakes on Saturn's moon Titan. These missions and the study results are described here. They provide a largely independent look at select Next-Generation RTG concepts as the teams performing the mission analyses were not a part of the Next-Generation RTG Study beyond the development of these mission concepts.

More detail on the RTG concepts discussed in this section can be found in Section 4.

John Hopkins University Applied Physics Laboratory (APL) also studied a retrofit of the Pluto New Horizons spacecraft. While there is not a detailed discussion of their work here, it should be noted that APL reported eight of the RTG concepts described in Section 4 of this report could replace the GPHS-RTG that powered the original mission, though some redesign would be needed to accommodate volume differences.

5.2 The Chiron Explorer Mission Concept

Chiron is a small rocky body approximately 200 km in diameter (see Fig. 5-1) in a highly elliptic heliocentric orbit, with perihelion near Saturn and aphelion near Uranus. It was chosen as it has high scientific value, orbits beyond the range of past solar-powered spacecraft, and utilizes a previously developed optimized electrical propulsion trajectory, which enables efficient flight dynamics trades and parametric studies. The Chiron Explorer's (ChirEx) mission would be to rendezvous with Chiron, remotely characterize the small body for approximately six months, then conduct in situ science operations via a lander at two surface locations for approximately 18 months.

A notional payload consistent with a small-body science investigation mission was provided to MDL for both the orbiter and the lander. For study purposes, the payload was essentially considered a black box with mass and power resource requirements to be accommodated; however, instances where the payload drove mission design are noted. Table 5-1 lists the ChirEx payload assumptions.



Fig. 5-1. Asteroid 2060 Chiron (artist concept provided courtesy of: Ian Amaral).

Table 5-1. Chiron Explorer notional payload.

Mission Element	Notional Payload	CBE Mass (kg)	MEV mass (kg)	CBE Science Operations Power (W)
Lander	Camera Suite, Magnetometer, Mass Spectrometry Instrumentation	31	40.3	34
Orbiter	Cameras (x2), V/IR Spectrometer, Gamma Ray/Neutron Detector	27	35.1	50

CBE = current best estimate

MEV = maximum expected value

5.2.1 Chiron Design Study Assumptions

The Chiron Explorer was required to utilize a launch vehicle on the existing NASA Launch Services contract, with RTGs as the only source of power (although batteries could be used for load leveling if necessary). GSFC engineers were given the freedom to choose from the catalog of Next-Generation RTGs shown in Table 5-2 to optimize the mission concept's mass and power margins; however, it was desirable to use the more generally applicable HSMRTG. As per typical early concept studies, and consistent with GSFC Gold rules (GSFC-STD-1000) [1], MDL was asked to maintain at least 25% launch vehicle margin on maximum expected value (MEV) mass and bus power, though this was not held as a requirement. As per electrical propulsion (EP) convention, 15% power margin was held on EP power. Critical spacecraft subsystems for the baseline concept were assumed to be fully redundant, and the mission duration was limited to 14 years from launch in keeping with the conceptual RTG design life.

Note that values of system power degradation in Table 5-2 were early estimates created during the first few months of the study. The Next-Generation RTG study eventually settled on 1.9% as the design goal for Next-Generation RTG concepts. Degradation rates listed in Table 5-2 include heat source decay and RTG degradation. A sensitivity analysis of this variable was performed by GSFC (see Section 5.2.6.3) and found to be a minor driver relative to other RTG parameters used in the ChirEx mission concept analyses.

Table 5-2. RTG types and variants. Mass estimates for CSRTG, CSMRTG, and CHSMRTGs in this table are outdated. The numbers displayed here were the initial mass estimates before detailed thermal modeling was performed. The ChirEx spacecraft conceptual design using CHSMRTGs was created by GSFC MDL based upon premature information submitted by the Next-Generation RTG Study Team.

Type and Variants (-N)	System Power Degradation, (Average %/year)	BOM Power (W)	Mass (kg)	Next-Generation RTG Concepts
GPHS-RTG	1.54	282	57	
MMRTG	4.80	95	45	
eMMRTG	2.50	137	45	
SMRTG-16	1.60	405	53	X
SMRTG-12	1.60	299	41	X
SMRTG - 8	1.60	195	28	X
SMRTG - 4	1.60	89	16	X
CSMRTG -16	1.60	466	58	X
CSMRTG-12	1.60	343	45	X
CSMRTG - 8	1.60	218	31	X
CSMRTG - 4	1.60	100	18	X
HSMRTG -16	1.60	365	61	X
HSMRTG-12	1.60	269	47	X
HSMRTG - 8	1.60	172	33	X
HSMRTG - 4	1.60	78	19	X
CHSMRTG -16	1.60	409	67	X
CHSMRTG-12	1.60	301	52	X
CHSMRTG - 8	1.60	189	37	X
CHSMRTG - 4	1.60	86	21	X
SRTG	1.60	458	53	X
CSRTG	1.60	526	58	X

5.2.2 ChirEx Mission Concept Phases

The ChirEx mission was divided into three phases: Cruise, Orbital Science Operations, and Surface Science Operations. Cruise begins at launch in June 2034 on an Atlas V 551 evolved expendable launch vehicle (EELV) with a STAR 48 booster motor, followed by a 12-year flight time to a 2046 rendezvous with Chiron. Rendezvous is near the Chiron perihelion at ~8.2 AU. Cruise thrust is provided by a Busek BHT-600 EP system and includes an unpowered Jupiter flyby in 2036. The ChirEx trajectory is shown in Figure 5-2.

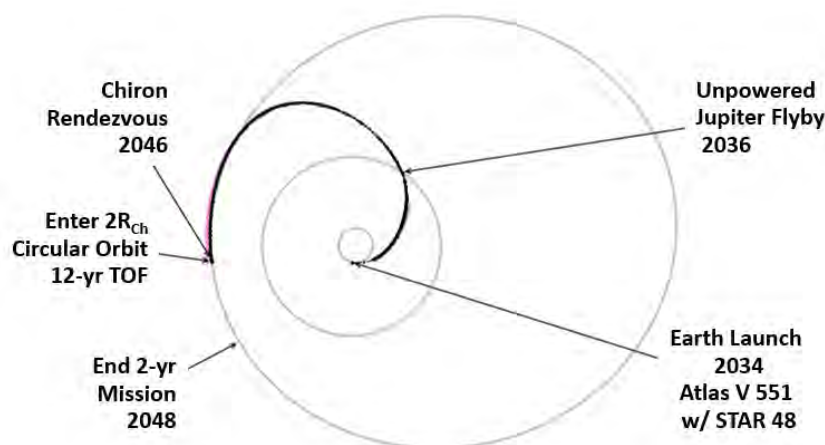


Fig. 5-3. ChirEx mission concept trajectory (TOF = time of flight); note that unlike solar EP (SEP), ChirEx's RTG-powered propulsion system's thrust is independent of solar distance, yielding the unusual shape seen here.

A six-month science campaign commences after rendezvous and initial capture into a high Chiron orbit. Here, extensive remote science observations would be made and gravity models developed during a slow inward spiral toward Chiron. At approximately 100 km in altitude, and with the Chiron surface sufficiently characterized, the ChirEx lander would be released for a 1.6-hour controlled descent to the surface, whereupon surface science operations begins. The mission concludes in 2048 after 18 months of surface science at two locations. ChirEx mission phases are summarized in Table 5-3.

Table 5-3. Summary of ChirEx mission concept phases.

Phase	Duration	Features
Cruise	12 years	<ul style="list-style-type: none"> Launch on Atlas V 551 LV with Star 48 booster Unpowered Jupiter flyby
Orbiter Science	6 months	<ul style="list-style-type: none"> Initial capture into high Chiron orbit Spiral inward as orbit is lowered to ~100 km Extensive mapping and characterization campaign using orbiter science instruments (cameras, GR/N detector, and visual/infrared [V/IR] spectrometer) and some lander instruments (magnetometer, mass spectrometers)
Surface Science	18 months at 2 locations	<ul style="list-style-type: none"> Land on surface using chemical propulsion Take continuous magnetometer and seismometer measurements Relay data to orbiter daily Take multiple surface samples and return them to the lander for mass spectrometry analysis Use lander propulsion system to relocate to a second site

5.2.3 Spacecraft Design

The notional Chiron Explorer spacecraft is shown in Fig. 5-3, with the lander in its stowed position. The spacecraft design employs a high-heritage hexagonal structure with instruments and avionics stored in distinct equipment bays that can be easily accessed and integrated separately. As per historic RTG missions, such as Cassini and New Horizons, RTGs would sit external to the spacecraft to enable efficient dissipation of heat and allow for launch pad integration.

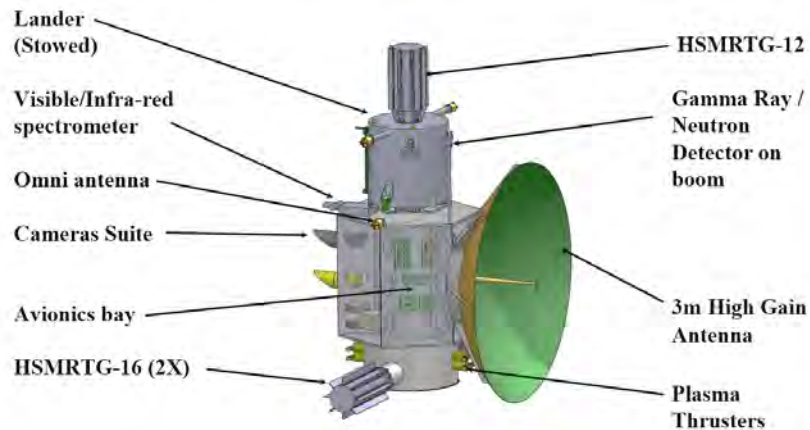


Fig. 5-3. Notional ChirEx spacecraft.

5.2.3.1 Propulsion System

Two Busek BHT-600 Hall thrusters would provide the main engine thrust for ChirEx at 39 mN each with 600 W input power for both. Meeting this high-thruster power draw was critical in RTG suite selection. The 709 kg of propellant required for cruise would be stored in a standard propellant tank located on the spacecraft centerline. Four small high-heritage Aerojet PRS-101 pulsed plasma thrusters would be used for momentum unloads.

5.2.3.2 RF Communications

The RF communication system design is driven by data downlinks to Earth at the 9.6-AU maximum Earth–Chiron distance. This range would be accommodated by a 3-m Ka-band high-gain antenna (HGA) and daily, 8-hr Deep Space Network (DSN) contacts, which allow for a 20 kbps link rate, while maintaining required link margins. Average downlink is estimated to be ~600 Mbit/DSN pass, which is quite reasonable for a deep space mission and satisfies the anticipated ChirEx data generation rate. The orbiter slews its HGA to communicate with the lander for an anticipated six minutes per day.

5.2.3.3 Thermal System

The baseline thermal subsystem is designed to utilize a portion of the RTG waste heat for spacecraft and lander heater power. Variable conductance heat pipes (VCHP) interface to the RTG and draw a portion of the heat to the instrument and avionics system. The RTGs dissipate in total more than 10,000 W of thermal power, and the spacecraft needs only 100 W to maintain operating temperature, so the majority of the RTG waste heat is dissipated to space. Louvered radiators modulate heat dissipation over the 1–8 AU range mission.

5.2.3.4 Electrical Power System

Both the orbiter and the lander would require a system to shunt excess power from the RTGs. During launch, the shunt load would be essentially the entire RTG suite output as there is little or no electrical demand during this early phase of the mission. Shunt load varies throughout the mission up to 600 W, depending on the phase. The orbiter did not require a battery, though a small 18 A-hr battery is needed on the lander, primarily for use during descent and landing, when lander communication, propulsion, and attitude control systems is active.

5.2.3.5 Baseline RPS Suite

The baseline ChirEx RTG mission would be powered by two HSMRTG-16 units on the orbiter and one HSMRTG-12 on the lander, and the electrical system is designed so lander RTG power can be used by the spacecraft bus while attached. This was required to satisfy electrical propulsion power requirements during cruise.

5.2.3.6 Additional Lander-Specific Details

The ChirEx lander has an approximately 1-m high by 1-m diameter body with multiple decks to accommodate lander hardware. Three deployable legs provide landing stability and a method of adhering to the surface. One HSMRG-12 would power the lander for its 18 months of surface operation. The lander has a hydrazine propulsion system for a controlled descent and hopping to a second location. A pumped liquid/heat exchanger system would be used to transfer a portion of the RTG waste to the lander to maintain design temperature during surface operations, with the rest dissipated to space. The ChirEx lander concept is shown in Fig. 5-4.

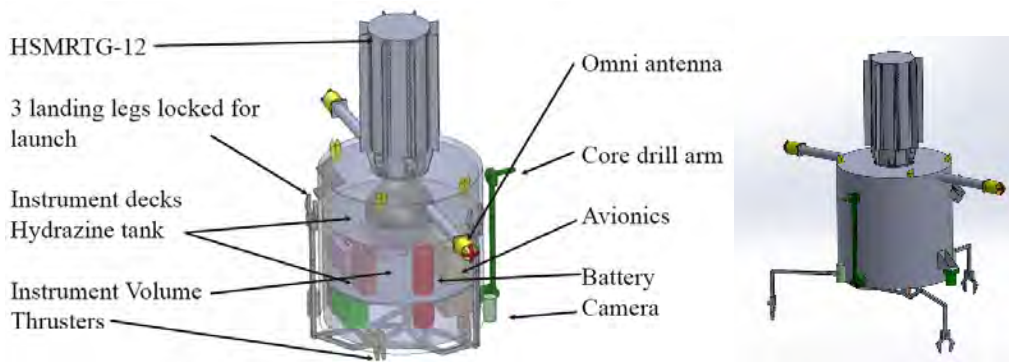


Fig. 5-4. ChirEx lander.

5.2.4 ChirEx Resources

5.2.4.1 Power

Two HSMRTG-16 and one HSMRTG-12 would provide roughly 1,000 W at beginning of mission (BOM). A 1.6% power degradation per year power leaves approximately 850 W at the rendezvous with Chiron and ~820 W at EOM. ChirEx’s EP thrusters’ power requirement of 600–700 W essentially uses all available power throughout cruise, with excess power shunted during launch, orbital science, and surface science operations when the propulsion system is off.

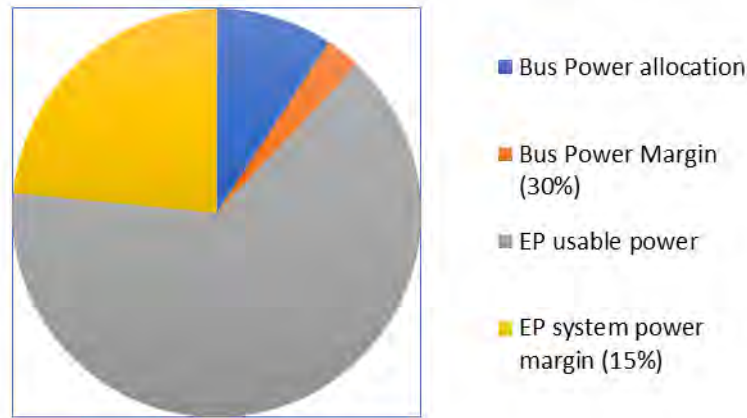


Fig. 5-5. ChirEx estimated power usage during cruise.

5.2.4.2 Mass

The CBE dry mass would be 260 kg for the lander and 548 kg for the orbiter, for a total dry CBE mass of 808 kg. An average contingency of ~15% made the MEV dry mass 935 kg, and 709 kg of propellant increases the overall wet mass to 1,644 kg. This leaves a 5% launch vehicle margin for the baseline mission. Mass resources are summarized in Table 5-4.

Table 5-4. Baseline ChirEx mission mass resources.

Spacecraft Element	CBE Mass (kg)	MEV mass (kg)
Lander Subtotal	260	279
Instrument Suite	27	35
Subsystems	206	244
Orbiter Subtotal	548	656
Payload	31	40
Instruments	517	616
Total Dry Mass		935
Total Propellant		709
Total Wet Mass		1644
Launch Vehicle Capability		1688
Mass Margin (%)		5

5.2.5 System Trades

The mass margin for the baseline ChirEx mission is less than the desired 25%, so from this standpoint, the mission did not close. This baseline was considered a point design from which trades and parametric studies could be made. Those trades are summarized below.

5.2.5.1 An Alternate RTG Choice: CSRTG

The HSMRTG was selected to power the baseline ChirEx mission as it has a relatively high power density, a low decay rate, and is suited for a greater variety of operating environments. While less versatile, the CSRTG has a similar decay rate and a higher power density, so an analysis was done assessing the impact of implementing one CSRTG on the ChirEx lander and one on the orbiter. Other mission concept parameters, such as flight duration and payload, remained the same. Results are shown in Table 5-5.

Table 5-5. HSMRTG vs. CSRTG trade.

	Two HSMRTG-16 on Orbiter One HSMRTG-12 on Lander	One CSRTG on Orbiter One CSRTG on Lander
BOM Power (W)	997	1052
Wet Launched Mass (kg)	1644	1534
Mass Margin (%)	4	15

Switching from the baseline HSMRTG (16+16+12) suite to two CSRTGs increased usable non-RTG mass to Chiron by 95 kg CBE and raised mass margin to 15%. However, since less power would be available during Surface Science Operations, the DSN data link rate was reduced by about 25%, which is likely still acceptable for the ChirEx mission.

5.2.5.2 Extending the Mission Duration beyond the RTG Design Life

Extending the cruise time from 12 to 15 years and utilizing an Earth flyby increased needed propellant from 709 kg to 992 kg, and also increased the deliverable mass to Chiron by ~300 kg due to the additional launch vehicle throw mass afforded by eliminating the STAR 48 booster motor. Mass margin for the baseline ChirEx concept increased to 25%, which is expected of missions in this early conceptual stage so this change essentially enabled the baseline mission. Results are summarized in Table 5-6.

Table 5-6. Extending baseline mission cruise from 12 to 15 years.

	Baseline 12-Year Cruise	15-Year Cruise
Spacecraft MEV Dry Mass (kg)	935	958
Spacecraft Propellant (kg)	709	992
Spacecraft MEV Wet Mass (kg)	1644	1950
Launch Vehicle Capacity (kg)	1688	2271
Mass Margin (%)	4	25

5.2.6 Flight Dynamics Parametric Studies

Trajectory design is critical in the design of planetary missions, as optimization delivers the maximum usable mass to the science destination. For EP mission concepts, trajectory design is highly dependent on power available during cruise. This proved to be true for ChirEx and was a driver in the selected suite of RTGs. A series of three generic parametric studies were conducted to assess the impact of RTG design parameters on the delivered mass to Chiron. These studies are not trades on the ChirEx orbiter/lander concept mission but serve to more generally illustrate the impact of RTG design parameters on any EP mission to Chiron.

5.2.6.1 Usable Mass at Chiron vs. RTG Type

The first study looked at varying the type of RTG powering the mission concept and assessing the impact on the amount of usable (non-RTG) mass available at Chiron, while maintaining the baseline 12-year cruise (results shown in Table 5-7). As expected, the total deliverable mass increased with BOM power, however, the delivered mass was dependent on the combination of BOM power and RTG suite power density.

Table 5-7. Delivered mass to Chiron vs. RTG suite.

	2X HSMRTG-16	2X SMRTG-16	2X CHSMRTG -16	2X SRTG	2X CSMRTG-16	2X CSRTG
Max Deliverable Mass (kg)	837	946	962	1033	1042	1086
BOM Power (W)	731	810	818	916	932	1052
RTG Mass (kg)	121	106	132	106	134	116
Non-RTG Mass (kg)	716	840	830	927	908	970

5.2.6.2 Usable Mass at Chiron vs. HSMRTG Modularity

The second study looked at the modularity of the HSMRTG and its impact on the usable mass delivered to Chiron (results shown in Table 5-8). Again, results show a clear, and expected, correlation between delivered mass and BOM power, regardless of how that RTG was packaged. Delivered usable non-RTG mass, again indicates a more complex relation involving BOM power and aggregate RTG power density, further emphasizing the need for carefully integrated propulsion, flight dynamics concepts, and electrical power systems in any RPS-powered EP mission.

The nomenclature of the left-most column in Table 5-8 is read as n generators \times (M GPHSs). Therefore, $1 \times (-16)$ should be interpreted as a single RTG, an HSMRTG in this case, that is fueled by 16 GPHS. The HSMRTG package identified as $2 \times (-16) + 1 \times (-8)$, the third package in the table, is a package consisting of two HSMRTGs, each fueled with 16 GPHS *plus* another HSMRTG using just eight GPHS, for a total of three RTGs in this package. The other entries in Table 5-8 should be interpreted similarly.

Table 5-8. Delivered mass to Chiron vs. HSMRTG modularity.

HSMRTG package	BOM Power (W)	Delivered Mass (kg)	Non-RTG Mass (kg)	Gain/Loss from Reference (kg)
Reference : $1 \times (-16) + 2 \times (-8)$	707	823	696	
$1 \times (-16) + 3 \times (-8)$	879	827	667	-29
$2 \times (-16) + 1 \times (-8)$	901	835	680	-16
$1 \times (-16) + 2 \times (-8) + 1 \times (-12)$	976	869	695	-1
$2 \times (-16) + 2 \times (-8)$	1072	903	715	+19

5.2.6.3 Usable Mass at Chiron vs RTG Decay Rate

Finally, a study of the impact of HSMRTG decay rate on delivered mass was completed and indicates insensitivity to this design parameter. This study maintained the RTG suite in the baseline ChirEx mission, as well baseline payload and cruise duration and varied only the rate at which the power provided by the RTGs decayed. Varying the decay rate from 0.6 to 4.6% resulted in a decrease of deliverable mass to Chiron of only ~5%. The theoretical lower limit of power degradation of an RTG is ~1.3%; so 0.6% is not achievable, and hence the actual effect on deliverable mass is even less than estimated here. This study's results are shown in Table 5-9.

Table 5-9. Mass delivered to Chiron vs. HSMRTG decay rate.

HSMRTG Power Decay Rate (Average %/year)	Delivered Mass (kg)	Propellant Mass (kg)
0.60%	991	702
1.60% ChirEx Baseline	978	709
2.60%	970	701
3.60%	955	689
4.60%	927	715

5.3 The Titan Turtle Mission Concept

Titan is Saturn’s largest moon and the only known moon in the solar system with clouds and a dense, planet-like atmosphere. This, and the abundance of hydrocarbons present, make Titan similar to primordial Earth, of interest to scientists looking for life signatures in the solar system. Observations by the Cassini mission also confirm the presence of large liquid methane and ethane sea surface bodies. Among these are Ligeia Mare, a 400-km-wide, ~200-m-deep lake in Titan’s north polar region, and Kraken Mare, Titan’s largest known surface liquid body. Ligeia Mare, imaged by the Cassini spacecraft, is shown in Fig. 5-6.

In 2014, the Compass Team at GRC developed a conceptual design for an RTG-powered submarine to explore Titan’s hydrocarbon seas. Dubbed the Titan Turtle, its baseline mission was to spend one year autonomously carrying out detailed scientific investigations above and below the surface of Ligeia Mare with an optional one-year extended mission to explore Kraken Mare. The Titan Turtle would carry a 78-kg MEV payload of sonar and imaging equipment and autonomously travel more than 2,000 km in the methane sea, examining surface weather and sampling bottom sediment.

The initial concept was powered by a single eMMRTG with design parameters listed in Table 5-10. For this report, the Compass Team assessed the impact of replacing the eMMRTG with a single CHMSRTG-8. Results of both studies are described here.

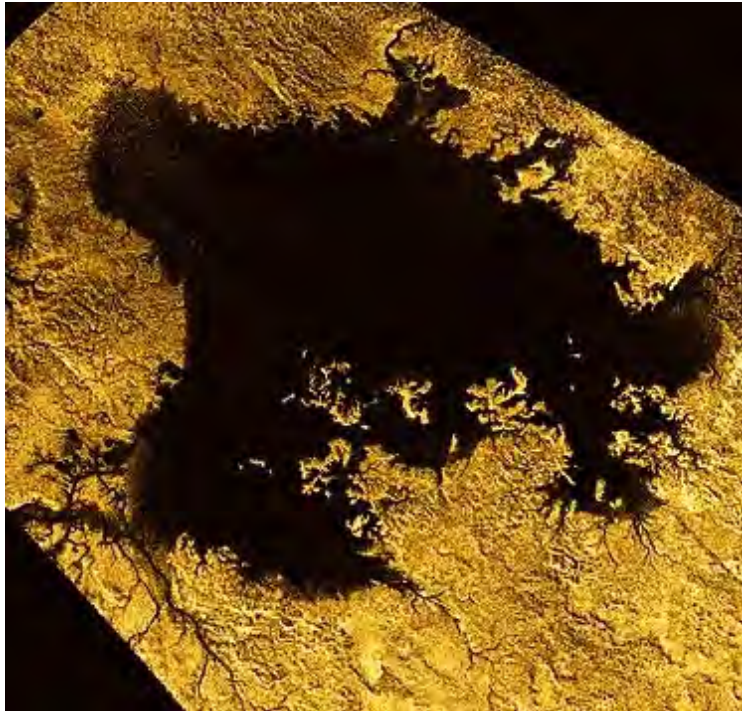


Fig. 5-6. Titan’s Ligeia Mare.

Table 5-10. eMMRTG specification in the initial Titan Turtle mission concept.

eMMRTG Design Parameters	
Power BOL (W)	166
Power (EOM) (W)	88
Mass (kg)	45
Diameter without fins (m)	0.25
Length (m)	0.69
Power Degradation Rate/year (%)	2.5%
Waste Heat (W)	2000

5.3.1 Initial Design Concept

The Titan Turtle is a 2-m-long, ellipsoid pressure-vessel designed to operate in Ligeia Mare's ~90 K liquid methane environment. It is the in situ portion of a larger Titan mission that includes a Titan orbiter. The Turtle would be delivered to Ligeia via a 2.7-m biconic aeroshell that slows descent and provides a soft landing. It has an external and closed helium ballast tank to allow for controlled submarine operations, submerging and hovering, as deep as 200 m below the surface where pressure is estimated to be high as 5 bar pressure. The submersible concept is shown in Fig. 5-7.

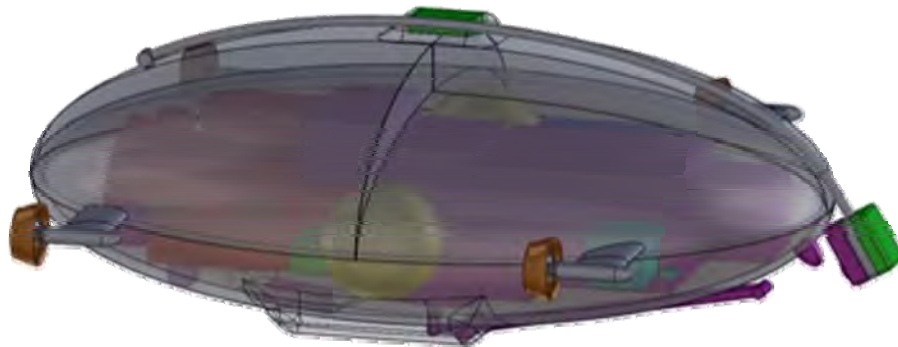


Fig. 5-7. Titan Turtle design concept.

The housing of the submersible uses a titanium pressure vessel with ring stiffeners and internal structure for mounting payload and hardware. The vehicle is fitted with a periscope arm to lift instruments to ~1 m above the surface and a sample arm to acquire and deliver samples to analysis instrumentation. Twenty-five millimeters of aerogel provide insulation between the internal hardware and the frigid thermal sink of the liquid methane sea. System thermal requirements are also maintained utilizing RTG waste heat. All power would be supplied from a single eMMRTG, loaded and integrated through a rear hatch while on the launch pad.

Four motors on booms provide up to 0.3 m/s of velocity while submerged and 0.2 m/s on the surface, as well as differential steering. The Turtle communicates via a 20-W UHF radio tied to antennas. These broadcast to the Titan orbiter at 1,500 km altitude. Data rates are ~100 kbps during five 30-minute orbiter passes per day, for a total of approximately 1 GB of data delivered per day.

The mission concept is designed around the timeline of autonomous command and data handling for four days of surface operation and 12 days of submerged exploration. Navigation utilizes an inertial measurement unit (IMU), orbiter tracking, and sonar scanning. Total CBE dry mass is 408 kg, and adding an 18% aggregate contingency, the MEV dry mass is 483 kg. System mass resources are shown in Table 5-11.

Table 5-11. eMMRTG powered Titan Turtle mass resources.

Spacecraft Element	CBE Mass (kg)	MEV mass (kg)
Science Payload	78	102
Attitude Control	6	6
Avionics	17	21
Communication	9	9
Electrical Power System	72	76
Thermal Control	25	29
Mobility	53	63
Structures and Mechanisms	149	176
Total Dry Mass	408	483

5.3.2 Switching to a CHMSRTG-8

The eMMRTG using eight GPHS was replaced with a CHSMRTG fueled with eight GPHS modules and the specifications listed in Table 5-12. It was assumed that, as per the eMMRTG, fins could be removed, as this was required for installation in the sub.

Table 5-12. CHSMRTG-8 specifications. Mass estimate for the CHSMRTG in this table is outdated. The mass here was the initial mass estimate before detailed thermal modeling was performed. The ChirEx spacecraft design using CHSMRTGs was created by the GSFC Mission Design Lab based upon premature information submitted by the Next-Generation RTG Study Team.

CHSMRTG-8 Design Parameters	
Power BOL (W)	198
Power (EOM) (W)	156
Mass (kg)	37
Diameter with fins (m)	0.56
Length (m)	0.68
Power Degradation Rate/year (%)	1.6%
Waste heat (W)	1952

5.3.2.1 Impact on Mission Concept Design

The CHMSRTG-8 mechanical and thermal design values were reasonably close to those of the eMMRTG, so the overall submarine design concept was minimally altered. However, the nearly doubling of mission power did have a significant impact on predicted science return in two ways:

- Science Return: Triple the science data collection and return was enabled throughout the mission due to the additional power available. The original, possible 1 Gb data delivery per day could be increased to 3 Gb per day with the CHSMRTG-8.
- Acquisition: Sub speed could be increased by ~30%, thus more of the Ligeia Mare can be explored.

5.4 References

- [1] NASA GSFC. August 3, 2009. Goddard Technical Standard: Rules for the Design, Development, Verification, and Operation of Flight Systems, NASA GSFC-STD-1000E, Greenbelt, MD. http://everyspec.com/NASA/NASA-GSFC/GSFC-STD/GSFC-STD-1000E_20173/

6 Conclusions

David F. Woerner

NASA Jet Propulsion Laboratory, 4800 Oak Grove Drive, Pasadena, CA 91109

This study developed concepts for Next-Generation RTGs using two engineering approaches in parallel, top-down and bottom-up. The top-down approach entailed review of past mission studies, preparation of new independent mission studies, review of potential destinations within the solar system, and review of recently flown RTGs to develop requirements. The bottom-up approach entailed review of current thermoelectric materials to propose thermoelectric couple configurations. RTG concepts described in this report were instantiated where the two approaches met.

Next-Generation RTG technical requirements were derived from GPHS-RTG, MMRTG, and eMMRTG requirements, and additional bases for requirements derived from review of mission studies and significant destinations within the solar system. Additionally, this approach resulted in identification of a few requirements not previously applied to RTGs, including a modular system requirement. A modularized system would allow users to select RTGs from a series of options with different lengths and power and mass values. Length, power, and mass would vary with the number of GPHS in an RTG. Little else in a modularized system would change. This one requirement maximizes utility of Next-Generation RTG concepts at destinations across the solar system and has the potential to serve the vast range of power needs across the Discovery, New Frontiers, and Flagship-class missions, a range from ~130 W to ~1,000 W. This requirement also provides a potential means to use the radioisotope fuel for RTGs more efficiently and reduce spacecraft integration issues.

While maximizing the utility of Next-Generation RTG concepts was an objective of this study, niche requirements for specialized RTG concepts were noted. A requirement was categorized for specialized RTGs if the requirement was meant for a minority of missions. These requirements might also be burdensome to the majority of potential missions. For example, exploration in the ice sheets and oceans on other worlds and on the surface of Venus requires any RTG considered for use at those destinations to have a pressure vessel housing due to hydrostatic and hydrodynamic pressures. This type of vessel would add tens to hundreds of kilograms to the mass of an RTG, making this type of RTG potentially unusable by many of the missions studied. A pressure vessel, however, could enable a set of potential and as-of-yet unattempted missions.

The bottom-up approach found a significant level of global research has been performed over the last decade to develop novel advanced thermoelectric materials. These advanced thermoelectric materials range from Zintl, skutterudite, chalcogenide, and half-Heusler materials to nanostructured materials, such as nanowires, quantum dots, quantum wells, thin film superlattices, combinatorial sputtered deposits, and many others. The University of Dayton Research Institute (UDRI) was engaged to lead this effort and provide a fresh review of recent research. However, UDRI's findings reinforced the understanding that many of these novel thermoelectric material systems are not suitable for incorporation into an RTG design intended for space applications. UDRI further noted that the efforts undertaken by JPL over the last few decades to identify novel thermoelectric materials potentially suitable for terrestrial and space RTGs is noteworthy. Those efforts, coupled with an ability to conduct research to mature potential materials to higher TRLs where they can be thoroughly assessed, enables NASA to have the ability to validate whether future investments should be made.

Thermoelectric couple efficiencies ranging from approximately 11–17% may be achievable by employing segmented thermoelectric couple architectures. Segmentation could be used to improve the efficiency of TECs by constructing the legs of TECs from segments each composed of a different material that has a peak figure of merit (ZT) at a different temperature, thus effectively designing a thermoelectric leg to provide a large average figure of merit over a specific temperature range. Segmentation has been used in thermoelectric couple designs such as the MMRTG TECs. Achieving segmentation for the

identified thermoelectric materials would demand some innovation, however, and many significant technical challenges must be addressed before any of the segmented configurations are flown.

This study has identified a strong need for a closely coordinated, parallel research and development effort focused on developing and validating methods and materials to bond the thermoelectric materials identified as segmented configurations, mitigate material diffusion across the segmented interfaces, and develop protective coatings to reduce sublimation. If the research and development efforts are not conducted in parallel and in a coordinated manner, then by default, the most mature configuration would become the baseline technology in Next-Generation RTG concepts.

A total of eight candidate thermoelectric couple configurations were identified for the Next-Generation RTG concepts. These new couples have the potential to deliver the same amount of power as a GPHS-RTG using just 44% of the fuel. The requirements for a Next-Generation RTG, when coupled with the candidate thermoelectric couples identified, resulted in six RTG concepts deemed worthy for further analysis. Three candidates remained after the initial six were scrutinized. The candidate RTGs for the next generation of NASA planetary science mission concepts are the SRTG, SMRTG, and HSMRTG; all other concepts studied failed to meet critical requirements. Table 6-1 provides a brief description of the candidate designs.

Table 6-1. Summary descriptions of the three candidate RTG concepts.

SRTG:	Segmented RTG. A generator with segmented thermoelectric couples. No modularity. Vacuum-only operations. Optimized for specific power. TC efficiency calculated at cold junction temperature (T_c): 450 K.
SMRTG:	Segmented-Modular RTG. A modularized generator with segmented thermoelectric couples. Vacuum-only operations. TC efficiency calculated at cold junction temperature (T_c): 450 K.
HSMRTG:	Hybrid Segmented-Modular RTG. A modularized generator with segmented thermoelectric couples relying upon a hybrid housing to allow operations in atmospheres and vacuum. TC efficiency calculated at cold junction temperature (T_c): 450 K.

Power estimates for these generators can be viewed as ranges along two orthogonal and related axes. One axis shows the concept’s promise power in the range of 400–600 W in RTGs using any one of the eight TECs identified in this report and 16 GPHS. On another axis, modularized generators with 2–16 GPHS offer the potential for power in the range of 50–60 W up to the 400–600 W upper limit. The two perspectives are combined in Fig. 6-1.

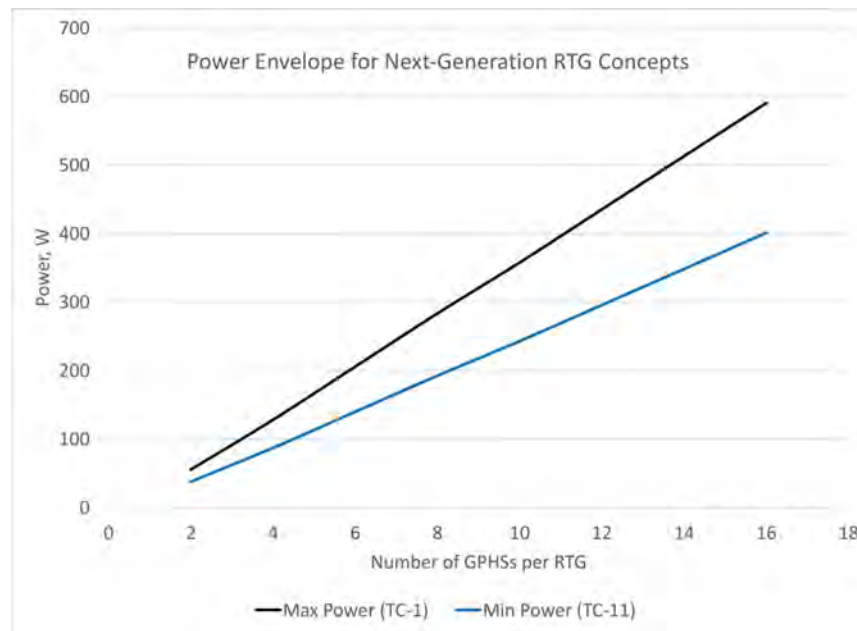


Fig. 6-1. The envelope of power estimates for Next-Generation RTG concepts from minimum to maximum power by TEC and number of GPHSs per RTG concept.

The value of modularity (along with their features supporting interchangeability) outweighed the perceived lower risk of a point design, as in the SRTG-16. The hybrid feature would add more development risk over the other two generator concepts, but is still a viable candidate. While none of these three were dropped from the study, they were prioritized as SMRTG, SRTG, and HSMRTG.

Finally, the MMRTG, and the potential eMMRTG, can provide radioisotope power for missions at Titan and Mars and balloon missions at Venus. This observation and the higher-level risk of the HSMRTG suggest one attractive strategy would be to sustain the MMRTG or complete the eMMRTG and develop the SMRTG.

The Next-Generation RTG concepts identified in this study match the needs of many potential mission concepts (both existing and new), derive from previous missions and proven RTGs, and have the potential to provide considerable mass and fuel savings, while boosting power by a factor of 1.5–2.0 over previous RTGs.

Appendices

Appendices Contents

A	Science Mission Concepts Analyzed for RTG Requirements.....	A-1
	A.1 Mission Data Sources	A-1
	A.1.1 PSDS Mission and Technology Studies	A-1
	A.1.2 RPS Program Mission Analysis Team Studies.....	A-2
	A.1.3 DSMCE Studies.....	A-2
	A.1.4 NPAS High Power Mission Concept Data Set	A-2
	A.1.5 GRC Studies	A-2
	A.1.6 GSFC Studies	A-2
	A.1.7 Other Studies	A-2
	A.2 RPS Mission Concept Database Summary.....	A-2
	A.3 References	A-5
B	Aerial Missions	B-1
	B.1 Balloons.....	B-2
	B.2 Rotary Wing Aerial Vehicle	B-7
	B.3 Summary.....	B-8
	B.4 References	B-9
C	Melt Probes	C-1
	C.1 Introduction	C-1
	C.2 Explanation of Terms	C-1
	C.3 References	C-2
D	Landers, Rovers, Boats, and Submarines.....	D-1
	D.1 Platform Types	D-1
	D.1.1 Manipulation Systems on Orbiting Platforms	D-1
	D.1.2 Aerial/Above-Surface Planetary Exploration.....	D-2
	D.1.3 Surface Ground Systems	D-2
	D.1.4 Subsurface Soil and Ice Penetrating Planetary Exploration	D-3
	D.1.5 Boats and Subsurface Liquid Robots.....	D-4
	D.2 Applications.....	D-5
	D.2.1 Assembly and Maintenance.....	D-5
	D.2.2 Science Observations.....	D-5
	D.2.3 Manipulation and Sampling	D-5
	D.3 Energy Requirements	D-6
	D.4 Selected Robotics Use Cases.....	D-6
	D.4.1 Large Space Manipulators.....	D-6
	D.4.2 Europa Lander Sampling System	D-7
	D.4.3 Titan Balloons	D-8
	D.4.4 ATHLETE	D-8
	D.4.5 Europa Deep Subsurface Ice Probe	D-9
	D.4.6 Titan Lake Submarine	D-10
	D.5 References	D-11
E	Probing Subsurfaces of Icy Bodies	E-1
	E.1 Introduction	E-1
	E.2 Pressure Profiles	E-2
	E.2.1 Fundamentals.....	E-2
	E.2.2 Calculating Pressures from Mass Density and Gravity	E-2
	E.2.3 Profiles for Europa, Ganymede, and Enceladus	E-3
	E.3 Temperature Profiles	E-7
	E.4 Reference.....	E-11

F	Temperatures across the Solar System and RTG Thermal Analyses	F-1
	F.1 Introduction	F-1
	F.2 Orbital Spacecraft.....	F-1
	F.3 Surface Landers on Worlds without Atmosphere.....	F-2
	F.4 Landers and Subsurface Vehicles on Worlds with Atmosphere or Ocean	F-5
	F.5 Special Cases	F-6
	F.5.1 Pressure Vessel for Subsurface Ocean Vehicles	F-6
	F.5.2 Excavation by Sublimation for Europa Lander	F-8
	F.6 References	F-15
G	Radiation Environments for Space Missions with RTGs.....	G-1
	G.1 Introduction	G-1
	G.2 Natural Space Radiation Environments.....	G-1
	G.2.1 Trapped Radiation	G-1
	G.2.2 Solar Energetic Particle or Solar Proton Event	G-2
	G.2.3 Galactic Cosmic Rays (GCR).....	G-7
	G.3 Radiation from RTGs	G-7
	G.3.1 Neutrons from RTG.....	G-9
	G.3.2 Gamma Rays from RTG.....	G-11
	G.4 Summary.....	G-12
	G.5 References	G-12
H	Planetary Protection: Requirements, Compliance, and Considerations for Missions Integrating Next-Generation RTG Technologies.....	H-1
	H.1 Introduction	H-1
	H.1.1 PP Considerations for Planetary Targets	H-2
	H.1.2 Special Region Designation and Possible Implications for Future Missions	H-3
	H.1.3 General PP Plan and Implementation Approach	H-3
	H.1.4 Other PP Considerations for Missions Employing Radioisotope Power Systems	H-5
	H.2 Summary.....	H-6
	H.3 References	H-6
	H.4 Acronyms	H-6
I	Micrometeoroids	I-1
J	Launch Vehicles and Mission Analyses.....	J-1
	J.1 Introduction	J-1
	J.2 Methodology and Tools.....	J-1
	J.2.1 Broad Trajectory Search Tool: Star.....	J-1
	J.2.2 Data Filtering and Post-Processing.....	J-1
	J.3 Assumptions	J-1
	J.3.1 Broad Trajectory Search Constraints.....	J-1
	J.3.2 Solar System Data Sources, Launch Vehicle Performance	J-3
	J.3.3 Assumed Performance Parameters	J-3
	J.3.4 Simple Calculations.....	J-3
	J.3.5 Historical Masses.....	J-3
	J.4 Results	J-4
	J.4.1 Quantification of the Utility of Gravity Assists for Outer Planetary Destinations	J-4
	J.4.2 Masses Delivered to Outer Planets.....	J-5
	J.4.3 Trajectories to Small Bodies	J-9
	J.4.4 Masses Delivered per Architectural Makeup	J-10
	J.5 Conclusions	J-10
	J.5.1 Methods for Improvement.....	J-11
	J.6 References	J-14

K Thermoelectric Technology Risk Assessment Details K-1

 K.1 Thermoelectric Materials Considered..... K-1

 K.2 Proposed RTG-Specific Thermoelectric Material Technology Readiness Level Definitions . K-8

 K.3 Thermoelectric Efficiency Modeling (T-MOD)..... K-10

 K.4 Thermoelectric Efficiency Modeling Results K-12

 K.5 Scorecard for Modeled Segmented and Non-Segmented Thermoelectric Configurations.... K-30

 K.6 References K-33

L Intensity Matrix L-1

M Destination Table M-1

N Reference RTGs: GPHS-RTG, MMRTG, and eMMRTG N-1

 N.1 GPHS-RTG..... N-1

 N.2 Multi-Mission RTG N-1

 N.3 enhanced MMRTG..... N-2

 N.4 References N-2

O Calculating RTG Fin Size and Mass O-1

 O.1 Introduction O-1

 O.2 Approach O-1

 O.3 Assumptions, Boundary Conditions, and Simplifications O-1

 O.3.1 Behavior of Common RTG Components When Scaled O-1

 O.3.2 Housing and Fin Dimensions O-1

 O.3.3 Assumptions and Simplifications Used in Thermal Modeling O-2

 O.3.4 Thermal Power Equations O-2

 O.4 Using the Model O-2

 O.4.1 Method..... O-2

 O.4.2 Validation O-2

 O.4.3 Determining Total Mass O-3

 O.5 References O-5

P Modeling Results for RTG Concepts P-1

 P.1 Introduction P-1

 P.2 Tables P-2

 P.3 Table Column Descriptions P-11

Q Factors of Safety – GPHS-RTG and MMRTG Q-1

 Q.1 Introduction Q-1

 Q.2 Tables Q-1

 Q.3 References Q-2

R Next-Generation RTG: Factors of Safety, Acoustics, and Random Vibrations..... R-1

 R.1 Introduction R-1

 R.2 Factors of Safety..... R-1

 R.3 Acoustic Sound Pressure Levels..... R-2

 R.4 Random Vibrations..... R-2

 R.5 Explanation of Terms R-2

 R.6 References R-4

A Science Mission Concepts Analyzed for RTG Requirements

Young Lee, Brian Bairstow

NASA Jet Propulsion Laboratory, 4800 Oak Grove Dr., Pasadena, CA 91109

To support the Next-Generation Radioisotope Thermoelectric Generator (RTG) Study with understanding of mission pull that is crucial to identify mission requirements for the next generation of RTGs, the Radioisotope Power Systems (RPS) Program Mission Analysis Team gathered information on past RPS mission studies by various organizations in the United States. Together with the Next Generation RTG Study team, the RPS Program Mission Analysis Team used these mission concepts to develop an RPS and mission concept database. The Next-Generation RTG Study team then used this database to aid in deriving RTG requirements.

This appendix will discuss the data sources and the 77 science mission concept entries in the RPS mission concept study database in greater detail.

A.1 Mission Data Sources

The 77 spacecraft concepts and their associated missions in the database were gathered from a variety of sources, broken down in Fig. A-1. Each of these sources is described in greater detail below.

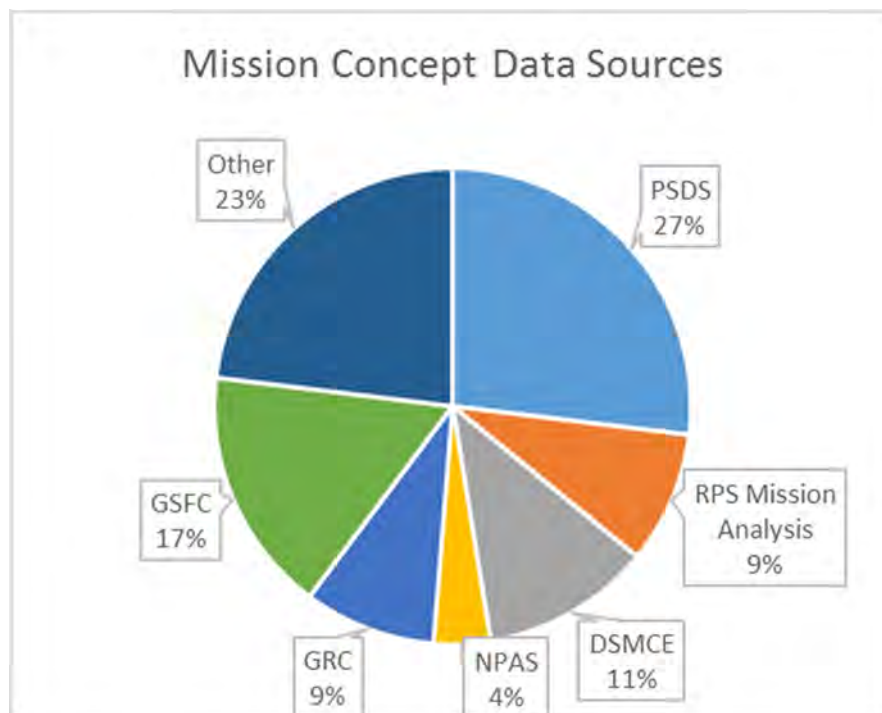


Fig. A-1. Breakdown of data sources of the RPS mission concepts in this study's database.

A.1.1 PSDS Mission and Technology Studies

A number of mission and technology studies were performed for the Planetary Science Decadal Survey (PSDS published in 2011 [1]). These studies ranged from architectural studies that looked across 10+ approaches with low fidelity to in-depth point concepts with high levels of detail. Twenty-one of the RPS mission concepts discussed in this report came from these mission studies, which were performed by design centers at Glenn Research Center (GRC, Goddard Space Flight Center (GSFC, Johns Hopkins

University (JHU)/ Applied Physics Lab (APL), Jet Propulsion Laboratory (JPL), and Marshall Space Flight Center (MSFC).

A.1.2 *RPS Program Mission Analysis Team Studies*

The RPS Program Mission Analysis Team has performed a number of RPS mission concept studies over the last several years and documented these in reports to the RPS Program. Data from seven missions in this study came from these RPS Program documents.

A.1.3 *DSMCE Studies*

The 2007 Discovery and Scout Mission Capabilities Expansion (DSMCE) studies were solicited by NASA, and nine investigations were funded to explore Discovery-class missions using RPS [2]. Curated data from these nine studies were gathered for the 2014 NPAS study [3] and also used for the Next-Generation RTG Study.

A.1.4 *NPAS High Power Mission Concept Data Set*

The 2014 Nuclear Power Assessment Study (NPAS) performed an analysis of mission power needs, focusing on high power mission concepts (higher than 500 W_e). Data was contributed from GRC, GSFC, JHU/APL and JPL. For most of those missions, primary sources were available (e.g., the original PSDS studies), but for three studies, the best available source was the data provided to the NPAS study team.

A.1.5 *GRC Studies*

The GRC COMPASS Team provided a summary table of the RPS studies it had performed. From this table, high-level data for seven mission concepts were included in the RPS mission concept study database.

A.1.6 *GSFC Studies*

Similarly, GSFC's Mission Design Lab provided a summary table of anonymized studies it has performed, studies that used RPS. From this table, high-level data for 13 mission concepts were included in the RPS mission concept study database.

A.1.7 *Other Studies*

The remaining 18 mission concepts in the RPS study database came from other publically available mission studies, or concepts described in published papers. These include the results from NASA Planetary Science Summer Seminar studies at JPL [4], the 2005 Advanced RPS Report published by JPL [5], the 2007 Titan Explorer Public Report published by JHU/APL [6], and others.

A.2 *RPS Mission Concept Database Summary*

In total, 77 RPS-powered spacecraft and their associated missions were evaluated and assessed for the Next-Generation RTG Study. The complete report for the Next-Generation RTG Study's database will be released later this year [7].

Table A-1 displays high-level data for the 77 missions in the database, as a summary for the important fields that impacted the Next-Generation RTG Study analyses.

Table A-1. Top-level data from RPS Study Database.

Spacecraft Concept	Associated Mission Type(s)	Associated Mission Subtype(s)	Associated Mission Destination(s)	Mass SC - Dry (kg)	Average Power (EOM)	Mission Time (y)
Centaur Scout SmallSat - RTG	FLYBY		Centaur	165.0	47.0	14.0
Centaur Scout SmallSat - SRG	FLYBY		Centaur	157.0	47.0	14.0
Chiron Orbiter (PSDS)	Orbiter		2060-Chiron	831.0	622.0	16.0
Comet Coma Rendezvous Sample Return (CCRSR)	SAMPLE RETURN		Comet	500.0	200.0	14.0
Comet Hopper (Chopper)	SURFACE	LANDER	Comet	600.0	246.0	10.0
Enceladus Flyby	Flyby		Enceladus	1000.0	409.0	10.0
	ORBITER		Saturn	1000.0	409.0	10.0
	FLYBY		Titan	1000.0	409.0	10.0
Enceladus Orbiter (EVE)	Orbiter		Enceladus	1244.0	166.0	13.0
	ORBITER		Saturn	1244.0	166.0	13.0
Enceladus Orbiter (FS)	Orbiter		Enceladus	1154.0	256.0	13.0
	ORBITER		Saturn	1154.0	256.0	13.0
	FLYBY		Titan	1154.0	256.0	13.0
	FLYBY		Rhea	1154.0	256.0	13.0
	FLYBY		Dione	1154.0	256.0	13.0
	FLYBY		Tethys	1154.0	256.0	13.0
Enceladus Sample Return (4)	Sample Return		Enceladus	1200.0	372.0	16.0
	ORBITER		Saturn	1200.0	372.0	16.0
	FLYBY		Titan	1200.0	372.0	16.0
	FLYBY		Rhea	1200.0	372.0	16.0
	FLYBY		Dione	1200.0	372.0	16.0
	FLYBY		Tethys	1200.0	372.0	16.0
Enceladus Sample Return Mission Concept (LIFE)	Sample Return		Enceladus	800.0	245.0	15.0
	ORBITER		Saturn	800.0	245.0	15.0
Enceladus SmallSats	FLYBY		Enceladus	253.0	43.0	13.0
	ORBITER		Saturn	253.0	43.0	13.0
	FLYBY		Titan	253.0	43.0	13.0
Europa Ice Sounder	Flyby		Europa	600.0	200.0	8.0
Europa Lander	Surface	Lander	Europa	300.0	125.0	2.5
Europa Lander (2005 Advanced RPS Report)	Surface	Lander	Europa	779.0	92.0	4.9
	ORBITER		Jupiter	779.0	92.0	4.9
GSFC Mission 1	SURFACE	Lander	Moon	1600.0	5.0	5.0
GSFC Mission 10	ORBITER		Europa	621.0	120.0	6.2
GSFC Mission 11	ORBITER		Trojan	506.0	400.0	17.0
GSFC Mission 12	Orbiter		Titan	957.0	205.0	10.0
GSFC Mission 13	Orbiter		Titan	984.0	176.0	12.0
GSFC Mission 2	Surface	Lander	Enceladus	814.0	270.0	7.2
GSFC Mission 3	Surface	Lander	Enceladus	602.0	405.0	17.4
GSFC Mission 4	Surface	Lander	Enceladus	169.0	488.0	19.4
GSFC Mission 5	Surface	Lander	Enceladus	79.0	405.0	10.4
GSFC Mission 6	Surface	Lander	Enceladus	1049.0	405.0	13.6
GSFC Mission 7	Surface	ROVER	Comet	373.0	205.0	10.0
GSFC Mission 8	SURFACE	LANDER	Near Earth Object (NEO)	309.0	240.0	10.7
GSFC Mission 9	Orbiter		Jupiter	834.0	384.0	10.0
International Lunar Network	Surface	Lander	Moon	203.0	67.0	6.0
International Lunar Network - sRPS	Surface	Lander	Moon	180.0	45.0	6.0
Io Observer	FLYBY		Io	821.0	370.0	8.5
	ORBITER		Jupiter	821.0	370.0	8.5
Io Volcano Observer (IVO)	Orbiter		Io	1100.0	262.0	8.0
Journey to Enceladus and Titan	FLYBY		Enceladus	653.0	124.0	8.2
	FLYBY		titan	653.0	124.0	8.2
	ORBITER		saturn	653.0	124.0	8.2
Jupiter Europa Orbiter	Orbiter		Europa	1715.0	539.0	9.0
	ORBITER		Jupiter	1715.0	539.0	9.0
	FLYBY		Io	1715.0	539.0	9.0
	FLYBY		Ganymede	1715.0	539.0	9.0
	FLYBY		Callisto	1715.0	539.0	9.0
KBO Orbiter	Orbiter		Kuiper Belt	1275.0	100.0	16.7
KBO Orbiter w/ REP	Orbiter		Kuiper Belt	1902.0	4105.0	17.0
Lunar Lander (EXOMOON)	Surface	Lander	Moon	550.0	79.0	1.0
Lunar Polar Volatile Explorer (JEDI)	Surface	Rover	Moon	1100.0	148.0	1.0
Lunar Polar Volatiles Explorer	Surface	Rover	Moon	483.0	54.0	1.0

Spacecraft Concept	Associated Mission Type(s)	Associated Mission Subtype(s)	Associated Mission Destination(s)	Mass SC - Dry (kg)	Average Power (EOM)	Mission Time (y)
Mars Geyser Hopper	Surface	Lander	Mars	700.0	123.0	2.4
Mars Hard Lander (MASER)	Surface	Lander	Mars	17.0	0.2	4.8
Mars Polar Climate Mission	Surface	Rover	Mars	350.0	140.0	3.0
Mars Polar Ice Borehole (Kuklos)	Surface	Lander	Mars	800.0	72.0	3.0
Mercury Surface Lander	Surface	Lander	Mercury	289.0	99.0	5.0
Neptune Orbiter w/ REP (2)	Orbiter		Neptune	3047.0	4058.0	18.0
	ATM PROBE		Neptune	3047.0	4058.0	18.0
Neptune Triton Flyby TRIDENT	Flyby		Neptune	1251.0	250.0	13.6
	FLYBY		Triton	1251.0	250.0	13.6
	ATM PROBE		Neptune	1251.0	250.0	13.6
Neptune Vision	Orbiter		Neptune	2600.0	430.0	15.0
	FLYBY		Triton	2600.0	430.0	15.0
	ATM PROBE		Neptune	2600.0	430.0	15.0
Neptune-Triton High Power Orbiter (1)	Orbiter		Neptune	1800.0	551.0	15.0
	FLYBY		Triton	1800.0	551.0	15.0
Neptune-Triton Orbiters (6)	Orbiter		Neptune	1400.0	330.0	15.0
	FLYBY		Triton	1400.0	330.0	15.0
Neptune-Triton-KBO Flybys (7)	Flyby		Kuiper Belt	1000.0	441.0	15.0
	FLYBY		Neptune	1000.0	441.0	15.0
	FLYBY		Triton	1000.0	441.0	15.0
REP Centaur Orbiter	ORBITER		Centaur	555.0	684.0	11.0
Saturn Moon Orbiter	Orbiter		Saturn	1490.0	877.0	14.0
Saturn Probe (Carrier-Relay)	Flyby		Saturn	675.0	175.0	6.8
	ATM PROBE		Saturn	675.0	175.0	6.8
Saturn Ring Observer	Orbiter		Saturn	1800.0	2476.0	12.0
	FLYBY		Titan	1800.0	2476.0	12.0
Titan Aviatr	AERIAL	FIXED WING	Titan	116.0	220.0	8.7
Titan Explorer (2007): Aerial	Aerial	Balloon	Titan	755.0	89.0	10.3
Titan Explorer (2007): Lander	Surface	Lander	Titan	499.0	177.0	10.3
Titan Explorer (2007): Orbiter	Orbiter		Titan	1349.0	447.0	14.0
Titan Lake Probe-Lander (FS)	Surface	Boat	Titan	411.0	250.0	9.0
	ORBITER		Saturn	411.0	250.0	9.0
Titan Lake Probe-Lander (NF)	Surface	Boat	Titan	406.0	170.0	6.0
Titan Mare Explorer (TIME)	Surface	Boat	Titan	750.0	254.0	7.5
Titan Orbiter (2005 Advanced RPS Report)	Orbiter		Titan	2130.0	1000.0	10.0
Titan Rover (2005 Advanced RPS Report)	Surface	Rover	Titan	376.0	42.0	10.6
Titan Saturn System Mission - NPAS	Orbiter		Titan	1538.0	847.0	13.5
	ORBITER		Saturn	1538.0	847.0	13.5
	FLYBY		Enceladus	1538.0	847.0	13.5
Titan Saturn System Mission: Montgolfiere	Aerial	Balloon	Titan	479.0	92.0	13.5
Titan Saturn System Mission: Orbiter	Orbiter		Titan	1413.0	394.0	13.5
	ORBITER		Saturn	1413.0	394.0	13.5
	FLYBY		Enceladus	1413.0	394.0	13.5
Titan Submarine	Subsurface	Liquid	Titan	1386.0	534.0	7.3
Trojan Asteroid Lander (Iliion)	SURFACE	LANDER	Trojan	600.0	202.0	11.0
Trojan Lander w/REP	SURFACE	LANDER	Trojan	635.0	695.0	9.5
Trojan Tour	ORBITER		Trojan	615.0	172.0	11.0
Trojan Tour w/REP	ORBITER		Trojan	689.0	810.0	9.0
Uranus Orbiter (CAELUS)	Orbiter		Uranus	1382.0	203.0	14.8
	FLYBY		Saturn	1382.0	203.0	14.8
Uranus Orbiter and Probe	Orbiter		Uranus	906.0	314.0	15.4
	ATM PROBE		Uranus	906.0	314.0	15.4
Uranus Orbiter and Probe - NPAS - RTG	Orbiter		Uranus	916.0	314.0	15.4
	ATM PROBE		Uranus	916.0	314.0	15.4
Uranus Orbiter and Probe - NPAS - SRG	Orbiter		Uranus	921.0	314.0	15.4
	ATM PROBE		Uranus	921.0	314.0	15.4
Uranus Orbiter and Probe (OCEANUS)	Orbiter		Uranus	1329.0	192.0	13.0
	ATM PROBE		Uranus	1329.0	192.0	13.0
Venus Atmospheric Long-Duration Observatory for in situ research (VALOR) (Balloon)	AERIAL	BALLOON	Venus	1700.0	84.0	1.0
Venus Rover (2005 Advanced RPS Report)	Surface	Rover	Venus	680.0	39.0	1.8

A.3 References

- [1] U.S. National Academies of Science. 2012. Planetary Science Decadal Survey Mission & Technology Studies, http://sites.nationalacademies.org/ssb/ssb_059331.
- [2] DSMCE studies selections, Solicitation: NNH07ZDA001N-DSMCE, NASA. April 8, 2008, <https://nspires.nasaprs.com/>
- [3] John Hopkins University, Applied Physics Laboratory. 2015. Nuclear Power Assessment Study, TSSD-23122. <http://solarsystem.nasa.gov/rps/npas.cfm>
- [4] Planetary Science Summer Seminar. <https://pscischool.jpl.nasa.gov/>
- [5] Jet Propulsion Laboratory. November 2005. Extending Exploration with Advanced Radioisotope Power Systems, JPL D-28903.
- [6] John Hopkins University, Applied Physics Laboratory. January 2008. Titan Explorer Flagship Mission Study.
- [7] Jet Propulsion Laboratory. 2017. RPS Heritage Study Database, maintained by JPL for NASA's Radioisotope Power Systems Program.

B Aerial Missions

John O. Elliott

NASA Jet Propulsion Laboratory, 4800 Oak Grove Drive, Pasadena, CA 91109

While landers dominate the history of in situ missions thus far, a number of concepts have been proposed for aerial exploration at those destinations with a suitable atmosphere. Flight projects have included balloons for Venus, as demonstrated by the USSR in the Vega 1 and Vega 2 missions in 1985 [1], and a small rotorcraft is currently being developed to fly with the Mars 2020 lander [2]. Mars has for some time been a particular focus for aerial exploration, with numerous concepts developed and proposed for balloons, airplanes, and rotorcraft over the last decades. Indeed, one of the earliest concepts for human exploration of Mars, developed by Dr. Wernher Von Braun in the 1950s, envisioned winged spacecraft that would use the tenuous Martian atmosphere to glide to a landing (Fig. B-1).



Fig. B-1. Winged landing craft from 1954 article in Colliers magazine, “Can we get to Mars?” by Wernher Von Braun, illustration by Chesley Bonestall.

While aerial missions to Venus and Mars can generally be powered by solar arrays and or batteries, missions to the outer solar system are likely to require radioisotope power. Destinations beyond the orbit of Mars leave few options for aerial exploration with one important exception. Many of the small bodies and moons of the outer solar system have been seen to retain trace atmospheres, however only one, Titan, has an enveloping atmosphere that is substantial enough to support aerial exploration. In fact, Titan’s

combination of a thick, mostly nitrogen atmosphere, low temperatures, and low gravity, makes it one of the destinations in the solar system most amenable to aerial vehicle designs.

B.1 Balloons

There are tremendous opportunities for the application of aerial mobility technology to the exploration of Titan. In particular, the thick atmosphere enables the use of compact, self-propelled buoyant vehicles that can access virtually any point of the planet over multimonth time scales with minimal consumption of scarce onboard electrical power. Depending on the level of autonomy incorporated, such an aerobot (robotic balloon vehicle) could acquire a wide spectrum of scientific data ranging from simple aerial imaging to acquisition of surface samples and onboard composition analysis. Even the simpler aerobot technology of wind-blown (unpropelled balloons) can yield valuable science, especially if the vehicle incorporates long-duration flight and/or altitude control capability to do atmospheric profiling and ground approach for surface sampling.

One very attractive exploration approach for a post-Cassini/Huygens mission at Titan consists of using a hot air ‘montgolfière’ balloon. Unlike terrestrial montgolfières, which require burning fuel, the Titan design would use the significant waste heat available from radioisotope thermoelectric generators (RTGs) to warm the Titan atmosphere inside the balloon envelope to provide buoyancy. This dual use of radioisotope power systems (RPSs) to provide a continuous source of heat as well as electrical power would give the balloon an inherent ability to float for a very long time in the atmosphere of Titan. Designs have been studied that would ride the easterly winds at a cruising altitude of about 10,000 km, occasionally changing altitude to take advantage of possible reverse wind directions and even descending to the surface to physically sample sites of interest. Seasonal and tidal north-south winds could allow the mission to explore different latitudes, which Cassini data have shown to be amazingly diverse in geologic nature. Communication from the aerial vehicle could be relayed through an accompanying orbiter spacecraft, as well as transmitted directly to Earth, providing the potential for data return from Titan’s surface equivalent to that provided by many comparable orbiter missions at much closer destinations. One particular design is shown in Fig. B-2. This montgolfière concept was developed by the European Space Agency (ESA) as part of the Titan Saturn System Mission (TSSM) study in 2008 [3]. A Multi-Mission Radioisotope Thermoelectric Generator (MMRTG) provides both electrical power (~100 W to the gondola) and heat (~1.7 kW for buoyancy). The balloon envelope, nearly 11 m in diameter, uses double-wall construction for improved thermal insulation. An aeroshell, a heat shield plus a back shell, protects the montgolfière from the thermal load of entry (Fig. B-3).

The orbiter would carry the montgolfière through Saturn orbit insertion (SOI) to the subsequent apoapsis, releasing it on a direct ballistic trajectory for entry at the first Titan flyby. After entry a pilot chute would pull off the back shell, deploying the main parachute that extracts the montgolfière from its heat shield. When the system has descended to ~40-km altitude, the balloon envelope would deploy and fill with ambient air, aided by the ram effect of the continuing descent. Heat from the MMRTG suspended within the envelope would warm the air to positive buoyancy at ~8 km altitude. Once at buoyant equilibrium, the montgolfière would drift passively with the winds at 1–2 m/s, actively maintaining its nominal 10-km altitude via barometric measurements and a vent valve at the balloon’s zenith. Fig. B-2 depicts the montgolfière in stable flight. The 10-km altitude was chosen to meet all science requirements while avoiding the risk from methane icing above ~14 km and the potential risks associated with near surface operations.

The total mass of the montgolfière element and its aeroshell for the Titan Saturn Study Mission (TSSM) study was estimated at 571 kg including contingency. Its 144-kg gondola includes a 25-kg payload allocation for atmospheric measurements, imaging, spectrometry, subsurface radar profiling, and electric and magnetic field measurements. Data would be transmitted to the orbiter via a steerable 50-cm high gain antenna (HGA), for relay to Earth.



Fig. B-2. TSSM montgolfière.

Although the montgolfière design is uniquely suited to Titan, other concepts for superpressure balloons have also been extensively studied. A helium-filled balloon is well suited to Titan exploration, able to easily carry large payloads in the dense atmosphere, low gravity environment. One such concept is illustrated in Fig. B-4. In this design, the aerial system is based upon a ~5-m diameter spherical helium super-pressure balloon that has the characteristic of flying at a constant altitude despite thermal and convective perturbations in the atmosphere, both of which are expected to be small at Titan. This design is very similar in type and size to the Vega balloons successfully deployed and flown at Venus. Thousands of helium super-pressure balloons have also flown on Earth for periods of up to 2 years. In this Titan example, the balloon is sized to carry a gondola mass of 160 kg, including ~20 kg of science payload.

Similar to the montgolfière, the gondola consists of a single platform, ~1.5 m diameter, with the avionics and payload located on the bottom side of the platform and the HGA installed on its upper surface. In this case, however, power would be provided by RPS units also located in the gondola, rather than in the balloon envelope as is necessary for the buoyancy of the advanced Stirling radioisotope generator (ASRG). In this design example, gondola power would be provided by 2 ASRGs able to deliver 120 W electrical power each (minimum end-of-life and waste heat of ~500 Wth each). The waste heat would be used for maintaining thermal balance during interplanetary cruise and while in the cold Titan atmosphere during the aerial mission.

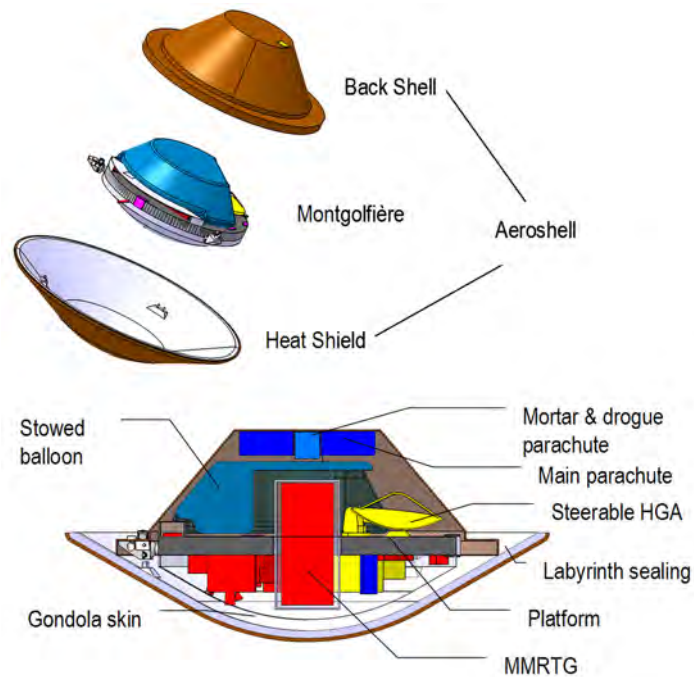


Fig. B-3. Conceptual design of the TSSM montgolfière integrates Huygens heritage with balloon element. An exploded view of entry system aeroshell is shown.



Fig. B-4. Titan superpressure helium balloon.

The calm winds predicted on Titan allow a balloon platform to maintain stability to allow direct communication with Earth using a telecom subsystem operating at X-band using a small (0.5–0.75 m steerable HGA). In combination with Deep Space Network (DSN 34-m ground stations, this design allows a downlink rate on the order of 200 to 400 bps. Deployment of the superpressure balloon has a few more steps than the montgolfière, as illustrated in Fig. B-5. The deployment phase begins after atmospheric entry and descent to a 9-km altitude. A small parachute (20 m² is required to provide a 5-

m/s descent speed, which provides a sufficiently low dynamic pressure (50 Pa) on the deploying balloon. The flow of helium gas starts soon after the deployment of the balloon envelope from its storage container, and continues for 10–20 minutes, filling the balloon. When finished, the parachute and inflation system are detached and the balloon and its payload ascend to the float altitude. The balloon is designed to pressurize to 1,000 Pa upon reaching 8 km and stabilizing at that altitude.

The 85-K cryogenic environment will ensure that negligible amounts of helium will be lost by diffusion through the balloon material during the science phase. Balloon float lifetime will therefore be limited only by leakage through pinhole defects. Analysis shows that a 3-month science mission can be achieved even with 20 pinholes of size 10 microns in diameter. At end-of-mission, a valve on the balloon can be opened to vent helium and provide a slow descent to the surface for additional scientific investigations.

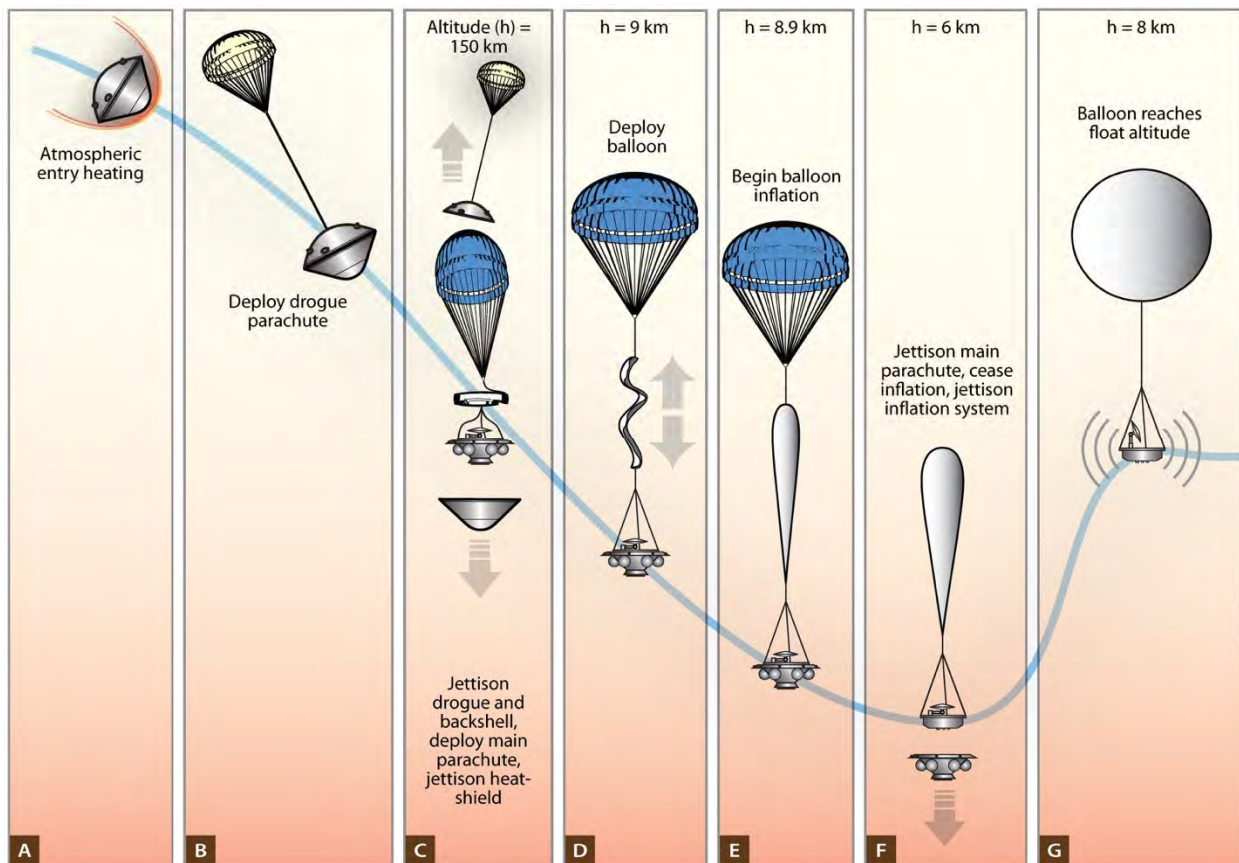


Fig. B-5. Entry and balloon deployment sequence.

The aspects of low gravity and high atmospheric pressure and density have also been recognized as being extremely advantageous to heavier-than-air craft. One particular example of that was developed in the Aerial Vehicle for In-situ and Airborne Titan Reconnaissance (AVIATR study, carried out in 2011 [4].

The AVIATR mission was specifically designed for the use of ASRGs. The assumed power density (in watts per kilogram, W/kg and power output of the ASRGs were critical to the design of an electrically powered aircraft able to sustain long-term flight (~1 year continuous flight operation for AVIATR on Titan. The combined worst-case power of two ASRGs (having an assumed mass of 64 kg, when allowing for additional power requirements for computers, actuators, and instruments, left an

estimated ~ 80 W to power the propeller for straight-and-level flight operations. The propeller's thrust in this configuration is sufficient to keep aloft an airplane with a mass up to ~ 120 kg. Given the assumed unit masses and power output data available at the time, it was found that the MMRTG would not be able to satisfy the physical requirements for heavier-than-air flight at Titan within appropriate engineering and risk constraints. With the current unavailability of the ASRG, this concept would likely need an advanced RTG to achieve the power density required.

The AVIATR Air Vehicle (AV) was designed as an unpiloted aerial vehicle (UAV) of conventional layout (Fig. B-6). The general AV configuration consists of a streamlined fuselage, a folding high wing attached at mid-fuselage, conventional empennage, and a two-bladed pusher propeller. The fuselage would be of monocoque shell construction, with the shell constructed of two epoxy-fiberglass face sheets separated by a polyurethane foam core. The foam core serves as a shear-load carrying member between the face sheets and also as a thermal insulating barrier. Due to its insulating qualities, the double wall fuselage also serves as a warm electronics box. The fuselage contains all components that need to function at or near room temperature, including avionics, communications gear, science instruments, flight control actuators, and power system components (Fig. B-7).



Fig. B-6. AVIATR Titan aerial vehicle concept.

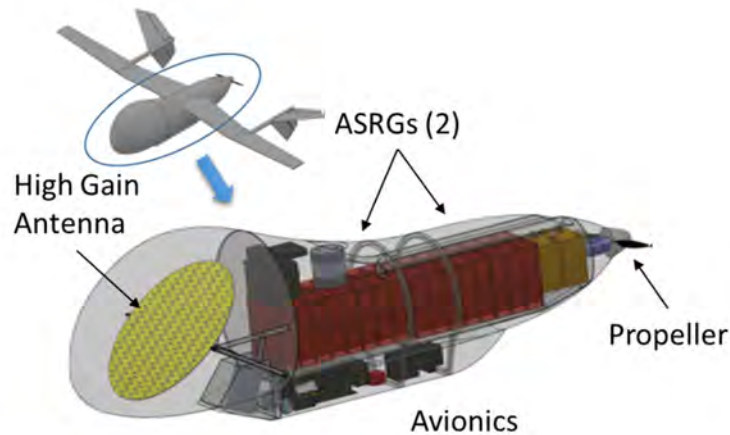


Fig. B-7. AVIATR internal layout.

Electrical power would be supplied by the two internally mounted ASRGs. An air intake at the nose of the vehicle would admit cold outside air into a duct, which directs the air to the cold side of the ASRGs and maintains their power output within the nominal range. Interior baffles direct the cooling airflow on a circuit throughout the fuselage where it picks up waste heat from the power-consuming components. An exhaust port at the aft end of the fuselage allows the heated air to exit. The study assumed that ASRG power with our advective cooling system would be the same as that of an ASRG radiating to space, for a total of two ASRGs at 128 W each (254 W total).

A two-bladed propeller powered by a rare-earth-magnet-driven brushless DC motor would provide propulsion. Science cameras would be mounted directly to the underbelly of the fuselage structure behind double-pane transparent windows. All flight control servo actuators are mounted internal to the fuselage and transmit control forces and torques to aerodynamic surfaces via thermally insulating pushrods and torque tubes. Penetrations of the fuselage for control rods and tubes have air flow baffles to prevent excessive heat leaks.

The AV communicates directly to Earth through a steerable HGA enclosed in a streamlined aerodynamic fairing. The antenna is parabolic, with an elliptical cross-section. The long axis of the ellipse (its steering axis) is placed parallel to the fuselage and is buried inside the outer mold line of the fuselage. The antenna is steerable inside the outer mold line of the fuselage over a roll range of $\pm 90^\circ$, centered on the zenith. The radio operates in X-band using redundant 75-W travelling wave tube amplifiers (TWTAs).

Preliminary mass estimates for the AVIATR vehicle predicted a mass of 116 kg, based on an assumption of 21 kg per ASRG. Given the growth in estimated mass of the ASRG since this study, and the significantly higher mass of MMRTGs and eMMRTGs, it is evident that this design, which is particularly sensitive to specific power, would benefit greatly from advanced RTG developments.

B.2 Rotary Wing Aerial Vehicle

One additional design that has recently been proposed in response to the New Frontiers call involves the use of a multicopter system to perform aerial and surface exploration of Titan. This concept, Dragonfly [5], would use a single MMRTG to provide power for spacecraft systems and charge batteries for vehicle propulsion. As shown in Fig. B-8, the Dragonfly vehicle uses a total of eight rotors; two at each corner, to provide lift. This allows the lander to relocate to multiple different locations across the surface of Titan, performing surface science in a variety of separate regions and terrain types.

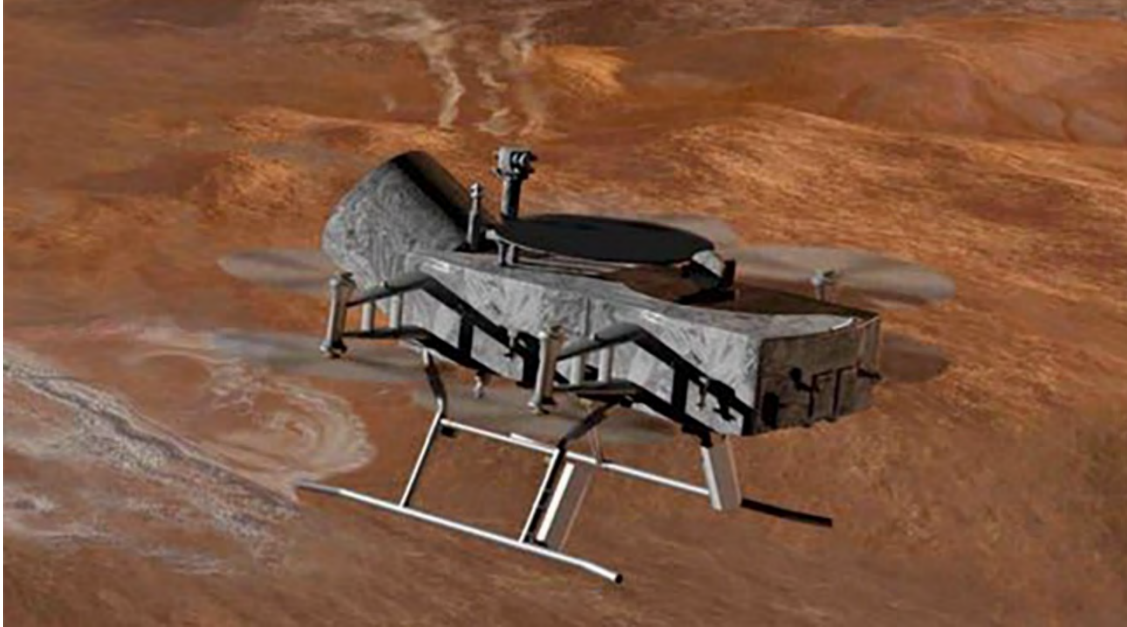


Fig. B-8. Dragonfly Titan rotorcraft concept.

The lander would spend most of its time on the surface performing site-specific science activities and charging its flight batteries from the MMRTG. When fully charged, the rotors would be engaged to allow the lander to take off from the surface and traverse a significant distance with a few hours of flight time available from a single charge. In this manner, a focused instrument suite can be used to characterize Titan's surface in a far more comprehensive manner than would be possible from a stationary lander or even a conventional surface rover.

B.3 Summary

Battery-powered aerial vehicles have been demonstrated at Venus in the 1980s, and a solar/battery powered rotorcraft design is currently being developed that may fly with Mars 2020. Farther out in the solar system, where solar power is less plentiful and data links and science requirements may demand longer missions than batteries alone can support, Saturn's moon Titan represents an especially attractive target for aerial exploration, but one that will require RPS. Titan brings together a fortuitous combination of low gravity with a cold, dense nitrogen atmosphere and mild winds that is extremely well suited to a variety of aerial platforms. Hot air balloons can make use of RTG waste heat to carry significant science payloads around the globe at constant altitudes, or employ Earth-like navigation techniques to take advantage of wind variations with altitude to navigate to targets of interest. Super-pressure helium balloons can explore Titan in the same way, and either balloon type can be enhanced with propellers for propulsion, allowing guided flight.

As with balloons, the Titan environment provides ideal conditions for fixed wing and rotor-craft. Only limited amounts of power are needed to propel significant payloads through the atmosphere. With high specific power, RPS continuous controlled flight using a fixed-wing aircraft could be sustained for years. Likewise, rotorcraft using current technology MMRTGs may be capable of repeated multi-hour flights that could enable detailed exploration at multiple sites around the globe.

Cassini has revealed Titan to be a fascinating world that is in many ways the most suitable place for aerial exploration in the solar system. Past studies have offered a glimpse at the rich variety of missions that could be enabled by RPS, and should be considered in refining the design of future systems.

B.4 References

- [1] Linkin, V.M., V.V. Kerzhanovich, A.N. Lipatov, K.M. Pichkadze, A.A. Shurupov, A.V. Terterashvili, et al.. March 1986. “VEGA Balloon Dynamics and Vertical Winds in the Venus Middle Cloud Region,” *Science*, 21, 231 (4744): 1417–9.
- [2] Jet Propulsion Laboratory. January 22, 2015. “Helicopter Could Be 'Scout' for Mars Rovers,” web site. <https://www.jpl.nasa.gov/news/news.php?feature=4457>.
- [3] European Space Agency. January 19, 2009. “TSSM NASA/ESA joint summary report,” web site. <http://sci.esa.int/tandem-tssm/44033-tssm-nasa-esa-joint-summary-report/>.
- [4] Barnes, J. et al. 2012. “AVIATR—Aerial Vehicle for In-situ and Airborne Titan Reconnaissance,” *Exp. Astron.*, 33, 55–127.
- [5] Turtle, E.P., J. Barnes, M. Trainer, R. Lorenz, S. MacKenzie, K. Hibbard, et al. 2017. “Dragonfly: exploring titan's prebiotic organic chemistry and habitability,” *Lunar and Planetary Science*, XLVIII.

C Melt Probes

Knut I. Oxnevad

NASA Jet Propulsion Laboratory, 4800 Oak Grove Dr., Pasadena, CA 91109

C.1 Introduction

One of the great benefits of an RTG is that it generates substantial amounts of direct thermal energy. For example, a 16-element RTG generates more than 3 kW. This level of thermal energy could make an RTG the perfect energy source for a probe that one day could melt through the ice of the ocean worlds. These probes will experience extremely high pressures, and part of them will need to be encapsulated in a pressure vessel. Melt probes, with or without additional features such as rotary drills or water jets, will be discussed in this appendix. A listing of different melt probe concepts is provided in Table C-1.

Table C-1. Melt probe reports.

Probe Name	Dimensions: d x l (m)	Mass (kg)	Power (kW)	Probe Concept			Max Depth (m)	Velocity (m/h)	Environment (Vacuum:V or Atmosphere:	Ice Temperature (K)	References
				Tether (Y/N)	Passive (Melt only): Y/N	Active (Water Jet: WJ or Drill: D)					
Probe I and II	I: 0.108x2.5; II: 0.108x3	NA	3.6	Y	Y	N	I: 218; II: 1005	2	A	243 (after cooling)	Philbert, K., 1968 [1]
CHIRPS and CRYOBOT	0.12x1.25	40	0.8 (th)	Y (also concept for tetherless)	N	WJ	CHIRPS: 5; Cryobot: 23	0.4 (P)/0.6	A	263	Zimmerman, W., 2001a [2] and Zimmerman, W., 2001b [3], French, L. [4]
SUSI type (AWI)	0.15x0.605 (0.1)	100's	0.6	Y	Y		0.2 (0.3)	0.13 (0.09)	V	100	Treffer, M., 2006, 628-634 [5] and Ulamec, S., 2007, 12 [6]
SUSI II (AWI)	0.1x2.25	100's	3.4	Y	Y		220	2.93	A	NA	Ulamec, S., 2007, 3 [6]
APL-UW Ice Diver	d: 0.07	NA	1.25	Y	Y		7	2	A	258	Winebrenner, D.P., 2013 [7]
VALKYRIE	2.8x0.25	NA	5 (surface laser)	Y	N	WJ	30	0.9	A	NA	Stone, W.C., 2014 [8]
EnEx Ice Mole	0.15x0.9	60	3.9	Y	N	Drill	10	1.1	A	NA	Dachwald, B., 2014, 17 [9]
IceCube	Weight stack: 24	Cable spool: 45000; Drill stack: 525	4700	Y	N	WJ	2500	83	A	NA (Antarctic surface: 240)	Benson, T., 2014 [10]

C.2 Explanation of Terms

The idea of using melt probes for the exploration of deep ice sheets was first explored in earnest in the 1960s with the invention of the “Philberth” probe by German independent physicist Karl Philberth [1]. Haldor W.C. Aamot at the U.S. Army Cold Regions Research and Engineering Laboratory (CREL) supported the effort. He also played a role in developing the early theories for melt probes [14]. Philberth’s tethered probes, descending at 2 m/h, reached in 1968 depths of 218 and 1005 m in the Greenland ice sheet before failing [1]. All later work on melt probes is based on their work.

Development of the SUSI and SUSI II melting probes took place at the Alfred Wegener Institute for Polar and Marine Research (AWI), Germany in the 1990s. SUSI II reached depths of 220 m in the 92/93 season in Antarctica [6]. In 1999, efforts started at JPL to develop melt probes, called cryobots. Out of this work came the Cryo-Hydro Integrated Robotic Penetrator System (CHIRPS) effort [2, 3]. The cryobot reached 23 m during testing on Svalbard Island [4]. A melt probe developed by the Applied Physics Laboratory at the University of Washington, Seattle reached a depth of 7 m in 2013 [7], and in 2014 Stone Aerospace presented their VALKYRIE using a water jet with power fed from the surface via a laser. It reached depths of 30 m [6]. The Enceladus Explorer (EnEx) Ice Mole, developed at the FH Aachen University of Applied Sciences' Astronautical Laboratory, Germany, using a combined melt and rotary drill system, reached 10-m depth in 2013 [8]. On the extreme, the IceCube Enhanced Hot Water Drill (EHWD) system, deploying 4.7 MW of power, with a cable spool weighing 45 tons, reached 2.5-km depth in 30 hours to place a neutrino observatory under Antarctic ice [9]. This is an industrial-scale system. Of, course, this would not be practical for exploring ice sheets on ocean worlds.

Neither of these systems are tetherless. However, the CHIRPS, that could go tetherless, utilizing a General Purpose Heat Source (GPHS) RTG system for power, and wirelessly communication through the ice.

On the communication side, using RF technologies (1 GHz patch antennas), it has been predicted that 14 communication devices, evenly spaced vertically, would be needed to communicate through a 10-km thick salty ice sheet. The communication devices would require 100 mW of continuous power, increasing to 400 mW during transmission [11]. Already, wireless transmission through 2.5 km of terrestrial ice, using a 1 W transmitter at 30 MHz has been demonstrated using a 0.1-mW transmitter, which managed to communicate through 1.7 km of ice [12]. Other work has predicted, based on experiments, that a 30-kHz (acoustic) system operating at 1 W transmitted power, can communicate through 1 km of ice [13].

The theory of melt probes is based on the early work of Aamot [14], and it was developed further in Germany and Austria [5, 6, 14]. The theories provide platform for predicting penetration velocity performance as a function of probe shape, thermal energy required for ice melting, and thermal conduction losses into surrounding ice. As part of this work, the impact of using different types of melt probe shapes were explored [5, 14, 15]. Finite element models have also been developed that show reasonable agreement with experiments [16].

A weakness with current theories and efforts is that they have been developed for surface and shallow ice. Questions such as how much more power will be required to rotate a drill in ice, at high hydrostatic pressures (180 atm at 15 km of ice on Europa), and whether these kinds of pressures will slow down a probe, or require more power at depth have not been addressed. To do that, would require theoretical work combined with testing of the developed theories in high pressure (max ice depth in Antarctica, 4.7 km) ice environments. A high-pressure ice testbed might also be considered.

C.3 References

- [1] Philberth, K. 1976. "The Thermal Probe Deep-Drilling Method by EGIG In 1968 At Station Jarl-Joset, Central Greenland," *Ice-Core Drilling*, ed. J. F. Splettstoesser, University of Nebraska Press, 117–131.
- [2] Zimmerman, W., R. Bonitz and J. Feldman. 2001. "Cryobot: An Ice Penetrating Robotic Vehicle for Mars and Europa," IEEE. doi: 10.1109/AERO.2001.931722.
- [3] Zimmerman, W., S. Bryant, J. Zitzelberger, and B. Nesmith. 2001. "Radioisotope Powered Cryobot for Penetrating the European Ice Shell," *American Institute of Physics, Conf. Proc.* 552, 707.
- [4] French, L., F.S. Anderson, F. Carsey, G. French, A.L. Lane, P. Shakkottai, and W. Zimmerman. 2001. "Cryobots: An Answer to Subsurface Mobility in Planetary Icy Environments," *Proceedings*

- of the 6th International Symposium on Artificial Intelligence and Robotics & Automation in Space (i-SAIRAS)*, Canadian Space Agency, St-Hubert, Quebec, Canada, June 18–22, 2001.
- [5] Treffer, M., N.I. Komle, G. Kargl, E. Kaufmann, S. Ulamec, J. Biele, A. Ivanov, and O. Funke. 2006. “Preliminary studies concerning subsurface probes for the exploration of icy planetary bodies,” *Planetary and Space Science*, 54 628–63.
- [6] Ulamec, S., J. Biele, O. Funke, and M. Engelhardt. 2007. “Access to glacial and subglacial environments in the Solar System by melting probe technology,” *Environ Sci Biotechnol*, 6: 71–94, 3 and 12. Doi: 10.1007/s11157-006-9108-x.
- [7] Winebrenner, D.P., E.W.T. Elam, V. Miller, and M.A. Carpenter. 2013. “Thermal Ice-Melt Probe for Exploration of Earth-Analogs to Mars, Europa and Enceladus,” *44th Lunar and Planetary Science Conference*. <http://www.lpi.usra.edu/meetings/lpsc2013/pdf/29>.
- [8] Stone, W.C., B. Hogan, V. Siegel, S. Lelievre, and C. Flesher. 2014. “Progress towards an optically powered cryobot,” *Annals of Glaciology*, 55 (65). doi: 10.3189/2014AoG65A200.
- [9] Dachwald, B., J. Mikucki, S. Tulaczyk, I. Digel, C. Espe, M. Feldmann, G. Francke, J. Kowalski, and C. Xui. 2014. “IceMole: a maneuverable probe for clean in situ analysis and sampling of subsurface ice and subglacial aquatic ecosystems,” *Annals of Glaciology*, 55 (65), 14–22. doi: 10.3189/2014AoG65A004.
- [10] Benson, T., J. Cherwinka, M. Duvernois, A. Elcheikh, F. Feyzi, L. Greenler, J. Haugen, A. Karle, M. Mulligan, and M. Paulos. 2014. “IceCube Enhanced Hot Water Drill functional description,” *Annals of Glaciology*, 55(68), 105–114. doi: 10.3189/2014AoG68A032 105.
- [11] Bryant, S. March 2002. “Ice-Embedded Transceivers for Europa Cryobot Communications,” IEEE 2002 Aerospace Conference, Big Sky, MT, pp. 349–346.
- [12] Smeets, C., W. Boot, A. Hubbard, R. Pettersson, F. Wilhelms, M.R. Van Den Broeke, and R.S.W. Van De Wal. 2012. “A wireless subglacial probe for deep ice applications,” *Journal of Glaciology*, Vol. 58, No. 211 , pp. 841–847 2012. doi: 10.3189/2012JoG11J130 841.
- [13] Lishman, B., J. Wadham, B. Drinkwater, J.-M. Kendall, S. Burrow, G. Hilton, and I. Craddock. 2013. “Assessing the utility of acoustic communication for wireless sensors deployed beneath ice sheets,” *Annals of Glaciology*, 54(64), p. 9. doi:10.3189/2013AoG64A022 1.
- [14] Aamot, H.W.C. 1967. Heat transfer and Performance Analysis of a Thermal Probe for Glaciers, U.S.A. CRREL Technical Report 194, U.S. Army Materiel Command Cold Regions Researchy & Engineering Laboratory, Hanover, NH.
- [15] Weiss, P., K.L. Yung, T.C. Ng, N. Komle, G. Kargl, and E. Kaufmann. 2008. “Study of a thermal drill head for the exploration of subsurface planetary ice layers,” *Planetary and Space Science*, 56, 1280–1292.
- [16] Erokhina, S.O. and E.N.A. Humachenko. May 13, 2015. “Technique to Simulate Melting Probe’s Movement and to Estimate Penetration Velocities’ Range,” *IEEE, 2015 Seventh Polyakhov's International Conference on Mechanics - Reading*.

D Landers, Rovers, Boats, and Submarines

Hari Nayar

4800 Oak Grove Drive, MS 198-219, Pasadena CA 91109

Appendix D discusses robotics systems for space and planetary exploration and the energy needs of deploying these systems in their relevant environments. The variety of platform types possible are described in the first section of this appendix. Section D.2 covers the uses and applications of the respective systems in space. The corresponding energy and power needs of the robotic systems are listed in Section D.3. We conclude this appendix with use cases to illustrate specific examples.

D.1 Platform Types

D.1.1 *Manipulation Systems on Orbiting Platforms*

Robot manipulators are mechanical arms used to move objects. In space applications (see Fig. D-1), they are either remotely controlled by human operators, autonomously controlled based on sensor inputs or use a shared control paradigm. A manipulator's actuators may be arranged in series, in parallel, or in a hybrid configuration [1] resulting in a variety of kinematic structures and properties. Manipulation systems have been used for assembly, deployment and construction of structures in space [2]. They have also been used for servicing, inspection, and maintenance operations of satellites and other assets in space, and for conducting experiments in the space micro-gravity environment. On planetary surfaces, manipulators have been used to deploy and operate spacecraft devices and instruments, and collect and process samples [3].

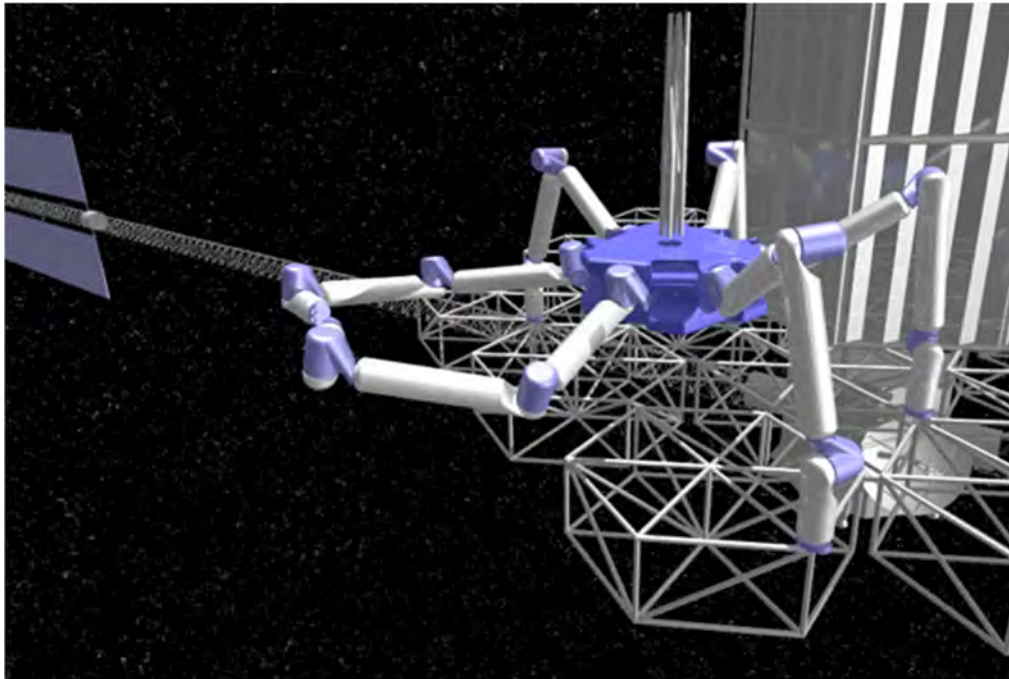


Fig. D-1. Space telescope assembly concept (provided by NASA Jet Propulsion Laboratory/California Institute of Technology, Jungon Kim, Rudra Mukherjee, and Paul Backes).

D.1.2 *Aerial/Above-Surface Planetary Exploration*

There are many configurations possible for robotic platforms with aerial or above surface mobility. For motion above bodies without or with atmospheres, the platform can be either launched from the ground or injected from orbit, propel itself and control its flight trajectory using thrusters or use a combination of these methods [4]. For motion above bodies with atmospheres [5], two classes of platforms are possible. One class of solutions are lighter-than-air platforms like balloons or blimps with controlled buoyancy or neutral buoyancy. Although never used on prior flight missions, heavier-than-air platforms like fixed-wing or flapping wing planes, or rotor-craft like copters (see Fig. D-2) are also possible and have been proposed for flight missions. Hybrids with elements of lighter-than-air and heavier-than-air platforms are also possible, for example, blimps with propellers for controlled flight.



Fig. D-2. Mars helicopter concept (NASA/JPL).

D.1.3 *Surface Ground Systems*

Robotic mobility on the ground has been shown to be a useful capability in planetary exploration because it provides a more complete understanding of the geology and origins of a body using in-situ observations over a wide area [6]. Static landers and wheeled platforms with two, three, four, six, and eight wheels have been deployed or proposed for space missions. The rocker-bogey suspension system (see Fig. D-3 and used on JPL's Mars Rovers) was designed at JPL [7] to accommodate varied terrain on Mars as an alternative to the independent passive spring or torsion bar suspension on each wheel used by vehicles on prior lunar missions. For wheeled mobility on very steep terrain, rappelling systems combined with two- and four-wheeled platforms have been proposed [8]. An example is the DuAxel concept illustrated on Fig. D-4. Continuous track or tank tread vehicles can be used for ground mobility and are especially advantageous for surfaces with low weight-bearing capacity. An alternative to rolling contact with the ground are limbed platforms. Four- and six-legged robots have been proposed for the moon and Mars [9]. Although capable of handling much more rugged terrain, walking robots are generally much more complex; each limb has at least two and usually three or more actuators. In addition to walking, limbed robots with appropriate gripping end effectors may be capable of climbing for construction and maintenance operations on space structures or for access to extreme terrains on planetary surfaces. Hybrid platforms with limbs and wheels have been proposed to combine the extreme environment advantages of limbs with the efficiencies of wheeled locomotion when the terrain permits. Manipulators are often incorporated in the design of mobility platforms for deployment of instruments and for sampling operations.



Fig. D-3. MSL Rover (NASA/JPL).

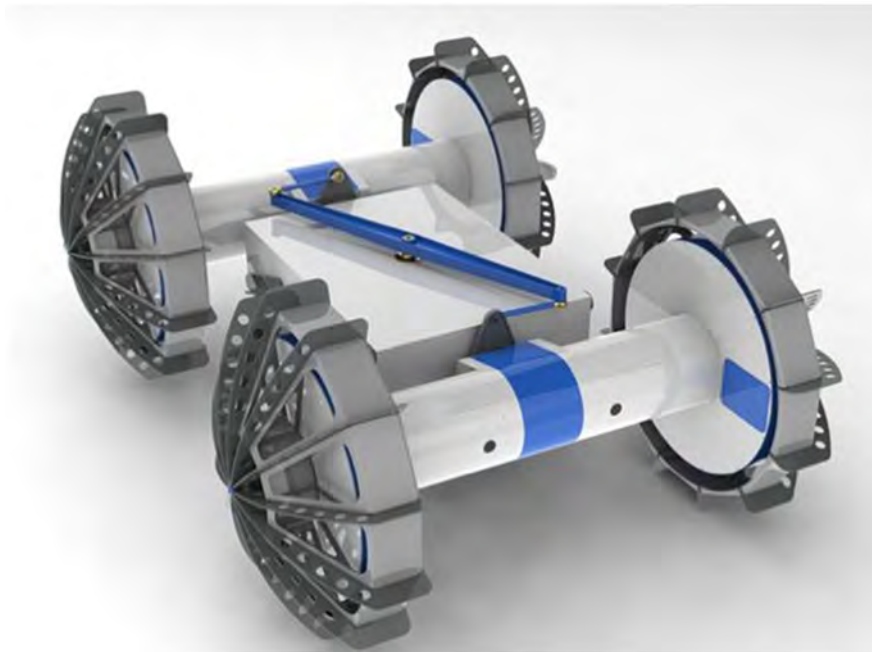


Fig. D-4. DuAxel rover concept (NASA/JPL).

D.1.4 Subsurface Soil and Ice Penetrating Planetary Exploration

Robotic subsurface access is desirable on many planetary surfaces to understand the geology and origins of the respective body. Shallow (less than 1 meter access using rotary and percussive drills and scoops, deployed at the surface, have been used on Mars. The Mars InSight mission HP³ instrument is planned to penetrate up to 5 meters below the surface using a self-contained impact hammer [10]. On ocean world bodies, deep (greater than 5 kilometers subsurface access is desirable in order to reach liquid water below the ice crusts, for example on Europa and Enceladus [11]. Surface penetration is possible with conventional approaches using rotary or percussive drills, grinding surfaces or saws. For ocean world bodies, melting the icy material is also possible [12] as illustrated in the cryoBot prototype developed at JPL (see Fig. D-5. Systems that combine two or more of these approaches have been

proposed. Two options are possible in order to conduct planetary science in a deep subsurface access mission. The first is to carry the requisite instruments, communication system and power source along with the deep subsurface access device to perform in-situ science and relay data to the surface and back to Earth. The alternative is to transport samples collected at depth back to the surface for processing and data relay to Earth. A hybrid option with a tether for power and communication may be used to overcome the drawbacks of each.

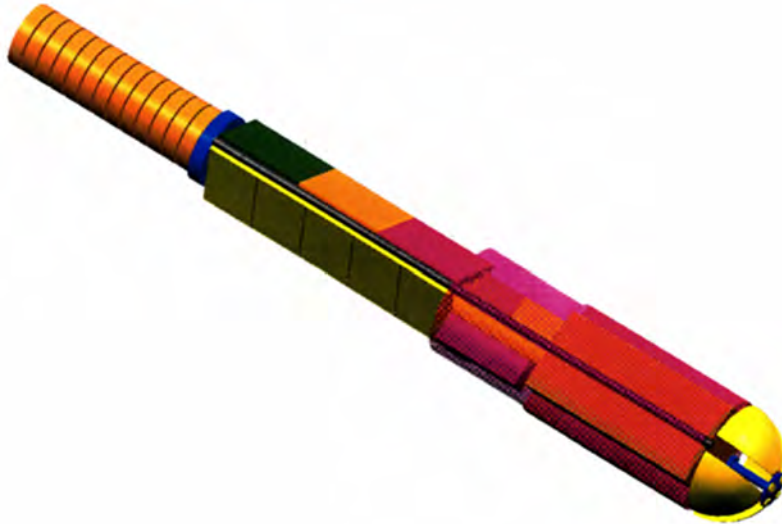


Fig. D-5. Cryobot for ice penetration (NASA/JPL).

D.1.5 *Boats and Subsurface Liquid Robots*

The only currently known body in our solar system besides Earth with large areas of liquid exposed at its surface is Titan. Robotic missions have been proposed to understand the chemistry of Titan's lake fluids [13], known to be primarily composed of methane. In particular, lake-shore interfaces and subsurface seeps where effluents may flow and mix are of interest because these dynamic sites are more likely to provide information on geology, exchange processes and astrobiological potential. Concepts of floating and amphibious platforms (see Fig. D-6) to explore in this environment have been proposed. Large volumes of subsurface liquid are believed to exist below cryogenic crusts on Titan, Europa, Enceladus, Ganymede, and other ocean world bodies in the outer solar system. A primary challenge for submarine robotic platforms to explore these environments is the need to first penetrate through multi-kilometer-thick crusts. Plume vents, known to occur on Europa and Enceladus, may provide alternative access routes to subsurface oceans.



Fig. D-6. BRUIE under ice rover (NASA/JPL).

D.2 Applications

D.2.1 *Assembly and Maintenance*

Robot manipulators are used in the construction and assembly of space structures [14]. These include laboratories and habitats in space or on planetary surfaces, space telescopes and observatories and associated infrastructure for support and maintenance of these systems. Very large structures are constructed in space using modular components delivered in multiple launches because of the payload limits of launch vehicles [15]. Other possible related applications include use in precursor missions to setup infrastructure for habitats and construction of large spacecraft from modular components for human exploration missions to Mars and destinations beyond. Robotics systems have also been proposed for use in the repair and reconfiguration of infrastructure in space.

D.2.2 *Science Observations*

Robotic missions for scientific exploration of space and planetary bodies comprise a large portion of NASA missions. Remotely operated spacecraft with increasing autonomous capabilities are deployed in the exploration of comets, asteroids, planets and their moons, and interplanetary and interstellar space. In this role, these spacecraft serve as platforms for deploying and operating science instruments and sensors for remote or in situ sensing [16]. Instruments and sensors are often operated in coordination with other spacecraft subsystems in order to optimally utilize resources, meet mission constraints, and for logging auxiliary information, for example, time, location and other environmental data tagging of sensor measurements.

D.2.3 *Manipulation and Sampling*

In situ science operations require the placement of sensors and science instruments, and preparation and collection of samples from the environment [17]. Robots perform these operations autonomously often using specialized tools like rotary-percussive drills and scoops for collecting samples, brushes to prepare surfaces for sampling, and imagers, spectrometers, etc. on the ends of robot arms to be positioned

on the surface to be investigated. In addition, samples may need to be transferred to other instruments for analyses onboard the lander or rover.

D.3 Energy Requirements

In conventional robotics systems, energy is needed for a number of subsystems. Electrical energy uses include the computing and control systems, sensors, and actuators. Actuators include DC motors, gear transmissions and solenoids in arm joints for the motion of limbs and wheel hubs for ground mobility. Due to weightlessness in space, the use of highly geared actuators and the slow motion of space robots, space robotics systems do not place a significant burden on power systems. Sensors include cameras, LIDAR, encoders, force-torque sensors, accelerometers, and IMUs. Specialized instruments are also used on robot platforms for science operations. Thermal energy is used for heating and cooling for temperature control of components, effecting the temperature or state of elements in the environment, for example, melting, and for buoyancy control of blimps and balloons. Hydraulic or pneumatic energy, typically converted from electrical energy with pumps, may be used for actuators. Energy generation and storage is an additional factor to consider in defining requirements for power systems on robotic platforms. For space missions, energy is generated using solar panels or from RTGs. It is possible to generate energy from in situ resources on planetary surfaces. Excess electrical energy can be stored in batteries, capacitors, phase-change materials or mechanically in springs or flywheels depending on the usage requirements.

Advanced concepts for robotics systems present some unconventional uses of energy for space missions. New types of actuators, including piezoelectric motors, electroactive polymers and electrostatic devices have been proposed. Pneumatics or compressed-spring launch mechanisms and compressed-air sample transport are possible for long reach sampling systems. Melt, drill, and hybrid melt-drill systems have been proposed for deep subsurface access on ocean world bodies. Among these applications, the power requirements are greatest for very large robotics systems (due to the acceleration and deceleration of massive articulated elements and inefficiencies in their gear transmissions [18]) and for processes involving thermal changes including phase-change (ice-melt probes [11]) and temperature control (buoyancy control for balloons [19]).

D.4 Selected Robotics Use Cases

The power needs for a few specific robotics platforms are discussed on this section. These case studies are based on research or space mission platforms or concepts for future missions that are described in published papers.

D.4.1 *Large Space Manipulators*

Large robotic arms are essential for the construction and maintenance of space structures [18]. Examples of large space manipulators are the Space Station Remote Manipulator System (shown on Fig. D-7, the Japanese Experiment Module Remote Manipulator System (JEMRMS, and the European Robotic Arm (ERA on the International Space Station (ISS. Among the challenges of operating these robot arms include the limited crew availability on the ISS and the need for coordinated motions among multiple arms. These arms span many meters (SSRMS – 7.1 m; JEMRMS – 7.9m; ERA – 7.8 m and are heavy (SSRMS – 1,336 kg; JEMRMS – 757 kg; ERA – 630 kg. Power needs for the arms are as follows: SSRMS – 1,360 W; JEMRMS – 2,300 W; ERA – 800 W. Other large structures that could be built in the future include space telescopes, solar sails and antennas.

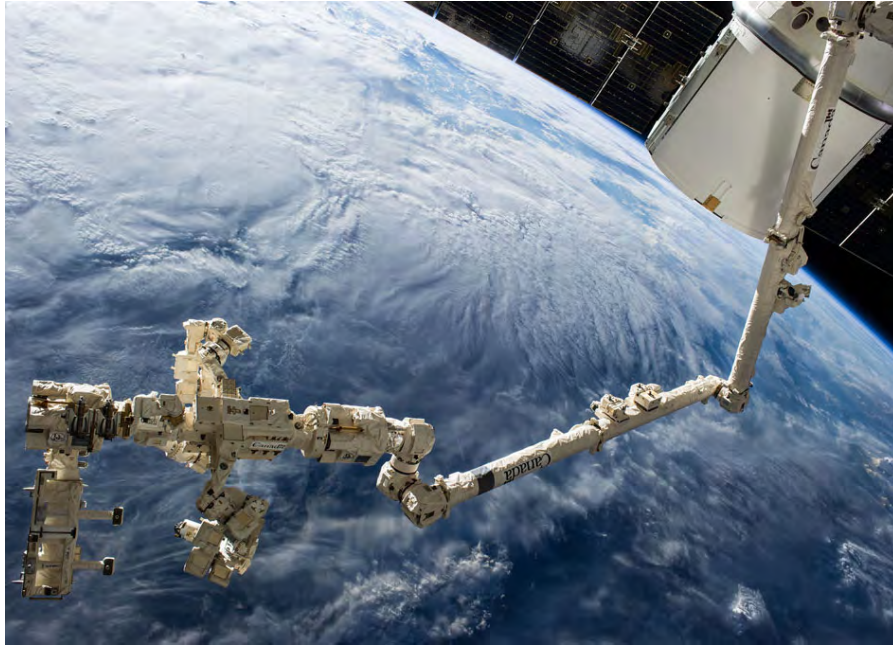


Fig. D-7. International Space Station Remote Manipulator System (NASA).

D.4.2 Europa Lander Sampling System

The Europa Lander (see Fig. D-8) [20], currently planned for launch in the 2025 timeframe is planned to have a nominal 20-day surface phase on Europa. This limit is due to the primary battery power source planned for the mission. Over those 20 days, there are expected to be five sample cycles using the sample excavation tool and sample collection device mounted on a robot arm. Each sample acquisition procedure is estimated to consume 1,250 Whr of energy over the 10-hour sampling period (average draw of 125 W). The other spacecraft operations and surface monitoring activities are estimated to consume 1,310 Whr over the 24-hour duration between each communication-from-Earth opportunity.

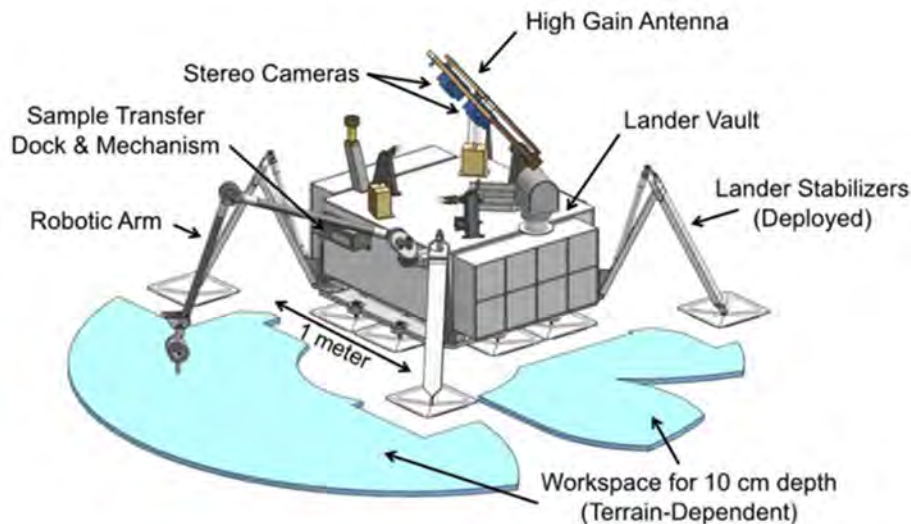


Fig. D-8. Europa Lander concept sampling system and workspace (NASA/JPL).

D.4.3 *Titan Balloons*

Several balloon mission concepts have been proposed for Titan (see Fig. D-9) [19] ranging from a few kg to 100+kg-class vehicles. A 100-kg class hot-air balloon could be operated with 100–200 W and a 200-kg balloon could be powered by two RPS power systems with the heat from the power supply used for buoyancy control. Small (0.5–10 W) RTGs could enable small, lightweight but long-life balloon vehicles. An additional consideration for balloon missions to Titan is the very cold atmospheric temperatures and consequent need for heating of electronics, instruments and actuators. Although buoyant gas balloons are possible, hot-air vehicles are more robust for long-duration missions. At the surface, there is negligible solar insolation so utilization of solar power is not possible. However, at high-altitude, solar-powered balloons are feasible. Battery-powered buoyant balloons for high-altitude applications but will have very limited lifetimes.



Fig. D-9. Titan balloon concept (NASA/JPL).

D.4.4 *ATHLETE*

The ATHLETE rover [9] is a hybrid limbed-wheeled rover developed for transporting future crew habitats on the surface of the moon (see Fig. D-10). It has been adapted for other applications in space. ATHLETE has a hexagonal chassis with six legs, each with a wheel at its end. A few scaled prototypes were built at JPL. The version in this case study had a total mass of 1,200 kg. Power draw on ATHLETE is primarily used for the avionics system, the six wheels and for operating the legs as limbs. Power needed to operate the avionics system is about 500 W. Limb operations also require about 500 W. The power draw of the wheels varies greatly depending on the terrain and the rate of traverse. On flat, hard terrain at moderate speed, the wheels draw approximately 4000 W. However, the wheels driving rapidly on challenging or soft sand terrain that is steep at peak power for short durations can draw up to 11,500 W. Therefore, the range of total power draw can vary between 5,000 W and 12,500 W.



Fig. D-10. ATHLETE rover (NASA/JPL).

D.4.5 *Europa Deep Subsurface Ice Probe*

A probe concept for deep subsurface access into the ice crust of Europa has been proposed [11] using a combination of cutting and melting technologies (see Fig. D-11). To progress into the ice, a saw blade protruding through a slit in an insulated chamber cuts the ice. Chips are drawn into the chamber and melted and pumped out at the rear of the probe. Melting within the insulated chamber ensures that heat is minimally lost to the surrounding environment. Periodic sampling of the melt water is conducted and samples are transported to the surface in capsules via a tube that pays out from the subsurface probe. Conductors embedded in the tube are used to supply electrical power from the surface. The concept relies on the supply of approximately 165 W of electrical power from the surface to power pumps and a saw and a pellet of GPHS plutonium-238 used in radioisotope thermoelectric generators (RTG) for 1,000 W of heat for melting. An analysis of the concept showed that it would be reach a depth of 10 km in about 815 days, progressing at a rate of 0.5m per hour.

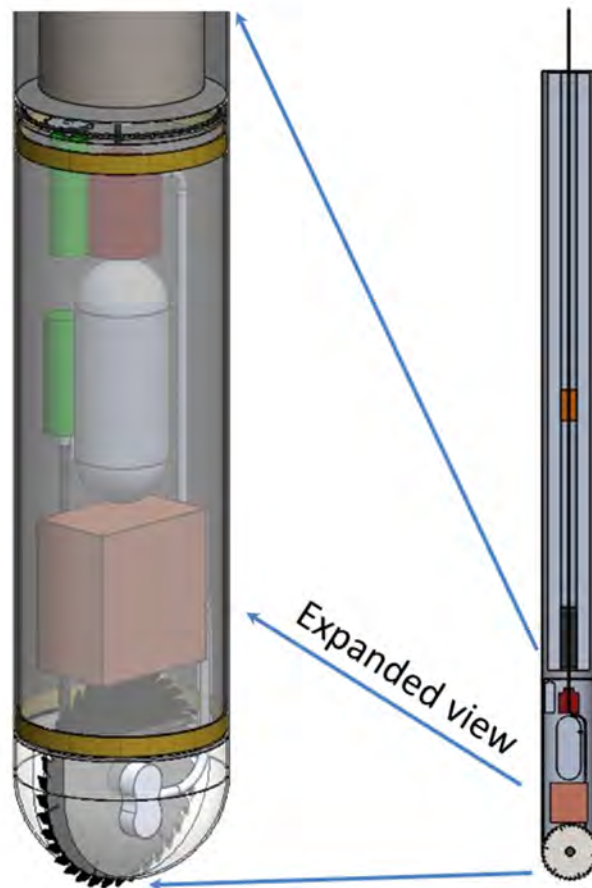


Fig. D-11. Deep subsurface ice probe (NASA/JPL).

D.4.6 Titan Lake Submarine

The design of a concept submarine for Titan was developed in a NASA Innovative Advanced Concepts (NIAC) effort [21, 13]. The concept was designed for a 90-day mission sailing at an average speed of 0.3 m/s in the Kraken Mare ethane lake. The concept was designed to reach depths of 1,000 m and operate alternatively at the surface and at depth. For the concept design, two 430-W Stirling radioisotope generators (SRGs) were used. Propulsion using thrusters consumed about 400 W. The avionics system used about 250 W. Other subsystems consuming power include: artificial lighting, science instruments (depth sounder, sample acquisition, a meteorology sensor), side-scan and depth sonar, a Doppler velocimeter and stabilizers for navigation, a surface imager, communication antennas and operating ballast tanks for buoyancy control.

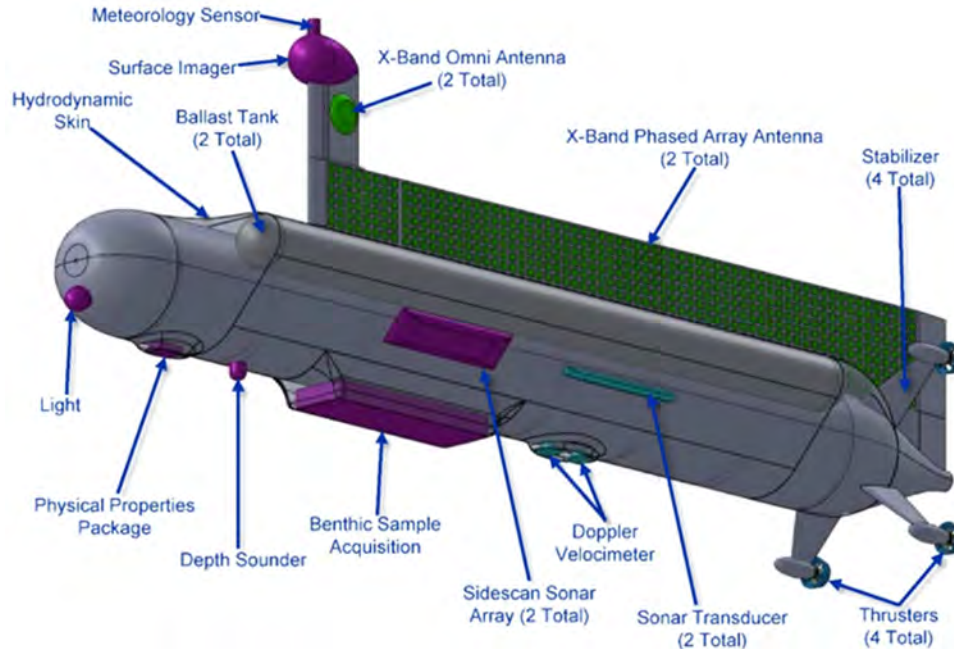


Fig. D-12. Titan lake submarine concept (NASA/JHU-APL).

D.5 References

- [1] Tsai, L.W. 1999. *Robot analysis: the mechanics of serial and parallel manipulators*, John Wiley & Sons, Hoboken, NJ.
- [2] Doggett, W. 2002. "Robotic assembly of truss structures for space systems and future research plans," *IEEE Aerospace Conference Proceedings*, Vol. 7.
- [3] Das, H., X. Bao, Y. Bar-Cohen, R. Bonitz, R. Lindemann, M. Maimone, et al. 1999. "Robot manipulator technologies for planetary exploration," *1999 Symposium on Smart Structures and Materials. International Society for Optics and Photonics*, Paper No. 3668-17.
- [4] Yoshida, K. 2009. "Achievements in space robotics," *IEEE Robotics & Automation Magazine*, 16.4.
- [5] Hall, J.L., V.V. Kerzhanovich, J.A. Jones, J.A. Cutts, A.A. Yavrouian, A. Colozza, and R.D. Lorenz. 2002. "Titan airship explorer," *IEEE Aerospace Conference Proceedings*, Vol. 1, pp. 1–336.
- [6] Maimone, M., J. Biesiadecki, E. Tunstel, Y. Cheng, and C. Leger. 2006. "Surface navigation and mobility intelligence on the Mars Exploration Rovers," *Intelligence for Space Robotics*, 45–69.
- [7] Bickler, D. 1998. "Roving over mars," *Mechanical Engineering*, 120.4, 74.
- [8] Nesnas, I.A., J.B. Matthews, P. Abad-Manterola, J.W. Burdick, J.A. Edlund, J.C. Morrison, and R.C. Anderson. 2012. "Axel and DuAxel rovers for the sustainable exploration of extreme terrains," *Journal of Field Robotics*, 29 (4), 663–685.
- [9] Wilcox, B., T. Litwin, J. Biesiadecki, J. Matthews, M. Heverly, J. Morrison, et al. 2007. "ATHLETE: A cargo handling and manipulation robot for the moon," *Journal of Field Robotics*, 24 (5), 421–434.
- [10] Trebi-Ollennu, A., A.L. Rankin, Y. Cheng, S. Tso, R.G. Deen, H. Aghazarian, et al. 2013. "Instrument deployment testbed: For planetary surface geophysical exploration," *IEEE Aerospace Conference*, pp. 1–14.

- [11] Wilcox, B., J. Carlton, J. Jenkins, and F. Porter. 2017. “A Deep Subsurface Ice Probe for Europa,” *2017 IEEE Aerospace Conference*, Big Sky, MT.
- [12] Zimmerman, W., R. Bonitz and J. Feldman. 2001. “Cryobot: An Ice Penetrating Robotic Vehicle for Mars and Europa,” IEEE. doi: 10.1109/AERO.2001.931722.
- [13] Lorenz, R.D., S. Oleson, J. Woytach, R. Jones, A. Colozza, P. Schmitz, and J. Walsh. March 2015. “Titan submarine: Vehicle design and operations concept for the exploration of the hydrocarbon seas of Saturn's giant moon,” *Lunar and Planetary Science Conference*, Vol. 46, p. 1259.
- [14] Flores-Abada, A., O. Maa, K. Phamb, and S. Ulrich. 2014. “A review of space robotics technologies for on-orbit servicing,” *Progress in Aerospace Sciences*, 68, 1–26.
- [15] Pedersen, L., D. Kortenkamp, D. Wettergreen, I. Nourbakhsh, and D. Korsmeyer. 2013. “A survey of space robotics,” nasa_techdoc_20030054507, NASA. https://archive.org/details/nasa_techdoc_20030054507.
- [16] Mishkin, A.H., J. Morrison, T. Nguyen, H. Stone, B. Cooper, and B. Wilcox. 1998. “Experiences with operations and autonomy of the mars pathfinder microrover,” *IEEE Aerospace Conference*, Vol. 2.
- [17] Arvidson, R.E., M.L. Robinson, J.L. Carsten, R.A. Volpe, A. Trebi-Ollennu, M.T. Mellon, et al. 2009. “Results from the Mars Phoenix lander robotic arm experiment,” *Journal of Geophysical Research: Planets*, Vol. 114.E1.
- [18] Laryssa, P., E. Lindsay, O. Layi, O. Marius, K. Nara, L. Aris, and E. Tabarah. November 2002. “International space station robotics: a comparative study of ERA, JEMRMS and MSS,” *Proc. 7th ESA Workshop Advanced Space Technologies Robotics Automation*.
- [19] Lorenz, R.D. 2008. “A review of balloon concepts for Titan,” *Journal of the British Interplanetary Society*, 61.1, 2.
- [20] Hand, K.P., A.E. Murray, J.B. Garvin, W.B. Brinckerhoff, B.C. Christner, et al. February 2017. Report of the Europa Lander Science Definition Team.
- [21] Oleson, S.R., R.D. Lorenz, and M.V. Paul. 2015. Phase 1 Final Report: Titan Submarine, NASA/TM—2015-218831, NASA.

E Probing Subsurfaces of Icy Bodies

Thomas R. Spilker

Independent Consultant, Monrovia, CA, USA

E.1 Introduction

The solar system’s icy bodies have the rapt attention of planetary scientists pursuing some of the big questions in planetary science and astrobiology. Aside from Mars, some of them appear to be the most likely locations in the solar system for answering the biggest of the big questions: Are we alone? Is there now, or has there been in the past, extraterrestrial life in the solar system? The thinking of three decades ago held that life would be found on the surfaces of bodies in the “Goldilocks zone”, i.e., at a heliocentric distance where liquid water could exist at the surface, beneath a substantial atmosphere. Since then, astrobiologists have realized that habitable environments can exist independent of the Sun, with energy sources from varied mechanisms such as decay of radioactive constituents and tidal heating that do not require location on a surface. The surfaces of most icy bodies are actually quite inhospitable, exposed to the vacuum of space, extreme temperatures, and ionizing radiation arising from several mechanisms. The expectation now is that any life at these icy bodies would be in the subsurface, not at the surface.

In particular, researchers are focusing more attention on icy bodies with subsurface repositories of liquid water, thought to be a fundamental requirement for life as we know it. We now have four icy bodies in the solar system with compelling evidence that liquid water oceans exist beneath their icy crusts: Enceladus, Europa, Ganymede, and Titan. This is the motivation for an entire new program within NASA's Planetary Science Directorate, the Ocean Worlds Program. There is strong evidence that other bodies currently harbor, or once had, interior regions of liquid water, including (but not limited to the asteroid Ceres, Jupiter's moon Callisto, Saturn’s moon Dione, Neptune's moon Triton, and possibly even Pluto. The Ocean Worlds Program embraces all these bodies, especially as they give evidence for potentially habitable regions.

Life and habitability are not the only major planetary science disciplines interested in icy body subsurfaces. Research into the origin and evolution of the solar system, and of the bodies within it, can benefit greatly from clues retained there. How did these bodies form? Did they evolve after formation to the states we see now, and if so, how? What processes on their surfaces and at the bottom of the water layer (liquid or solid might provide sources of chemical energy? Some sources of information about interior geophysics, such as ice-penetrating radar, can be acquired without in situ investigation. At Enceladus, the ice shell’s south polar cracks dubbed “tiger stripes” spew material from the interior ocean into space, so samples of the ocean can be accessed by flying through those plumes. But some important investigations, including some at Enceladus, will require subsurface access. For example, instrumented in situ platforms such as submarines are envisioned for exploring the oceans of both Europa and Enceladus to find hydrothermal vents, features that on Earth are prime examples of thriving ecosystems not dependent on sunlight.

In situ exploration of the subsurfaces of these bodies will expose the vehicles and their subsystems and instruments to a huge range of environmental conditions, specifically pressures and temperatures. Our focus is the subsystem supplying electric power, and possibly heat, to the entire vehicle. For most of the mission concepts for icy world exploration a radioisotopic power system (RPS) is the best choice. The motivation for this facet of the Next-Generation Radioisotope Thermoelectric Generator (RTG) Study is to investigate the range of environmental conditions an RPS might need to tolerate if it is to be a part of a subsurface craft at an icy world.

E.2 Pressure Profiles

E.2.1 Fundamentals

The structural design of a device descending deeply into an icy body's ice shell or liquid water reservoir depends critically on the range of pressures the device will encounter. Estimates of vertical pressure profiles can be calculated using some simplifying assumptions. To avoid complications of lateral density gradients and nonvertical gravitational accelerations, spherical symmetry of the bodies is assumed. In both liquid water and ice, the assumption of hydrostatic equilibrium is useful and nearly always appropriate. This assumption is equivalent to assuming that all material in the depth range of interest is a static fluid, with no strength and no hydrodynamic effects. In that case, the pressure at a specified depth is given by the weight of the column of material above that depth divided by the lateral area supporting the column:

$$P(r) = W(r)/A \quad (\text{Eq. E-1})$$

where $P(r)$ is the hydrostatic pressure at radius r from the body's center (depth d is just the body's surface radius r_p minus r), and $W(r)$ is the weight of the material being supported by horizontal area A at radius r .

E.2.2 Calculating Pressures from Mass Density and Gravity

In calculations of $P(r)$, $W(r)$ is a function of the vertical mass density profile $\rho(r)$, which in general is not constant, and the gravitational acceleration profile $g(r)$, also not constant. Considering a differential volume element dV with lateral area A and vertical extent dr , the mass of that element is given by its volume ($= Adr$) times its mass density ρ . Its weight is just that mass times the gravitational acceleration g , $W = g\rho Adr$. If that element's top surface is at the body's surface, the bottom of the element will be at a depth dr , (radius $r_p - dr$ and the pressure at the bottom of the element will be the element's weight (for this top element, call its weight W_0) divided by the area A , so $P(r_p - dr) = g\rho dr$ (note that A cancels out). The next volume element downward has a weight given by $W_1 = g\rho Adr$, but g and ρ will be slightly different from those of the top element. The weight being supported at the bottom of this next element is the sum of the weight of that element plus the weight it is supporting at its top, i.e., the weight of the top element, and the pressure at the bottom of the new element will be that summed weight, $W_0 + W_1$, divided by A . Continuing down the column, the weight supported at a given radius is the sum of the weights of all the elements above that radius, so the pressure at that radius (and any given radius is an integral involving $\rho(r)$ and $g(r)$) from that radius to the surface.

There are complicating factors that make this integral less than straightforward. Liquid water reservoirs in contact with or communicating with a silicate core will have a significant salinity, the degree of which will be highly uncertain until they are sampled directly. That salinity affects the mass density of the liquid. The most challenging factor arises from the fact that, in general, $g(r)$ is a function of $\rho(r)$ and $\rho(r)$ is actually a function of $P(r)$. The latter is true even for pure liquid water and ice. The density of water at a given temperature is often treated as constant with pressure, varying only with temperature. This is sufficiently accurate when dealing with pressures in the hundreds of bars or less. But at 10,000 bars, the density of pure water at 0°C is greater than 1,200 kg/m³, ~20% higher than the low-pressure value, a significant influence on the calculations. For the smaller icy bodies, or ones with very thin water shells, this is not a concern, but for the large bodies with very deep water shells, such as Callisto, Ganymede, and Titan, this is important. There is yet another complication: high-pressure forms of ice. The common form of ice found at standard temperatures and pressures is called Ice I. It has a characteristic lattice geometry that gives it its characteristic density, slightly less than that of liquid water. At temperatures above 0°C (273 K, this form is unstable and melts to liquid water. But at very high pressures, there are other forms of water ice with different lattice structures that are stable at higher temperatures. Each form has its own characteristic lattice structure, stability range in temperature and pressure, mass density range, and rheological characteristics (plastic flow behavior. Generally, the higher

the pressure, the higher the mass density of the ice phases at those pressures. These alternate forms of ice are designated “Ice N”, where N is an integer Roman numeral, currently up to N = XVI. The satellites mentioned above have water shells deep enough that liquid water's density varies significantly over the range of depths, and some of the high-pressure forms of ice, specifically Ice V and Ice VI, can form.

In those cases where $g(r)$ and $\rho(r)$ vary significantly with $P(r)$, the equation for the pressure profile has $P(r)$ on the left side (by definition) and a complex integral involving the quantities such as $g(r)$ mentioned above, temperature, and notably $P(r)$ itself, on the right side; thus, it is an *integral equation*, the integral analog of a differential equation. Because the phase diagram of water is a complex function of pressure and temperature, and its derivative is sometimes discontinuous, this equation usually must be solved numerically. Research funding for calculating pressure profiles is limited, so only a few icy bodies have received this kind of analysis. Dr. Steve Vance, a planetary scientist at JPL, has calculated as-yet unpublished profiles for Europa and Ganymede, and those are included below.¹ Enceladus, with its relatively thin water shell and low pressures, is a simpler problem; the author did that modeling (also included here),² and derived a simple depth-pressure equation for small icy bodies, now included in the “destinations characteristics” database developed for this study.

E.2.3 Profiles for Europa, Ganymede, and Enceladus

Figure E-1 shows a comparison of cross-sections of these bodies, to scale. Part of the large range of icy body sizes is immediately evident, though the smallest end of the range is not represented here: icy bodies such as comets can be only 1 km or less in diameter. Also evident is the large range of water fractions for these bodies. Ganymede has a water shell ~800–900 km deep, representing roughly 65–75% of the satellite's total volume. Europa, the next satellite inward from Ganymede at Jupiter, has a water shell only ~100-km deep representing only 15–20% of its volume. Enceladus, despite having a diameter less than one tenth that of Ganymede, is an intermediate case for water shell volume fraction, showing that size alone does not determine water abundance. Enceladus has attracted much attention in the scientific community due to its south polar activity, vents akin to geysers spewing water vapor and ice particles from the interior ocean into space. Data from Cassini suggest that Enceladus's ice crust is not uniform in thickness but instead is significantly thinned in the south polar region by this thermal activity, as shown in Fig. E-2.

Charts of the pressure profiles of Europa, Ganymede, and Enceladus are shown below in Figures E-3, E-4, and E-5, respectively. The profile of Enceladus is appropriate for a location at the south pole, where the crust is thinnest and scientific interest is focused. The trend of increasing slope of the curves with increasing depth mirrors the increase in water or ice mass density with increasing pressure. The large range of pressures at the water shell bottoms is immediately evident, from only ~130 bars at Enceladus, to nearly 2,000 bars at Europa, to 18,000 bars at Ganymede. Fine details of the profile at Ganymede are uncertain because the precise structure of the water shell is uncertain. Some models suggest that there might be two or more separate shells of high-pressure ice at Ganymede with shells of liquid water between, so there could be multiple liquid water oceans (shells) separated by shells of high-pressure ice [1].

¹ Steven Vance (Jet Propulsion Laboratory), “Vertical pressure and temperature profiles of Europa and Ganymede from numerical models,” unpublished data.

² Thomas R. Spilker (independent consultant, Monrovia, CA), Vertical pressure and temperature profiles of Enceladus from a numerical model, unpublished data.

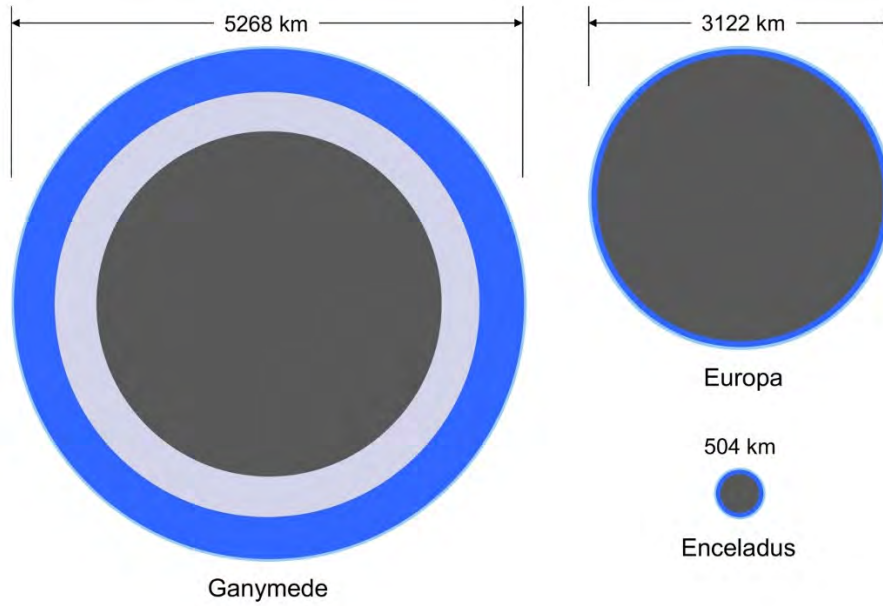


Fig. E-1. Graphical comparison of the sizes and water shell thicknesses of Ganymede, Europa, and Enceladus.

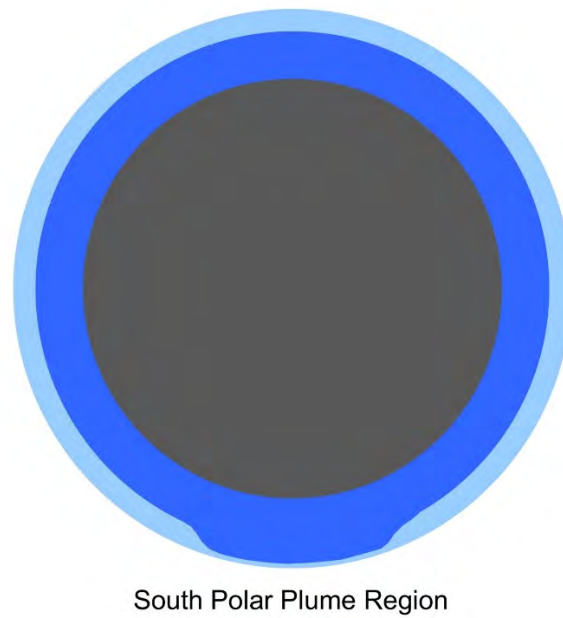


Fig. E-2. Pole-to-pole cross section of Enceladus, showing the thinning of the ice shell at the south pole.

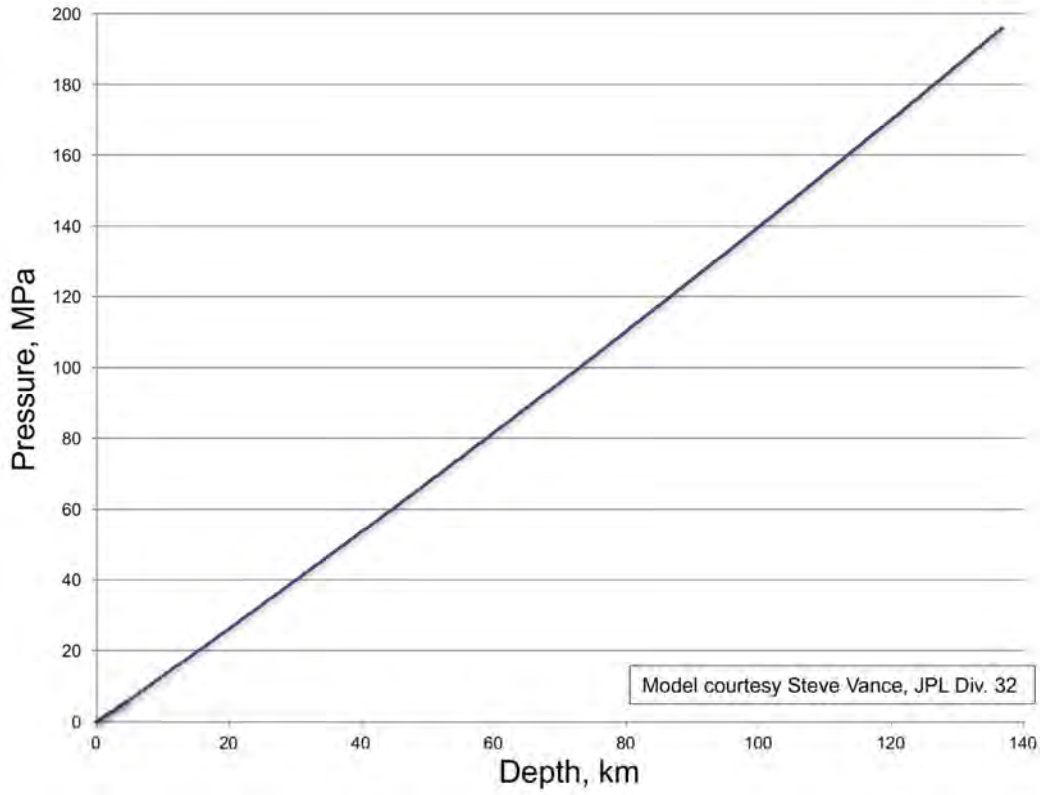


Fig. E-3. Model results showing estimated hydrostatic pressure vs. depth at Europa. Model courtesy S. Vance [unpublished data].

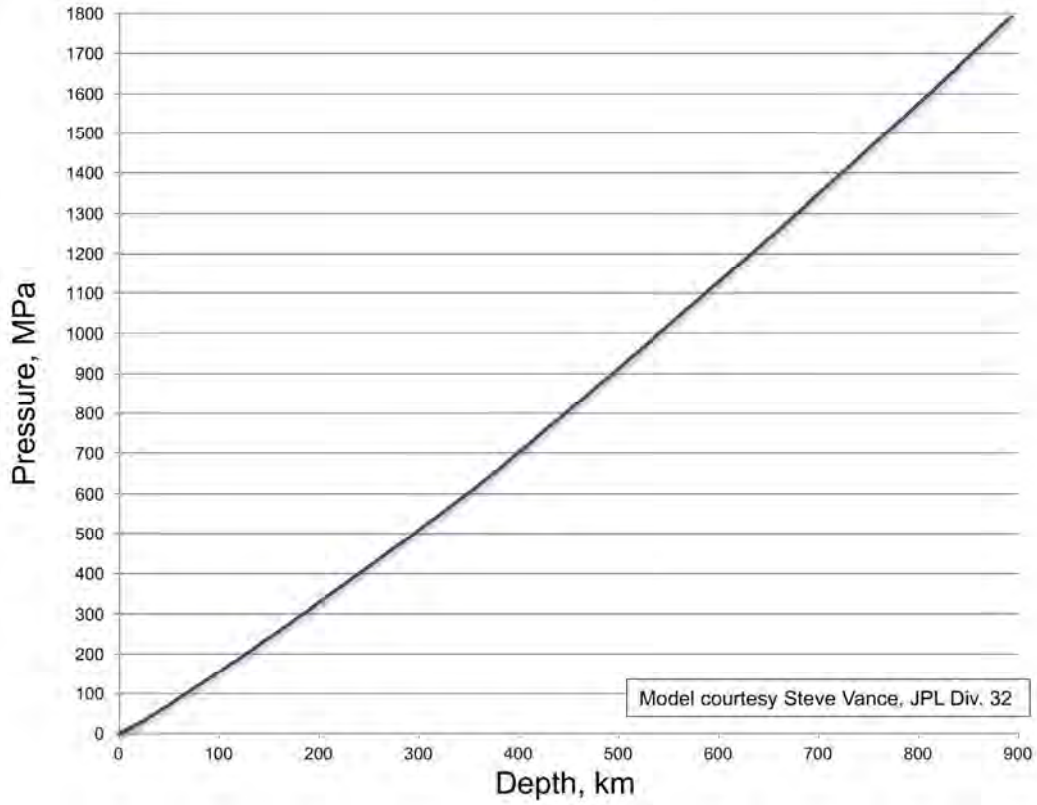


Fig. E-4. Model results showing estimated hydrostatic pressure vs. depth at Ganymede. Model courtesy S. Vance [unpublished data].

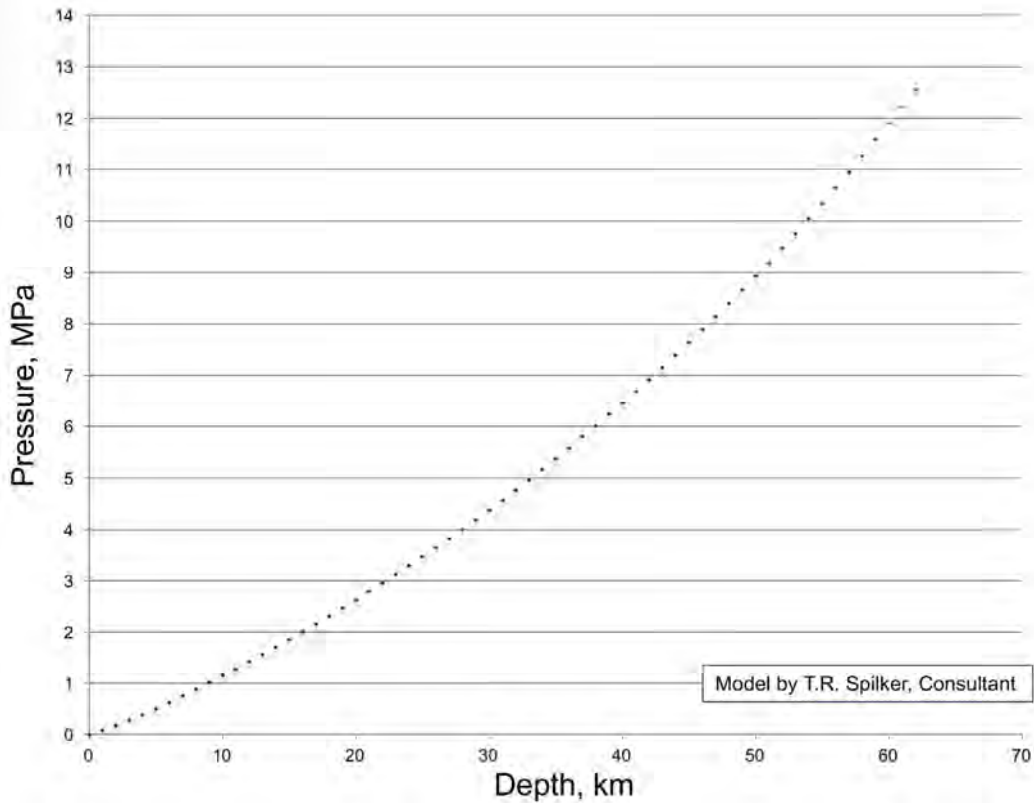


Fig. E-5. Model results showing estimated hydrostatic pressure vs. depth at Enceladus. Model courtesy of T.R. Spilker [unpublished].

E.3 Temperature Profiles

Nearly all solar system bodies with diameters larger than a few tens of kilometers, including satellites and other major bodies such as asteroids, have vertical temperature profiles showing increasing temperatures with depth. This arises from a number of factors. The process of accretion supplies the accreting bodies with the heat of inelastic collisions. Some of that heat is radiated away at the surface, but some penetrates into the body's interior. Radioactive materials, such as ^{26}Al , uranium, and thorium, incorporated into bodies as they form, release heat as they decay. Such heat produced near the surface is easily transported to the surface where it is radiated into space. But at depth, it accumulates, dissipating only as it diffuses to the surface, a very slow process given the poor thermal conductivities of most refractory materials thought to be present during the formative stages of the solar system. After accretion, bodies of sufficient size can reach internal temperatures that allow plastic flow, and the materials can differentiate, i.e., the heavier constituents sink to the body's core, leaving lighter constituents at higher levels. This differentiation releases gravitational potential energy in the form of heat in the body's interior. All these lead to higher internal temperatures than at the surface.

The exceptions to this general feature are comets and small outer solar system bodies such as Centaur objects and Kuiper Belt objects. They are thought to have formed very early in the solar system's formation period, in the far outer regions of the protoplanetary nebula. Their temperatures were very low (a few tens of K or less and heliocentric orbit speeds were slow, leading to low-velocity collisions during accretion that release relatively little heat. Since these colliding bodies have large ice fractions, much of the heat produced goes into phase change of the ice during the collisions. These bodies' small sizes allow radiogenic heat to transport to the surface and radiate away relatively quickly, so the internal temperatures

of these bodies are thought to reflect the low nebular temperature environment present during their formation. Centaur and Kuiper Belt objects experience little solar heating so their surface temperatures deviate only slightly from their internal temperatures. Comets, later in their histories, have their orbits perturbed such that they approach much nearer to the Sun, where insolation heats their surfaces. Comet surfaces are heterogeneous, in some locations exposing water ice while in others having a relatively thick ‘mantle’ of refractory materials such as silicate dust. During perihelion passages, the temperatures of the icy regions can approach 273 K while the mantled regions can exceed 350 K. Thus, the interiors of comets, especially larger ones with nucleus diameters of 10 km or more, can be significantly cooler than their surfaces.

In all cases, heat in these bodies flows according to local thermal gradients: heat flows from higher temperatures toward lower temperatures. For the larger solar system bodies, the thermal gradients between their warmer interiors and cooler surfaces maintain the flow. If the effective thermal conductivity of the bodies were uniform from center to surface, the thermal profile would be a smooth curve. But as mentioned in Section E.2, many characteristics of the liquid and icy materials can vary considerably, including effective thermal conductivity. “Effective” is used here because convection can cause the rate of heat transfer through a material to be much faster than by conduction alone. Convection is not limited to liquids; solids can convect also, especially at large scales and at temperatures not far from their melting points.

When there is a temperature contrast across a stratified inhomogeneous material, with the stratifications perpendicular to the direction of the thermal gradient, the maximum thermal gradients tend to concentrate in zones of lowest thermal conductivity, while zones of highest thermal conductivity tend to be more nearly isothermal. Liquid water’s low viscosity promotes rapid convection yielding a very high effective thermal conductivity, so interior oceans are typically nearly isothermal. Some ices have low effective conductivities, such as water’s Ice I at the very low temperatures of outer planet satellite surfaces, where its rigidity greatly impedes convection. The rheology of the high-pressure forms of ice is less well known, so their effective thermal conductivities are not well characterized.

Figures E-6, E-7, and E-8 show the vertical temperature profiles resulting from thermal modeling of Europa, Ganymede, and Enceladus, respectively. Because the effective thermal conductivities of the high-pressure ices are poorly constrained, the model for Ganymede ends at a depth of 400 km, soon after the first high-pressure ice is encountered. These profiles do not have the smooth, monotonic character of the pressure profiles, but instead show large changes in temperature at some boundaries between liquids and ices, and some steep temperature gradients in very cold Ice I.

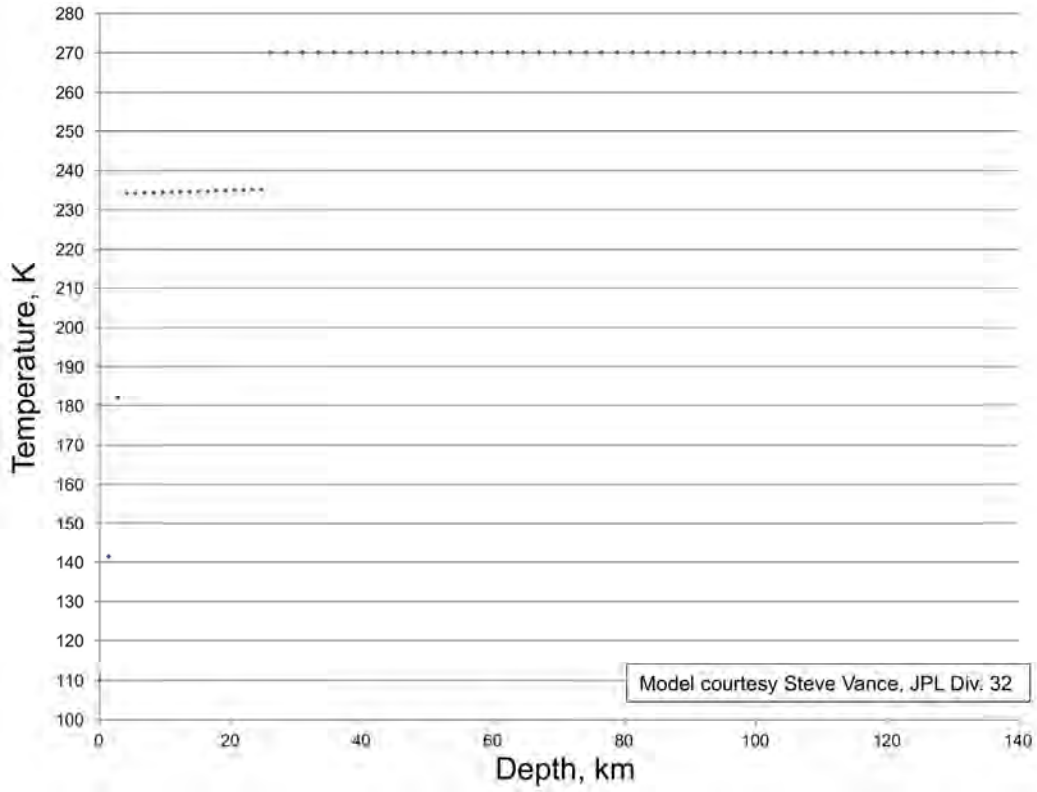


Fig. E-6. Model results showing estimated temperature vs. depth at Europa. Model courtesy S. Vance [unpublished].

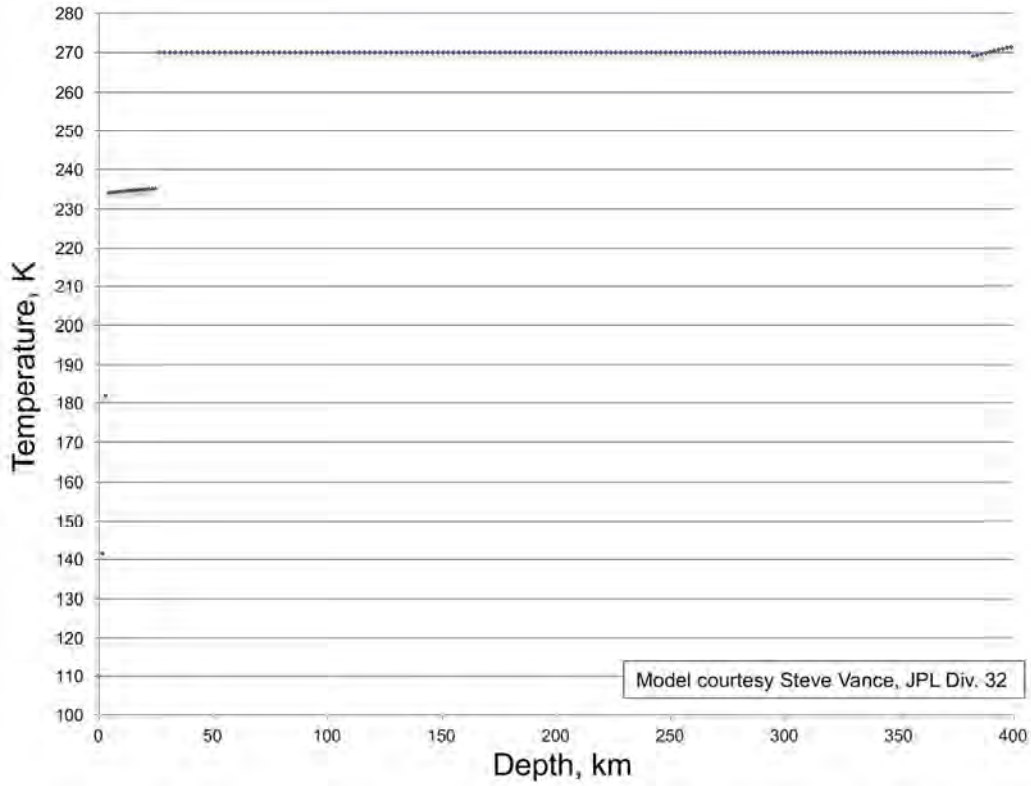


Fig. E-7. Model results showing estimated temperature vs. depth at Ganymede. Model courtesy S. Vance [unpublished].

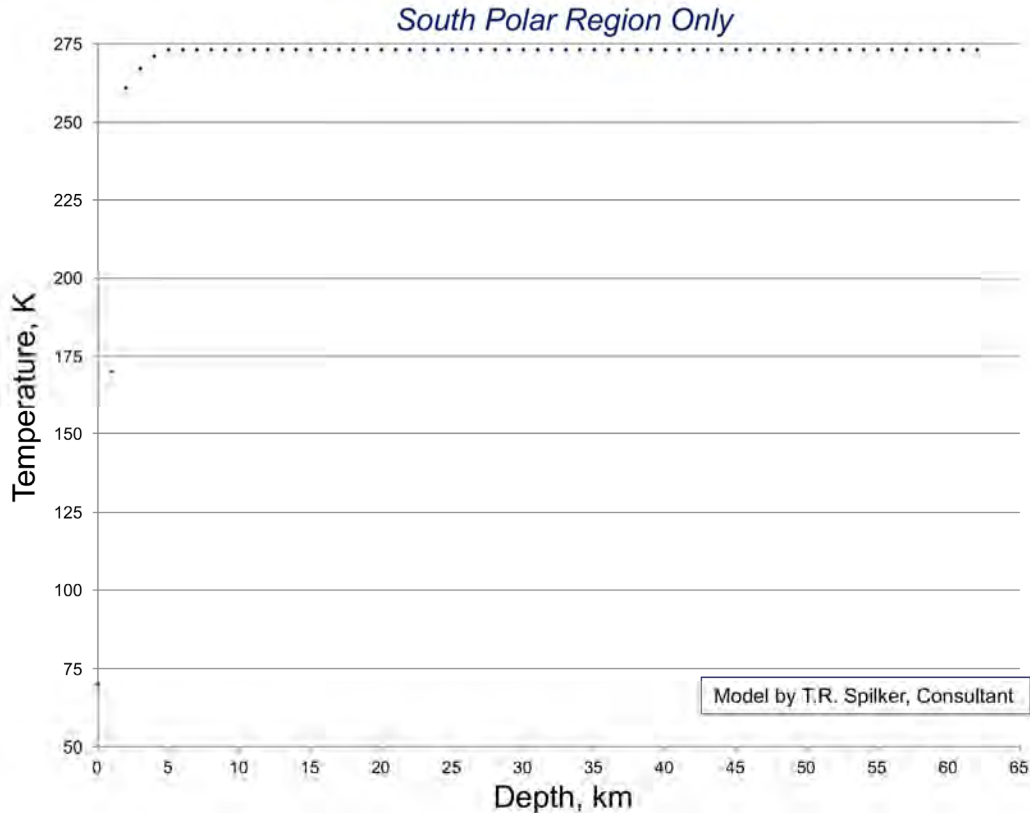


Fig. E-8. Model results showing estimated temperature vs. depth at Enceladus. Model courtesy of T.R. Spilker [unpublished]

The profiles share some important characteristics. Near the surfaces, the thermal gradient is quite large due to the convection-impeding rigidity of very cold Ice I. At only 3–5 km depth, the temperature has increased above 200 K so convection becomes the primary mechanism of heat transport. Below that level, the temperature gradient decreases significantly. Upon reaching the bottom of the Ice I shell, the very low viscosity of liquid water allows rapid convection, so the ocean is essentially isothermal near the freezing point. That temperature is likely to be slightly colder than 273 K because salinity can depress the freezing point. Enceladus and Europa maintain roughly that temperature all the way to the water shell bottom. At Ganymede, pressures and temperatures are such that somewhere near 400 km depth the first shell of high-pressure ice forms, Ice VI or possibly Ice V. Slower convection there will make the profile deviate from isothermal, to an extent poorly constrained by our uncertain models of high-pressure ice rheology.

Multiple factors add uncertainties to these profiles. Thicknesses of ice shells are uncertain and are most likely variable with lateral position. The salinity of these oceans is not precisely known, so their mass densities are uncertain to the few percent level. And the precise depths to the bottoms of the water shells are uncertain. Nonetheless, these models should yield some useful constraints on the environmental conditions in the subsurfaces of icy bodies.

E.4 Reference

- [1] Vance, S., M. Bouffard, M. Choukroun, and C. Sotina. April 12, 2014. “Ganymede’s internal structure including thermodynamics of magnesium sulfate oceans in contact with ice,” *Planetary and Space Science*, 96: 62–70.

F Temperatures across the Solar System and RTG Thermal Analyses

Daniel F. Berisford

NASA Jet Propulsion Laboratory, 4800 Oak Grove Drive, Pasadena, CA 91109

F.1 Introduction

This appendix summarizes thermal environments for potential RTG-equipped missions throughout the solar system, and presents preliminary calculations for RTG thermal performance in various settings. Except where noted, all RTG calculations assume shell dimensions of a standard MMRTG, either with or without fins. This geometry consists of a 0.3-m-diameter \times 0.65-m-long cylinder with eight equally spaced radial fins, each protruding 0.15 m in the radial direction. The thermal environments are divided into three groups, each considering different heat transfer mechanisms, including:

- Orbiters
 - Radiation only
- Landers on worlds with no atmosphere
 - Radiation only
- Landers and subsurface vehicles on worlds with atmosphere or ocean
 - Radiation, conduction, convection

In addition, we present preliminary analyses of pressure vessels for subsurface ocean vehicles, and sublimation excavation for an RTG-powered Europa lander.

F.2 Orbital Spacecraft

The thermal environment for orbital spacecraft throughout the solar system is determined based on radiative heat transfer between the spacecraft, Sun, planet, and deep space. This analysis expands upon previous unpublished work performed by Pradeep Bhandari at JPL in June 2014. The analysis assumes a standard MMRTG geometry with fins, and assumes a uniform coating of white paint with solar absorptivity (α) = 0.2, and infrared emissivity (ϵ) = 0.85. The model accounts for incident direct solar radiation, reflected solar radiation from a planet's surface (planet shine), and infrared blackbody radiation emitted by a planet's surface. Fig. F-1 depicts the modeled geometry and heat fluxes.

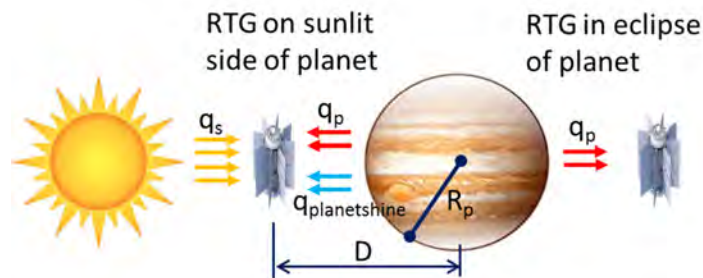


Fig. F-1. Orbital heating sources diagram.

Using the method of equivalent sink temperatures [1], shown below in Equations (F-1) – (F-3), we use the assumptions listed above to calculate the radiation thermal environment for an MMRTG in orbit during sunlit and eclipse portions of the orbit.

$$T_{\text{sink}} = [\{q_p * F_p + q_s * (\alpha/\epsilon) * (\rho_p * F_p / 2 + 1/\pi)\} / \sigma]^{1/4} \quad (\text{Eq. F-1})$$

$$T_{RTG} = [Q_{RTG}/(\sigma * A * \epsilon) + T_{sink}^4]^{1/4} \quad (\text{Eq. F-2})$$

$$F_p = [(R_p/D)^2]/2 \quad (\text{Eq. F-3})$$

T_{sink} = Equivalent radiation sink temperature

q_p = Planet blackbody IR flux

F_p = Radiation view factor from RTG to planet

q_s = Solar flux

α = Solar absorptivity for spacecraft white paint (0.2)

ϵ = IR emissivity for spacecraft white paint (0.85)

ρ_p = Planet albedo

σ = Stefan-Boltzmann constant

T_{RTG} = RTG surface (fin root) temperature

Q_{RTG} = RTG internal heat output (1,900 W)

A = RTG radiating surface area including fins

R_p = Planet radius

D = Orbital distance

Table F-1 shows the calculated sink temperatures and RTG surface temperatures for orbiters about the worlds considered for this study. Values for planetary surface properties were obtained from the cited references in the table, and from internal JPL sources where not noted. Figs. F-2 and F-3 (courtesy of Pradeep Bhandari at JPL) show plots of the RTG surface temperatures and effective sink temperatures as a function of distance from the Sun in astronomical units (AU). Note that for worlds farther from the sun than Mars, there is little difference in RTG temperature due to the cold radiation environment.

F.3 Surface Landers on Worlds without Atmosphere

The thermal environment for landers on worlds with no atmosphere is similar to that of orbital spacecraft, with stronger radiative thermal coupling between the spacecraft and planet surface due to the proximity to the planet surface. Here we define “no atmosphere” as any planetary surface at which radiation heat transfer to the planet surface dominates convection heat transfer by at least a factor of 100. The analysis for this case is similar to the orbital spacecraft case, with the exception that the radiation view factor (F_p) between the RTG and the planet surface for thermal radiation heat transfer is equal to 0.5 for all worlds. This assumes that half of the radiating area of the spacecraft couples to the planet surface, and half couples to space. Equations (F-1) and (F-2) apply and produce the results shown in Table F-2.

Table F-1. Orbital spacecraft thermal environment and MMRTG exposed surface temperatures.

Body	AU	Sfc T, mean (K)	Planet Radius (Miles)	Planet IR Flux, q_p (W/m^2)	Albedo P_p	Low Altitude from Planet Sfc. (miles)	View Factor to Planet Sfc., F_p	Sink		RTG		
								Sink T. Eclipse of planet (C)	Sink T. Sunlit side of planet (C)	RTG T. Eclipse of planet (C)	RTG T. Sunlit side of planet (C)	
Mercury	0.39	340	1490	2167	0.07	100	0.44	360	414	197	225	[4]
Venus	0.72	737	3758	161	0.76	100	0.47	192	287	155	171	
Moon	1.00	220	1079	133.0	0.136	100	0.42	177	233	154	160	
Mars	1.52	210	2112	128	0.15	100	0.46	179	208	154	157	
Ceres	2.77	155	294	32.8	0.09	100	0.28	113	142	151	152	[5, 6]
Jupiter	5.20	102	44348	6.2	0.51	100	0.50	86	110	151	151	[7]
Io	5.20	110	1132	8.3	0.63	100	0.42	89	112	151	151	[8, 9]
Ganymede	5.20	110	1637	8.3	0.43	100	0.44	90	111	151	151	[9]
Callisto	5.20	134	1498	18.3	0.22	100	0.44	109	122	151	151	[9, 10]
Europa	5.20	102	975	20	0.67	100	0.41	110	125	151	151	[9]
Saturn	9.52	109	37472	1.9	0.5	100	0.50	64	82	151	151	[11, 12]
Mimas	9.52	86	123	3.1	0.96	100	0.15	54	76	151	151	[9]
Enceladus	9.52	75	311	1.8	0.99	100	0.29	55	78	151	151	[9]
Tethys	9.52	86	331	3.1	0.8	100	0.29	63	81	151	151	[13]
Dione	9.52	87	349	3.3	0.7	100	0.30	64	81	151	151	[9]
Rhea	9.52	77	474	1.9	0.7	100	0.34	58	79	151	151	[9]
Titan - Sfc	9.52	94	1601	4.4	0.22	100	0.44	77	87	151	151	[11, 12]
Iapetus	9.52	110	456	8.3	0.2	100	0.34	84	92	151	151	[9, 13]
Uranus	19.21	59	16087	0.3	0.66	100	0.49	40	56	151	151	[9, 14]
Miranda	19.21	60	147	0.7	0.32	100	0.18	39	53	151	151	[15]
Ariel	19.21	59	360	0.7	0.23	100	0.31	44	55	151	151	[14, 15]
Umbriel	19.21	63	363	0.9	0.18	100	0.31	47	56	151	151	[9, 14, 15]
Titania	19.21	60	490	0.7	0.27	100	0.34	46	56	151	151	[9, 14, 15]
Oberon	19.21	73	696	1.6	0.24	100	0.38	57	64	151	151	[9, 14]
Neptune	30.09	64	15373	0.16	0.62	100	0.49	34	46	151	151	[16]
Triton	30.09	38	841	0.1	0.76	100	0.40	30	44	151	151	[17]
Pluto	39.75	44	1841	0.19	0.16	100	0.45	35	41	151	151	[18]
Comets	40.00	170	var	47.4	0.05	100	0.50	143	143	152	152	[19, 20]
KBO's	50.00	40	var	0.1	var	100	0.50	34	var	151	var	[21, 22]

Color Legend

Non - Ocean World
Possible Ocean World
Calculated IR Flux from Sfc. T
IR flux from Literature
Calculated Sink T
Calculated RTG T

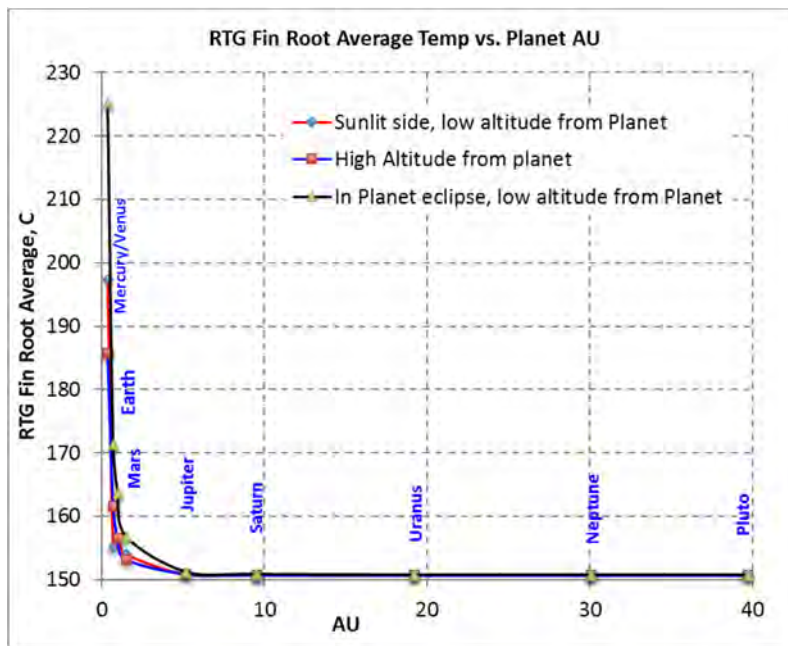


Fig. F-2. RTG skin temperature vs AU for orbital spacecraft at 100-mi altitude.

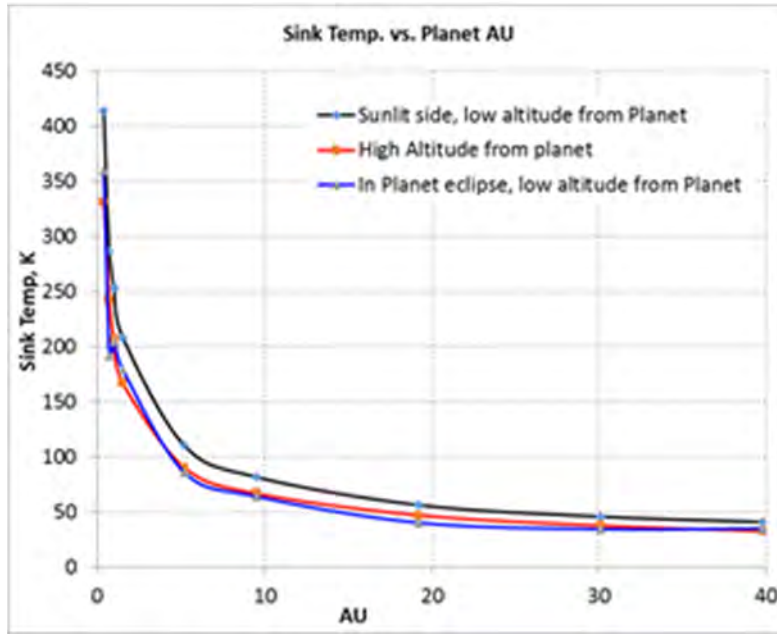


Fig. F-3. Effective sink temperature vs AU for orbital spacecraft at 100-mi altitude.

Table F-2. Lander thermal environment and MMRTG surface temperatures for worlds without atmosphere.

Planet	AU	Sfc T, min (K)	Sfc T, mean (K)	Sfc T, max (K)	Planet IR Flux, (W/m ²)	Albedo	View Factor F _v	Sink		RTG		
								Night Sink Temp. (K)	Day Sink Temp. (K)	Night RTG Temp. (C)	Day RTG Temp. (C)	
Mercury	0.39	100	437	700	5.7	0.07	0.50	84	336	151	364	[4]
Moon	1.00	100	220	390	133.0	0.136	0.50	185	237	154	161	
Io	5.20	90	110	1300	8.3	0.63	0.50	92	115	151	151	[8, 9]
Ganymede	5.20	70	110	152	8.3	0.43	0.50	92	113	151	151	[9]
Callisto	5.20	80	134	165	18.3	0.22	0.50	113	124	151	151	[9, 10]
Europa (equator)	5.20	50	102	135	20	0.67	0.50	115	129	151	152	[9, 10]
Europa (pole)	5.20		50		0.3	0.67	0.50	40	101	151	151	[9]
Mimas	9.52	74	86	98	3.1	0.96	0.50	72	89	151	151	[9]
Enceladus	9.52	33	75	145	1.8	0.99	0.50	63	85	151	151	[9]
Tethys	9.52	?	86	94	3.1	0.8	0.50	72	88	151	151	[13]
Dione	9.52	?	87	100	3.3	0.7	0.50	73	88	151	151	[9]
Rhea	9.52	53	76.5	100	1.9	0.7	0.50	64	83	151	151	[9]
Iapetus	9.52	90	110	130	8.3	0.2	0.50	92	99	151	151	[9, 13]
Miranda	19.21	?	60	86	0.7	0.32	0.50	50	60	151	151	[9, 14]
Ariel	19.21	?	59	84	0.7	0.23	0.50	50	59	151	151	[15]
Umbriel	19.21	?	63	?	0.9	0.18	0.50	53	61	151	151	[14, 15]
Titania	19.21	?	60	?	0.7	0.27	0.50	50	59	151	151	[9, 14, 15]
Oberon	19.21	?	73	85	1.6	0.24	0.50	61	67	151	151	[9, 14, 15]
Triton	30.09	?	38	?	0.1	0.76	0.50	32	45	151	151	[9, 14]
Ceres	2.77	110	155	235	32.8	0.09	0.50	130	152	152	152	[16]
Pluto	39.75	33	44	55	0.19	0.16	0.50	36	41	151	151	[18]
Comets **	var	?	170	220	47.4	0.05	0.50	143	var	var	var	[19, 20]
KBO's ***	var	?	40	?	0.1		0.50	34	var	var	var	[21, 22]

Comets have highly varying AU and Temperature. *KBO's may vary in temperature due to differences in albedo

F.4 Landers and Subsurface Vehicles on Worlds with Atmosphere or Ocean

Convective heat transfer contributes significantly to the thermal environment for landers on worlds with atmospheres, and dominates for subsurface craft in liquid oceans. For this analysis, we use Equation F-2 to account for radiation heat transfer to the local environment, with T_{sink} equal to the ambient fluid temperature. This assumption holds for worlds with thick atmosphere or liquid ocean, but fails for thin atmosphere worlds such as Mars, which can have greatly differing upward- and downward-looking sink temperatures due to cold sky and warm ground. To account for convective heat transfer we use the method given in [2, 3] for free convection past a horizontal cylinder (Equations F-4 through F-6 below).

$$Ra_D = \frac{g\beta(T_{RTG} - T_{ambient})D^3}{\nu\alpha} \quad (\text{Eq. F-4})$$

$$Nu_D = \left\{ 0.6 + 0.387Ra_D^{1/6} \left[1 + \left(\frac{0.559}{Pr} \right)^{9/16} \right]^{-8/27} \right\}^2 \quad (\text{Eq. F-5})$$

$$h = \frac{Nu_D k}{D} \quad (\text{Eq. F-6})$$

Ra_D = Rayleigh number for horizontal cylinder (instability of fluid layer due to vertical T and density gradients)

g = Local gravity

β = Volume expansivity (fluid property vs. T)

D = Cylinder diameter

ν = Kinematic viscosity (fluid property vs. T)

α = Thermal diffusivity (fluid property vs. T)

Nu_D = Nusselt number (ratio of convective/ conductive heat Xfer across boundary layer)

Pr = Prandtl number (fluid property vs. T) (ratio of momentum diffusivity to thermal diffusivity)

h = Heat transfer coefficient

k = Thermal conductivity (fluid property vs. T)

Here we assume a finless MMRTG geometry, immersed directly in the atmosphere or liquid ocean with no additional insulation or active thermal control. Ambient fluid properties vary as a function of film temperature, which is defined as the mean value between RTG surface and ambient temperatures; no consideration was made for whether an MMRTG could actually survive the modeled temperatures, rather this was used to shed light on the environmental effects and suggest requirements on an RTG. We obtained temperature-dependent fluid properties from NIST data, using the REFPROP (Reference Fluid Thermodynamic and Transport Properties) software package, version 9.1, with data from NIST database version 23.³ Fluid properties used from this database include thermal conductivity, kinematic viscosity, thermal diffusivity, volume expansivity, and Prandtl number. Table F-3 shows calculated data for landers and subsurface craft on worlds with convective media, including RTG skin temperature (T_{RTG}), convective heat transfer coefficient between the RTG surface and ambient fluid (h), convective heat flow from the RTG surface to the ambient fluid ($Q_{convection}$), radiative heat flow from the RTG surface to the

³ See National Institute of Science and Technology website at <https://www.nist.gov/programs-projects/reference-fluid-thermodynamic-and-transport-properties-database-refprop>

local environment ($Q_{radiation}$), and fluid properties at the film temperature. Note that convective heat transfer dominates in liquid environments, due to the higher thermal conductivity and higher Rayleigh and Prandtl numbers of liquids compared to gases. Radiation dominates the heat transfer for worlds with gaseous atmospheres except Venus and Titan’s surface.

Table F-3. Lander thermal environment and MMRTG surface temperatures for worlds with atmosphere or ocean.

	Fluid	P [atm]	g [m/s ²]	T _{ambient} [K]	T _{RTG} [°C]	k [W/m/K]	v [m ² /s]	α [m ² /s]	β [1/K]	Pr	Ra ₀	Nu ₀	h [W/m ² /K]	Q _{convection} [W]	Q _{radiation} [W]
Earth	N ₂ gas	1	9.81	300	194	0.03	2.5E-05	3.5E-05	2.7E-03	0.7	1.4E+08	63	6.19	633	1367
Mars	CO ₂ gas	0.011	3.70	227	218	0.02	1.1E-03	1.4E-03	2.3E-03	0.7	4.0E+04	6	0.44	71	1929
Europa Ocean floor	H ₂ O	1745	1.31	273	10	0.69	9.2E-07	1.6E-07	3.5E-04	5.6	8.4E+08	136	312	1969	31
Europa Ocean 1atm	H ₂ O	1	1.31	273	16	0.58	1.3E-06	1.4E-07	9.0E-05	9.2	2.9E+08	101	195	1950	50
Ganymede	H ₂ O	11290	1.43	273	9	0.78	1.3E-06	1.6E-07	4.2E-04	7.0	7.4E+08	132	346	1972	28
Callisto	H ₂ O	3855	1.24	273	10	0.71	1.1E-06	1.7E-07	4.2E-04	6.5	7.7E+08	134	318	1970	30
Mimas*	H ₂ O	63	1.31	273	12	0.59	1.0E-06	1.4E-07	2.2E-04	7.1	6.9E+08	130	256	1962	38
Enceladus- 1atm	H ₂ O	1	0.11	273	26	0.59	1.2E-06	1.4E-07	1.3E-04	8.7	6.0E+07	61	120	1915	85
Enceladus- floor	H ₂ O	38	0.13	273	26	0.60	7.2E-07	6.0E-07	2.5E-04	6.8	5.6E+07	59	118	1914	86
Titan - Surface	N ₂ gas	1.5	1.35	94	112	0.02	6.7E-06	9.2E-06	3.2E-03	0.7	5.4E+08	96	7	1235	765
Titan - Lakes	C ₂ H ₆	3	1.35	94	-163	0.25	1.0E-06	1.7E-07	1.6E-03	6.1	5.4E+09	247	203	1998	2
Titan - Subsurface Ocean	H ₂ O	4000	1.35	273	10	0.71	1.1E-06	1.7E-07	4.2E-04	6.5	8.2E+08	136	325	1970	30
Triton	H ₂ O/NH ₃	3000	0.78	230	-35	0.98	6.7E-07	3.2E-07	9.0E-04	2.1	7.3E+08	120	392	1985	15
Pluto	H ₂ O/NH ₄	2200	0.62	230	-34	0.91	6.3E-07	3.0E-07	1.0E-03	2.1	7.6E+08	122	371	1984	16
Venus	CO ₂ gas	92	8.87	737	486	0.05	5.2E-07	7.1E-07	1.5E-03	0.7	2.1E+10	306	56	741	1259
Neptune	H ₂ gas	1	10.8	72	-83	0.10	3.3E-05	4.7E-05	1.4E-02	0.7	3.2E+08	80	27	1955	45

* Ocean properties not well known - liquid mixture may behave more like mantle material

F.5 Special Cases

F.5.1 Pressure Vessel for Subsurface Ocean Vehicles

RTG-equipped craft for exploring subsurface oceans will likely require a pressure vessel enclosing the RTG or the entire craft. Here we present a preliminary analysis to estimate the thickness and mass of a simplified pressure vessel for several planetary oceans.

This analysis assumes a cylindrical pressure vessel with hemispherical endcaps, with an internal diameter of 0.4 m and length of the cylindrical section of 0.8 m, as shown in Fig. F-4. These dimensions accommodate a finless MMRTG with minimal clearance for additional hardware. Notional materials considered for the pressure hull include aluminum 6061-T6, titanium Ti-6AL-4V, inconel 625, and silicon carbide. Table F-4 shows mechanical properties for these materials.

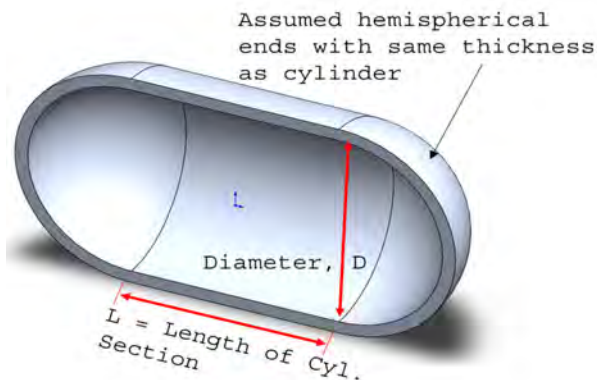


Fig F-4. Simplified pressure vessel design for ocean missions.

Table F-4. Mechanical material properties for pressure vessel hull.

	Aluminum Al 6061-T6	Titanium Ti-6Al-4V	Inconel 625	Silicon Carbide
Elastic Modulus (N/m ²)	6.89E+10	1.14E+11	2.05E+11	4.10E+11
Poisson's Ratio	0.33	0.342	0.3	0.14
density (kg/m ³)	2700	4430	8440	3100

For the calculation of minimum required wall thickness and associated shell mass, we use the critical pressure for buckling of a cylindrical pressure vessel with external pressure [42], given by Equation (F-7):

$$P_{cr} = \frac{2E}{(1-\nu^2)} \left(\frac{t}{d}\right)^3 \quad (\text{Eq. F-7})$$

$$t = \frac{\left(\left(P + \frac{(1-\nu^2)}{2E}\right)^{\frac{1}{3}}\right) d_i}{\left(1 - 2\left(\left(P + \frac{(1-\nu^2)}{2E}\right)^{\frac{1}{3}}\right)\right)} \quad (\text{Eq. F-8})$$

$$Mass = \left(\frac{\pi}{4}((d_i + 2t)^2 - d_i^2)L + \frac{4}{3}\pi\left(\left(\frac{d_i}{2} + t\right)^3 - \left(\frac{d_i}{2}\right)^3\right)\right)\rho \quad (\text{Eq. F-9})$$

$$P_{depth} = P_{cr} = \rho_{fluid}H_{ocean}g \quad (\text{Eq. F-10})$$

P_{cr} = Critical buckling pressure

E = Elastic modulus

ν = Poisson's ratio

t = Hull thickness

d = Cylinder, outer diameter

d_i = Cylinder, inner diameter

L = Length of cylinder section

ρ = Hull material density

ρ_{fluid} = Ambient ocean fluid density

H_{ocean} = Ocean depth

g = Local gravity

Solving (F-7) for t in terms of inner diameter gives Eq. (F-8), and Eq. (F-9) gives the shell mass. Equation (F-10) gives pressure at depth for the various worlds based on local hydrostatic pressure. Tables F-5 and F-6 show results of these calculations, respectively, for maximum ocean floor depths and estimated ice sheet thickness depths. Note that this analysis does not include a factor of safety for critical buckling pressure, nor does it include provisions for hull penetrations by instruments, propulsion systems, etc. In this regard, the estimate is nonconservative. However, a functional pressure hull design would likely include ribs, spanners, or other stiffening structural members that are not considered here. These additional elements would make the structure more mass efficient, and in this regard, the estimate is

conservative. This analysis should be considered a preliminary, zeroth-order estimation to show the importance of considering pressure vessel mass in mission design.

Table F-5. Ocean properties and pressure vessel sizing for ocean floor depth.

	Fluid	g (m/s ²)	h max (km)	fluid density (kg/m ³)	P max (atm)	shell thick Al (cm)	shell mass Al (kg)	shell thick Ti (cm)	shell mass Ti (kg)	shell thick Inconel (cm)	shell mass Inconel (kg)	shell thick SiC (cm)	shell mass SiC (kg)
Earth	H ₂ O	9.81	11	1000	1065	4.31	202	3.52	263	2.84	396	2.25	113
Ganymede	H ₂ O	1.43	850	1000	11996	13.2	800	10.1	920	7.72	1251	5.86	330
Callisto	H ₂ O	1.24	315	1000	3855	7.49	386	5.96	482	4.71	698	3.67	193
Europa	H ₂ O	1.31	140	1000	1810	5.37	260	4.35	334	3.48	496	2.74	140
Enceladus**	H ₂ O	0.11	70	1000	78	1.60	69	1.34	93	1.10	145	0.88	43
Titan - Lakes	C ₂ H ₆	1.35	0.3	650	2.6	0.49	20	0.41	28	0.34	44	0.28	13
Titan - Subsurface	H ₂ O	1.35	300	1000	4003	7.62	394	6.06	491	4.79	710	3.73	197
Triton	H ₂ O/NH ₃	0.78	392	1000	3014	6.70	337	5.37	426	4.26	622	3.34	174
Pluto	H ₂ O/NH ₃	0.62	365	1000	2233	5.88	288	4.74	368	3.78	544	2.97	153

**Pressure can be up to 20atm higher if calculated using thick ocean approximation, and gravity increases to .133 near the ocean floor

Table F-6. Ocean properties and pressure vessel sizing for under-ice sheet depth.

	Fluid	g (m/s ²)	h max (km)	fluid density (kg/m ³)	P max (atm)	shell thick Al (cm)	shell mass Al (kg)	shell thick Ti (cm)	shell mass Ti (kg)	shell thick Inconel (cm)	shell mass Inconel (kg)	shell thick SiC (cm)	shell mass SiC (kg)
Earth	H ₂ O	9.81	11	1000	1065	4.31	202	3.52	263	2.84	396	2.25	113
Ganymede	H ₂ O	1.43	144	1000	2032	5.64	275	4.56	352	3.64	522	2.87	147
Callisto	H ₂ O	1.24	150	1000	1836	5.40	261	4.37	336	3.50	499	2.76	141
Europa	H ₂ O	1.31	30	1000	388	2.90	130	2.39	173	1.95	264	1.56	77
Mimas*	H ₂ O	0.06	100	1000	63	1.49	64	1.24	86	1.02	134	0.82	39
Enceladus**	H ₂ O	0.11	40	1000	45	1.31	56	1.10	76	0.90	118	0.73	35
Ceres***	H ₂ O	0.27	80	1000	213	2.32	102	1.92	136	1.57	210	1.26	61
Titan - Lakes	C ₂ H ₆	1.35	0.3	650	2.6	0.49	20	0.41	28	0.34	44	0.28	13
Titan - Subsurface	H ₂ O	1.35	100	1000	1334	4.73	224	3.85	291	3.09	435	2.45	124
Triton	H ₂ O/NH ₃	0.78	200	1000	1538	5.02	240	4.07	310	3.27	462	2.58	131
Pluto	H ₂ O/NH ₃	0.62	260	1000	1591	5.09	244	4.13	315	3.31	469	2.61	133

*ocean may not exist/ plastic ice mantle

** ice thickness highly variable - estimated 6km thick at south pole.

*** may not have liquid ocean

F.5.2 Excavation by Sublimation for Europa Lander

An RTG-equipped lander on the surface of Europa will radiate heat from the warm RTG to the cold European ice surface. Due to the very low pressures on Europa (~10⁻¹² Torr, no liquid phase of water exists, and the warming of surface ice from this heat load will cause sublimation. This sublimation can excavate a hole in the ice surface beneath a radiating RTG, possibly causing instability in a lander’s position.

To analyze the possible excavation by sublimation, we consider a finless MMRTG close to a flat ice surface, as shown schematically in Fig. F-5. We assume that the source radiates 2 kW of thermal energy uniformly as a line source.

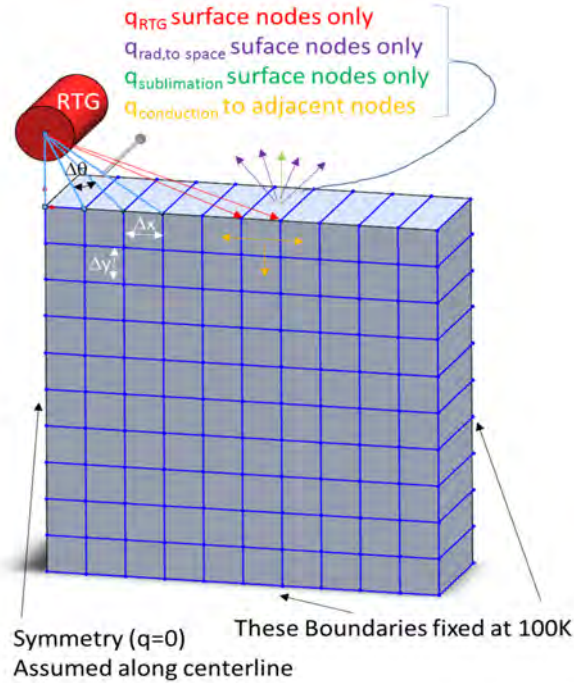


Fig. F-5. 2-D model setup showing nodalization and radiating angles for sublimation analysis.

The model considers the European ice as a two-dimensional slab, divided into nodes as shown in the schematic. The boundary nodes (or boundary conditions) at 2-m depth and 2-m laterally are held fixed at the bulk ice temperature of 100 K. The model considers two-dimensional transient conduction of heat between adjacent nodes, using forward-time finite differencing. Heat enters the surface nodes via radiation from the line-source RTG. Surface nodes also lose energy via radiation to space as gray bodies. Heat input into surface nodes from the RTG is calculated based on the fraction of total radiating angle for the line source (2π) subtended by each node (Equations F-11–F-13):

$$q_{input,i} = \frac{Q_{RTG}}{L_{RTG}} \cdot \frac{d\theta_i}{2\pi} \quad (\text{Eq. F-11})$$

$$\theta_i = \tan^{-1} \frac{i \cdot dx}{H_{RTG}} \quad (\text{Eq. F-12})$$

$$d\theta_i = \theta_i - \theta_{i-1} \quad (\text{Eq. F-13})$$

$q_{input,i}$ = Heat input into each surface node from RTG

Q_{RTG} = Total RTG source power (2 kW)

L_{RTG} = Length of RTG line source (0.65 m)

i = Index of node along surface ($i=1$ at centerline)

$d\theta_i$ = Angle from line source subtended by node I (Fig. F-5)

θ_i = Angle from line source to node i

dx = Node spacing along surface (Fig. F-5)

H_{RTG} = RTG height above surface

In this model, the ice has constant thermal properties, with specific heat (C_p) of 1.3kJ/kg/K, latent heat of sublimation (L_{sub}) of 2.6 MJ/kg, density (ρ) of 500kg/m³, and surface emissivity (ε) of 0.9 [43]. Note, the porosity and density of the ice on the surface of Europa is controversial as of this writing. For separate model runs, we vary thermal conductivity between 0.001 W/m/K (1/10th the value for terrestrial fresh snow) and 5 W/m/K (value for solid ice at 100 K).

In a hard vacuum, with ambient pressure well below the equilibrium vapor pressure of water, the sublimation rate of water ice depends on surface temperature and is a strong nonlinear function. Equations F-14 and F-15 describe the relation, and F-16 calculates cumulative sublimation depth over time. Figure F-6 shows a plot of sublimation rate vs. ice surface temperature [44, 45]. Modeled surface nodes also lose heat via latent heat of sublimation, which creates a cooling effect at the surface (Equation F-17).

$$P_{sat} = e^{(28.9074 - 6143.7/T)} \quad (\text{Eq. F-14})$$

$$\dot{m}_{sub} = P_{sat} \left[\frac{MW}{2\pi RT} \right]^{1/2} \quad (\text{Eq. F-15})$$

$$H_{sub} = \int \frac{\dot{m}_{sub}}{\rho_{ice} \cdot dx} dt \quad (\text{Eq. F-16})$$

$$q_{sub} = -\dot{m}_{sub} L_{sub} \quad (\text{Eq. F-17})$$

$$q_{cond,i,j} = -k \frac{dy}{dx} (T_{i,j} - T_{i+1,j}) - k \frac{dy}{dx} (T_{i,j} - T_{i-1,j}) - k \frac{dx}{dy} (T_{i,j} - T_{i,j+1}) - k \frac{dx}{dy} (T_{i,j} - T_{i,j-1}) \quad (\text{Eq. F-18})$$

$$q_{net} = q_{RTG} + q_{rad} + q_{sub} + q_{cond} \quad (\text{Eq. F-19})$$

$$dT = q_{net} \frac{dt}{m \cdot C_p} \quad (\text{Eq. F-20})$$

P_{sat} = Equilibrium saturation vapor pressure

\dot{m}_{sub} = Mass loss rate due to sublimation

MW = Molar weight of water (fixed at 18.015 g/mol)

H_{sub} = Cumulative sublimation depth integrated over time

q_{sub} = Heat loss due to sublimation

L_{sub} = Latent heat of sublimation

$q_{cond,i,j}$ = Heat conduction into node i,j

j = Index of node downward (j=1 at ice surface)

k = Ice thermal conductivity

dy = Vertical node spacing

q_{RTG} = RTG radiation heat into surface nodes (q_{input} in Eq. F-11)

q_{rad} = Ice surface node radiation heat loss to space

dt = Model timestep

m = Node mass

C_p = Ice specific heat

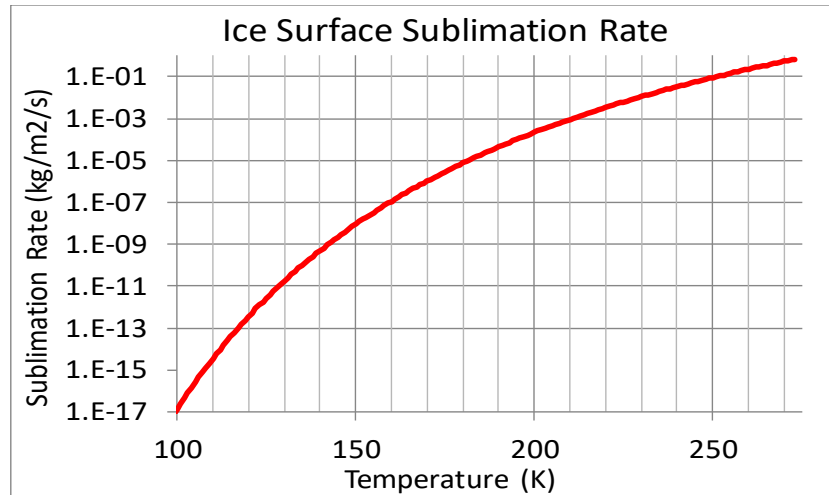


Fig. F-6. Ice surface sublimation rate for ice in hard vacuum.

Equation F-18 shows the net heat flow into an internal node from conduction with adjacent nodes. At a given timestep, the conductive heat flow is calculated from temperatures computed at the end of the previous timestep. The net heat into each node, Equation F-19, is the sum of RTG radiant heat input (surface nodes only, radiated heat to space, sublimated heat loss, and conduction to surrounding nodes). The temperature change during each timestep is then given by Equation F-20.

The model assumes a fixed geometry, which implies a conservative estimate due to the lower heat flux into surface nodes as the surface sublimates and recedes away from the RTG. In reality, a lander would sink with the subsidence of surface ice sublimated under a lander's supports to create an unpredictable distance relation. The modeling of the RTG as a radiating line source is only valid when the distance from the source to the ice is smaller than the length of the RTG, and larger than the diameter of the RTG. For larger distances, it will behave more like a point source, with heat flux at the ice surface scaling as $1/r^2$. For very close distances, it will behave more like a three-dimensional source. Therefore, our model over-predicts heating and sublimation at long values of RTG height, and likely under-predicts for short values.

Figure F-7 consists of three contour plots of predicted ice temperatures for varying RTG heights above the surface. In these plots, the gray circle in the upper-left corner of each contour shows the location and approximate size (even though it is modeled as a line source with zero diameter of the RTG). The y- and x- coordinates are, respectively, depth into the ice and lateral distance from the RTG centerline. The model assumes symmetry about the y-axis, therefore the left side of the plot is not shown. A maximum ice temperature of approximately 200 K is common to the analysis for all cases. This is due to the cooling “feedback” effect of the latent heat of sublimation, which cools the surface more as temperatures rise and sublimation increases. It is approximately the “knee” in the sublimation curve (Fig. F-6, at which sublimation rate begins to increase much more rapidly with temperature). Fig. F-8 shows a similar set of plots for varying ice thermal conductivity values.

Figure F-9 shows a plot of cumulative depth of sublimated ice directly under an RTG centerline vs. time for various RTG heights above the ice. Significant excavation of order 1 m can occur for RTGs very close to the ice surface. Fig. F-10 shows a similar plot for various values of ice thermal conductivity. The effect of changing k is significant at the higher values. A value of 5 W/m/K is associated with solid ice at 100 K. Fig. F-11 shows a similar plot for varying values of ice specific heat (C_p). Fig. F-12 shows a similar plot for different thermoelectric couple efficiencies. For this model, the electrical efficiency of RTGs using the same quantity of heat will change the total radiative thermal power output of a line source, resulting in a less powerful heat source for more efficient thermoelectric couple designs. The effect is small, but amplified over long mission durations, durations measured in days. Note that we used

a constant ice density of 500 kg/m^3 for this study. Sublimation depth varies approximately inversely with density (Equation F-16), which is not well known for the surface layers of most icy moons.

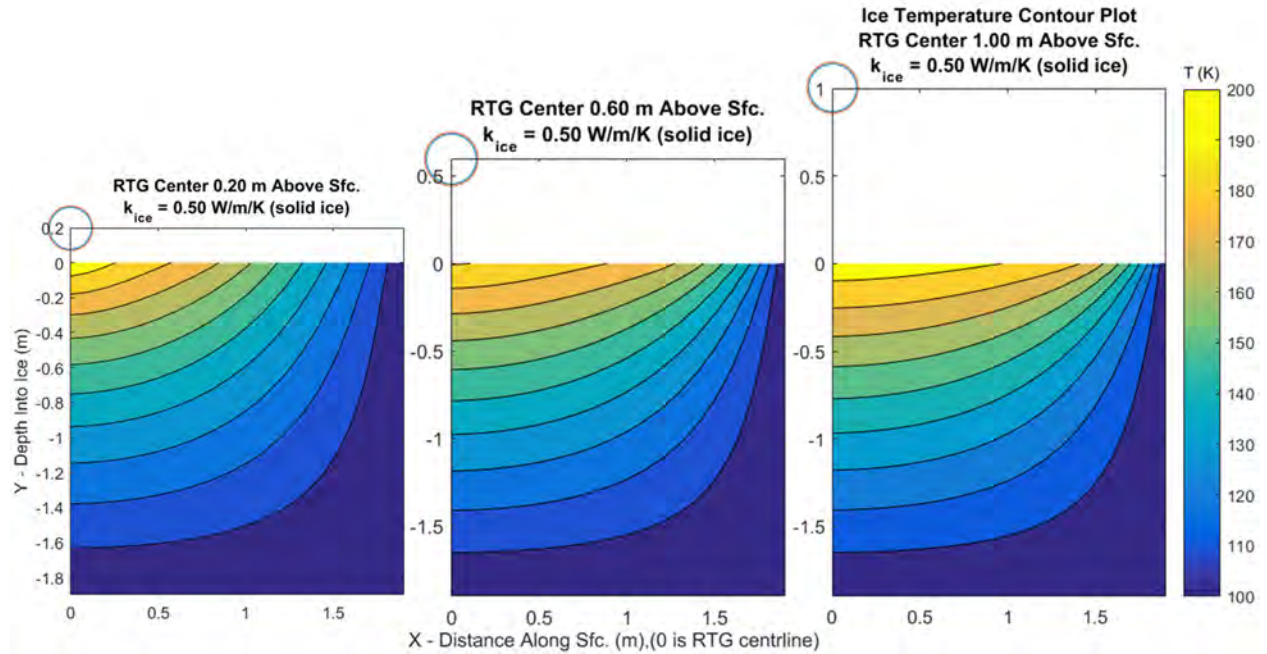


Fig. F-7. Contour plots of ice temperature throughout the modeled 2-D slab, for varying RTG height above the ice surface. The circle shows location of RTG relative to the surface. Point with coordinates 0,0 is directly under the RTG centerline, and the ice surface is the line $y = 0$. Note the left-hand side of the plots are not shown due to assumed symmetry about the y-axis.

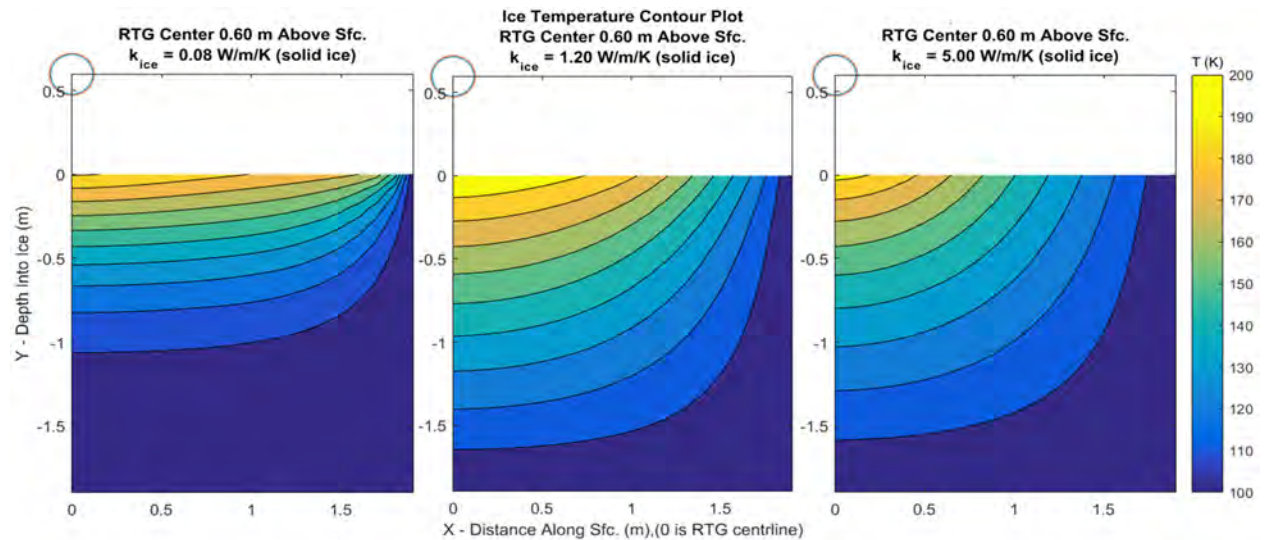


Fig. F-8. Contour plots of ice temperature throughout the modeled 2-D slab, for varying ice thermal conductivity. The circle shows location of RTG relative to the surface. Point with coordinates 0,0 is directly under the RTG centerline, and the ice surface is the line $y = 0$. Note the left-hand side of the plots are not shown due to assumed symmetry about the y-axis.

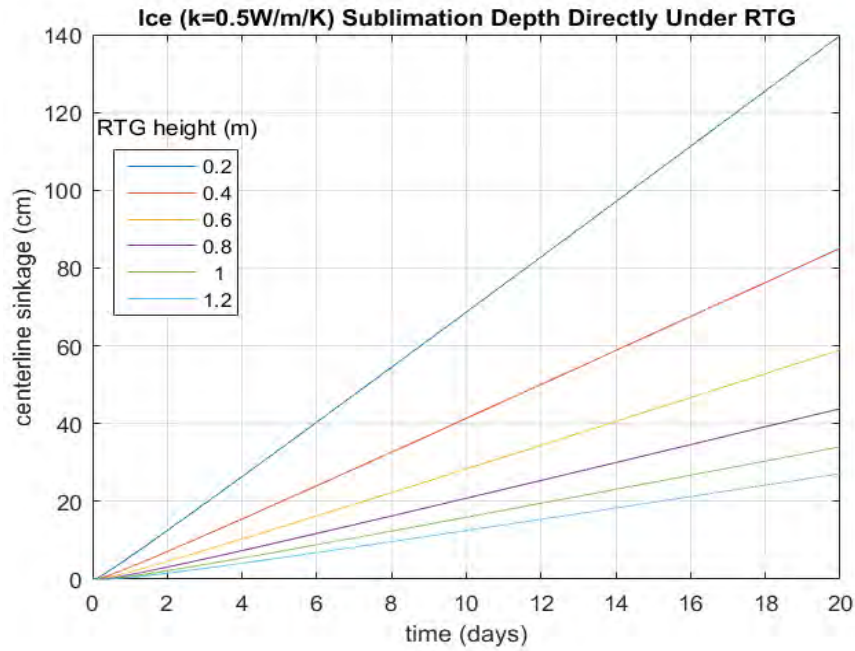


Fig F-9. Centerline sublimation depth beneath RTG for different heights. Note height here is from RTG edge, 15 cm closer than centerline.

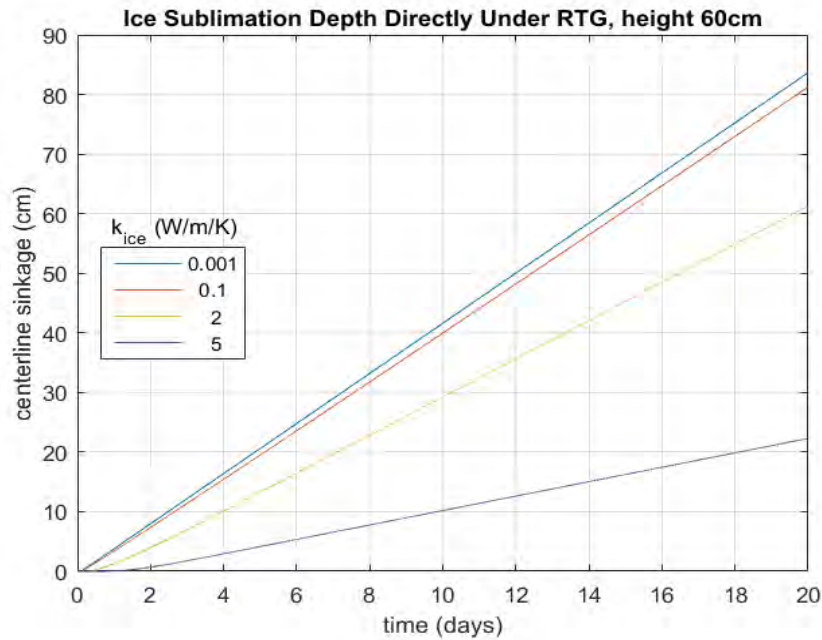


Fig F-10. Centerline sublimation depth beneath RTG for ice thermal conductivity values.

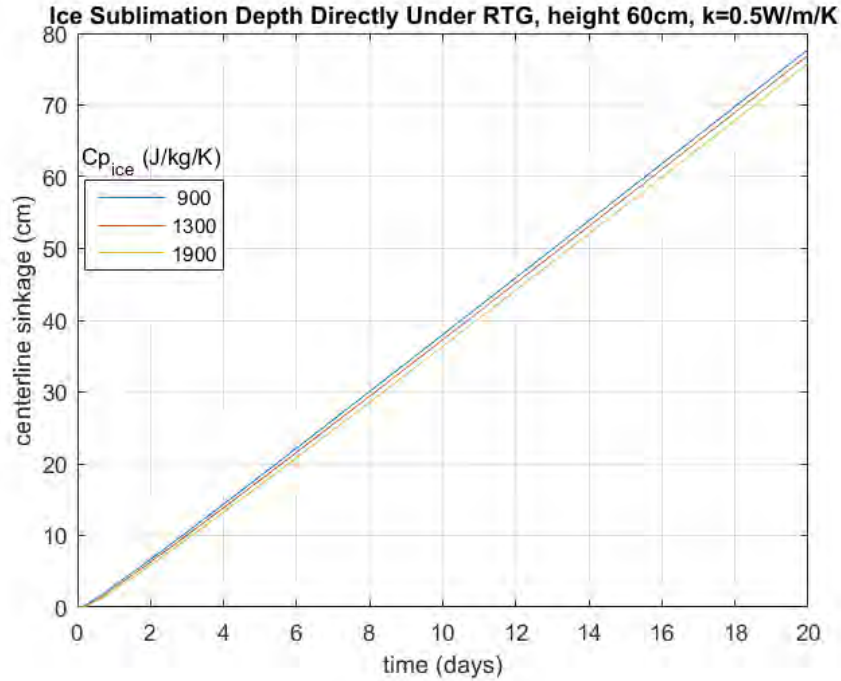


Fig F-11. Centerline sublimation depth beneath RTG for different ice specific heat values.

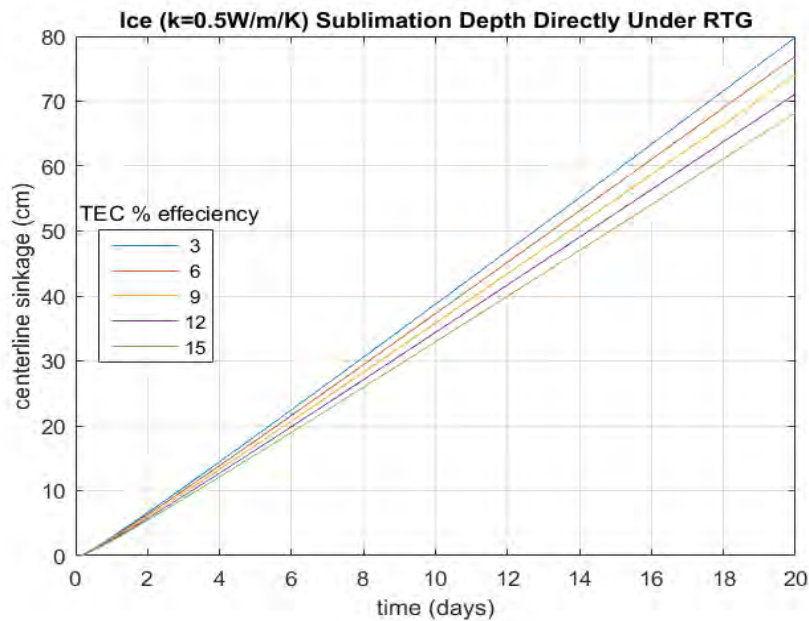


Fig. F-12. Centerline sublimation depth beneath RTG for different couple efficiency values.

Note that this analysis assumes no thermal radiation shielding between an RTG and the ice. The sublimation excavation can likely be mitigated by application of a radiation shield below an RTG, to direct waste heat upwards into space instead of into the ice. As in the previous section, this analysis should be considered a preliminary approximation. The analysis shows that excavation due to sublimation

from radiative heating on an icy moon lander can be significant and must be considered in the design of such a mission.

F.6 References

- [1] Gilmore, D.G and M. Donabedian, eds. 2003 *Spacecraft Thermal Control Handbook: Cryogenics*, Vol. 2. AIAA, p. 513.
- [2] Incropera, F.P. 2006. *Introduction to Heat Transfer*, 5th edition, John Wiley and Sons, Hoboken, NJ, eqn. 9.34.
- [3] Chapman, A.J. 1984. *Heat Transfer*, 4th ed., Prentice Hall, eqn. 9.42.
- [4] Vasavada, A.R., D.A. Paige, and S.E. Wood. 1999. "Near-surface temperatures on Mercury and the Moon and the stability of polar ice deposits," *Icarus* 141.2, pp 179–193.
- [5] Bland, M.T. et al. 2016. "Composition and structure of the shallow subsurface of Ceres revealed by crater morphology," *Nature Geoscience*, 9.7, pp 538–542.
- [6] Schorghofer, et al. N. 2016. "The permanently shadowed regions of dwarf planet Ceres," *Geophysical Research Letters*, 43.13, pp. 6783–6789.
- [7] Bagenal, F., T.E. Dowling, and W.B. McKinnon. 2006. *Jupiter: The planet, Satellites and Magnetosphere*, Cambridge University Press.
- [8] Keszthelyi, L. 2007. "New estimates for Io eruption temperatures: Implications for the interior," *Icarus*, 192.2, pp. 491–502.
- [9] Grundy, W.M. et al. 1999. "Near-infrared spectra of icy outer Solar System surfaces: Remote determination of H₂O ice temperatures," *Icarus*, 142.2, pp. 536–549.
- [10] Moore, J.M. et al. 2004. "Callisto," *Jupiter. The Planet, Satellites and Magnetosphere*," pp 397–426.
- [11] Williams, D.R. September 2006. Saturn Fact Sheet, NASA, archived from the original on April 9, 2014.
- [12] NASA. Updated 2010. "Cassini: unlocking Saturn's secrets," web site. http://www.nasa.gov/mission_pages/cassini/multimedia/pia12867.html.
- [13] Spencer, J.R. and T. Denk. 2010. "Formation of Iapetus' extreme albedo dichotomy by exogenically triggered thermal ice migration," *Science*, 327.5964, pp. 432–435.
- [14] Hanel, R. et al. 1986. "Infrared observations of the Uranian system," *Science*, 233.4759, pp. 70–74.
- [15] Grundy, W.M. et al. 2006. "Distributions of H₂O and CO₂ ices on Ariel, Umbriel, Titania, and Oberon from IRTF/SpeX observations," *Icarus*, 184.2, pp. 543–555.
- [16] Pearl, J.C. and B.J. Conrath. 1991. "The albedo, effective temperature, and energy balance of Neptune, as determined from Voyager data," *Journal of Geophysical Research: Space Physics*, 96.S01, pp. 18921–18930.
- [17] Cruikshank, D.P. et al. 1993. "Ices on the surface of Triton," *Science*, 261.5122, pp. 742–746.
- [18] Owen, T.C. et al. 1993. "Surface ices and the atmospheric composition of Pluto," *Science*, 261.5122, pp. 745–748.
- [19] Groussin, O. et al. 2007. "Surface temperature of the nucleus of Comet 9P/Tempel 1," *Icarus*, 191.2, pp. 63–72.
- [20] Tosi, F. et al. 2014. "Comet 67P/CG: Surface Temperatures as Derived by Rosetta/VIRTIS in the Mapping Phase," *AGU Fall Meeting Abstracts*, V1.

- [21] Brown, M.E., C.A. Trujillo, and D.L. Rabinowitz. 2005. “Discovery of a planetary-sized object in the scattered Kuiper belt,” *The Astrophysical Journal Letters*, 635.1, p. L97.
- [22] Jewitt, D., H. Aüssel, and A. Evans. 2001. “The size and albedo of the Kuiper-belt object (20000) Varuna,” *Nature*, 411.6836, pp. 446–447.
- [23] Delitsky, M.L., A.L. Lane. 1998. “Ice chemistry of Galilean satellites,” *J. of Geophys. Res.*, 103 (E13), pp 31,391–31,403.
- [24] Quick, L.C. and B.D. Marsh. 2016. “Heat transfer of ascending cryomagma on Europa,” *Journal of Volcanology and Geothermal Research*, 319, pp. 66–77.
- [25] Kuskov, O.L. and V.A. Kronrod. 2005. “Internal structure of Europa and Callisto,” *Icarus*, 177.2, pp. 550–569.
- [26] Billings, S.E. and S.A. Kattenhorn. 2005. “The great thickness debate: Ice shell thickness models for Europa and comparisons with estimates based on flexure at ridges,” *Icarus*, 177.2, pp. 397–412.
- [27] Vance, S., M. Bouffard, M. Choukroun, and C. Sotina. 2014. “Ganymede’s internal structure including thermodynamics of magnesium sulfate oceans in contact with ice,” *Planetary and Space Science*, 96, pp. 62–70.
- [28] Hussmann, H., F. Sohl, and T. Spohn. 2006. “Subsurface oceans and deep interiors of medium-sized outer planet satellites and large trans-neptunian objects,” *Icarus*, 185.1, pp. 258–273.
- [29] Tajeddine, R. et al. 2014. “Constraints on Mimas’ interior from Cassini ISS libration measurements,” *Science*, 346.6207, pp. 322–324.
- [30] Less, L. et al. 2014. “The Gravity Field and Interior Structure of Enceladus,” *Science*, 344.6179, pp. 78–80.
- [31] Olgin, J.G., B.R. Smith-Konter, and R.T. Pappalardo. 2011. “Limits of Enceladus's ice shell thickness from tidally driven tiger stripe shear failure,” *Geophysical Research Letters*, 38.2.
- [32] Tyler, R.H. 2009. “Ocean tides heat Enceladus,” *Geophysical Research Letters*, 36.15.
- [33] Mitri, G. et al. 2007. “Hydrocarbon lakes on Titan,” *Icarus*, 186.2, pp. 385–394.
- [34] Lorenz, R.D. et al. 2008. “Titan's rotation reveals an internal ocean and changing zonal winds,” *Science*, 319.5870, pp. 1649–1651.
- [35] Encrenaz, T., R. Kallenbach, T. C. Owen, and C. Sotin. 2005. *The Outer Planets and Their Moons*, Springer.
- [36] Cordier, D. et al. 2009. “An estimate of the chemical composition of Titan’s lakes,” *The Astrophysical Journal Letters*, 707.2, p. L128.
- [37] Stofan, E.R. et al. 2007. “The lakes of Titan,” *Nature*, 445.7123, pp. 61–64.
- [38] Kerr, R.A. 2012. “Cassini Spies an Ocean Inside Saturn’s Icy, Gassy Moon Titan,” *Science*, 336.6089, pp. 1629–1629.
- [39] Ruiz, J. 2003. “Heat flow and depth to a possible internal ocean on Triton,” *Icarus*, 166.2, pp. 436–439, 2003.
- [40] Von Zahn, U. et al. 1983. “Composition of the Venus Atmosphere,” Chapter 13 in *Venus*, p. 299, University of Arizona Press.
- [41] D. P. Cruikshank, M. S. Matthews, and A. M. Schumann, eds., *Neptune and Triton*, University of Arizona Press, 1995.
- [42] Chattopadhyay, S. 2004. *Pressure Vessels Design and Practice*, Chapter 5, CRC Press.
- [43] Gudipati, M.S. and J. Castillo-Rogez, eds. 2012. *The Science of Solar System Ices*, Vol. 356, Chapter 11, Springer Science & Business Media.

- [44] Murphy, D.M. and T. Koop. 2005. “Review of the vapour pressures of ice and supercooled water for atmospheric applications,” *Quarterly Journal of the Royal Meteorological Society*, 131.608, pp. 1539–1565.
- [45] Andreas, E.L. 2007. “New estimates for the sublimation rate for ice on the Moon,” *Icarus*, 186.1, pp. 24–30.

G Radiation Environments for Space Missions with RTGs

Insoo Jun and Henry Garrett

NASA Jet Propulsion Laboratory, 4800 Oak Grove Drive, Pasadena, CA 91109

G.1 Introduction

Any space mission is subject to harmful effects from the natural space radiation. This environment is primarily comprised of charged particles (electrons, protons, and heavier ions) from planetary trapped radiation belts, solar particle events, and galactic cosmic rays. In the meantime, if a mission utilizes power from an on-board nuclear battery such as radioisotope thermoelectric generator (RTG), there are other components of radiation that need to be included: neutral particles (neutrons and gamma rays) originating from the decay of the radioisotopes (e.g., ^{238}Pu) used in the RTG.

For robotic missions, total ionizing dose (TID), displacement damage dose (DDD), and single-event effects (SEE) are typical radiation effects that have to be considered for electronics, detectors/sensors, and materials. Here we will describe the general characteristics of the radiation environments that would cause these effects and would be expected for a space mission with an on-board nuclear power source. Note that it is not the intent of this section and not practical to comprehensively describe the details of the radiation environment for each destination in the solar system. Rather, we will provide a general overview of the environment. Each mission should develop its own radiation environment specification based on the actual mission target (Jupiter, Saturn, an asteroid, the interplanetary environment, etc.) and on the mission characteristics (duration, trajectory, etc.)

G.2 Natural Space Radiation Environments

G.2.1 *Trapped Radiation*

Any planetary body in the solar system that possesses an intrinsic magnetic field can trap charged particles. They are called Van Allen radiation belts, named after the scientist who discovered the existence of Earth's radiation belts during the Explorer 1 mission. In addition to Earth, radiation belts exist at Jupiter, Saturn, Uranus, and Neptune. It is also postulated that large asteroids such as Psyche 16 could trap particles with a remnant magnetic field.

The strength of a magnetic field (which in turn depends on the strength of magnetic dipole moment and the size of the planetary body in question) is the main parameter that determines energy and intensity of the trapped particles. Electrons and protons are typically found in those belts. Heavier ions can be also trapped, but their energy and flux levels are insignificant and can be ignored in our discussion. Table G-1 compares some relevant physical parameters for Earth, Jupiter, Saturn, and Uranus as examples.

Magnetic field strength at the Equator is proportional to the magnetic moment divided by cube of the radial distance. Therefore, for example, as Jupiter is roughly 10 times the size of the Earth while its magnetic moment is 20,000 times larger, the Jovian magnetic field is in proportion to its size about 20 times larger than the Earth's at comparable distances in planetary radii. Therefore, the energy and flux levels of trapped particles in the Jovian magnetospheric system can be much higher than those at the Earth. Using the same argument, it can be also shown that Saturn's magnetic field strength is comparable with the Earth's at similar planetary radii.

Fig. G-1 through Fig. G-4 are contour plots of the modeled radiation environments at Earth, Jupiter, Saturn, and Uranus at selected energies of electrons and protons in planetary radii. The radiation belt models used for these plots are: AP8/AE8 for Earth [1, 2], GIRE for Jupiter [3], SATRAD for Saturn [4], and UMOD for Uranus [5]. These plots illustrate the global structure and relative severity of the radiation belt at each planet.

G.2.2 Solar Energetic Particle or Solar Proton Event

A solar energetic particle (SEP) or solar proton event (SPE) are names for a very energetic process on the Sun that typically happens when the Sun is in an active phase, and thus when magnetic fields are unstable. All types of charged particles can be emitted during an SEP. High-energy protons and heavy ions are, however, more important for assessing damage to electronics or materials in terms of TID, DDD, and SEE. The occurrence of SEPs is statistical in nature – we cannot predict when an SEP will occur with what intensity. Therefore, we rely on numerical models developed using the historical SEP data to estimate mission environments.

Table G-1. Physical parameters for several planetary magnetosphere.

	Equatorial Radius (km)	Magnetic Moment (G-cm ³)
Earth	6.4 x 10 ³	8.1 x 10 ²⁵
Jupiter	7.1 x 10 ⁴	1.59 x 10 ³⁰
Saturn	6.0 x 10 ⁴	4.3 x 10 ²⁸
Uranus	2.6 x 10 ⁴	~1.9 x 10 ²⁸

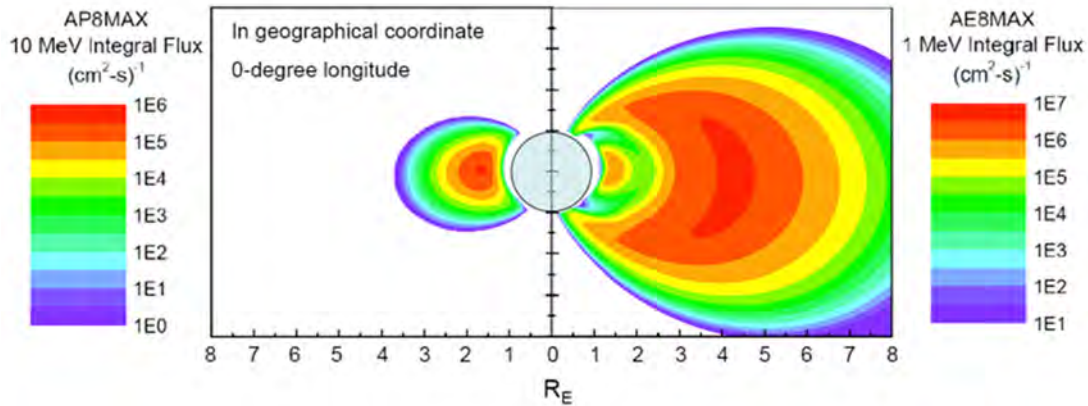


Fig. G-1. Contour plot showing ≥ 1 -MeV electron and ≥ 10 -MeV proton integral fluxes at Earth. The coordinate system used in this plot is geographical, rather than in a magnetic coordinate system, B-L. The models used are the AP8 solar maximum model and the AE8 solar maximum model. The contour plane is for the 0-degree meridian.

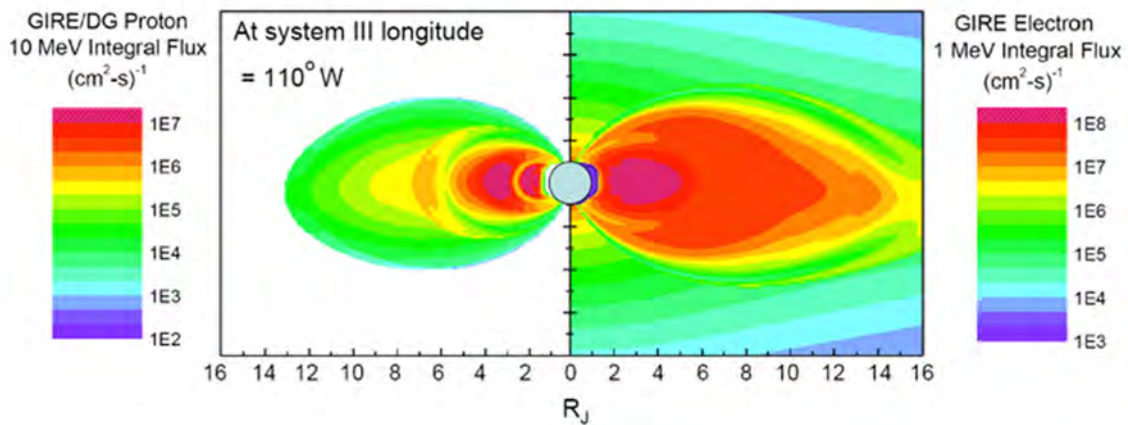


Fig. G-2. Contour plot showing ≥ 1 -MeV electron and ≥ 10 -MeV proton integral fluxes at Jupiter. The coordinate system used in this plot is jovi-centric, rather than B-L. The models used are the JPL GIRE [3] model. The contour plane is for the System III 110-degree west meridian.

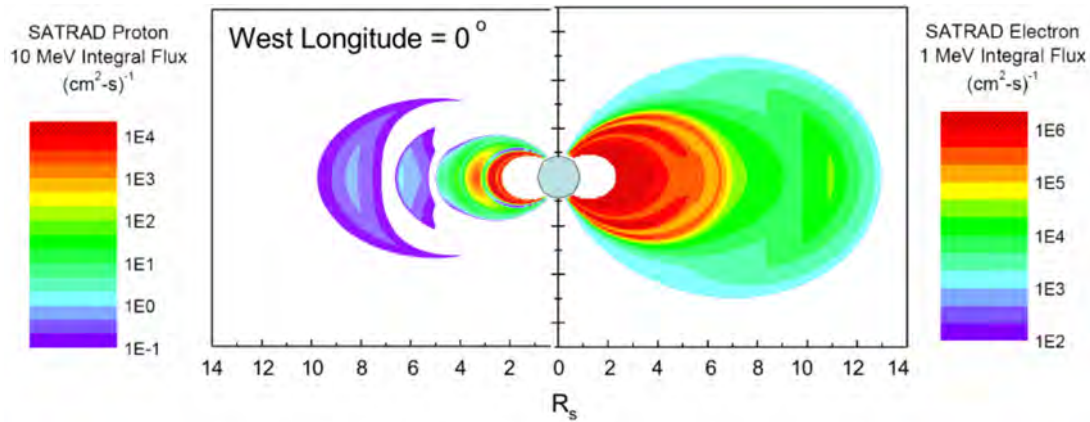


Fig. G-3. Contour plot showing ≥ 1 -MeV electron and ≥ 5 -MeV proton integral fluxes at Uranus. The coordinate system used in this plot is B-L. The model used is the JPL UMOD model [5]. The plot is for a meridian profile (i.e., idealized dipole coordinates R - λ) of the Uranian radiation belts. Note that there is an absence of data inside $\sim 4 R_U$ – this does not represent the absence of radiation flux in this region.

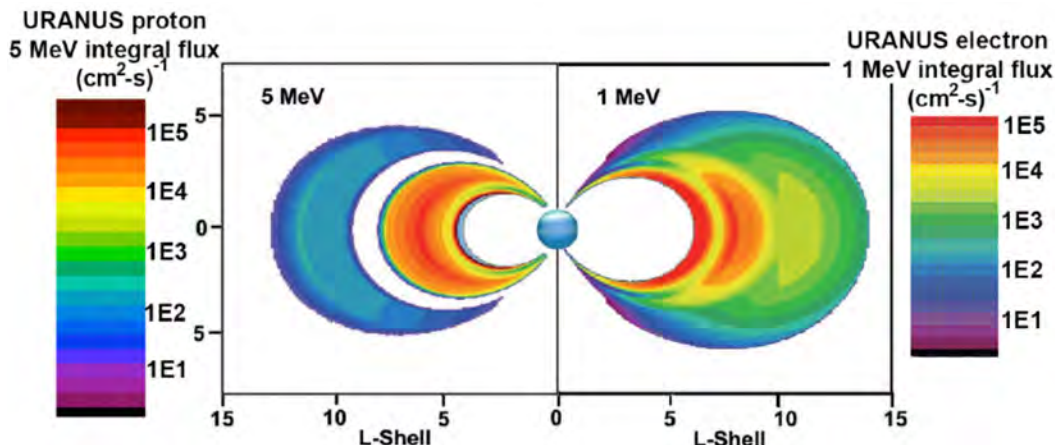


Fig. G-4. Contour plot showing ≥ 1 MeV electron and ≥ 5 MeV proton integral fluxes at Uranus. The coordinate system used in this plot is B-L. The model used is the JPL UMOD model [5]. The plot is for a meridian profile (i.e., idealized dipole coordinates $R-\lambda$) of the Uranian radiation belts. Note that there is an absence of data exists inside $\sim 4 R_u$ – this does not represent the absence of radiation flux in this region.

For TID and DDD that requires the knowledge of mission fluence, the solar protons are important and there are several statistical solar proton fluence models available. Among those, we use the JPL solar proton model, also called the Feynman model [6, 7], where the size distribution of historical solar proton event fluences observed at 1 AU (150 million kilometers) is found to follow a log-normal distribution. For example, Fig. G-5 plots the cumulative probability of the occurrence of a solar proton event fluence of the indicated level or less between 1963 and 1991 (the non-standard scale used is such that a log-normal distribution will appear as a straight line on the graph). Fig. G-6 uses these data to predict the probability of seeing a total >10 MeV proton fluence equal or less than the graphed value for various mission lengths during solar maximum. Similar plots are available for other energies. Feynman assumed [6, 7] that a solar cycle is 11-year and consists of 7 years of solar maximum and 4 years of solar minimum. The proton flux is assumed to be 0 during solar minimum period in the model. Furthermore, we apply a scaling factor based on the time-averaged $1/r^2$ to estimate the fluences for missions not staying at 1 AU. This means that the solar proton environment will be trajectory dependent for interplanetary missions.

To evaluate SEEs for electronics during SEPs, we use the CREME96 model [8], which provides three heavy ions flux models (in terms of linear energy spectra or LET based on the October 1989 event – worst week, worst day, and 5 m peak fluxes). Fig. G-7 shows the integral LET spectra for these three fluxes obtained using CREME96 behind a 100-mil (or 2.5 mm aluminum shielding at 1 AU).

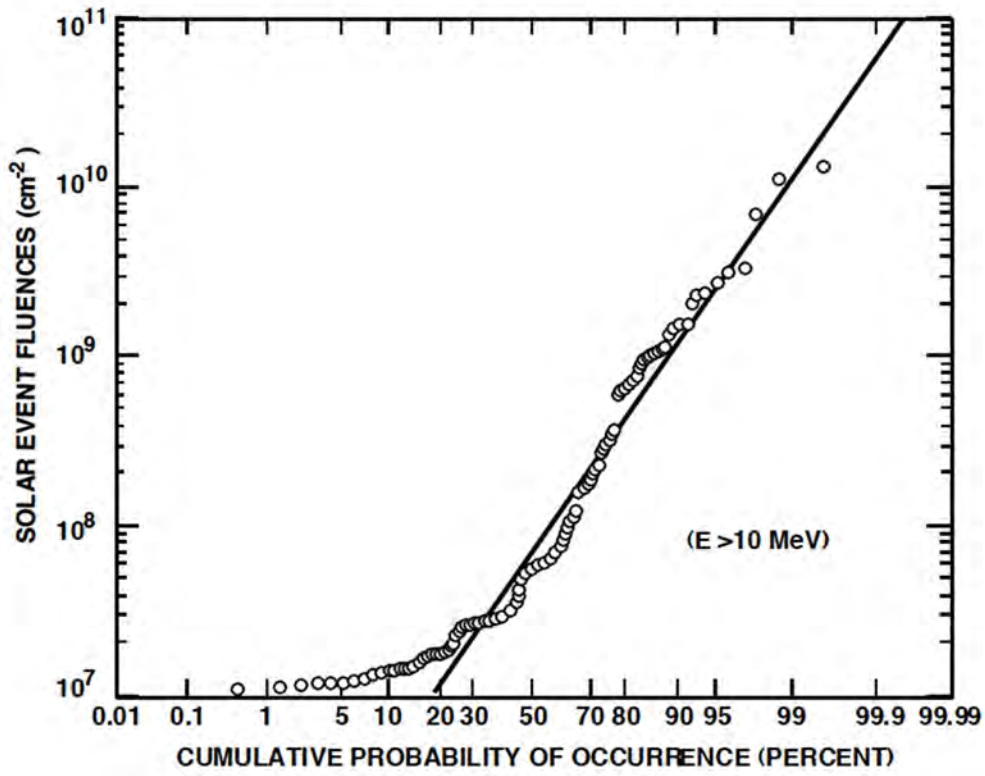


Fig. G-5. Distribution of solar event fluences for solar active years between 1963 and 1991 for protons of energy > 10 MeV for which the daily averaged flux exceeds 1.0 cm⁻²-s⁻¹-sr⁻¹. The straight line is the selected log normal distribution.

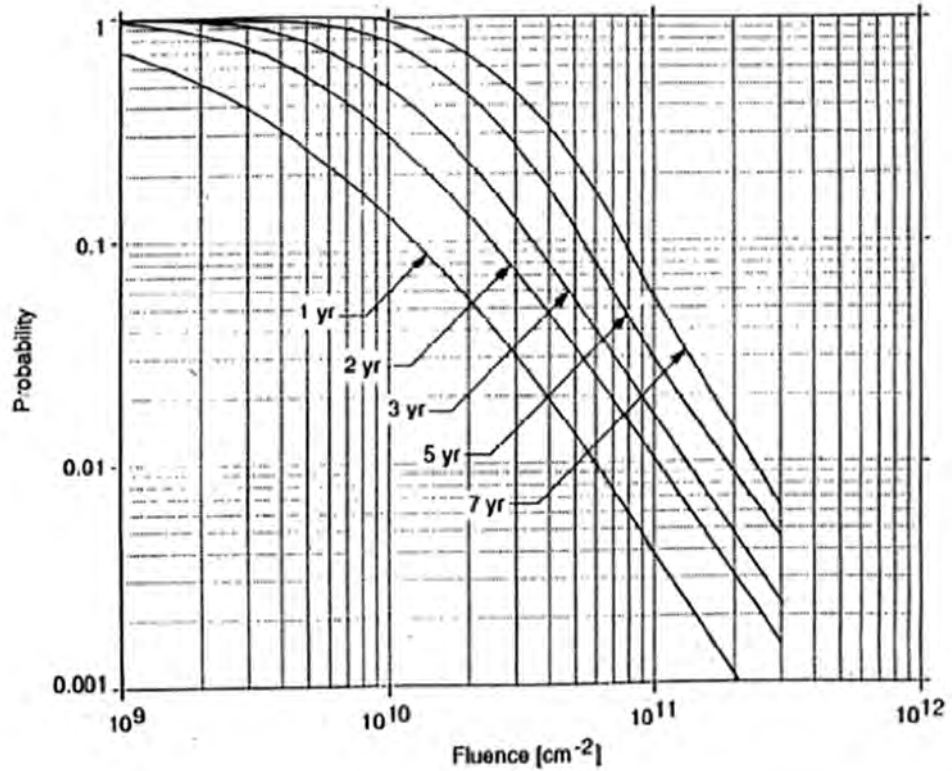


Fig. G-6. Fluence probability curves for protons of energy greater than 10 MeV for various mission lengths.

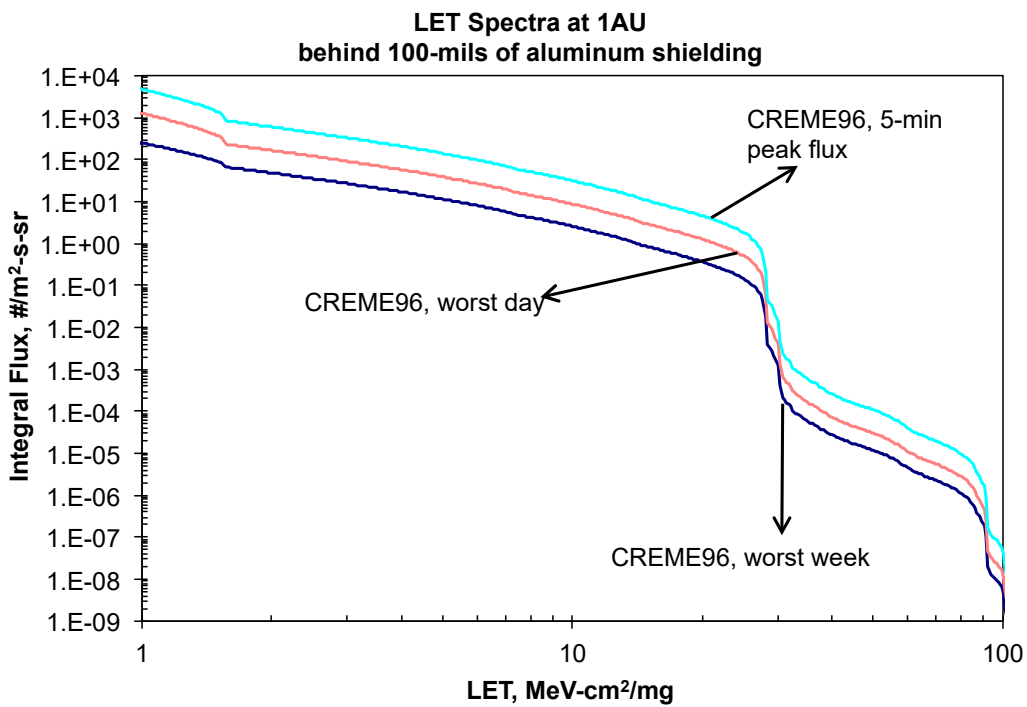


Fig. G-7. Heavy ion fluxes expressed in terms of linear energy transfer integral spectra based on the CREME96 model with a 100-mil (or 2.5 mm aluminum shielding at 1 AU.

G.2.3 *Galactic Cosmic Rays (GCR)*

The third source of radiation is galactic cosmic rays (GCR). GCRs constitute a major part of the space radiation environment in the solar system. GCRs are very energetic charged particles—protons and atomic nuclei—likely accelerated by vast spheroidal blast waves from supernova explosions that propagate in the interstellar gas [9]. The accelerated cosmic rays enter the heliosphere on their way to the inner solar system. Typical energies of GCR found near Earth are in the range of 0.1 to 10 GeV/nucleon although extremely high energy of GCRs (> 1 TeV/nucleon) have been observed. All of the naturally occurring atomic nuclei are found in GCR—protons (~87%), alpha particles (~12%), and heavier nuclei (~1%).

The GCR environment is solar-cycle dependent—higher GCR levels during solar minimum periods and lower GCR levels during solar maximum periods. There are several models available—CREME96 [8], a model used in [10], a model used in [11], the Badhwah-O’Neill 2010 model [12], etc.—each uses a different approaches to account for the solar-cycle dependency. A comparison of different GCR models is described in [13], where a way was suggested to relate one model to another. A review paper on these commonly used GCR models has recently been published by [14]. Note that all the GCR models available are based on the data collected at or near 1 AU and that the GCR intensities are expected to be higher as the distance from the Sun increases.

In the meantime, although GCRs possess very high energy, the intensities are low, and we typically do not consider them for the TID and DDD effects for electronics and materials. However, they can induce SEEs in electronics.

Fig. G-8 shows the GCR proton energy spectra obtained from the CREME96 solar maximum (i.e., GCR minimum) model and from the maximum and minimum GCR proton models from McKinney et al. [11]. In the McKinney model, Φ is the solar modulation potential value that describes magnetic field effects on the GCR intensity. Fig. G-9 is an integral LET spectrum of the GCR heavy ions behind a 100-mil aluminum shielding at 1 AU obtained using CREME96 for solar minimum condition.

G.3 **Radiation from RTGs**

An RTG is a nuclear battery that uses the heat produced in the radioactive α -decay of plutonium isotopes (primarily from the decay of ^{238}Pu with a half-life of 86.4 years) in the PuO_2 fuel used as a power source. There are two types of radiation that an RTG emits: neutrons and gamma rays. In this section, in the absence of detailed design information for the Next-Generation RTG, we present the radiation environment characteristics of a typical RTG based on a Multi-Mission RTG (MMRTG) used for the Mars Science Laboratory.

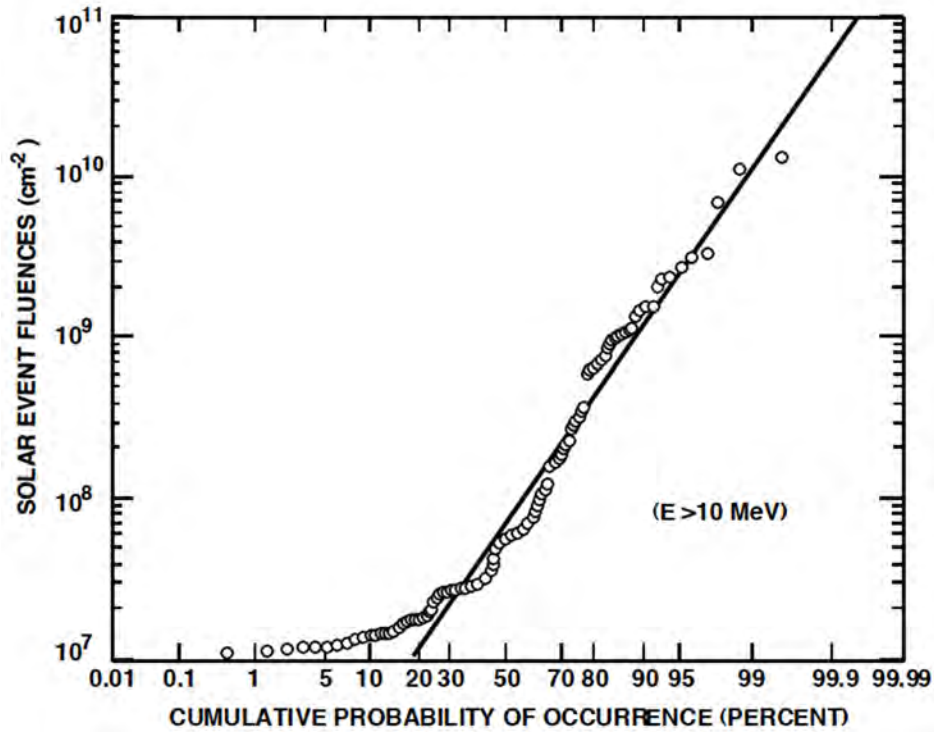


Fig. G-8. Distribution of solar event fluences for solar active years between 1963 and 1991 for protons of energy > 10 MeV for which the daily averaged flux exceeds 1.0 cm⁻²-s⁻¹-sr⁻¹. The straight line is the selected log normal distribution.

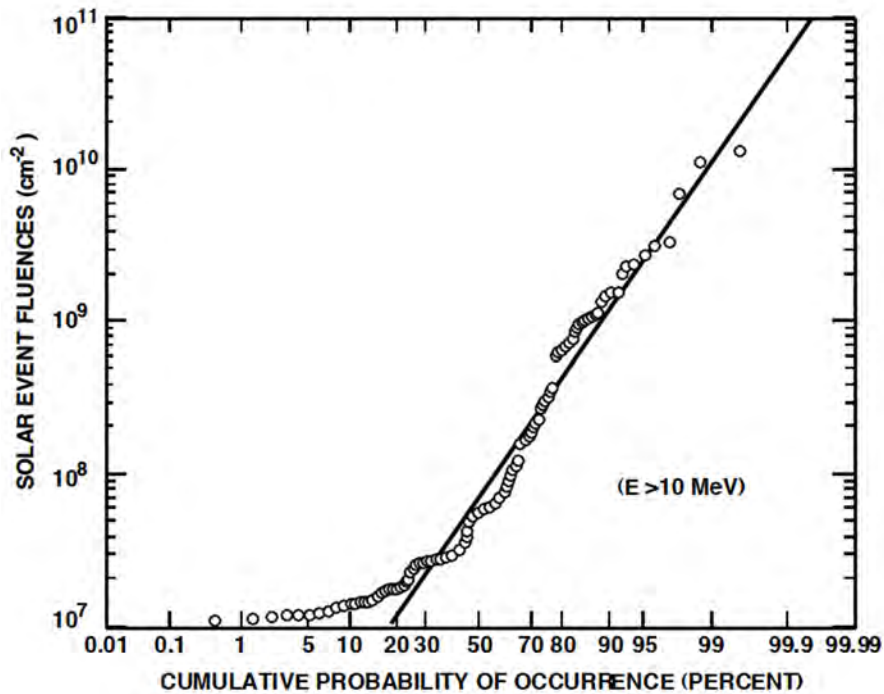


Fig. G-9. Distribution of solar event fluences for solar active years between 1963 and 1991 for protons of energy > 10 MeV for which the daily averaged flux exceeds 1.0 cm⁻²-s⁻¹-sr⁻¹. The straight line is the selected log normal distribution.

The MSL MMRTG is made of a PuO₂ fuel purchased from Russia and its main normalized isotopic contents are shown in Table G-2. These values are used to compute the neutron and gamma ray characteristics of the MMRTG. The major physical mechanisms of the radiation sources in the MSL MMRTG are radioactive decays, spontaneous fissions of plutonium isotopes, and (α , n) reactions with low-Z materials (especially with ¹⁶O) present in the fuel. The physics of radioactive decay and spontaneous fission are very well known and the neutron sources can be accurately estimated based on the nuclear data.

Table G-2. Normalized fuel composition data for the MMRTG, which were used to compute the energy spectra of the MMRTG neutrons. Only the major elements are shown.

Component	Weight % in PuO ₂
Oxygen and other impurities	13.054
²³⁸ Pu	74.587
²³⁹ Pu	10.322
²⁴⁰ Pu	1.8697
²⁴¹ Pu	0.1282
²⁴² Pu	0.0397

G.3.1 Neutrons from RTG

The spontaneous fission neutron spectrum is represented by a Maxwellian distribution:

$$N(E) \propto \text{sqrt}(E) \exp(-E/T) \quad (\text{Eq. G-1})$$

where E is the energy of emitted neutrons in MeV and T is the temperature of the nucleus when modeled as a Fermi gas. There are several different plutonium isotopes in the fuel, each having slightly different Fermi temperatures. Here, we used $T = 1.34$ MeV for ²³⁸Pu [15] because ²³⁸Pu is the main constituent of the MSL MMRTG PuO₂ fuel (> 85% of the total plutonium mass). Fig. G-10 shows the energy spectrum of the spontaneous neutrons obtained using (1 in terms of number of neutrons-per-second-per-gram of PuO₂ in the fuel).

Alpha particles from the decay of plutonium isotopes can also generate neutrons by undergoing (α ,n) reactions with impurities and any oxygen present in the fuel as long as the energies of the α particles are greater than the threshold energy of the reaction. The energies of α particles from the plutonium isotopes are in the 4–6 MeV range, so the reaction probability with high-Z materials would be small because of their higher Coulomb barrier height. Nuclear characteristics (half-lives, α particle energies, branching ratios, etc.) are readily found in the open literature (e.g., the Table of Isotopes; see <http://ie.lbl.gov/toi.html> for common plutonium isotopes (e.g., ²³⁸Pu, ²³⁹Pu, ²⁴⁰Pu, ²⁴¹Pu, ²⁴²Pu, etc.) in the fuel. In this α particle energy range, the ¹⁶O present in the PuO₂ fuel itself will be the main source of the (α ,n) reaction. The slowing-down and ionization of α particles within the fuel should be also included in the computation of reaction rates. All of these physical processes are modeled in the computer program SOURCES [16], and the neutron spectrum due to the (α ,n) reactions is computed by using this program. The spectrum is also shown in Fig. G-10 in terms of number of neutrons-per-second-per-gram of PuO₂ in the fuel. When integrated over the energy, about 67% of neutrons are from the (α ,n) reactions and the rest are from the spontaneous fission reactions. The neutron source strength reported here was computed based on the maximum neutron emission rate of ~6000 neutrons/(g-of-PuO₂ second) measured at Los Alamos National Laboratory (LANL).

Neutrons do not induce appreciable TID because of their neutral charge, but they can induce DDD. Fig. G-11 shows a contour plot of 1 year DDD levels for different locations around the MSL MMRTG. Note that the DDD levels are expressed in terms of 1 MeV neutron equivalent fluence.

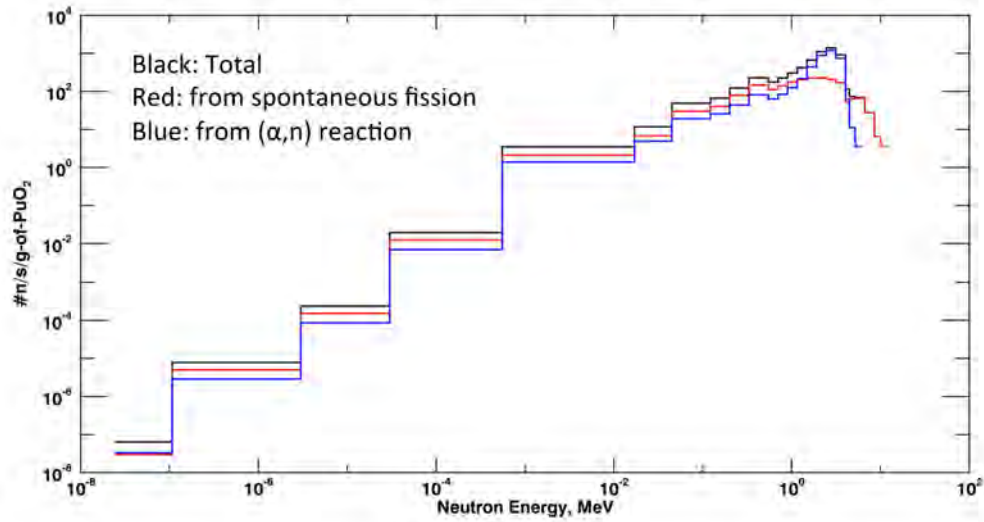


Fig. G-10. Energy spectra for spontaneous fission neutrons (red line) and neutrons from (α,n) reactions (blue line) in the fuel. The spectrum for total neutrons is shown with a black line. Spectra shown are in terms of the number of neutrons-per-second-per-g of PuO₂ in the fuel.

1 Year Fluence. The units are # of
1MeV neutrons/cm²

Neutron Displacement Damage, 25 cm grid

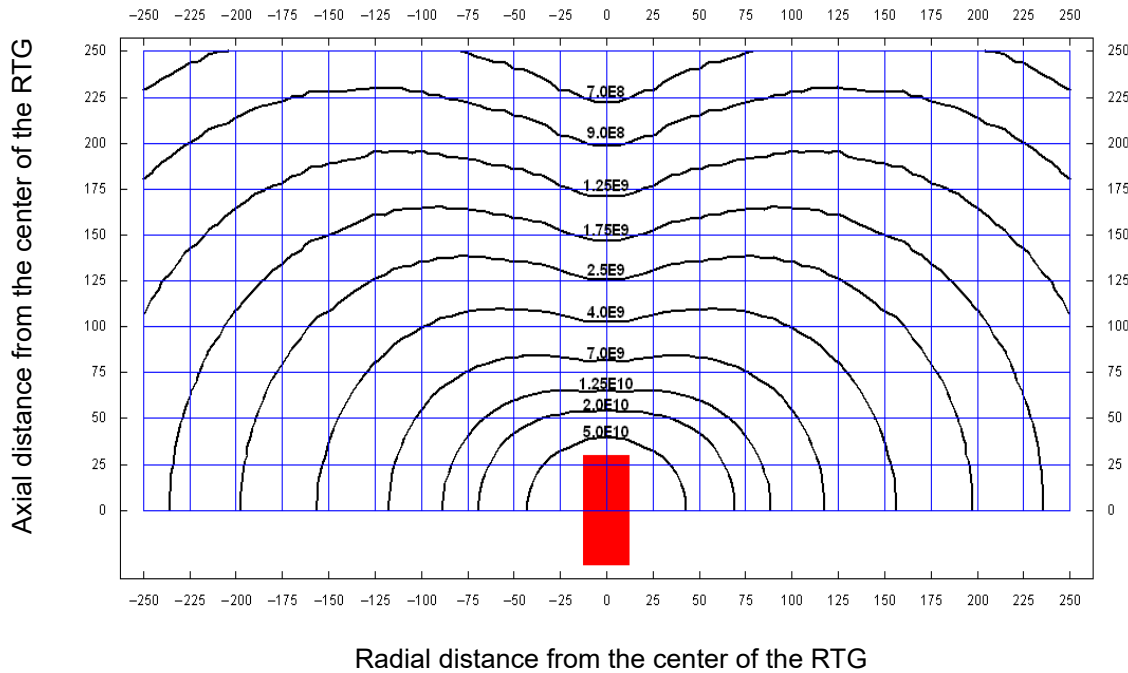


Fig. G-11. The DDD levels due to the MMRTG neutrons, expressed in terms of 1 MeV neutron fluence for 1 year. The red block in the bottom of the figure denotes the size of MMRTG.

G.3.2 *Gamma Rays from RTG*

Gamma rays are also emitted from an RTG. The physical processes responsible for the gamma ray emissions are radioactive decays, gammas from fissions, and gammas from (α ,n) reaction. All of these processes are included in the gamma ray source strength, and we assumed a 10 year old 2 kW (thermal) RTG. Table G-3 provides the gamma ray source spectrum, and Fig. G-12 illustrates a TID contour plot for the MSL MMRTG for 1 year.

Table G-3. Gamma ray source spectrum for a 10-year old 2 kW (thermal) MSL MMRTG.

Energy Bin		γ 's/(g-of-PuO ₂ second)
Low-side Energy Boundary, MeV	High-side Energy Boundary, MeV	
0.001	0.044	4.78×10^{10}
0.044	0.2	6.08×10^7
0.2	0.3	3.52×10^4
0.3	0.4	1.28×10^7
0.4	0.5	6.49×10^3
0.5	0.6	1.25×10^4
0.6	0.7	2.18×10^3
0.7	0.8	2.05×10^5
0.8	0.9	2.27×10^4
0.9	1.0	8.42×10^3
1.0	1.2	8.48×10^3
1.2	1.4	1.37×10^3
1.4	1.6	6.61×10^2
1.6	1.8	5.73×10^2
1.8	3.0	1.11×10^4
3.0	4.0	2.07×10^2
4.0	5.0	6.30×10^1
5.0	6.0	2.00×10^1
6.0	7.0	7.00

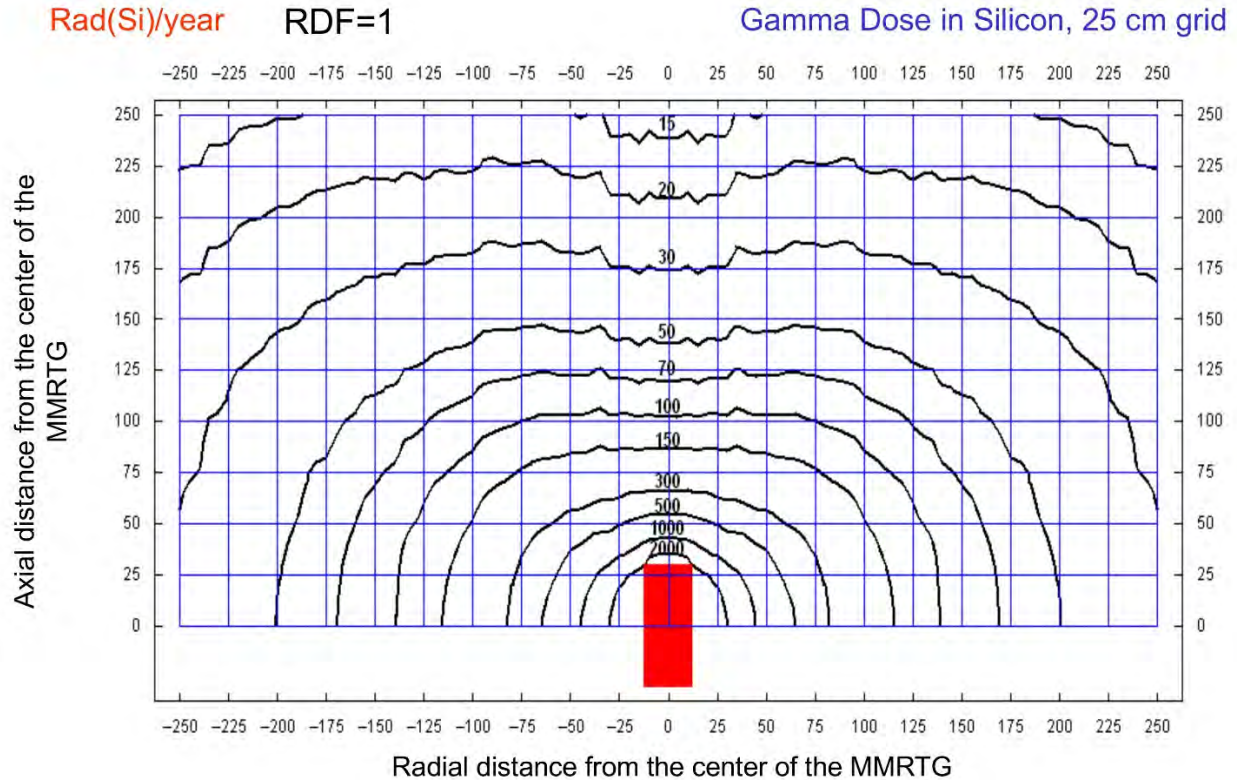


Fig. G-12. The TID levels due to the MMRTG gammas, expressed in terms of rad(Si) for 1 year. The red block in the bottom of the figure denotes the size of MMRTG.

G.4 Summary

The general characteristics of the radiation environment from natural origins and from RTGs were introduced in this section. The natural radiation environments are charged particles trapped in the planetary magnetic fields, solar energetic particles, and galactic cosmic rays. An RTG emits neutrons and gamma rays, which are neutral. We also note that the radiation environment specifications for actual mission(s) are dependent on: (1) the particular mission target, (2) trajectory, and (3) whether or not the mission uses onboard nuclear power sources. Thus, each mission should define the specific radiation environment using appropriate mission profiles and radiation environment models.

G.5 References

- [1] Sawyer, D.M. and J.I. Vette. 1976. "AP-8 trapped proton environment for solar maximum and solar minimum," NSSDC/WDC-A-R&S, 76-06, NASA/Goddard Space Flight Center, Greenbelt, MD.
- [2] Vette, J.I. 1991. "The AE-8 trapped electron model environment", NSSDC/WDC-A-R&S 91-24, NASA/Goddard Space Flight Center, Greenbelt, MD.
- [3] Garrett, H.B., I. Jun, J.M. Ratliff, R.W. Evans, G.A. Clough, and R.E. McEntire. 2003. Galileo Interim Radiation Electron Model, JPL Publication 03-006. Note that more recent GIRE models are available. For example, see H.B. Garrett to G. Arakaki, D. Brinza, and I. Jun, "Updating Jovian Radiation Environment Software Tool (GIRE3)," JPL IOM 5130-16-005, December 16, 2016.
- [4] Garrett, H.B., J.M. Ratliff, and R.W. Evans. October 2005. Saturn Radiation (SATRAD) Model, JPL Publication 05-9.
- [5] Garrett, H.B., R.W. Evans, and L. Martinez-Sierra, to M Boyles. September 29, 2015. "UMOD Radiation Model Description and Fortran Code," JPL Inter-Office Memorandum 5130-15-002.

- [6] Feynman, J., G. Spitale, and J. Wang. 1993. “Interplanetary proton fluence model: JPL 1991,” *J. of Geophys. Res.*, 98, pp. 13, 281–13, 294.
- [7] Feynman, J., A. Ruzmaikin, and V. Berdichevsky. 2002. “The JPL proton model: an update,” *Journal of Atmospheric and Solar-Terrestrial Physics*, 64 (A8), pp. 1679–1686.
- [8] Tylka, A. et al. 1997. “CREME96: A revision of the cosmic ray effects on micro-electronics code,” *IEEE Transactions on Nuclear Science*, Vol. 44, p. 2150.
- [9] Jokipii, J.R. 2010. “The heliosphere and cosmic rays,” Chapter 9 in *Heliophysics — Evolving Solar Activity and the Climates of Space and Earth* (C.J. Schrijver and G.L. Siscoe, eds.), Cambridge University Press, NY.
- [10] Masarik, J. and R.C. Reedy. 1996. “Gamma ray production and transport in Mars,” *Journal of Geophysical Research*, 101, 18891-18912.
- [11] McKinney, G.W., D.J. Lawrence, T.H. Prettyman, R.C. Elphic, W.C. Feldman, and J.J. Hagerty. 2006. “MCNPX benchmark for cosmic ray interactions with the Moon,” *Journal of Geophysical Research*, 111, E06004. doi:10.1029/2005JE002551.
- [12] O’Neill, P.M. 2010. “Badhwar–O’Neill 2010 galactic cosmic ray flux model—revised,” *IEEE Transactions on Nuclear Science*, 57, pp. 3148–3153.
- [13] Usoskin, I.G., K. Alanko-Huotari, G.A. Kovaltsov, and K. Mursula. 2005. “Heliospheric modulation of cosmic rays: Monthly reconstruction for 1951-2004,” *Journal of Geophysical Research*, 110, A12108. doi:10.1029/2005JA011250.
- [14] Mrigakshi, A.I., D. Matthia, T. Berger, G. Reitz, and R.F. Wimmer-Schweingruber. 2012. “Assessment of galactic cosmic ray models,” *Journal of Geophysical Research*, 117, A08109. doi:10.1029/2012JA017611.
- [15] Taherzadeh, T. 1972. Neutron radiation characteristics of plutonium dioxide fuel, Technical Report 32-1555, Jet Propulsion Laboratory, California Institute of Technology, Pasadena, CA.
- [16] Wilson, W.B., R.T. Perry, W.S. Charlton, T.A. Parish, G.P. Estes, T.H. Brown, E.D. Arthur, M. Bozoian, T.R. England, D.G. Madland, and J.E. Stewart. 1999. “SOURCES 4A: A code for calculating (α ,n), spontaneous fission, and delayed neutron sources and spectra,” LA-13639-MS, Los Alamos National Laboratory.

H Planetary Protection: Requirements, Compliance, and Considerations for Missions Integrating Next-Generation RTG Technologies

Brian Shirey

NASA Jet Propulsion Laboratory, 4800 Oak Grove Dr, Pasadena, CA 91109

H.1 Introduction

The primary aim of Planetary Protection (PP) is to protect planetary environments, and preserve the integrity of mission science by preventing contamination of a destination by spacecraft-borne organisms and materials originating upon the Earth (forward contamination), and to ensure the Earth's biosphere is protected from extraterrestrial materials (backward contamination) returned on NASA missions. NASA planetary protection policy is detailed in NASA Policy Directive NPD 8020.7G [1], and compliance guidelines and requirements are described in NASA Procedural Requirements NPR 8020.12D: Planetary Protection Provisions for Robotic Extraterrestrial Missions [2]. Compliance is administered by NASA's Planetary Protection Officer (PPO), who levies formal implementation requirements assigned to each NASA mission.

Each mission is assigned a planetary protection category according to 1) mission type (e.g., flyby, orbiter, lander), 2) target body (e.g. Mars, Europa, Jupiter), and 3) mission science objectives [2]. Requests for PP mission categorization are submitted to the PPO by the mission Project Manager, and must include a mission description identifying the target object and any other solar system bodies encountered by the spacecraft trajectory. The request must also include an overview of mission operations, and end-of-mission contingencies must be described. Upon review, the PPO will respond with written documentation detailing the appropriate PP categorization, along with any explanatory information or supplemental conditions deemed appropriate. In addition to mission categorization, the NASA PPO outlines specific PP requirements for each planned mission in accordance with NPR 8020.12D [2].

Increased PP requirements stringency is levied on missions that target planetary bodies with environments that are more likely to support life and on missions with science objectives centered on life detection and/or biosignature detection. These planetary bodies can include planets, moons, and other solar system bodies that may be important to understanding the processes of chemical evolution and/or the origin of life. For missions utilizing gravity assist by means of a flyby of another planet, PP requirements will typically reflect that of the planetary body encountered during the mission that is designated with the highest mission PP category. In some cases, missions targeting or encountering multiple planets, may be assigned more than one PP category. Further information regarding planetary protection mission categories are detailed in Tables H-1 and Table H-2 as adapted from NPR 8020.12D [2].

Table H-1. Mission Planetary Protection Categories. Based on the planetary protection priorities of each extraterrestrial solar system body and the mission plan. Mission PP category is determined by the NASA Planetary Protection Officer, upon request from the flight project.

Mission PP Category	Implementation Documentation
I	Documentation only
II	Documentation only
III	Impact avoidance and/or contamination control including: cleanroom assembly, microbial reduction, and trajectory biasing
IV	Impact avoidance and contamination control including: cleanroom assembly, microbial reduction, trajectory biasing, and organics archiving
V (Unrestricted)	As appropriate for the specified PP category of the outbound mission. No inbound PP requirements
V (Restricted)	Impact avoidance and contamination control including: cleanroom assembly, microbial containment of sampling chain of contact with target planet, sample containment and biohazard testing in receiving laboratory

Table H-2. Summary of Planetary Protection Implementation Requirements by Mission PP Category.

Planetary Target Priority	Mission Type	PP Category
Not of direct interest for understanding the process of chemical evolution or where exploration will not be jeopardized by terrestrial contamination. No protection of such planets is warranted, and no requirements are imposed	Any	I
Of significant interest relative to the process of chemical evolution, but only a remote chance that contamination by spacecraft could compromise future investigations	Any	II
Of significant interest relative to the process of chemical evolution and/or the origin of life and for which scientific opinion provides a significant chance that contamination by spacecraft could compromise future investigations.	Flyby, Orbiter	III
Of significant interest relative to the process of chemical evolution and/or the origin of life and for which scientific opinion provides a significant chance that contamination by spacecraft could compromise future investigations.	Lander, Probe	IV
Any solar system mission	All Earth return	V

With the exception of restricted sample return missions (Category V Restricted), the most stringent requirements to date have been levied on missions associated with Mars and icy planetary bodies. For these missions, implementation documentation and requirements can include:

- Planetary Protection Plan outlining intended or potential impact targets
- Planetary Protection Implementation Plan detailing the strategy to meet and maintain PP compliance through the mission
- Pre-Launch PP Report detailing the degree to which all PP requirements have been met including values of the microbial burden at launch and the organics inventory
- Post-Launch PP Report updating the Pre-Launch PP Report
- End-of-Mission Report providing a complete report of compliance including the final actual disposition of launched hardware
- Breakup and Burn-Up Report detailing the analysis for end-of-mission spacecraft disposition, which demonstrates that the spacecraft, or portions thereof, reach the required temperature and time required to meet bioburden sterilization upon atmospheric entry to planetary impact
- Landed spacecraft condition estimates
- Microbial reduction plan and verification of microbial bioburden
- Impact probability calculations

Detailed PP documentation requirements are outlined in NPR 8020.12D [2].

H.1.1 *PP Considerations for Planetary Targets*

Planetary Protection requirements for small solar system bodies (e.g., comets, asteroids, small Kuiper-Belt objects, and others) may not warrant forward contamination controls and will be determined on a case-by-case basis. These missions are likely to be categorized as I or II, as there is little to no chance that contamination could compromise current or future science objectives. Six questions have been posed when evaluating the stringency of PP requirements necessary for exploring small solar system bodies:

1. Was there ever liquid water in or on the target body?
2. Are/were metabolically useful energy sources ever present?
3. Is/was organic material and reducing material present in sufficient amounts to support life?
4. Has the target body remained below the temperature of presumptive biological sterilization subsequent to the disappearance of liquid water?

5. Has the target body been exposed to sufficient radiation for presumptive biological sterilization?
6. Is there any natural influx to Earth for the transport of material equivalent to a sample return?

Missions to icy satellites require particularly strict attention to contamination risks. Three bodies in particular (Europa, Enceladus, and Triton) may present special PP concerns and require increased scrutiny. Per NPR 8020.12D, PP requirements for flybys, orbiters, and landers to icy satellites shall be applied which reduce the probability of inadvertent contamination of an ocean or other liquid water body. This probability of contaminating a putative icy moon ocean with a single viable terrestrial organism was, as of this writing, defined as less than 10^{-4} , and includes conservative estimates of poorly known parameters. It is anticipated that any landed mission to an icy moon will be expected to address the following factors at minimum:

- Bioburden reduction plans and calculations of spacecraft bioburden
- Cruise stage survival for contaminating organisms
- Organism survival after exposure to radiation from adjacent targets
- Nominal/non-nominal landing probabilities
- Probability of an organism surviving target impact
- Transport mechanisms for delivering organisms to the surface
- Organism survival before, during, and after transfer to the subsurface
- Sample return missions to Europa or Enceladus are expected to be Category V (Restricted) missions

H.1.2 *Special Region Designation and Possible Implications for Future Missions*

A Special Region is currently defined as a region within which terrestrial organisms are likely to replicate; namely, regions with environmental parameter thresholds associated with water activity and temperature. Currently, the Special Region designation is applied only to Mars missions; however, the parameters discussed are particularly relevant to any mission that targets an icy satellite or planetary bodies with possible hydrothermal and/or geothermal activity. Granting access to Special Regions, whether on Mars or other planetary bodies with comparable environmental conditions, will require increased PP precautions. Some of the parameters that define Special Regions include [2]:

- Upper and lower limits for water activity (0.5 and 1.0 aw, respectively)
- Lower temperature limit of -25°C , no upper limit defined
- Gullies and streaks possibly associated with liquid water
- Subsurface below 5 meters
- Possible geothermal sites
- Areas with hydrothermal activity

In addition, and particularly pertinent to missions employing RTG technology, the potential for creating spacecraft-induced Special Regions must also be addressed and evaluated.

H.1.3 *General PP Plan and Implementation Approach*

A NASA project's Planetary Protection Plan (PPP) documents the approach taken by project personnel to ensure PP requirements are met. Depending on mission categorization, implementation requirements can range from no documentation required (Category I, to architecting a detailed PP strategy, which can include hardware sampling, bioburden reduction and accounting, cleaning, archiving, documenting, and recontamination prevention (Category IV). The implementation strategy is captured in the Planetary Protection Implementation Plan (PPIP, which describes the overall strategy, methods,

materials, and analyses required to meet PP requirements and maintain compliance throughout the mission. The standard approach for PP implementation for Category IV missions include:

1. Microbial bioburden reduction via heat microbial reduction (HMR), isopropanol cleaning, or vaporized hydrogen peroxide (VHP)
2. Identification of spacecraft surfaces exempt from accountable bioburden requirements due to isolation behind HEPA filters or separated from the planetary surface behind two or more enclosures
3. Cleanroom assembly
4. Identification of key inspection points for cleaning and bioassay sampling
5. Spacecraft hardware and ground support equipment (GSE) sampling and bioburden verification through bioassay
6. Recontamination prevention strategy

The Planetary Protection implementation approach can be tailored to individual hardware. An appropriate implementation strategy must consider implementation feasibility, process flow, hardware assembly and integration details, and surface accessibility. Hardware compatibility with PP implementation processes must be considered in the early stages of hardware design as well. Hardware should be compatible with surface cleaning with isopropanol alcohol and compatibility with minimum HMR requirements must be addressed early in the mission. Other requirements dictate hardware transport and that assembly requirements (such as assembly shall be performed in an ISO-8 (or better cleanroom environment; however, in the case of RTG development and manufacturing, safety precautions may necessitate requests for deviations from the implementation plan.

Heat microbial reduction is the standard PP microbial reduction modality. HMR can be especially useful on hardware with large surface areas, those which are difficult to clean, difficult to access, and on surfaces with nonmetallic materials such as insulations, composite materials, and electronic components. The minimum temperature for HMR bakeouts is 110°C. In practice, the standard HMR employed to reach a 4-log reduction in microbial bioburden is 112°C ± 2°C for 132.18 hours for exposed spacecraft surface hardware. Encapsulated (nonmetallic and bulk materials surfaces require longer heat treatment. Microbial reduction credit can also be taken for curing processes, which can occur during manufacturing of nonmetallic materials if the time/temperature meet minimum HMR values. In addition, if operational temperatures of a particular hardware component or subsystem exceed minimum HMR values, credit can be applied for those processes as well. For hardware that is not compatible with HMR, microbial reduction by isopropanol cleaning the surface can be utilized. Alcohol cleaning must be followed by bioassay to verify bioburden density. VHP is also an approved microbial reduction modality that can be employed on heat sensitive hardware, but hardware compatibility considerations for VHP must be addressed as well. The tables below provide examples of HMR time/temperature requirements administered by JPL PP engineers for the current Mars missions. These values were revised to include a 25% margin as a requirement for these missions.

Table H-3. Standard heat microbial reduction (HMR) tables for exposed (A), and encapsulated (B) spacecraft surfaces.

(A)	Temperature (°C)	Time (hr)		
		3-log	4-log	6-log
	112	15.6	132.2	-
	125	3.8	88.6	-
	150	0.3	8.1	24.3
	200	0.01	0.07	0.2

(B)	Temperature (°C)	Time (hr)		
		3-log	4-log	6-log
	116	-	582.6	-
	125	-	442.9	-
	150	1.2	40.4	121.3
	200	0.01	0.3	1.0

A non-standard heating approach may satisfy HMR requirements for RTG hardware and will be evaluated on a case-by-case basis. This approach may take advantage of the heat produced during normal RTG operations, which may meet or exceed the minimum requirements. Among other tests as determined by the mission PP requirements, an evaluation of both hot-side and cold-side surface temperatures should be performed. Currently, JPL is implementing a heritage approach by using spare Mars Science Laboratory (MSL) MMRTG units on the Mars 2020 rover. Due to the high temperatures generated by the MMRTG unit (in excess of 150°C), the unit will be considered “self-sterilizing” with the exception of the fins and the mounting structure. In many instances, radiation modeling will be key to determining which hardware receives a sufficient dose of radiation to satisfy microbial reduction requirements, and to identify which RTG components will need HMR or other approved reduction modalities to meet PP compliance requirements.

H.1.4 *Other PP Considerations for Missions Employing Radioisotope Power Systems*

Radioisotope power systems (RPS that include RTGs require some special considerations when developing a Planetary Protection compliance strategy. With regard to Special Regions, there are several possible mechanisms by which these regions could become contaminated during a mission. Current NASA PP requirements dictate that if the probability of a non-nominal landing in a special region is greater than 0.01, then the entire landed system shall be sterilized to a verified 4-log reduction from the original Category IVa surface cleanliness requirement. The current strategy for preserving Special Regions on Mars; however, is to impose landing site restrictions, which includes prohibiting access to locations with ice or hydrated minerals at depths of less than 5 meters for which exposure to an RTG could cause liquid to be sufficiently liberated to mobilize a particle of less than 50 nm in length.

Landing site restrictions mitigate some risks associated with delivering an RTG onto Special Regions during an off-nominal landing event; however, other mechanisms can impact Special Region considerations as well. Unlike off-nominal landing or impact scenarios, Special Region implications do not always require physical contact between the RTG and the planetary surface. Spacecraft-induced Special Regions can result in the formation of transient Special Regions where surface ice is melted from RTG heating during normal operations. Another consideration is whether the temperature gradient from RTG to unheated surfaces is sufficient to create induced Special Regions on the rover surface through air condensation. The absence of transient or spacecraft-induced special regions must be demonstrated through test and analysis.

H.2 Summary

The goal of Planetary Protection is to preserve planetary environments and mission science through a careful yet rigorous approach to contamination prevention. As Next-Generation RTG concepts are developed, the PP Engineer will provide key insights into PP procedures and requirements, and promote early and active dialog to relay this information to all groups involved with the project. Throughout the early planning stages of Next-Generation RTG development, the PP Engineer will also gain valuable insight on proposed RTG materials, design features, hardware coatings, and environmental parameters. This insight will allow the project team to take a proactive approach to address potential questions early in project development.

H.3 References

- [1] NASA. February 19, 1999. Biological Contamination Control for Outbound and Inbound Planetary Spacecraft, NPD 8020.7G, Revalidated November 25, 2008.
- [2] NASA. April 20, 2011. Planetary Protection Provisions for Robotic Extraterrestrial Missions, NPR 8020.12D, Rev. D.

H.4 Acronyms

GSE	Ground Support Equipment
HMR	Heat Microbial Reduction
MMRTG	Multi-Mission Radioisotope Thermoelectric Generator
MSL	Mars Science Laboratory
NPD	NASA Policy Directive
NPR	NASA Procedural Requirement
PP	Planetary Protection
PPO	Planetary Protection Officer
PPP	Planetary Protection Plan
RPS	Radioisotopic Power System
RTG	Radioisotope Thermoelectric Generator
VHP	Vaporized Hydrogen Peroxide

I Micrometeoroids

John Martin Ratliff

NASA Jet Propulsion Laboratory, 4800 Oak Grove Dr., Pasadena, CA 91109

Meteoroid flux approaches a spacecraft from more than one direction, the flux is distributed in angle. Ergo, shielding solutions will need to be applied to all sides of the radioisotope thermoelectric generator (RTG). The exact magnitude and the size and velocity distributions of the flux are a function of location in the solar system. Proximity to a planet modifies this further, with the planet's physical presence blocking meteoroids from certain directions, while a planet's gravity accelerates others to higher impact speeds. The increased spacecraft speed of an orbiter results in even higher relative speeds.

A given mission's exposure will vary according to where a spacecraft's trajectory takes it, and how much time it spends there. The RTG's placement in the flight system will also affect the need for dedicated shielding. Therefore, generalizations about the required amount of shielding are not possible.

However, as with other spacecraft hardware, RTGs will need to be sufficiently protected against meteoroid impacts, and sufficiency will be dependent upon some key factors:

1. Is the RTG a sealed vessel that must remain sealed?
2. Is any cover gas in the RTG evacuated in flight?
3. Will the RTG be transported to its destination in a larger vessel such as an aeroshell or entry body that will be jettisoned upon atmospheric entry?

Nothing in designs to-date of RTGs has been inherently at odds with typical methods of protecting hardware from meteoroid-induced impact damage. However, the answers to the questions above have a strong effect on the level of protection that must be added directly to an RTG or surrounding an RTG. The body of the RTG can be made less vulnerable to impact by employing a typical double-walled design (with a gap between the two walls, sometimes called a Whipple shield or Whipple bumper, which is more effective at stopping meteoroids than a single wall of the same mass. This or similar protection would be needed if the answer to number one is "yes."

An RTG that is evacuated in flight will have less need for protection than a sealed vessel but will still likely require either a protective shield provided by the spacecraft or the RTG provider. The purpose of this shield is to protect the electrical circuit elements exposed to a micrometeoroid environment or protected by too thin of a housing.

RTGs inside of aerobodies, as were the cases for the Viking lander missions and the Mars Science Laboratory, need no additional shielding, per se, as the aeroshells provided the protection. A heavier structure may be needed for gas-filled RTGs, where achieving the desired survival probability includes maintaining the pressure envelope.

J Launch Vehicles and Mission Analyses

Alan Didion, Damon Landau

NASA Jet Propulsion Laboratory, 4800 Oak Grove Drive, Pasadena, CA, 91109

J.1 Introduction

To better understand the mission requirements to be placed on a Next-Generation Radioisotope Thermoelectric Generator (RTG) power system, the upper limits of flight system mass for various mission concepts were examined. This appendix details the methodology for determining limits on flight system mass, time of flight (TOF), and launch year as functions of target body, launch vehicle, and mission architecture given the state of current and near-future launch and propulsion technology. To span the space properly, the utility of planetary gravity assists were quantified, and assumptions applied to spacecraft performance values (e.g., specific impulse, entry system mass fraction).

J.2 Methodology and Tools

Traditional mission design entails detailed construction and analysis of a specific trajectory. The broad nature of this investigation calls for a comprehensive search of a wide trajectory tradespace at lower fidelity. The mass delivery capabilities of the current and near-future range of launch vehicles are characterized for the full gambit of solar system destinations and various transfer options. A patched conic method is used to accurately represent two-body mechanics and facilitate rapid tradespace generation. This kinematic method neglects third body effects and solar radiation pressure in favor of orders of magnitude improvement in computational speed over dynamical methods, while precluding low-thrust trajectories. Trajectories designed with this method can be further optimized through use of dynamical n-body modeling.

J.2.1 *Broad Trajectory Search Tool: Star*

Star is a trajectory broad-search tool developed at JPL to search for impulsive trajectory solutions for interplanetary space missions; it runs in MATLAB. Star uses patched conics to generate large numbers of trajectory families in a short time period, allowing for broad and agile exploration of a mission design tradespace in the early formulation stage. Star allows the investigator to model gravity-assist flybys, deep-space maneuvers (DSMs), and small body destinations, but does not model low-thrust trajectories. Workflow in the tool consists of defining allowable launch years, flyby/destination bodies, and DSM timing/magnitudes, as well as placing filtering constraints on total mission ΔV and launch characteristic energy (C3). Star returns large numbers of trajectories that satisfy the constraints, displayed in a scatter-plot format (see Fig. J-1). The user is then able to assess the tradespace and select specific options for further investigation. The output data is then converted from ΔV to delivered mass given a set of performance assumptions, producing the results found in Sections J.4 and J.5. For more information regarding the Star tool itself, please contact the authors.

J.2.2 *Data Filtering and Post-Processing*

Star provides kinematic trajectory solutions, i.e., position and velocity time series that meet the basic constraints defined by the user. From these series, candidates that do not meet the desired performance (e.g., mission ΔV , TOF, C3) are filtered out. From these solutions, one can determine the total delivered mass that a specific launch vehicle and flyby sequence can deliver to a target body through the rocket equation and a set of spacecraft performance assumptions, discussed in Section J.3.

J.3 Assumptions

This section collects the assumptions that were made throughout this investigation, including those affecting the trajectories, the spacecraft, and the celestial bodies of the solar system.

J.3.1 *Broad Trajectory Search Constraints*

The tradespace of interest for this investigation is defined by the bounds detailed in Table J-1. The launch date range is specifically chosen to investigate missions relevant to the decadal survey, which

would presumably enter into preliminary investigation soon after the time of writing. Boundaries like TOF and mission ΔV reflect reasonable expectations from current and near-future spacecraft equipment, assuming another few years of operation at the target body after reaching the destination.

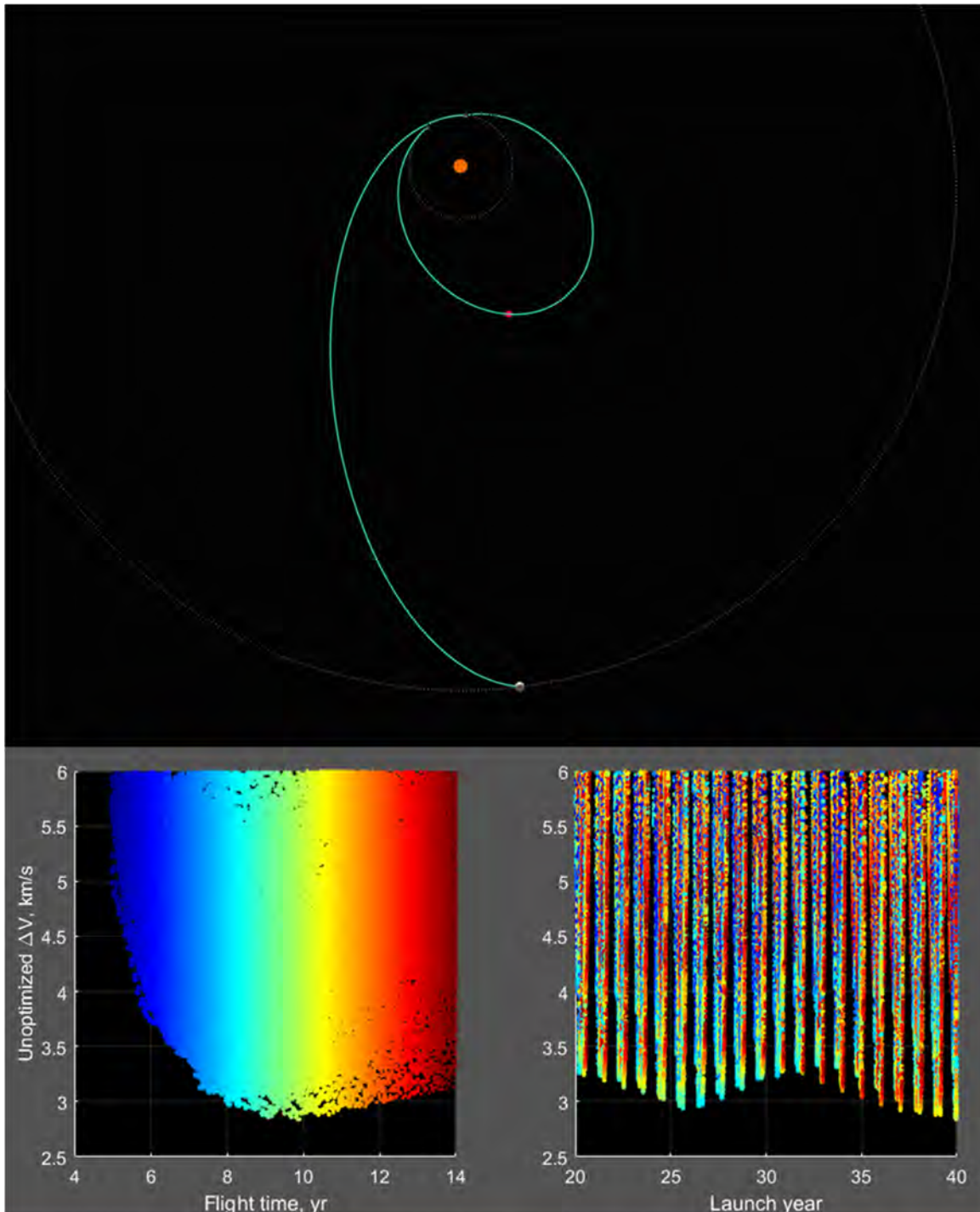


Fig. J-1. Example output plot of the Star tool: includes scatter plots of mission delta-V vs. time of flight as well as vs. launch year (color-coded by time of flight). Each data point is a solution, and selecting one displays the trajectory plot for that specific solution. Shown here is an Earth–Earth–Jupiter (EEJ) trajectory, which makes use of an Earth gravity assist and a DSM to arrive at Jupiter. A final insertion maneuver at Jupiter closes the orbit.

Table J-1. Broad trajectory search constraints.

Parameter	Value	Unit
Launch Date	2020-2040	[yr CE]
Time of Flight	< 14	[yr]
Time of Flight (NEAs)	< 6	[yr]
Mission ΔV	< 6	[km/s]

J.3.2 *Solar System Data Sources, Launch Vehicle Performance*

All of the source data used in this investigation is publicly available. The solar system body data used by Star and the subsequent postprocessing operations is all sourced from the NASA JPL Solar Systems dynamics database and HORIZONS system [1], including physical body characteristics such as mass, gravity, and radii as well as ephemerides.

The Atlas V (551) launch vehicle performance data used in the delivered mass postprocessing operation is sourced from the NASA Launch Services Program’s launch vehicle performance website [2]. Space Launch System (SLS) performance data was sourced from recent literature [3]. A plot of the raw performance data can be found in Section J.6.

J.3.3 *Assumed Performance Parameters*

The hypothetical spacecraft travelling along each trajectory, and subsequently undertaking whatever injection, landing, or atmospheric entry behavior, was assumed to exhibit a common set of performance characteristics, detailed below in Table J-2. These are based on typical modern spacecraft equipment performance values derived from historical actuals.

Table J-2. Assumed spacecraft performance.

Table Head	Table Column Head		
	Parameter	Value	Unit
ISP	Specific Impulse	300	[s]
ma	Aeroshell Mass Fraction	0.5	N/A

J.3.4 *Simple Calculations*

For speed, calculating parameters such as wet mass fraction for a landing vehicle was done using the rocket equation and various ‘rule of thumb’ ΔV values to deorbit and land. Capturing into orbit is defined as slowing from a hyperbolic to a parabolic trajectory. Landing on a body without an atmosphere requires the spacecraft to propulsively capture and then slow to zero velocity and cancel gravity losses, while landing on a body with an atmosphere assumes that the entry system constitutes 50% of the mass delivered to a flyby, and no propulsion is assumed. No assumptions are made on the mass fraction of landing systems (legs, rover wheels, mechanical structure). The mass delivered to orbit/flyby/landing is the entire mass of the spacecraft.

In this investigation, transfers to inner planets are direct transfers from an Earth launch. Trajectories to Jupiter are Δ VEGA transfers, i.e., one Earth gravity-assist (EGA) and one DSM. Trajectories to planets beyond Jupiter use a Δ VEGA transfer to a Jupiter gravity-assist (JGA). Near-Earth asteroid (NEA) destinations are reached via direct transfers from Earth, and must arrive in <6 yr. These transfer sequences were chosen to be representative of the overall tradespace, but are not exhaustive.

J.3.5 *Historical Masses*

For context, Table J-3 details the delivered masses of various heritage missions. These masses are included to add an intuitive element to the results, i.e., results can be mapped to Cassini-class, Juno-class, or New Horizons-class.

Table J-3. Historical spacecraft dry masses.

Spacecraft	Value	Unit
Cassini	2,523	[kg]
Galileo	2,380	[kg]
Juno	1,593	[kg]
New Horizons	401	[kg]

J.4 Results

The results of this investigation are plotted as delivered mass to a given target for a given launch vehicle, for a given architectural option (flyby, orbit, land). This section displays select results with discussion of the implications. The final results are compiled into “maps” (see Section J.5).

J.4.1 Quantification of the Utility of Gravity Assists for Outer Planetary Destinations

One of the primary goals of this investigation is to quantify the utility of gravity-assist trajectories as opposed to direct transfers. The most pronounced effect can be seen through use of a JGA. As seen in the following figures, use of a JGA can nearly triple the delivered mass of a Uranus-bound orbiter, but is subject to a launch window of only a few years, while direct launches can be had during an approximately annual window.

In Fig. J-2, the lower and upper dotted lines represent the delivered masses of Juno and Cassini respectively. This demonstrates that use of a JGA en route to Uranus can mean the difference between a Juno- and Cassini-class delivered mass. However, note in Fig. J-3 how the mass delivered to flyby is nearly equal for two launch windows rather than the one pronounced window of Fig. J-2. This is due to the spacecraft arriving at Jupiter with high relative velocity for that family of trajectories, which does not affect the flyby mass, but which heavily penalizes an orbiter architecture that must slow down and capture.

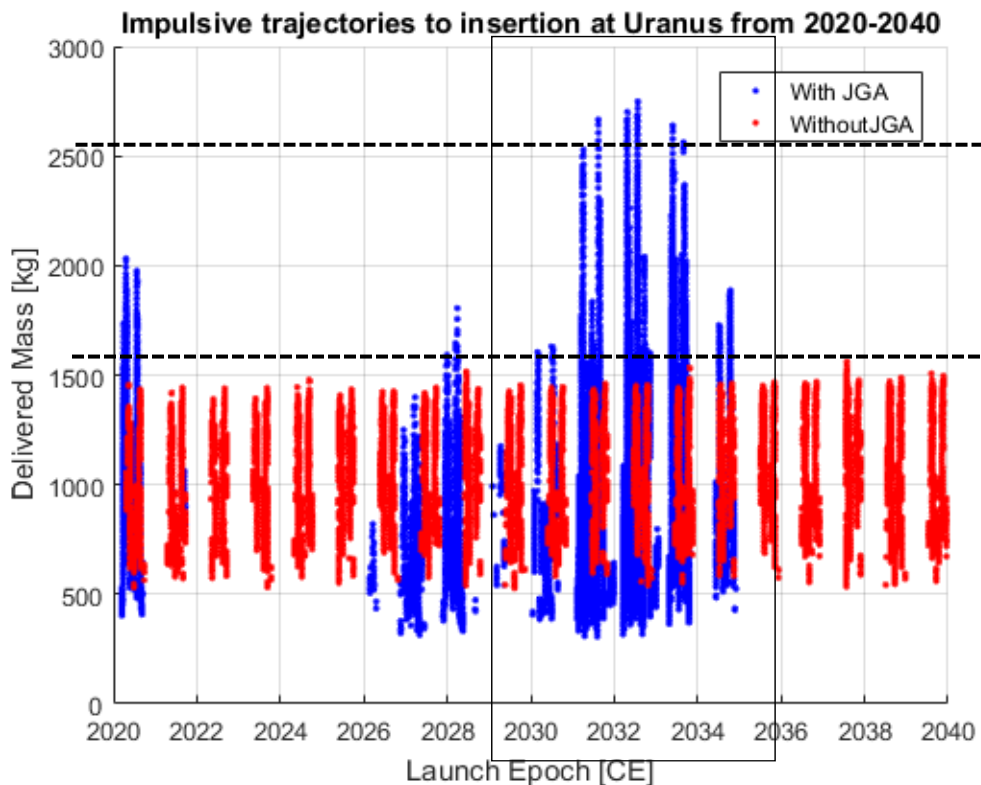


Fig. J-2. Mass delivered to orbit insertion at Uranus, as launched on an Atlas V (551, with and without a JGA).

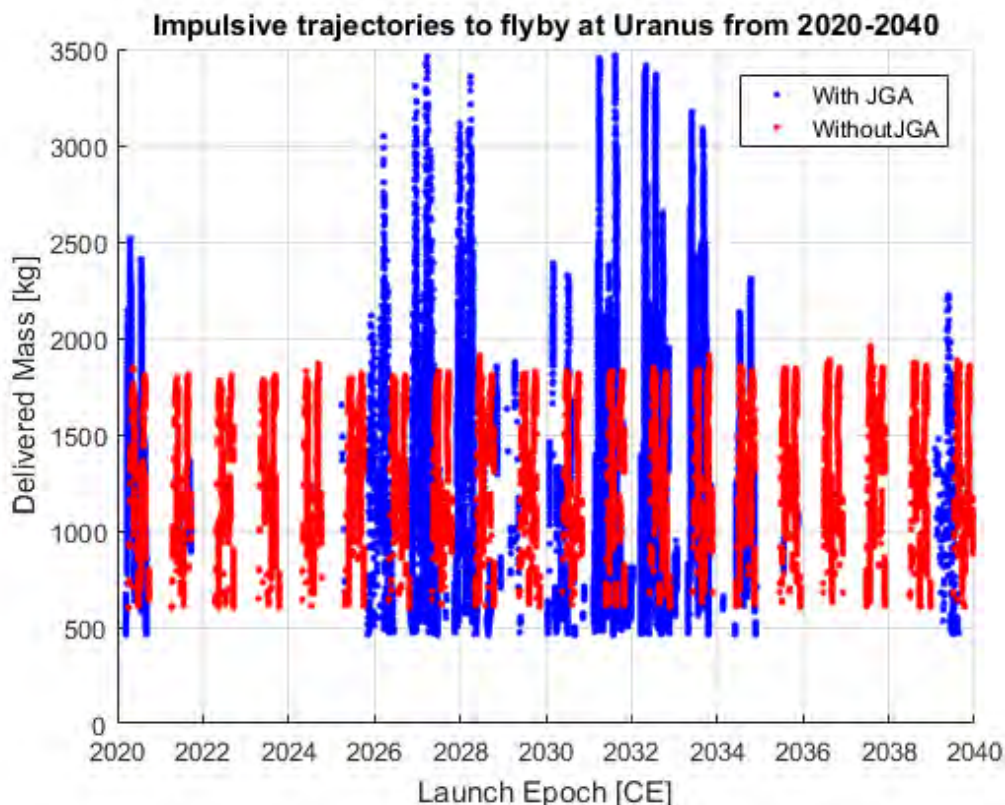


Fig. J-3. Mass delivered to a flyby at Uranus, as launched on an Atlas V (551), with and without a JGA.

A similar window can be seen in the case of a Saturn gravity assist (SGA). In Fig. J-4, the dotted line represents the delivered mass of Juno, and it is evident that an SGA can be favorable, but is subject to a less frequent launch window. Saturn's orbital period is approximately 30 years, compared to Jupiter's period of approximately 12 years; also note that alignment must be made with Uranus, whose orbital period is nearly 165 yrs. The SGA does not boost the delivered mass quite as much as a JGA because Saturn is only 30% as massive as Jupiter. Further, Saturn flyby parameters are constrained by Saturn's rings, giving it a much larger effective radius than Jupiter.

J.4.2 *Masses Delivered to Outer Planets*

This section contains similar figures (Figs. J-5 through J-10 for the mass delivered to each outer planetary destination flyby and orbit, with and without a JGA, launched on an Atlas V (551). Delivered mass for the SLS Block 1 was on average 4 times in magnitude. These results can be seen on the mass maps in Section J.5.

In Fig. J-8, one can see that the Atlas V (551) can easily deliver a Voyager or New Horizons-type spacecraft to Pluto flyby, but only through use of a JGA. Also, the launch window is fairly short, and will be separated by more than 12 years, as Jupiter revolves to align with Pluto, whose orbital period is nearly 250 years. Note that New Frontiers did indeed use a JGA to assist it in reaching its Pluto-flyby trajectory. New Frontiers launched in 2006, which was two launch opportunities prior to the one shown in this figure.

No trajectory solutions were found within these constraints to enable a Pluto orbiter (or lander, as either the TOF is prohibitively long, or the propulsive cost of orbit capture is prohibitively high. In order to understand what a Pluto orbiter would require, the constraints were relaxed in order to find solutions. Fig. J-9 shows these solutions with respect to the original 'reasonable constraints' of the original investigation.

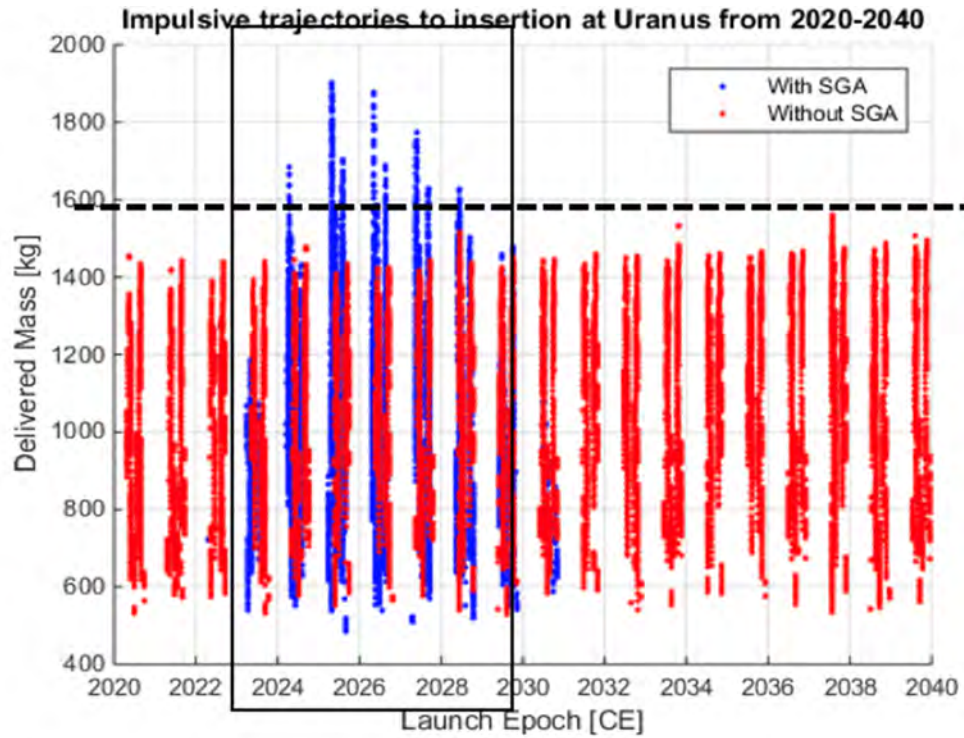


Fig. J-4. Mass delivered to orbit insertion at Uranus, as launched on an Atlas V (551), with and without a JGA. Mass delivered to a orbit insertion at Uranus, as launched on an Atlas V (551), with and without an SGA. Note that the red (without SGA) band is the same band seen in Fig. J-2.

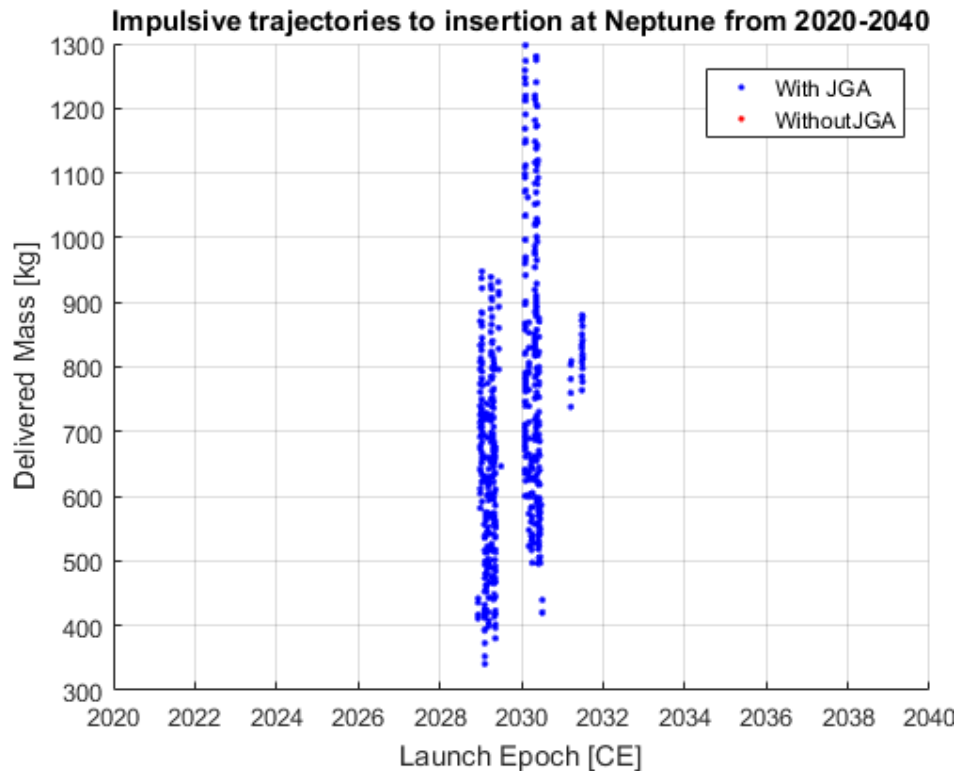


Fig. J-5. Mass delivered to an orbit insertion at Neptune, as launched on an Atlas V (551), with and without a JGA. Note that no solutions were found without use of a JGA.

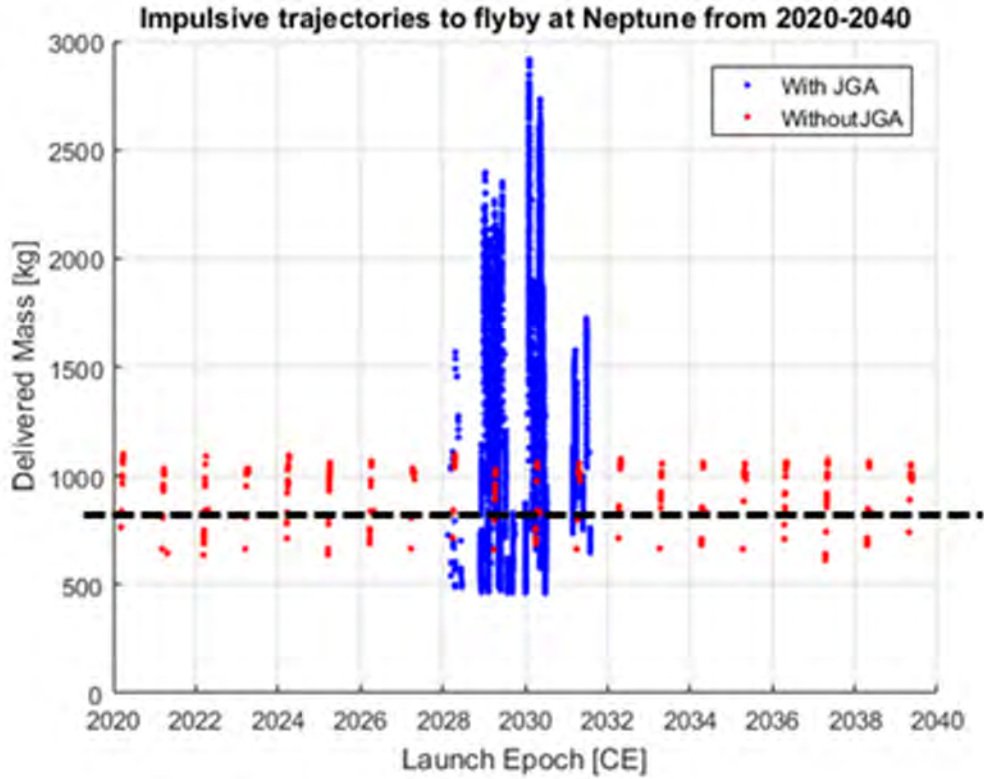


Fig. J-6. Mass delivered to a flyby at Neptune as launched on an Atlas V (551), with and without a JGA. The dotted line represents the mass of either Voyager probe.

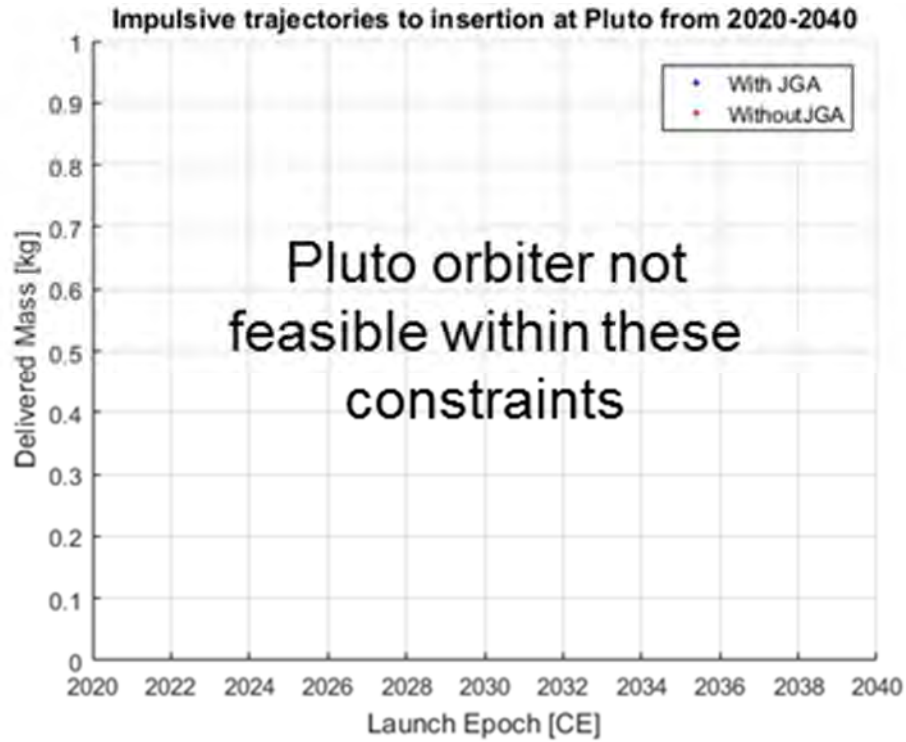


Fig. J-7. Mass delivered to orbit insertion at Pluto as launched on an Atlas V (551, with and without a JGA. No valid solutions were found for either an Atlas V (551 or an SLS).

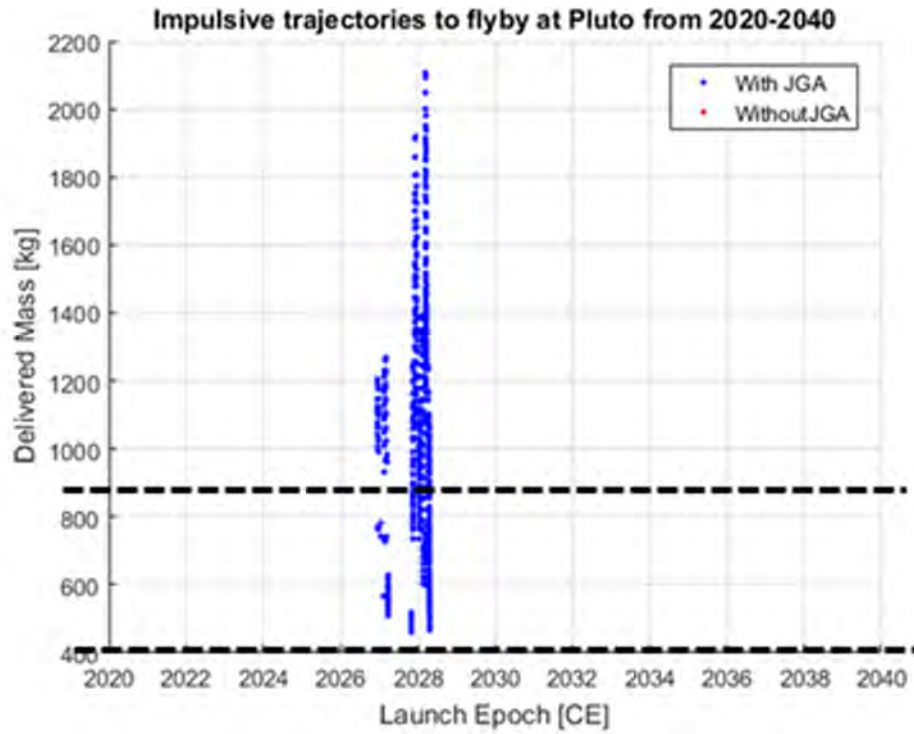


Fig. J-8. Mass delivered to flyby of Pluto as launched on an Atlas V (551), with and without a JGA. No valid solutions were found without use of a JGA within these constraints. The upper and lower dotted lines represent the masses Voyager and New Horizons, respectively.

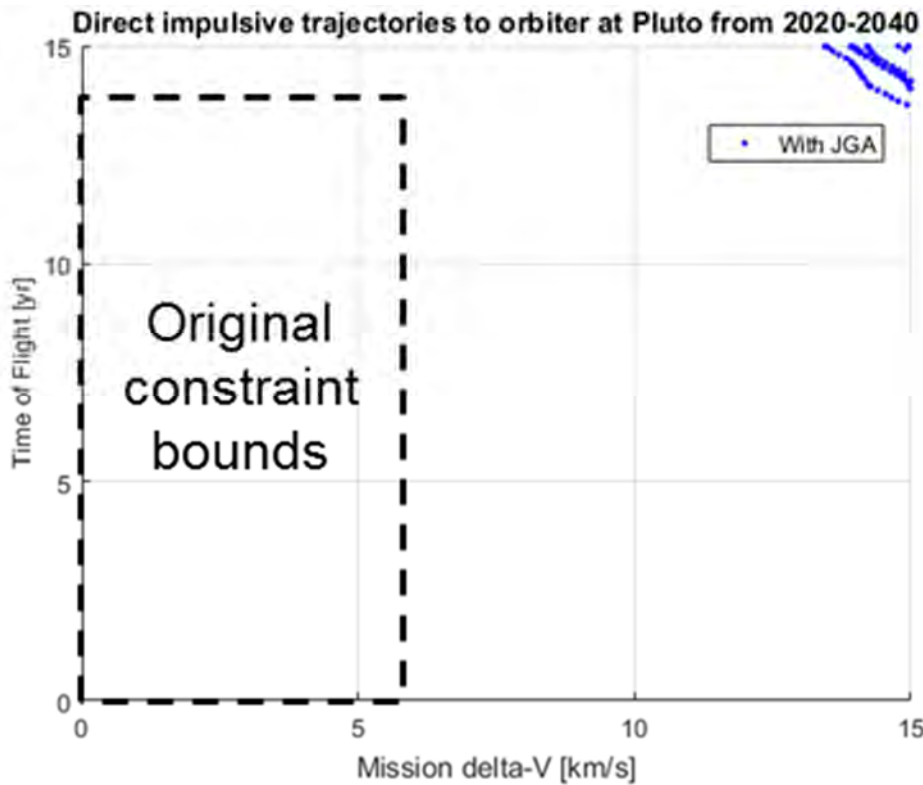


Fig. J-9. In order to find viable Pluto orbiter candidates, constraints were relaxed heavily. In this plot, note the dotted box representing the bounds of the original study and the solutions in a regime of high ΔV and TOF.

J.4.3 Trajectories to Small Bodies

An additional investigation was conducted to examine candidate trajectories to NEAs, in which case the spacecraft would launch from Earth and transfer directly to any given NEA. Figure J-10 shows a scatter of maximum delivered masses to NEAs for an Atlas V (551).

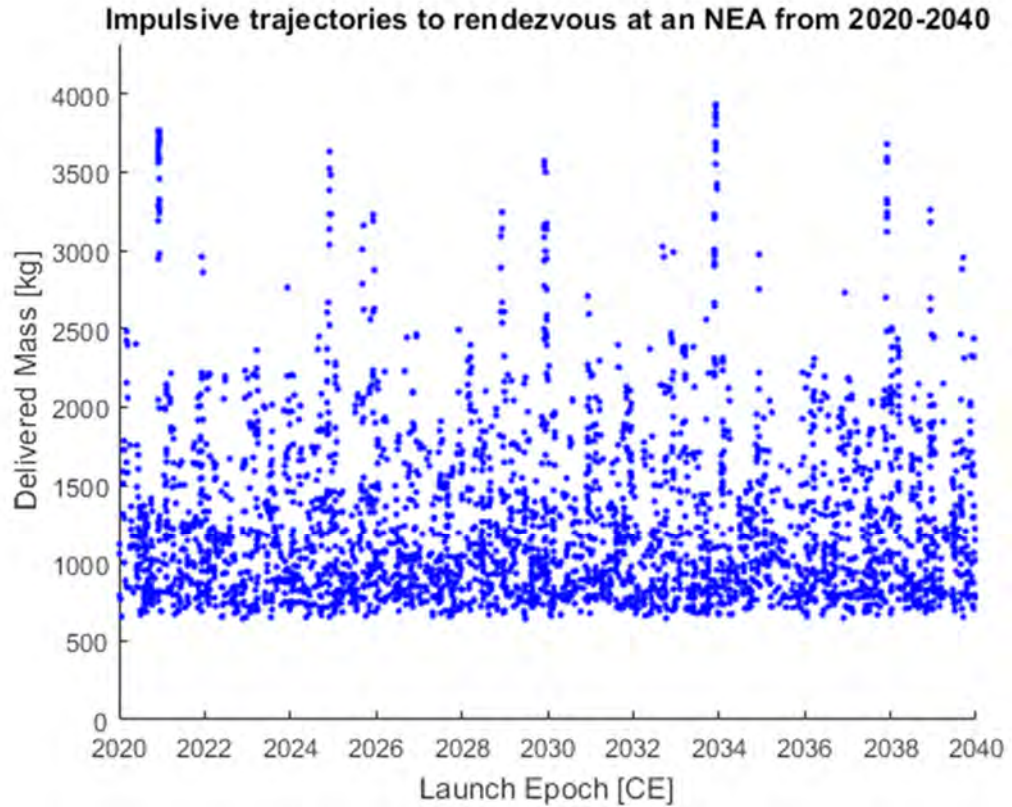


Fig. J-10. Mass delivered to rendezvous at any given NEA, as launched on an Atlas V (551).

Additionally, direct impulsive trajectories to Ceres orbit insertion were examined, with results plotted in Fig. J-11. Note the very pronounced windows and sparsity of trajectory solutions. Ceres has an orbital period of 4.6 years and low mass, making it expensive for a spacecraft to propulsively insert into orbit around it.

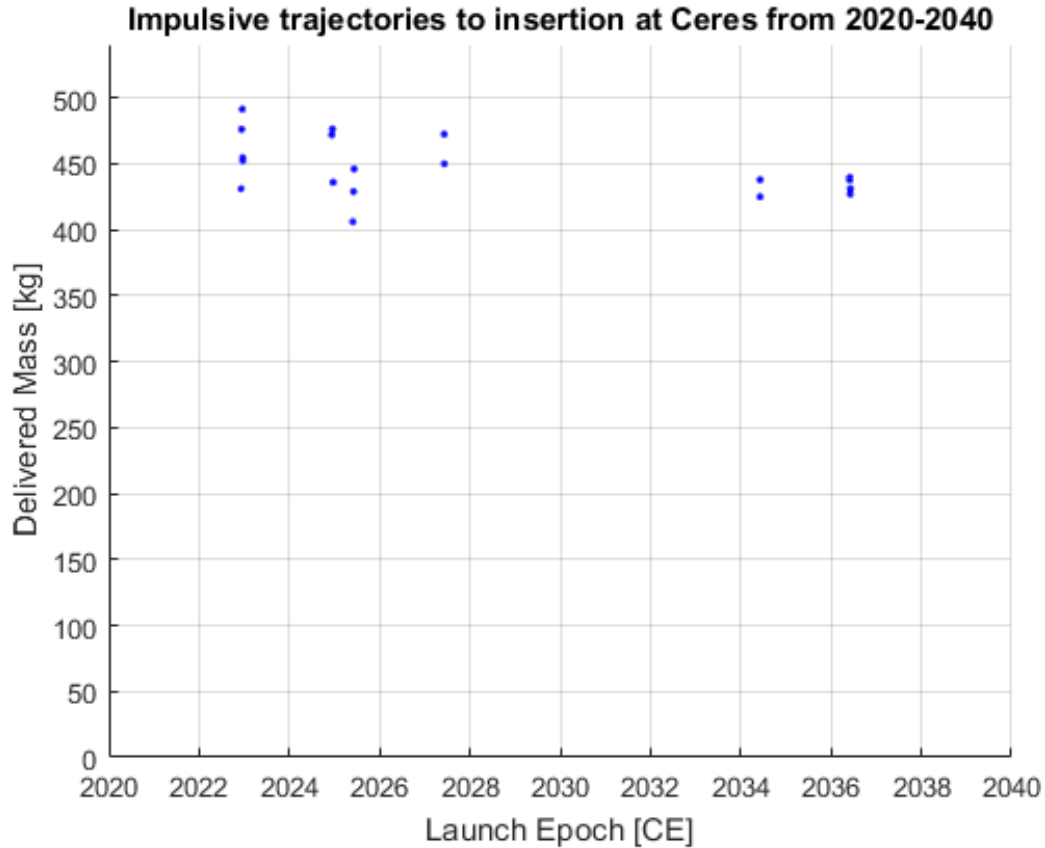


Fig. J-11. Mass delivered to orbit insertion at Ceres, as launched on an Atlas V (551).

J.4.4 *Masses Delivered per Architectural Makeup*

Using the methods defined in Section J.2, applying the constraints and assumptions defined in Section J.3, and collecting the results, of which a subset has been presented here in Section J.4, “maps” can be made to display the amount of mass that can be delivered to each solar system body. The maps display the maximum amount of mass that a mission planner can expect to be able to deliver to each target if launched between 2020 and 2040 on an Atlas V (551) and SLS Block 1, respectively. Bars are grouped and color-coded, showing the mass differences between each architecture type, i.e., flyby, orbiting, landed. Also included is a set of launch vehicle mass allocation vs. C3 curves. Note that the Falcon Heavy and Delta IV Heavy fall between the Atlas V (551) and SLS Block 1, so the extremes were used for mass mapping. Results are presented in Figures J-12 and J-13.

J.5 Conclusions

This investigation produced visual representations of the delivered mass capability of current and near-future launch and propulsion technology to a wide range of solar system destinations and architectural options. These results are intended to inform Next-Generation RTG requirement investigations of the order of magnitude of spacecraft mass that is reasonably available for a given mission architecture.

Within the assumptions and constraints of this investigation, several key findings were made:

1. The NASA SLS can greatly increase the delivered mass to several destinations over the current high-performance vehicles, and can enable such architectures as a Mercury lander or heavy lift to Mars.

2. Making use of a JGA can decrease mission ΔV by up to 75% in some cases, and can enable architectures such as a Neptune orbiter or Pluto flyby probe. SGAs are significantly less beneficial, and are subject to much shorter and sparser launch windows.
3. The highest-mass combination of an SLS with a JGA does not enable all architectures (e.g., Pluto orbiter) with near-term technology; see Figures J-8 and J-9.

J.5.1 *Methods for Improvement*

Only a few gravity-assist bodies were considered in this investigation. When designing a specific trajectory, one can trade TOF for delivered mass by employing additional gravity-assist flybys, but this investigation can itself have a multidimensional tradespace within just one of the cases of this broad exploration.

This investigation does not consider electric propulsion (EP) trajectories. Low-thrust trajectories require dynamical integration methods, which require orders of magnitude more computational effort than patched-conic Lambert solving, so they were neglected for the sake of speed given the broad nature of this problem. RTG-powered SEP has little heritage and typically requires massive power systems and long flight times. However, such a spacecraft may be capable of achieving Pluto orbit [4]. The use of solar EP (SEP) for inner solar system gravity assists prior to crossing the orbit of Jupiter could boost the mass delivered to outer planets in return for TOF penalties. Including EP options would widen the tradespace, and new options could become available.

The trajectory solutions provided by the Star output are not optimized. The only form of optimization done in this investigation is by the user selecting the maximum of interest from the scatter distributions, typically after filtering the data for TOF and launch constraints and choosing the highest possible delivered mass. Optimization may increase these maxima, but due to the density of the distribution, the improvement is expected to be minor. Further, the optimization would have to be run again for each change of objective and constraints, which is not the case with the current methodology of filtering a large data set spanning the tradespace.

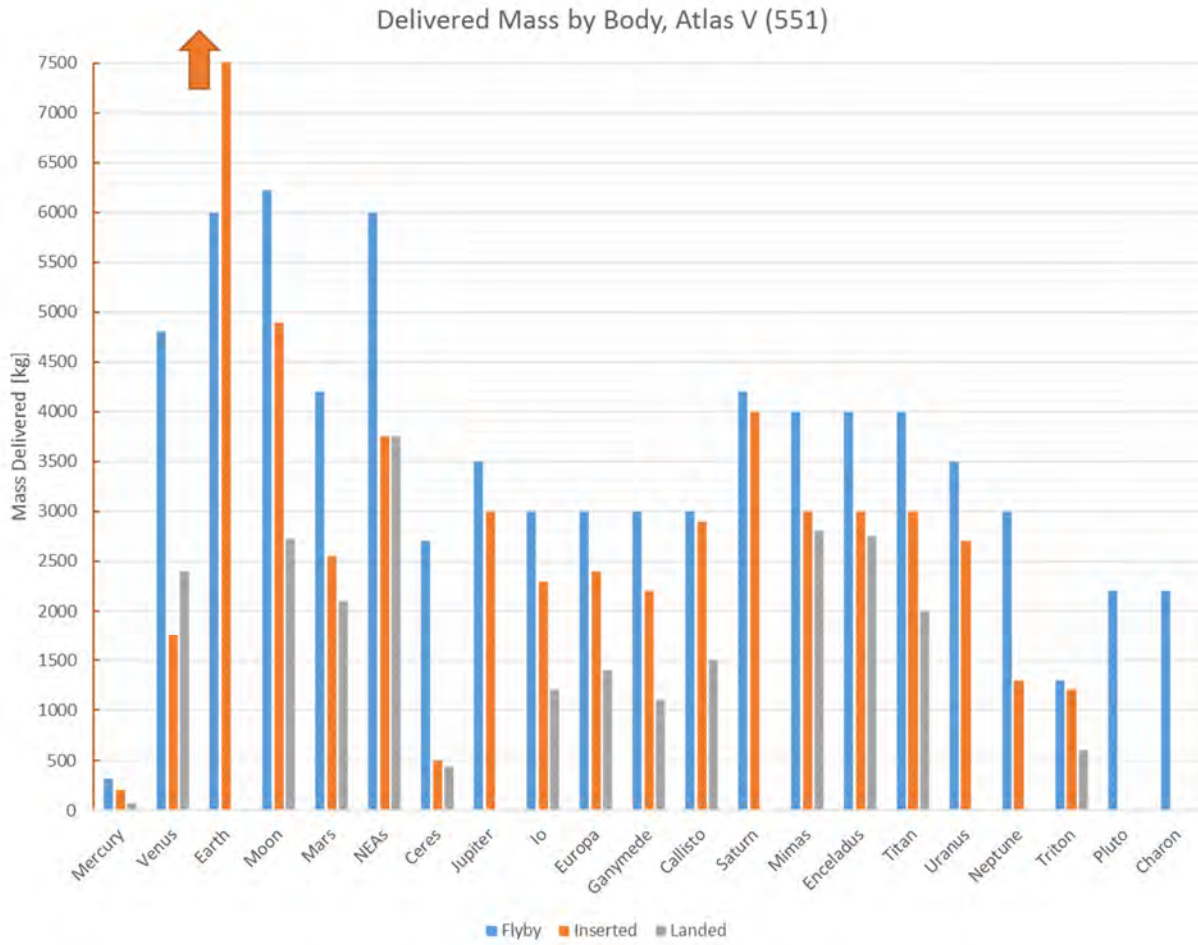


Fig. J-12. Delivered mass (kg) as mapped to each solar system destination, by mission architecture, for the Atlas V (551) launch vehicle. LEO mass is 17,855 kg.

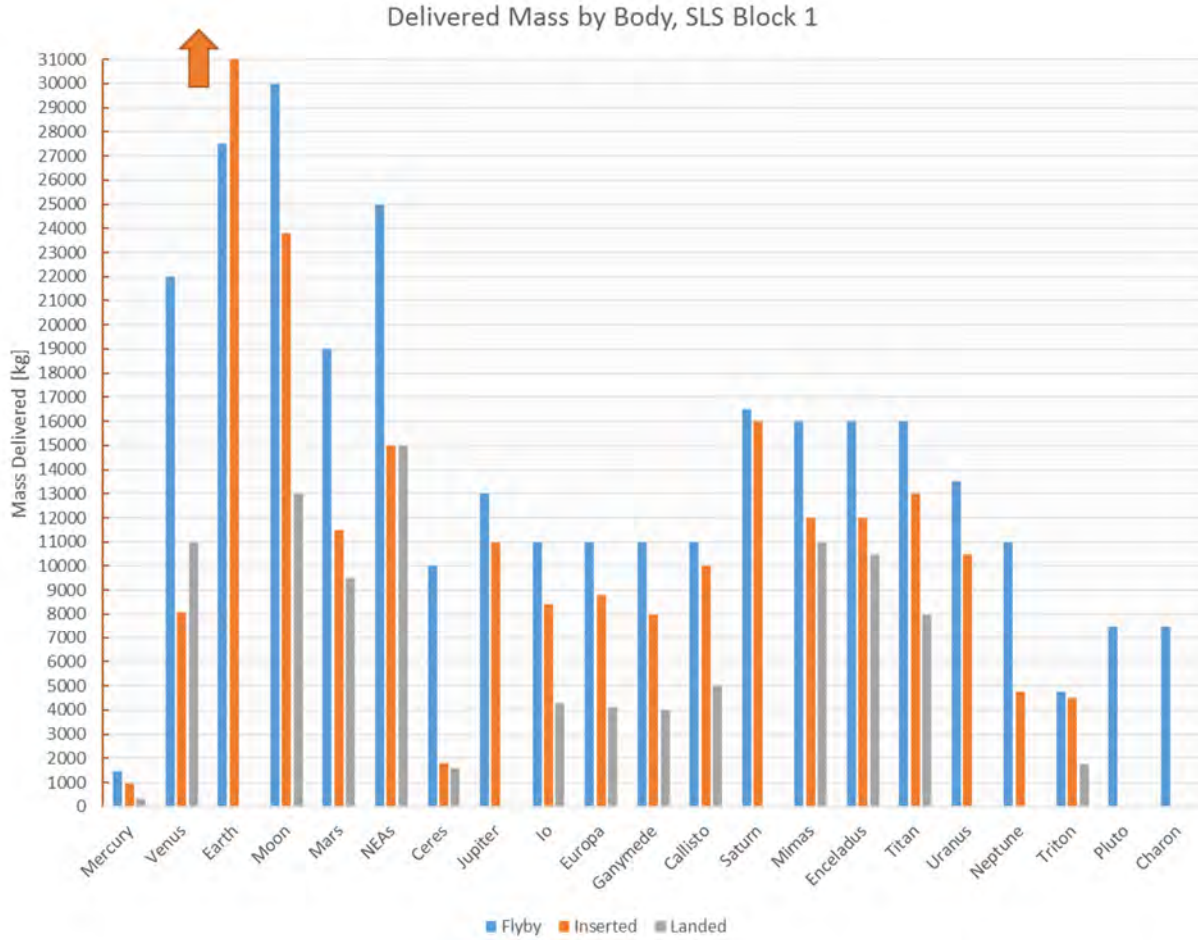


Fig. J-13. Delivered mass [kg] as mapped to each solar system destination, by mission architecture, for the SLS Block 1 launch vehicle. LEO mass is 81,500 kg.

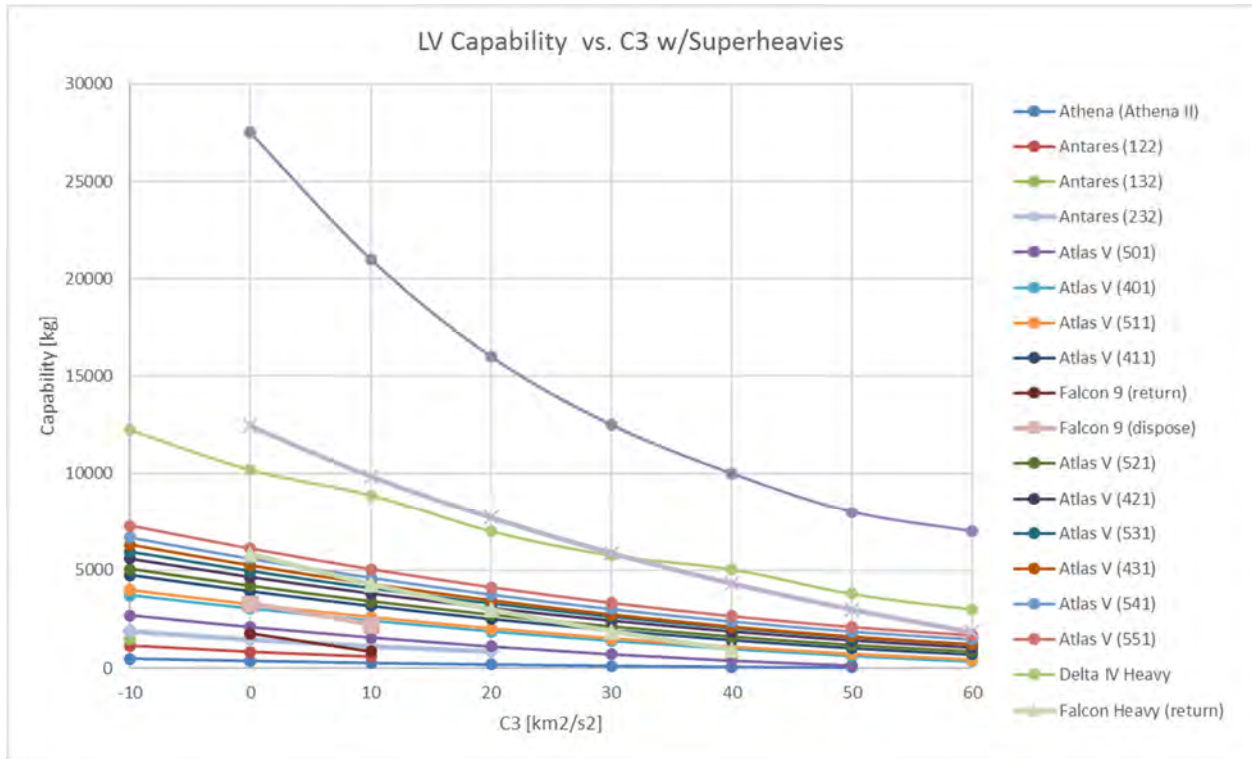


Fig. J-14. Raw launch vehicle capability (kg) vs. launch C3 (km^2/s^2).

J.6 References

- [1] NASA Jet Propulsion Laboratory. 2016. “Solar System Dynamics,” web site, accessed Aug. 18, 2016. <https://ssd.jpl.nasa.gov/>.
- [2] NASA Launch Services Program. 2016. “Launch Vehicle Performance,” web site, accessed Aug. 18, 2016. <https://elvperf.ksc.nasa.gov/Pages/Query.aspx>.
- [3] Donahue, B. and D. Sauvegeau. 2016. “The Space Launch System Capabilities for Beyond Earth Missions,” web site, Aug 18, 2016. <http://www.spacepropulsion.org/uploads/2/5/3/9/25392309/spaceaccess2014-25.pdf>.
- [4] Arora, N., A. Petropoulos, and J. Elliott. 2016. “Mission Design Trades for a Near Term Pluto Orbiter,” *American Astronomical Society*, AAS 16–535.

K Thermoelectric Technology Risk Assessment Details

Dr. Chadwick Barklay

University of Dayton research Institute, 300 College Park, Dayton, Ohio 45469-0172

Dr. Jean-Pierre Fleurial and Dr. Terry Hendricks

NASA Jet Propulsion Laboratory, 4800 Oak Grove Dr., Pasadena, CA 91109

K.1 Thermoelectric Materials Considered

Table K-1. n-Type thermoelectric materials.

Thermoelectric Material	Material System	ZT _{max}	Max Operating Temp. (K)	TRL	Country	Year	Reference
(Hf,Zr)NiSn	n-half heusler	1.2	875	3	USA, China	2014	Chen, S. and Ren, Z., "Recent progress of half-Heusler for moderate temperature thermoelectric applications", <i>Materials Today</i> , Vol. 16, 10 (2013), Pages 387–395
(Pb _{0.95} Sn _{0.05} Te) _{0.92} (PbS) _{0.08}	PbTe-based nanocomposite	1.5	642	2	USA	2007	J. Androulakis, C.H. Lin, H.J. Kong, C. Uher, C.I. Wu, T. Hogan, et al., Spinodal decomposition and nucleation and growth as a means to bulk nanostructured thermoelectrics: enhanced performance in Pb _{1-x} Sn _x Te–PbS, <i>Journal of the American Chemical Society</i> , 129 (2007), pp. 9780–9788
Ag _{0.53} Pb ₁₈ Sb _{1.2} Te ₂₀	PbTe-based nanocomposite	1.7	700	2	USA	2009	B.A. Cook, M.J. Kramer, J.L. Harringa, M.K. Han, D.Y. Chung, M.G. Kanatzidis, Analysis of nanostructuring in high figure-of-merit Ag(1-x)Pb(m)SbTe(2+m) thermoelectric materials, <i>Advanced Functional Materials</i> , 19 (2009), pp. 1254–1259
Ag _{0.8} Pb _{22.5} SbTe ₂₀	PbTe-based nanocomposite	1.5	700	2	China/Japan	2008	M. Zhou, J. Li, T. Kita, Nanostructured AgPbmSbTem+2 system bulk materials with enhanced thermoelectric performance, <i>Journal of the American Chemical Society</i> , 130 (2008), pp. 4527–4532
AgPb ₁₈ SbTe ₂₀	PbTe-based nanocomposite	2.2	800	1	USA	2004	K.F. Hsu, S. Loo, F. Guo, W. Chen, J.S. Dyck, C. Uher, et al., Cubic AgPbmSbTe _{2+m} : bulk thermoelectric materials with high figure of merit, <i>Science (New York, NY)</i> , 303 (2004), pp. 818–821
Ba _{0.08} La _{0.05} Yb _{0.04} Co ₄ Sb ₁₂	Skutterudite - CoSb ₃	1.2	850	2.5	China/USA	2011	X. Shi, J. Yang, J.R. Salvador, M. Chi, J.Y. Cho, H. Wang, et al., Multiple-filled skutterudites: High thermoelectric figure of merit through separately optimizing electrical and thermal transports, <i>Journal of the American Chemical Society</i> , 133 (2011), pp. 7837–7846
Ba _{0.14} In _{0.23} Co ₄ Sb _{11.84}	Skutterudite - CoSb ₃	1.34	850	2.5	China	2009	W. Zhao, P. Wei, Q. Zhang, C. Dong, L. Liu, X. Tang, Enhanced thermoelectric performance in barium and indium double-filled skutterudite bulk materials via orbital hybridization induced by indium filler, <i>Journal of the American Chemical Society</i> , 131 (2009), pp. 3713–3720.
Bi ₂ Te _{2.7} Se _{0.3}	Bi ₂ Te ₃ -based nanocomposite	1.04	498	1	USA	2010	X. Yan, B. Poudel, Y. Ma, W.S. Liu, G. Joshi, H. Wang, et al., Experimental studies on anisotropic thermoelectric properties and structures of n-Type Bi(2)Te(2.7)Se(0.3), <i>Nano Letters</i> , 10 (2010), pp. 3373–3378

Thermoelectric Material	Material System	ZT _{max}	Max Operating Temp. (K)	TRL	Country	Year	Reference
Bi ₂ Te ₃	Bi ₂ Te ₃ -based nanocomposite	1	450	2	China	2009	X.B. Zhao, S.H. Yang, Y.Q. Cao, J.L. Mi, Q. Zhang, T.J. Zhu, Synthesis of nanocomposites with improved thermoelectric properties, <i>Journal of Electronic Materials</i> , 38 (2009), pp. 1017–1024
Bi ₂ Te ₃ /Bi ₂ Te _{2.83} Se _{0.17}	2D Material: quantum well/superlattice	1.4	300	3	USA	2001	R. Venkatasubramanian, E. Siivola, T. Colpitts, B. O'Quinn, Thin-film thermoelectric devices with high room-temperature figures of merit, <i>Nature</i> , 413 (2001), pp. 597–602
Bi-Te JPL	Bismuth Antimony Telluride	0.9	500	4	USA		JPL measured; materials synthesized at JPL; similar to TESI and Hi-Z materials
CoSb _{2.75} Sn _{0.05} Te _{0.20}	Skutterudite - CoSb ₃	1.1	823	2.5	China	2008	W.S. Liu, B.P. Zhang, L.D. Zhao, J.F. Li, Improvement of thermoelectric performance of CoSb(3-x)Te(x) skutterudite compounds by additional substitution of IVB-group elements for Sb, <i>Chemistry of Materials</i> , 20 (2008), pp. 7526–7531
In _{0.25} Co ₄ Sb ₁₂	Skutterudite - CoSb ₃	1.2	575	2	USA	2006	T. He, J. Chen, H.D. Rosenfeld, M.A. Subramanian, Thermoelectric properties of indium-filled skutterudites, <i>Chemistry of Materials</i> , 18 (2006), pp. 759–762
In _{0.2} Ce _{0.15} Co ₄ Sb ₁₂	Skutterudite - CoSb ₃	1.4	625	2	USA	2011	K. Biswas, M. Good, K. Roberts, M. Subramanian, T. Hendricks, "Thermoelectric and Structural Properties of High-Performance In-Based Skutterudites for High-Temperature Energy Recovery", <i>Journal of Materials Research</i> , 26, Issue 15 (2011), pp 1827-1835.
In _{0.2} Co ₄ Sb ₁₂	Skutterudite - CoSb ₃	1.2	625	2	USA	2011	K. Biswas, M. Good, K. Roberts, M. Subramanian, T. Hendricks, "Thermoelectric and Structural Properties of High-Performance In-Based Skutterudites for High-Temperature Energy Recovery", <i>Journal of Materials Research</i> , 26, Issue 15 (2011), pp 1827-1835.
In ₄ Se _{3-x} Cl _{0.03}	In ₄ Se ₃	1.53	698	2	Korea	2011	J.S. Rhyee, K. Ahn, K.H. Lee, H.S. Ji, J.-H. Shim, Enhancement of the thermoelectric figure-of-merit in a wide temperature range in In ₄ Se _{3-x} Cl _{0.03} bulk crystals, <i>Advanced Materials</i> , 23 (2011), pp. 2191–2194
In ₄ Se _{3-δ}	In ₄ Se ₃	1.48	705	1	Korea	2009	J.S. Rhyee, K.H. Lee, S.M. Lee, E. Cho, S.I. Kim, E. Lee, et al., Peierls distortion as a route to high thermoelectric performance in In ₄ Se _{3-δ} crystals, <i>Nature</i> , 459 (2009), pp. 965–968
K _{0.95} Pb ₂₀ Sb _{1.2} Te ₂₂	PbTe-based nanocomposite	1.6	750	2.5	USA	2010	P.F.P. Poudeu, A. Gueguen, C.-I. Wu, T. Hogan, M.G. Kanatzidis, High figure of merit in nanostructured n-type KPb(m)SbTe(m+2) thermoelectric materials, <i>Chemistry of Materials</i> , 22 (2010), pp. 1046–1053
LaTe _{1.46} ***	Lanthanum Chalcogenide	1.17	1273	3.5	USA	2013	T. Caillat, S. Firdosy, B. Li, C. Huang, V. Ravi, N. Keyawa, H. Anjunyan, J. Paik, D. Uhl, J. Chase, L. Lara, J. Fleurial. Progress Status Of The Development Of High-Efficiency Segmented Thermoelectric Couples. 11th International Energy Conversion Engineering Conference, " (2013). DOI 10.2514/6.2013-3928
LaTe _{1.46} +Ni composite ***	Lanthanum Chalcogenide	1.33	1273	3	USA	2016	J. Ma, S. Bux, J. Fleurial, V. Ravi, S. Firdosy, K. Star, R. Kaner, "High Performance High Temperature Thermoelectric Composites With Metallic Inclusions", Patent application: 20160111619, April 21, 2016.

Thermoelectric Material	Material System	ZT _{max}	Max Operating Temp. (K)	TRL	Country	Year	Reference
Mg _{2.20} Si _{0.49} Sn _{0.5} Sb _{0.01}	n-silicide	1.2	800	3	Wuhan, China/USA	2011, 2014	W. Liu, X. Tang, H. Li, J. Sharp, X. Zhou, and C. Uher, Optimized Thermoelectric Properties of Sb-Doped Mg ₂ (1+z)Si _{0.5} -ySn _{0.5} Sb _y through Adjustment of the Mg Content, Chem. Mater., 2011, 23 (23), pp 5256–5263.
Mg ₂ Si	n-silicide	0.8	873	2	Japan/China	2011, 2012	T. Nemoto, T. Iida, J. Sato, T. Sakamoto, T. Nakajima, Y. Takanashi, Power Generation Characteristics of MgSi Uni-Leg Thermoelectric Generator, Journal of Electronic Materials . Jun2012, Vol. 41 Issue 6, p1312-1316.
Na _{0.48} Co ₄ Sb ₁₂	Skutterudite - CoSb ₃	1.25	850	2.5	USA, China	2009	Y.Z. Pei, J. Yang, L.D. Chen, W. Zhang, J.R. Salvador, J.H. Yang, Improving thermoelectric performance of caged compounds through light-element filling, Applied Physics Letters, 95 (2009), p. 042101
n-PbTe (MMRTG) ****	PbTe	0.99	825	9	USA	1996	D.M. Rowe, "Preparation of improved PbSnTe thermoelectric alloys and evaluation of their figure of merit. Final technical report, 1986-1987, AD-A-191346, United States Army, 1987.
n-Si ₇₈ Ge ₂₂ (RTG) ***/****	SiGe	0.94	1300	9	USA	1990	MHW-RTG and GPHS-RTG; DOE/JPL/Industry measured
n-Si ₈₀ Ge ₂₀	SiGe-based nanocomposites	1.25	1073	2	France	2012	A. Kallel, G. Roux, T. Derycke, C. L. Martin, M. Marinova, C. Cayron, Microstructure and thermoelectric properties of bulk and porous n-type silicon-germanium alloy prepared by HUP, AIP Conf. Proc. 1449, 409 (2012); 10.1063/1.4731583
n-Si ₈₀ Ge ₂₀ (nano MIT/JPL)	SiGe-based nanocomposites	1.3	1273	2.5	USA	2008	X.W. Wang, H. Lee, Y.C. Lan, G.H. Zhu, G. Joshi, D.Z. Wang, et al., Enhanced thermoelectric figure of merit in nanostructured n-type silicon germanium bulk alloy, Applied Physics Letters, 93 (2008), p. 193121
Pb _{9.6} Sb _{0.2} Te ₃ Se ₇	PbTe-based nanocomposite	1.2	650	1	USA	2006	P.F.P. Poudeu, J. D'Angelo, H. Kong, A. Downey, J.L. Short, R. Pcionek, et al., Nanostructures versus solid solutions: low lattice thermal conductivity and enhanced thermoelectric figure of merit in b _{9.6} Sb _{0.2} Te _{10-x} Se _x bulk materials, Journal of the American Chemical Society, 128 (2006), pp. 14347–14355
PbSeTe/PbTe	2D Material: quantum well/superlattice	2	300	1	USA	2002	T.C. Harman, P.J. Taylor, M.P. Walsh, B.E. LaForge, Quantum dot superlattice thermoelectric materials and devices, Science (New York, NY), 297 (2002), pp. 2229–2232
PbTe/Pb _{1-x} Eu _x Te	2D Material: quantum well/superlattice	2	300	1	USA	1996	L.D. Hicks, T.C. Harman, X. Sun, M.S. Dresselhaus, Experimental study of the effect of quantum-well structures on the thermoelectric figure of merit, Physical Review B, 53 (1996), p. R10493
PbTe–PbS8%	PbTe-based nanocomposite	1.4	750	1	USA	2010	S.N. Girard, J. He, C. Li, S. Moses, G. Wang, C. Uher, et al., In situ nanostructure generation and evolution within a bulk thermoelectric material to reduce lattice thermal conductivity, Nano Letters, 10 (2010), pp. 2825–2831
PbTe–Pb–Sb	PbTe-based nanocomposite	1.4	700	2	USA	2008	J.R. Sootsman, H. Kong, C. Uher, J.J. D'Angelo, C.-I. Wu, T.P. Hogan, et al., Large enhancements in the thermoelectric power factor of bulk PbTe at high temperature by synergistic nanostructuring, Angewandte Chemie, International Edition, 47 (2008), pp. 8618–8622

Thermoelectric Material	Material System	ZT _{max}	Max Operating Temp. (K)	TRL	Country	Year	Reference
PbTe–Si	PbTe-based nanocomposite	0.9	675	2	USA	2010	J.R. Sootsman, J. He, V.P. Dravid, S. Ballikaya, D. Vermeulen, C. Uher, et al., Microstructure and thermoelectric properties of mechanically robust PbTe–Si eutectic composites, <i>Chemistry of Materials</i> , 22 (2010), pp. 869–875
TM JPL n-SKD ***	eMMRTG Skutterudite - CoSb ₃	1.22	875	4	USA	2016	T. Caillat, S. Firdosy, B. Li, C. Huang, B. Cheng, J. Paik, J. Chase, T. Arakelian, L. Lara, and J.-P. Fleurial, "Progress Status Of The Development Of High-Efficiency Segmented Thermoelectric Couples" (2013) in: 11th international energy conversion engineering conference. DOI 10.2514/6.2013-3928
Yb _{0.19} Co ₄ Sb ₁₂	Skutterudite - CoSb ₃	1	600	2	USA	2000	G.S. Nolas, M. Kaeser, R.T. Littleton, T.M. Tritt, High figure of merit in partially filled ytterbium skutterudite materials, <i>Applied Physics Letters</i> , 77 (2000), pp. 1855–1857
Yb _{0.2} Co ₄ Sb _{12.3}	Skutterudite - CoSb ₃	1.26	800	2.5	China	2008	H. Li, X.F. Tang, X.L. Su, Q.J. Zhang, Preparation and thermoelectric properties of high-performance Sb additional Yb(0.2)Co(4)Sb(12+y) bulk materials with nanostructure, <i>Applied Physics Letters</i> , 92 (2008), p. 202114
Yb _{0.3} Co ₄ Sb _{12.3}	Skutterudite - CoSb ₃	1.3	800	2.5	China	2008	H. Li, X.F. Tang, Q.J. Zhang, C. Uher, Rapid preparation method of bulk nanostructured Yb(0.3)Co(4)Sb(12+y) compounds and their improved thermoelectric performance, <i>Applied Physics Letters</i> , 93 (2008), p. 202114
Mg _{3+δ} Sb ₂	1-2-2 Zintl	1.25	725	2	USA/Japan	2016	H. Tamaki, H. K. Sato, T. Kanno, Isotropic Conduction Network and Defect Chemistry in Mg _{3+δ} Sb ₂ -Based Layered Zintl Compounds with High Thermoelectric Performance. <i>Adv. Mater.</i> (2016) doi:10.1002/adma.201603955

Table K-2. p-type thermoelectric materials.

Thermoelectric Material	Material System	ZT _{max}	Max Operating Temp. (K)	TRL	Country	Year	Reference
(BiSb) ₂ Te ₃	Bi ₂ Te ₃ -based nanocomposite	1.47	440	2	China	2008	Y.Q. Cao, X.B. Zhao, T.J. Zhu, X.B. Zhang, J.P. Tu, Syntheses and thermoelectric properties of Bi(2)Te(3)/Sb(2)Te(3) bulk nanocomposites with laminated nanostructure, Applied Physics Letters, 92 (2008), p. 143106
(BiSb) ₂ Te ₃	Bi ₂ Te ₃ -based nanocomposite	1.5	390	1	China/USA	2010	W. Xie, J. He, H.J. Kang, X. Tang, S. Zhu, M. Laver, et al., Identifying the specific nanostructures responsible for the high thermoelectric performance of (Bi,Sb) ₂ Te ₃ nanocomposites, Nano Letters, 10 (2010), pp. 3283–3289
(Hf,Zr)CoSn	p-half heusler	1	975	3	USA, China	2014	Chen, s. and Ren, Z., "Recent progress of half-Heusler for moderate temperature thermoelectric applications", Materials Today, Vol. 16, 10 (2013), Pages 387–395
2%SrTe-containing PbTe	PbTe-based nanocomposite	1.7	800	1	USA	2011	K. Biswas, J. He, Q. Zhang, G. Wang, C. Uher, V.P. Dravid, et al., Strained endotaxial nanostructures with high thermoelectric figure of merit Nature Chemistry, 3 (2011), pp. 160–166
Ag _{0.5} Pb ₆ Sn ₂ Sb _{0.2} Te ₁₀	PbTe-based nanocomposite	1.45	630	1	USA	2006	J. Androulakis, K.F. Hsu, R. Pcionek, H. Kong, C. Uher, J.J. Dangelo, et al., Nanostructuring and high thermoelectric efficiency in p-type Ag(Pb _{1-y} Sny)(m)SbTe _{2+m} , Advanced Materials, 18 (2006), pp. 1170–1173
Bi _{0.4} Sb _{1.6} Te ₃	Bi ₂ Te ₃ -based nanocomposite	1.8	316	2	Singapore	2010	S. Fan, J. Zhao, J. Guo, Q. Yan, J. Ma, H.H. Hng, p-type Bi(0.4)Sb(1.6)Te(3) nanocomposites with enhanced figure of merit, Applied Physics Letters, 96 (2010), p. 182104
Bi _{0.4} Sb _{1.6} Te ₃	Bi ₂ Te ₃ -based nanocomposite	1.5	300	2	Singapore	2010	S. Fan, J. Zhao, J. Guo, Q. Yan, J. Ma, H.H. Hng, p-type Bi(0.4)Sb(1.6)Te(3) nanocomposites with enhanced figure of merit, Applied Physics Letters, 96 (2010), p. 182104
Bi _{0.52} Sb _{1.48} Te ₃	Bi ₂ Te ₃ -based nanocomposite	1.56	300	2	China/USA	2009	W. Xie, X. Tang, Y. Yan, Q. Zhang, T.M. Tritt, Unique nanostructures and enhanced thermoelectric performance of melt-spun BiSbTe alloys, Applied Physics Letters, 94 (2009), p. 102111
Bi ₂ Te ₃ /Sb ₂ Te ₃	2D Material: quantum well/superlattice	2.4	300	5	USA	2001	R. Venkatasubramanian, E. Siivola, T. Colpitts, B. O'Quinn, Thin-film thermoelectric devices with high room-temperature figures of merit, Nature, 413 (2001), pp. 597–602
BiSbTe	Bi ₂ Te ₃ -based nanocomposite	1.4	373	1	USA	2008	B. Poudel, Q. Hao, Y. Ma, Y. Lan, A. Minnich, B. Yu, et al., High-thermoelectric performance of nanostructured bismuth antimony telluride bulk alloys, Science (New York, NY), 320 (2008), pp. 634–638
BiSbTe	Bi ₂ Te ₃ -based nanocomposite	1.3	373	1	USA	2008	Y. Ma, Q. Hao, B. Poudel, Y. Lan, B. Yu, D. Wang, et al., Enhanced thermoelectric figure-of-merit in p-type nanostructured bismuth antimony tellurium alloys made from elemental chunks, Nano Letters, 8 (2008), pp. 2580–2584
BiSbTe	Bi ₂ Te ₃ -based nanocomposite	1.4	373	1	USA	2009	Y. Lan, B. Poudel, Y. Ma, D. Wang, M.S. Dresselhaus, G. Chen, et al., Structure study of bulk nanograined thermoelectric bismuth antimony telluride, Nano Letters, 9 (2009), pp. 1419–1422

Thermoelectric Material	Material System	ZT _{max}	Max Operating Temp. (K)	TRL	Country	Year	Reference
BiSbTe	Bi ₂ Te ₃ -based nanocomposite	1.2	300	3	USA	2008	B. Poudel, Q. Hao, Y. Ma, Y. Lan, A. Minnich, B. Yu, et al., High-thermoelectric performance of nanostructured bismuth antimony telluride bulk alloys, <i>Science</i> (New York, NY), 320 (2008), pp. 634–638
Bi-Te JPL	Bismuth Antimony Telluride	1.23	500	4	USA		JPL measured; materials synthesized at JPL; similar to TESI and Hi-Z materials
Ca ₉ Zn _{4.6} Sb ₉	9-4-9 Zintl	0.93	900	2	USA/China	2016	J. Shuai, Y. Wang, Z. Liu, H.S. Kim, J. Mao, J. Sui, Z. Ren, "Enhancement of thermoelectric performance of phase pure Zintl compounds Ca _{1-x} YbxZn ₂ Sb ₂ , Ca _{1-x} EuxZn ₂ Sb ₂ , and Eu _{1-x} YbxZn ₂ Sb ₂ by mechanical alloying and hot pressing," <i>Nano Energy</i> 25 (2016) 136–144.
Cu ₁₂ Sb _{4-x} Te _x S ₁₃ x=0.2-1.5	Tetrahedrite	1	725	3	USA	2015	Lu, X. and Morelli, D., "The Effect of Te Substitution for Sb on Thermoelectric Properties of Tetrahedrite", <i>Journal of Electronic Materials</i> , Vol. 43, No. 6, 2014
MnSi _{1.73}	p-silicide	0.8	873	3	China	2012	A.Zhou, H. Cui, J. Li, T. Zhu, X. Zhao, Bulk higher manganese silicide thermoelectric materials and modules, <i>Procedia Engineering</i> , Volume 27, 2012, Pages 94-102
Na _{0.95} Pb ₂₀ SbTe ₂₂	PbTe-based nanocomposite	1.7	700	3	USA	2006	P.F.R. Poudeu, J. D'Angelo, A.D. Downey, J.L. Short, T.P. Hogan, M.G. Kanatzidis, High thermoelectric figure of merit and nanostructuring in bulk p-type Na _{1-x} PbmSbyTe _{m+2} , <i>Angewandte Chemie, International Edition</i> , 45 (2006), pp. 3835–3839
NaPb ₁₈ BiTe ₂₀	PbTe-based nanocomposite	1.3	670	3	USA/Greece	2009	Al Gue'guen, P.F.P. Poudeu, C.-P. Li, S. Moses, C. Uher, J. He, et al., Thermoelectric properties and nanostructuring in the p-type materials NaPb _{18-x} Sn _x MTe ₂₀ (M=Sb, Bi), <i>Chemistry of Materials</i> , 21 (2009), pp. 1683–1694
p-(Pb,Sn)Te (MMRTG) ****	PbTe	0.63	825	9	USA	1996	D.M. Rowe, "Preparation of improved PbSnTe thermoelectric alloys and evaluation of their figure of merit. Final technical report, 1986-1987, AD-A-191346, United States Army, 1987.
p-Si ₇₈ Ge ₂₂ (RTG) ***/****	SiGe	0.51	1300	9	USA	1990	MHW-RTG and GPHS-RTG; DOE/JPL/Industry measured
p-Si ₈₀ Ge ₂₀ (nano MIT/JPL)	SiGe-based nanocomposites	0.95	1173	2.5	USA	2008	G. Joshi, H. Lee, Y. Lan, X. Wang, G. Zhu, D. Wang, et al., Enhanced thermoelectric figure-of-merit in nanostructured p-type silicon germanium bulk alloys, <i>Nano Letters</i> , 8 (2008), pp. 4670–4674
p-TAGS (MMRTG) ****	TAGS	0.78	675	9	USA	1976	E.A. Skrabek, et al., Thermoelectric Device Including an Alloy of GeTe and AgSbTe: As the P-Type Element" United States Patent 3945855, 1976.
Si nanowires	Nanowire-based	0.6	300	2	USA	2008	A.I. Hochbaum, R. Chen, R.D. Delgado, W. Liang, E.C. Garnett, M. Najarian, et al., Enhanced thermoelectric performance of rough silicon nanowires, <i>Nature</i> , 451 (2008), pp. 163–165
Si nanowires	Nanowire-based	1	200	2	USA	2008	A.I. Boukai, Y. Bunimovich, J. Tahir-Kheli, J.-K. Yu, W.A. Goddard III, J.R. Heath, Silicon nanowires as efficient thermoelectric materials, <i>Nature</i> , 451 (2008), pp. 168–171

Thermoelectric Material	Material System	ZT _{max}	Max Operating Temp. (K)	TRL	Country	Year	Reference
TM JPL p-SKD ***	eMMRTG Skutterudite - CeFe ₄ Sb ₁₂	0.88	875	4	USA	2016	Caillat TC, Firdosy SA, Li B "Progress Status Of The Development Of High-Efficiency Segmented Thermoelectric Couples" (2013) in: 11th international energy conversion engineering conference. DOI 10.2514/6.2013-3928
Yb ₁₄ MnSb ₁₁ Zintl ***	14-1-11 Zintl	1.34	1273	3.5	USA	2008	A. May, J. Fleurial, G. Snyder, "Thermoelectric performance of lanthanum telluride produced via mechanical alloying, Physical Review B 78, 125205 (2008)
β-Cu _{2-x} Se	Cu ₂ Se	1.5	1000	1	China/USA	2012	H. Liu, X. Shi, F. Xu, L. Zhang, W. Zhang, L. Chen, et al., Copper ion liquid-like thermoelectrics, Nature Materials, 11 (2012), pp. 422–425
β-Zn ₄ Sb ₃	p-Zn ₄ Sb ₃	1.35	673	1	USA/ Denmark/ Japan	2004	G.J. Snyder, M. Christensen, E. Nishibori, T. Caillat, B.B. Iversen, Disordered zinc in Zn ₄ Sb ₃ with phonon-glass and electron-crystal thermoelectric properties, Nature Materials, 3 (2004), pp. 458–463

K.2 Proposed RTG-Specific Thermoelectric Material Technology Readiness Level Definitions

Technology Readiness Levels (TRLs) are a set of metrics that enable the standardized assessment of the maturity of a particular technology and the consistent comparison of the maturity between different types of technology in the context of a specific application, implementation, and operational environment. The proposed TRL definitions were derived using the NASA Systems Engineering Processes and Requirements [1] and the JPL Technology Readiness Assessment Guideline [2].

Table K-3. Proposed RTG-specific thermoelectric material TRL definitions.⁴

TRL	Definition from NPR 7123.1e [1]	Completion Criteria RTG TE	Mission Requirements	Performance/Function	Fidelity of Analysis	Fidelity of Build	Level of Integration	Environment Verification
1	Basic principles observed and reported	Temperature-dependent thermoelectric (TE) properties as a function of composition, microstructure and morphology	Generic class of missions	TE properties as a function of temperature; basic thermal and chemical stability assessment.	Physics of transport properties identified	N/A	Basic lab-scale material samples	High temperatures, Vacuum/inert gas
2	Technology concept and/or application formulated	TE property optimization and reproducibility – basic physical properties measured	Generic class of missions	ZT values; device-level performance prediction; Initial estimate for upper range of operating temperatures	Transport property model developed; predicted conversion efficiency in relevant temperature range	N/A	Basic lab-scale material samples	High temperatures, Vacuum/inert gas
3	Analytical and/or experimental proof-of-concept of critical function	Initial validation of TE properties at device level; high temperature physical properties and thermal stability documented	Generic class of missions	Proof-of-Concept couple BOL performance matches initial prediction; initial estimate for thermal/mechanical stability	Efficiency prediction based on BOL performance; Initial testing for degradation mechanisms	Low-fidelity TE couple and/or module; initial tech development of interfaces, hot/cold shoes	Thermally insulated stand-alone TE device	High temperatures, Vacuum/inert gas
4	Component and/or breadboard validated in laboratory environment	Documented extended test performance under relevant conditions for components (TE materials, interfaces, dielectrics, insulation)	Generic class of missions	Proof-of-Concept couple BOL and extended performance; Component level life testing completed; degradation mechanisms identified	Lifetime performance prediction models developed at the component levels through accelerated testing;	Medium fidelity: RTG-configured TE couples/modules with prototypic hot/cold shoes	Component/ TE couple/ module	High temperatures, Vacuum/inert gas testing of TE devices with prototypic thermal insulation

⁴ The TRL definitions were derived by Dr. Jean-Pierre Fleurial of the Jet Propulsion Laboratory.

TRL	Definition from NPR 7123.1e [1]	Completion Criteria RTG TE	Mission Requirements	Performance/Function	Fidelity of Analysis	Fidelity of Build	Level of Integration	Environment Verification
5	Component and/or brassboard validated in relevant environment	Documented extended test performance under relevant conditions for couples/modules. Documented definition of scaling requirements	Generic or specific class of missions	Couple/module BOL and extended performance under nominal/ accelerated conditions broadly meet target performance goals	Lifetime performance prediction models developed at the device level through accelerated testing; Initial prediction for system level	Medium fidelity: RTG-configured TE couples/modules with realistic interfaces and thermal packaging/mechanical support	TE couples/modules	High temperatures, Vacuum/inert gas testing of TE devices with prototypic thermal insulation and converter parts
6	System/subsystem model or prototype demonstrated in a relevant environment	Documented extended test performance under relevant conditions for modules. Documented definition of flight system requirements	Generic or specific class of missions	Module BOL and extended performance under nominal/ accelerated conditions meet target performance goals	Lifetime performance prediction models validated at the device level through accelerated testing; updated prediction for system level.	High fidelity: electrically heated performance demonstrator (EPD) prototype that addresses all couple/module critical scaling, packaging and integration issues	TE modules integrated into EPD (can be discrete array of couples)	High temperatures, Vacuum/inert gas testing of TE devices with prototypic thermal insulation and converter parts
7	System prototype demonstration in an operational environment	Documented test performance demonstrating agreement with analytical predictions	Technology demonstration mission or specific mission	Required functionality/performance demonstrated	High fidelity: Initial validation of Early Life Performance Prediction at the EU RTG level as a function of operational environments	High fidelity: EU-RTG developed that addresses all critical scaling issues; BOL performance demonstration under electrical heating	TE modules integrated into electrically heated EU RTG system	EU RTG unit tested in actual operational environment
8	Actual system completed and "flight-qualified" through test and demonstration	Documented test performance verifying requirements and analytical predictions	Specific mission	Required functionality/performance demonstrated	High fidelity: validation of life performance prediction at the EU RTG level (stand-alone unit); verification of integrated system performance (QU RTG)	Final product: Life-tested EU-RTG; QU-RTG performance tested; flight unit fabricated	EU and QU RTG systems; QU may be fueled	EU and QU RTG units tested in project environmental verification program. EU-RTG Completed initial life-tests
9	Actual system flight-proven through successful mission operations	Documented mission operational results verifying requirements	Specific mission	Required flight RTG functionality/performance demonstrated	High fidelity: validation at the flight unit level of key performance parameters and life-limiting factors as a function of operational environments	Final product: RTG flight unit	Fueled flight RTG system	Operated in actual operational environment

K.3 Thermoelectric Efficiency Modeling (T-MOD)

The optimization of power output and efficiency of the modeled couple level architectures is dependent on the thermophysical properties and dimensions of the thermoelectric materials, as well as the couple-level electrical and thermal resistances. Additionally, the efficiency analyses of segmented thermoelectric couple architectures involve an added layer of complexity due to the additional number of electrical and thermal contact/interface materials and potential metallization layers. However, JPL has developed a T-MOD based on the semianalytical approach developed by Swanson et al. that includes smaller effects such as the Peltier and Thompson contributions and contact resistance in order to optimize and calculate the expected properties of a given configuration [3]. Since the performance of a thermoelectric couple design is highly dependent on the relationship between actual material and system-level parameters, T-MOD incorporates temperature dependent material properties, n- and p-type material properties, electrical and thermal contact resistances, and hot side and cold side heat loss factors.

As previously discussed, the efficiency of a thermoelectric material to convert heat into electricity is characterized by the dimensionless figure of merit (ZT):

$$ZT = \frac{\sigma S^2 T}{\lambda} \quad (1)$$

where σ is the electrical conductivity, S is the Seebeck coefficient, T is the temperature, and λ is the thermal conductivity. The relationship between ZT and efficiency (η) for a thermoelectric element is expressed in the following:

$$\eta = \frac{T_h - T_c}{T_h} \cdot \frac{\sqrt{1 + Z\bar{T}} - 1}{\sqrt{1 + Z\bar{T}} + T_c/T_h} \quad (2)$$

where T_h and T_c are the temperatures of the hot-side and cold-side temperatures of the element, respectively, and \bar{T} is the average of T_h and T_c .

It should be noted that the uncertainties of the predicted efficiency values derived from the T-MOD are not associated with the intrinsic calculations of the model, but are a function of the propagated uncertainties of experimental measurements of the variables used to calculate ZT and efficiency (η). Unfortunately, the raw data for the thermophysical measurements of many of the materials included in this study are not available, nor is the error of the devices used to make the measurements known. The exceptions to this observation are the materials specifically tested by JPL or other well-known sources. Thus, it was necessary to make some assumptions regarding the quality of the experimental measurements of the variables used to calculate ZT and efficiency (η). For simplicity, it was assumed that the accuracy and precision of all measurement equipment used to generate information used in this study are all equal and of high quality, and equivalent to the equipment employed at JPL.

According to a detailed assessment of uncertainty analysis performed by Mackey et al., the measurement uncertainties associated with a thermoelectric device are temperature dependent [4]. By employing the uncertainties calculated by Mackey et al., with measurement uncertainties from high-quality equipment, the following uncertainties were used to calculate a propagation of uncertainties for the predicted efficiency values derived from the T-MOD:

1. Uncertainty of electrical conductivity ($\Delta\sigma$) (S/m) = $\pm 7\%$;
2. Uncertainty of Seebeck coefficient (ΔS) ($\mu\text{V/K}$) = $\pm 4\%$;
3. Propagated uncertainty of thermal conductivity ($\Delta\lambda$) (W/m K) = $\pm 3.33\%$; and
4. Uncertainty of temperature (ΔT) (K) = $\pm 0.2\%$.

The propagated uncertainty for the figure of merit (ZT) was determined using the following expression:

$$\Delta ZT = ZT \sqrt{(\Delta\sigma/100)^2 + 4(\Delta S/100)^2 + (\Delta\lambda/100)^2 + (\Delta T/100)^2} \quad (3)$$

Since the propagation of uncertainty for efficiency (η) only includes the uncertainties for ZT and temperature (ΔT), then the uncertainty of efficiency ($\Delta\eta$) for the thermoelectric configurations modeled by T-MOD were assessed to be $\pm 12\%$.

K.4 Thermoelectric Efficiency Modeling Results

Configuration 1																			
Hot Junction Temperatures (K)	Cold Junction Temperatures (K)																		
	125	150	175	200	225	250	275	300	325	350	375	400	425	450	475	500	525	550	575
Average Figure of Merit (ZT_{Ave})																			
1275	0.97	0.99	1.01	1.03	1.05	1.07	1.08	1.09	1.09	1.10	1.11	1.12	1.14	1.15	1.17	1.19	1.21	1.23	1.25
Calculated Efficiency (%)																			
1175	23.03	22.53	22.00	21.44	20.85	20.24	19.60	18.90	18.10	17.50	16.80	16.30	15.70	15.10	14.60	14.04	13.53	13.00	12.46
1225	23.63								18.82	18.20	17.60	17.00	16.40	15.88	15.40	14.85	14.34	13.82	13.29
1275	24.17	23.70	23.20	22.67	22.12	21.53	20.93	20.31	19.50	18.90	18.30	17.70	17.20	16.60	16.10	15.59	15.09	14.57	14.05
p-leg Compatibility Factor																			
1175										2.75	2.7	2.64	2.59	2.54	2.5	2.46			
1225										2.82	2.76	2.7	2.64	2.59	2.54	2.5			
1275										2.86	2.8	2.73	2.66	2.6	2.55	2.51			
n-leg Compatibility Factor																			
1175										2.91	2.84	2.78	2.73	2.69	2.66	2.65			
1225										2.94	2.94	2.82	2.78	2.74	2.71	2.7			
1275										2.94	2.88	2.84	2.8	2.77	2.73	2.72			

Configuration 2																			
Hot Junction Temperatures (K)	Cold Junction Temperatures (K)																		
	125	150	175	200	225	250	275	300	325	350	375	400	425	450	475	500	525	550	575
Average Figure of Merit (ZT_{Ave})																			
1275	0.87	0.89	0.91	0.93	0.95	0.96	0.97	0.98	0.97	0.97	0.99	1.00	1.00	1.01	1.02	1.05	1.06	1.07	1.08
Calculated Efficiency (%)																			
1175	21.82	21.34	20.83	20.29	19.73	19.14	18.52	17.89	17.10	16.40	15.60	15.10	14.60	14.00	13.50	13.09	12.58	12.06	11.52
1225	22.57								17.50	17.00	16.40	15.80	15.20	14.60	14.10	13.74	13.24	12.72	12.19
1275	22.66	22.21	21.73	21.22	20.69	20.13	19.55	18.95	18.10	17.50	17.00	16.40	15.80	15.30	14.70	14.35	13.85	13.34	12.82
p-leg Compatibility Factor																			
1175									2.64	2.59	2.54	2.48	2.43	2.38	2.35				
1225									2.67	2.62	2.56	2.51	2.46	2.41	2.37				
1275									2.67	2.61	2.56	2.51	2.46	2.42	2.38				
n-leg Compatibility Factor																			
1175									2.53	2.48	2.44	2.40	2.63	2.33	2.31				
1225									2.54	2.50	2.45	2.41	2.38	2.34	2.32				
1275									2.54	2.50	2.46	2.41	2.38	2.35	2.33				

Configuration 3																			
Hot Junction Temperatures (K)	Cold Junction Temperatures (K)																		
	125	150	175	200	225	250	275	300	325	350	375	400	425	450	475	500	525	550	575
Average Figure of Merit (ZT_{Ave})																			
1275	0.96	0.98	1.00	1.02	1.03	1.04	1.05	1.06	1.05	1.04	1.05	1.05	1.05	1.06	1.09	1.10	1.12	1.13	1.15
Calculated Efficiency (%)																			
1175	23.41	22.85	22.26	21.63	20.98	20.29	19.58	18.85	17.80	17.10	16.40	15.70	15.00	14.40	13.26	13.47	12.95	12.44	11.92
1225	23.76								18.53	17.80	17.20	16.50	15.80	15.30	14.73	14.18	13.67	13.17	12.67
1275	24.09	23.58	23.04	22.46	21.86	21.23	20.57	19.89	19.10	18.30	17.70	17.00	16.35	15.74	15.36	14.83	14.33	13.85	13.36
p-leg Compatibility Factor																			
1175									3.73	3.64	3.55	3.46	3.38	3.32	3.26				
1225									3.66	3.57	3.49	3.41	3.33	3.27	3.21				
1275									3.56	3.48	3.40	3.32	3.25	3.19	3.14				
n-leg Compatibility Factor																			
1175									3.70	3.64	3.57	3.52	3.47	3.42	3.37				
1225									3.70	3.64	3.58	3.52	3.48	3.43	3.38				
1275									3.68	3.62	3.56	3.51	3.46	3.42	3.37				

Configuration 4																			
Hot Junction Temperatures (K)	Cold Junction Temperatures (K)																		
	125	150	175	200	225	250	275	300	325	350	375	400	425	450	475	500	525	550	575
Average Figure of Merit (ZT_{Ave})																			
1275	0.85	0.87	0.88	0.90	0.91	0.92	0.92	0.93	0.92	0.92	0.92	0.91	0.91	0.91	0.92	0.94	0.94	0.95	0.96
Calculated Efficiency (%)																			
1175	21.93	21.39	20.82	20.22	19.59	18.93	18.25	17.54	16.70	15.90	15.20	14.50	13.90	13.30	12.80	12.25	11.68	11.19	10.70
1225	22.11								17.10	16.30	15.70	15.00	14.40	13.80	13.30	12.89	12.26	11.83	11.30
1275	22.30	21.82	21.30	20.75	20.17	19.56	18.93	18.28	17.50	16.80	16.20	15.50	14.90	14.30	13.80	13.42	12.80	12.35	11.87
p-leg Compatibility Factor																			
1175									3.54	3.45	3.36	3.27	3.20	3.14	3.08				
1225									3.45	3.37	3.29	3.21	3.13	3.07	3.02				
1275									3.33	3.26	3.19	3.11	3.05	2.99	2.93				
n-leg Compatibility Factor																			
1175									3.13	3.07	3.00	2.94	2.89	2.84	2.79				
1225									3.06	3.00	2.94	2.88	2.83	2.78	2.73				
1275									2.99	2.93	2.87	2.82	2.78	2.72	2.67				

Configuration 5																			
Hot Junction Temperatures (K)	Cold Junction Temperatures (K)																		
	125	150	175	200	225	250	275	300	325	350	375	400	425	450	475	500	525	550	575
Average Figure of Merit (ZT_{Ave})																			
1275	0.96	0.98	1.00	1.02	1.03	1.04	1.05	1.06	1.06	1.06	1.07	1.08	1.09	1.10	1.10	1.12	1.13	1.14	1.15
Calculated Efficiency (%)																			
1175	23.41								17.90	17.30	16.60	16.00	15.30	14.70	14.05	13.51	12.95	12.38	11.80
1225	23.76								18.60	17.90	17.30	16.70	16.00	15.40	14.10	14.26	13.72	13.16	12.59
1275	24.09	23.58	23.04	22.46	21.86	21.23	20.57	19.89	19.20	18.50	17.90	17.30	16.70	16.10	15.50	14.96	14.42	13.88	13.32
p-leg Compatibility Factor																			
1175									3.42	3.35	3.27	3.20	3.12	3.06	2.92				
1225									3.32	3.24	3.17	3.10	3.03	2.98	3.00				
1275									3.17	3.10	3.04	2.97	2.91	2.86	2.81				
n-leg Compatibility Factor																			
1175									3.30	3.24	3.17	3.11	3.07	3.03	3.01				
1225									3.38	3.24	3.14	3.13	3.08	3.05	3.00				
1275									3.28	3.22	3.16	3.11	3.06	3.03	2.99				

Configuration 6																			
Hot Junction Temperatures (K)	Cold Junction Temperatures (K)																		
	125	150	175	200	225	250	275	300	325	350	375	400	425	450	475	500	525	550	575
Average Figure of Merit (ZT_{Ave})																			
1275	0.85	0.87	0.89	0.90	0.91	0.92	0.92	0.93	0.90	0.92	0.90	0.90	0.90	0.91	0.91	0.95	0.97	1.00	1.03
Calculated Efficiency (%)																			
1175	21.40								16.00	15.30	14.60	13.90	13.30	12.70	12.20	11.96	11.54	11.20	10.85
1225	21.90								16.60	16.00	15.30	14.70	14.00	13.50	13.00	12.75	12.33	12.00	11.66
1275	22.35	21.85	21.33	20.77	20.19	19.58	18.95	18.29	17.30	16.80	16.00	15.40	14.70	14.20	13.70	13.48	13.07	12.74	12.40
p-leg Compatibility Factor																			
1175									3.10	3.10	3.01	2.93	2.85	2.79	2.74				
1225									3.08	3.00	2.93	2.86	2.79	2.73	2.68				
1275									2.95	2.88	2.82	2.75	2.69	2.63	2.59				
n-leg Compatibility Factor																			
1175									3.83	3.76	3.69	3.62	3.55	3.51	3.50				
1225									3.78	3.71	3.63	3.57	3.51	3.47	3.45				
1275									3.68	3.62	3.55	3.49	3.43	3.40	3.38				

Configuration 7																			
Hot Junction Temperatures (K)	Cold Junction Temperatures (K)																		
	125	150	175	200	225	250	275	300	325	350	375	400	425	450	475	500	525	550	575
Average Figure of Merit (ZT_{Ave})																			
1275	0.93	0.95	0.96	0.98	0.99	1.01	1.01	1.02	1.02	1.03	1.03	1.04	1.04	1.05	1.06	1.09	1.09	1.10	1.11
Calculated Efficiency (%)																			
1175	22.70								17.48	16.83	16.16	15.50	14.85	14.25	13.68	13.13	12.61	12.09	11.57
1225	23.15								18.12	17.49	16.84	16.20	15.57	14.98	14.42	13.89	13.38	12.87	12.36
1275	23.55	23.05	22.52	21.96	21.37	20.75	20.11	19.45	18.70	18.09	17.46	16.84	16.23	15.66	15.14	14.71	14.08	13.59	13.08
p-leg Compatibility Factor																			
1175									3.55	3.48	3.39	3.32	3.24	3.17	3.11				
1225									3.42	3.35	3.28	3.21	3.14	3.08	3.02				
1275									3.26	3.19	3.12	3.06	2.99	2.99	2.89				
n-leg Compatibility Factor																			
1175									3.33	3.27	3.20	3.14	3.09	3.05	3.02				
1225									3.33	3.27	3.21	3.15	3.11	3.07	3.03				
1275									3.30	3.24	3.18	3.13	3.08	3.05	3.01				

Configuration 8																			
Hot Junction Temperatures (K)	Cold Junction Temperatures (K)																		
	125	150	175	200	225	250	275	300	325	350	375	400	425	450	475	500	525	550	575
Average Figure of Merit (ZT_{Ave})																			
1275	0.97	0.99	1.01	1.03	1.04	1.06	1.06	1.06	1.03	1.03	1.04	1.04	1.05	1.05	1.07	1.09	1.10	1.12	1.14
Calculated Efficiency (%)																			
1175	23.54								17.69	17.02	16.33	15.65	15.00	14.38	13.84	13.33	12.84	12.34	11.82
1225	23.93								18.28	17.63	16.97	16.31	15.67	15.07	14.54	14.04	13.57	13.08	12.57
1275	24.27	23.76	23.21	22.64	22.03	21.40	20.70	19.90	18.80	18.18	17.54	16.90	16.28	15.65	15.18	14.70	14.23	13.75	13.27
p-leg Compatibility Factor																			
1175									3.42	3.34	3.25	3.15	3.08	302.00	2.95				
1225									3.22	3.15	3.08	3.00	2.94	2.88	2.83				
1275									3.08	3.01	2.99	2.86	2.82	2.76	2.72				
n-leg Compatibility Factor																			
1175									3.86	3.78	3.72	3.65	3.60	3.57	3.54				
1225									3.80	3.73	3.67	3.61	3.56	3.53	3.50				
1275									3.72	3.66	3.59	3.54	3.49	3.46	3.43				

Configuration 9																				
Hot Junction Temperatures (K)	Cold Junction Temperatures (K)																			
	125	150	175	200	225	250	275	300	325	350	375	400	425	450	475	500	525	550	575	
Average Figure of Merit (ZT_{Ave})																				
1275													0.68	0.69	0.69	0.70	0.71	0.72	0.72	0.73
Calculated Efficiency (%)																				
1175													11.60	11.20	10.80	10.50	10.04	9.61	9.17	8.72
1225													12.10	11.70	11.30	11.00	10.54	10.11	9.68	9.24
1275													12.60	12.20	11.80	11.40	11.04	10.62	10.19	9.76
p-leg Compatibility Factor																				
1175													1.73	1.70	1.68					
1225													1.67	1.64	1.62					
1275													1.57	1.55	1.53					
n-leg Compatibility Factor																				
1175													1.88	1.86	1.83	1.75				
1225													1.68	1.82	1.80	1.80				
1275													1.59	1.80	1.78	1.81				

Configuration 10																			
Hot Junction Temperatures (K)	Cold Junction Temperatures (K)																		
	125	150	175	200	225	250	275	300	325	350	375	400	425	450	475	500	525	550	575
Average Figure of Merit (ZT_{Ave})																			
1275									0.69	0.73	0.76	0.79	0.82	0.85	0.88	0.91	0.94	0.97	1.01
Calculated Efficiency (%)																			
1275									14.45	14.33	14.18	14.01	13.81	13.59	13.35	13.10	12.83	12.54	12.24

Configuration 11																			
Hot Junction Temperatures (K)	Cold Junction Temperatures (K)																		
	125	150	175	200	225	250	275	300	325	350	375	400	425	450	475	500	525	550	575
Average Figure of Merit (ZT_{Ave})																			
1275									0.53	0.56	0.58	0.60	0.63	0.65	0.67	0.70	0.72	0.75	0.77
Calculated Efficiency (%)																			
1275									11.88	11.79	11.69	11.56	11.42	11.25	11.07	10.88	10.66	10.44	10.19

Configuration 12																				
Hot Junction Temperatures (K)	Cold Junction Temperatures (K)																			
	125	150	175	200	225	250	275	300	325	350	375	400	425	450	475	500	525	550	575	
Average Figure of Merit (ZT_{Ave})																				
1275										0.45	0.47	0.48	0.50	0.51	0.53	0.54	0.56	0.57	0.58	0.60
Calculated Efficiency (%)																				
1275										10.49	10.36	10.19	10.01	9.82	9.61	9.39	9.16	8.93	8.69	8.44

Configuration 13																				
Hot Junction Temperatures (K)	Cold Junction Temperatures (K)																			
	125	150	175	200	225	250	275	300	325	350	375	400	425	450	475	500	525	550	575	
Average Figure of Merit (ZT_{Ave})																				
525	0.67	0.70	0.73	0.76	0.78	0.79	0.80	0.80	0.79	0.76										
Calculated Efficiency (%)																				
475	14.37	13.40	12.50	11.55	10.50	9.50	8.40	7.30	6.30	5.34										
525	14.53	13.64	12.71	11.81	10.81	9.77	8.71	7.63	6.56	5.68										

Configuration 14																			
Hot Junction Temperatures (K)	Cold Junction Temperatures (K)																		
	125	150	175	200	225	250	275	300	325	350	375	400	425	450	475	500	525	550	575
Average Figure of Merit (ZT_{Ave})																			
1275	0.85	0.86	0.88	0.89	0.90	0.91	0.91	0.91	0.91	0.91	0.91	0.90	0.90	0.90	0.91	0.92			
Calculated Efficiency (%)																			
1175	21.31				18.96				16.17				13.44			11.69			
1225	21.79				19.52				16.83				14.09			12.47			
1275	22.21	21.71	21.18	20.62	20.02	19.41	18.76	18.10	17.42	16.74	16.06	15.40	14.76	14.17	13.64	13.18			

Configuration 15																			
Hot Junction Temperatures (K)	Cold Junction Temperatures (K)																		
	125	150	175	200	225	250	275	300	325	350	375	400	425	450	475	500	525	550	575
Average Figure of Merit (ZT_{Ave})																			
875	0.87	0.90	0.92	0.93	0.95	0.96	0.96	0.96	0.96	0.95	0.94	0.95	0.93	0.93	0.94	0.87	0.90	0.92	0.93
Calculated Efficiency (%)																			
775	19.69				16.34				12.50		10.58		8.84						
875	20.89	20.17	19.40	18.60	17.77	16.90	16.01	15.09	14.17	13.25	12.34	11.64	10.68	9.96	9.30				

Configuration 16																			
Hot Junction Temperatures (K)	Cold Junction Temperatures (K)																		
	125	150	175	200	225	250	275	300	325	350	375	400	425	450	475	500	525	550	575
Average Figure of Merit (ZT_{Ave})																			
825	0.69	0.71	0.73	0.75	0.76	0.77	0.77	0.78	0.77	0.77	0.76	0.76	0.75						
Calculated Efficiency (%)																			
775	17.49				14.56				11.19				7.92						
825	17.59	16.89	16.29	15.58	14.84	14.07	13.28	12.47	11.65	10.84	10.03	9.25	8.52						

Configuration 17																			
Hot Junction Temperatures (K)	Cold Junction Temperatures (K)																		
	125	150	175	200	225	250	275	300	325	350	375	400	425	450	475	500	525	550	575
Average Figure of Merit (ZT_{Ave})																			
1275	0.84	0.86	0.88	0.89	0.90	0.91	0.92	0.93	0.93	0.93	0.93	0.93	0.94	0.94	0.94	0.95	0.96	0.96	0.96
Calculated Efficiency (%)																			
1175	20.60		20.40				18.00				14.35				12.82				10.60
1225	21.80						18.47				15.85				13.43				11.26
1275	22.10	21.70	21.20	20.60	20.08	19.50	18.90	18.28	17.64	17.00	16.36	15.74	15.14	14.56	14.00	13.47	12.95	12.42	11.87
p-leg Compatibility Factor																			
1175									3.42	3.35	3.27	3.20	3.12	3.06	2.92				
1225									3.32	3.24	3.17	3.10	3.03	2.98	3.00				
1275									3.17	3.10	3.04	2.97	2.91	2.86	2.81				
n-leg Compatibility Factor																			
1175									3.30	3.24	3.17	3.11	3.07	3.03	3.01				
1225									3.38	3.24	3.14	3.13	3.08	3.05	3.00				
1275									3.28	3.22	3.16	3.11	3.06	3.03	2.99				

Configuration 18																			
Hot Junction Temperatures (K)	Cold Junction Temperatures (K)																		
	125	150	175	200	225	250	275	300	325	350	375	400	425	450	475	500	525	550	575
Average Figure of Merit (ZT_{Ave})																			
1275	0.76	0.77	0.79	0.80	0.81	0.81	0.82	0.82	0.82	0.81	0.81	0.81	0.81	0.81	0.81	0.82	0.84	0.86	0.88
Calculated Efficiency (%)																			
1275	20.65	20.19	19.69	19.17	18.62	18.04	17.44	16.82	16.19	15.55	14.91	14.29	13.69	13.13	12.62	12.17	11.81	11.49	11.15
p-leg Compatibility Factor																			
1175									3.10	3.10	3.01	2.93	2.85	2.79	2.74				
1225									3.08	3.00	2.93	2.86	2.79	2.73	2.68				
1275									2.95	2.88	2.82	2.75	2.69	2.63	2.59				
n-leg Compatibility Factor																			
1175									3.83	3.76	3.69	3.62	3.55	3.51	3.50				
1225									3.78	3.71	3.63	3.57	3.51	3.47	3.45				
1275									3.68	3.62	3.55	3.49	3.43	3.40	3.38				

Configuration 19																			
Hot Junction Temperatures (K)	Cold Junction Temperatures (K)																		
	125	150	175	200	225	250	275	300	325	350	375	400	425	450	475	500	525	550	575
Average Figure of Merit (ZT_{Ave})																			
1275	0.81	0.82	0.84	0.85	0.86	0.87	0.88	0.88	0.88	0.88	0.88	0.88	0.88	0.88	0.89	0.90	0.91	0.91	0.92
Calculated Efficiency (%)																			
1175			19.79								14.67								
1275	20.65	20.19	19.69	19.17	18.62	18.04	17.44	16.82	16.19	15.55	14.91	14.29	13.69	13.13	12.62	12.17	11.81	11.49	11.15
p-leg Compatibility Factor																			
1175									3.55	3.48	3.39	3.32	3.24	3.17	3.11				
1225									3.42	3.35	3.28	3.21	3.14	3.08	3.02				
1275									3.26	3.19	3.12	3.06	2.99	2.99	2.89				
n-leg Compatibility Factor																			
1175									3.33	3.27	3.20	3.14	3.09	3.05	3.02				
1225									3.33	3.27	3.21	3.15	3.11	3.07	3.03				
1275									3.30	3.24	3.18	3.13	3.08	3.05	3.01				

Configuration 20																			
Hot Junction Temperatures (K)	Cold Junction Temperatures (K)																		
	125	150	175	200	225	250	275	300	325	350	375	400	425	450	475	500	525	550	575
Average Figure of Merit (ZT_{Ave})																			
1275	0.84	0.85	0.87	0.88	0.89	0.90	0.91	0.91	0.91	0.91	0.91	0.91	0.91	0.91	0.92	0.93	0.94	0.95	0.95
Calculated Efficiency (%)																			
1175			20.50				17.99				15.15				12.64				
1275	22.06	21.58	21.06	20.52	19.94	19.34	18.72	18.07	17.42	16.75	16.09	15.44	14.82	14.24	13.72	13.25	12.79	12.30	11.80
p-leg Compatibility Factor																			
1175									3.42	3.34	3.25	3.15	3.08	302.00	2.95				
1225									3.22	3.15	3.08	3.00	2.94	2.88	2.83				
1275									3.08	3.01	2.99	2.86	2.82	2.76	2.72				
n-leg Compatibility Factor																			
1175									3.86	3.78	3.72	3.65	3.60	3.57	3.54				
1225									3.80	3.73	3.67	3.61	3.56	3.53	3.50				
1275									3.72	3.66	3.59	3.54	3.49	3.46	3.43				

Configuration 21																			
Hot Junction Temperatures (K)	Cold Junction Temperatures (K)																		
	125	150	175	200	225	250	275	300	325	350	375	400	425	450	475	500	525	550	575
Average Figure of Merit (ZT_{Ave})																			
1275	0.70	0.71	0.72	0.73	0.73	0.74	0.74	0.74	0.73	0.73	0.72	0.72	0.71	0.71	0.71	0.71	0.72	0.75	0.77
Calculated Efficiency (%)																			
1175			17.73				15.31				12.61				10.20				
1275	19.49	19.02	18.53	18.00	17.45	16.88	16.28	15.66	15.03	14.40	13.76	13.14	12.55	11.99	11.48	10.99	10.68	10.44	10.19

Configuration 22																			
Hot Junction Temperatures (K)	Cold Junction Temperatures (K)																		
	125	150	175	200	225	250	275	300	325	350	375	400	425	450	475	500	525	550	575
Average Figure of Merit (ZT_{Ave})																			
875														0.93	0.94	0.87	0.90	0.92	0.93
Calculated Efficiency (%)																			
875														9.96	9.30				

K.5 Scorecard for Modeled Segmented and Non-Segmented Thermoelectric Configurations

Configuration	Segments per Leg	Segment TRL (L/M/H)		TRL Config.	Efficiency			TE Cavity Atmosphere rating	Sublimation rating		Segmentation Ratings				Hot Side Metallization Rating		Score	
		n-type	p-type		1275K T _{hj} 450K T _{cj}	875K T _{hj} 450K T _{cj}	Efficiency 875K T _{hj} 350K T _{cj}		n-leg	p-leg	CTE mismatch	Complexity	n-leg Top/Mid Segment Interface	p-leg Top/Mid Segment Interface	n-leg	p-leg	Weighted	Unweighted
1	3	9/2/2	9/2.5/3.5	1	16.5			4	4	3	4	2	3	4	4	3	273	49
2	3	9/2/3.5	9/2.5/3.5	1	15.3			4	4	3	4	2	3	4	4	3	263	47
3	3	9/4/2	9/4/3.5	2	15.8			4	4	3	1	2	2	2	4	3	254	43
4	3	9/4/3.5	9/4/3.5	3	14.3			4	4	3	1	2	2	2	4	3	256	42
5	3	9/3/2	9/3/3.5	0	16.1			4	1	3	3	2	1	1	4	3	223	38
6	3	9/3/2	9/3/3.5	0	14.3			4	4	3	1	2	3	3	4	3	220	41
7	3	9/9/2	9/9/3.5	1	15.6			2	3	3	3	2	3	3	4	3	243	43
8	3	9/9/2	9/9/3.5	1	15.6			2	3	3	3	2	3	3	4	3	243	43
9	2	3/2.5	3/2.5	0	11.8			4	1	4	1	3	3	3	1	1	175	33
10	1	2	3.5	2	13.8			4	4	3	4	3	4	4	4	3	271	49
11	1	3.5	3.5	3.5	11.3			4	4	3	4	4	4	4	4	3	275	49
12	1	2.5	2.5	2.5	9.8			4	4	4	4	4	4	4	1	1	233	42
14	2	9/2	9/3.5	1	14.0			4	4	3	4	3	3	3	4	3	253	46
17	3	9/3/3.5	9/3/3.5	0	14.5			4	1	4	3	2	1	1	4	3	214	38
18	3	9/3/3.5	9/3/3.5	0	13.1			4	4	3	1	2	3	3	4	3	211	40
19	3	9/9/3.5	9/9/3.5	1	14.0			2	3	3	3	2	3	3	4	3	230	41
20	3	9/9/3.5	9/9/3.5	1	14.3			2	3	3	3	2	3	3	4	3	232	41
21	2	9/3.5	9/3.5	2	12.0			4	4	3	4	3	3	3	4	3	251	45
Weighting				14	8	8	8	5	4	4	6	3	3	3	4	4		
				<1							High: $\geq 10^{-4}$ g/cm ² /hr	$\geq 30\%$	Significant Development Effort Required (>3 Years)					
				1≤x<2	<12%	<12%	<12%	Ar only	Medium: $10^{-4}>x>10^{-5}$ g/cm ² /hr		20≤x<30%	Major Development Effort Required (2-3 Years)				<230	<42	
				2≤x<3	12≤x<14%	12≤x<14%	12≤x<14%	Vacuum/Ar	Low: $10^{-5}>x>10^{-6}$ g/cm ² /hr		10≤x<20%	Minor Development Effort Required (1 -2 Years)				230≤x<250	42≤x<47	
				≥3	≥14%	≥14%	≥14%		Very Low: $\leq 10^{-6}$ g/cm ² /hr		<10%	Minimal Development Required (≤ 1 year)				≥250	≥47	

Low- and Mid-Temperature Configurations

Configuration	Segments per Leg	Segment TRL (L/M/H)		TRL	Efficiency			TE Cavity Atmosphere rating	Sublimation rating		Segmentation Ratings				Hot Side Metallization Rating		Score	
		n-type	p-type	Config.	875K T _{hj} 450K T _{cj}	875K T _{hj} 350K T _{cj}	Efficiency 525K T _{hj} 350K T _{cj}		n-leg	p-leg	CTE mismatch	Complexity	n-leg Top/Mid Segment Interface	p-leg Top/Mid Segment Interface	n-leg	p-leg	Weighted	Unweighted
13	1	9	9	6			5.68	4	2	2	4	4	4	4	4	4	258	44
15	2	9/4	9/4	3		13.25		4	4	3	2	3	4	4	4	3	269	47
16	2	9/9	9/9	6		10.75		2	2	2	3	3	4	4	4	4	279	45
22	1	4	4	4	9.96			4	4	3	2	3	4	4	4	3	257	45
		Weighting		14	8	8	8	5	4	4	6	3	3	3	4	4		
				<1					High: ≥10 ⁻⁴ g/cm ² /hr		≥30%	Significant Development Effort Required (>3 Years)						
				1≤x<2	<12%	<12%	<12%	Ar only	Medium: 10 ⁻⁴ >x>10 ⁻⁵ g/cm ² /hr		20≤x<30%	Major Development Effort Required (2-3 Years)				<230	<42	
				2≤x<3	12≤x<14%	12≤x<14%	12≤x<14%	Vacuum/Ar	Low: 10 ⁻⁵ >x>10 ⁻⁶ g/cm ² /hr		10≤x<20%	Minor Development Effort Required (1 -2 Years)				230≤x<250	42≤x<47	
				≥3	≥14%	≥14%	≥14%		Very Low: ≤10 ⁻⁶ g/cm ² /hr		<10%	Minimal Development Required (≤ 1 year)				≥250	≥47	

A Listing of the Twenty Two (22) Modeled Thermoelectric Couple Level Configurations

Configuration	n-type			p-type		
	Low (300–473 K)	Mid (473–873 K)	High (873–1273 K)	Low (300–473 K)	Mid (473–873 K)	High (873–1273 K)
1	BiSeTe	Mg _{3+δ} Sb ₂	Nano Ni 15% La ₃ Te ₄	BiSbTe	Ca ₉ Zn _{4.6} Sb ₉	Yb ₁₄ MgSb ₁₁
2	BiSeTe	Mg _{3+δ} Sb ₂	ATEC 2014 LaTe	BiSbTe	Ca ₉ Zn _{4.6} Sb ₉	Yb ₁₄ MgSb ₁₁
3	BiSeTe	SKD-CoSb ₃	Nano Ni 15% La ₃ Te ₄	BiSbTe	SKD-CeFe ₄ Sb ₁₂	Yb ₁₄ MgSb ₁₁
4	BiSeTe	SKD-CoSb ₃	ATEC 2014 LaTe	BiSbTe	SKD-CeFe ₄ Sb ₁₂	Yb ₁₄ MgSb ₁₁
5	BiSeTe	Mg ₂ SiSn	Nano Ni 15% La ₃ Te ₄	BiSbTe	Cu ₁₂ Sb _{4-x} Te _x S ₁₃	Yb ₁₄ MgSb ₁₁
6	BiSeTe	(Hf,Zr)NiSn	Nano Ni 15% La ₃ Te ₄	BiSbTe	(Hf,Zr)CoSn	Yb ₁₄ MgSb ₁₁
7	BiSeTe	PbTe	Nano Ni 15% La ₃ Te ₄	BiSbTe	TAGS	Yb ₁₄ MgSb ₁₁
8	BiSeTe	nano PbTe	Nano Ni 15% La ₃ Te ₄	BiSbTe	TAGS	Yb ₁₄ MgSb ₁₁
9	—	Mg ₂ SiSn	Nano SiGe	—	MnSi _{1.7}	nano SiGe
10	—	Nano Ni 15% La ₃ Te ₄		—	Yb ₁₄ MgSb ₁₁	
11	—	ATEC 2014 LaTe		—	Yb ₁₄ MgSb ₁₁	
12	—	Nano SiGe		—	nano SiGe	
13	BiSeTe	—	—	BiSbTe	—	—
14	BiSeTe	Nano Ni 15% La ₃ Te ₄		BiSbTe	Yb ₁₄ MgSb ₁₁	
15	BiSeTe	SKD-CoSb ₃	—	BiSbTe	SKD-CeFe ₄ Sb ₁₂	—
16	BiSeTe	PbTe	—	BiSbTe	TAGS	—
17	BiSeTe	Mg ₂ SiSn	ATEC 2014 LaTe	BiSbTe	Cu ₁₂ Sb _{4-x} Te _x S ₁₃	Yb ₁₄ MgSb ₁₁
18	BiSeTe	(Hf,Zr)NiSn	ATEC 2014 LaTe	BiSbTe	(Hf,Zr)CoSn	Yb ₁₄ MgSb ₁₁
19	BiSeTe	PbTe	ATEC 2014 LaTe	BiSbTe	TAGS	Yb ₁₄ MgSb ₁₁
20	BiSeTe	nano PbTe	ATEC 2014 LaTe	BiSbTe	TAGS	Yb ₁₄ MgSb ₁₁
21	BiSeTe	ATEC 2014 LaTe		BiSbTe	Yb ₁₄ MgSb ₁₁	
22	—	SKD-CoSb ₃	—	—	SKD-CeFe ₄ Sb ₁₂	—

K.6 References

- [1] NASA Office of the Chief Engineer. April 18, 2013. NASA Systems Engineering Processes and Requirements, NPR 7123.1B, NASA, Washington, DC, effective April 18, 2013 [cited September 8, July 2016]. <http://nodis3.gsfc.nasa.gov/>
- [2] Frerking, M.A. and P.M. Beauchamp. 2016. “JPL technology readiness assessment guideline,” *2016 IEEE Aerospace Conference*, Big Sky, MT, pp. 1–10. doi: 10.1109/AERO.2016.7500924
- [3] Swanson, B.W., E.V. Somers, and R.R. Heike. 1961. “Optimization of a sandwiched thermoelectric device,” *Journal of Heat Transfer*, pp. 77–82.
- [4] Mackey, J., F. Dynys, and A. Sehirlioglu. 2014. “Uncertainty analysis for common Seebeck and electrical resistivity measurement systems,” *Rev. Sci. Instrum.*, 85, 085119.

L Intensity Matrix

Knut I. Oxnevad

NASA Jet Propulsion Laboratory, 4800 Oak Grove Dr, Pasadena, CA 91109

Two tables showing number of missions per mission type and per destination are provided in this appendix. Table L-1 shows all of the 248 missions launched (successful) and studied. Table L-2 shows the 125 missions studied.

The cells in the tables in this appendix are color coded: strong green indicates new mission opportunity; slight green (low), via salmon, to orange (high) indicates the number of missions suggested of a specific mission type at a given location. Missions types not available for a certain location are marked “NA” and are color-coded grey.

Table L-1. Intensity table: number of missions per destinations and per mission type: all missions flown (successful) and studied.

Destination	FLYBY	ORBITER	ATM PROBE	AERIAL			SURFACE				SUBSURFACE			SAMPLE RETURN	Sum
				BALLOON	FIXED WING	HELICOPTER	IMPACT	LANDER	ROVER	BOAT	LIQUID	SOIL	ICE		
Sun			NA	NA	NA	NA					NA	NA	NA		1
Mercury			NA	NA	NA	NA					NA	NA	NA		5
Venus											NA	NA	NA		12
Lagrange Point 1			NA	NA	NA	NA	NA	NA	NA	NA	NA	NA	NA		1
Earth											NA	NA	NA		0
Moon			NA	NA	NA	NA					NA	NA	NA		28
Near Earth Object (NEO)			NA	NA	NA	NA					NA	NA	NA		1
433 Eros			NA	NA	NA	NA					NA	NA	NA		1
Mars											NA	NA	NA		22
9969 Braille			NA	NA	NA	NA					NA	NA	NA		1
Main Asteroid Belt			NA	NA	NA	NA					NA	NA	NA		0
Ceres			NA	NA	NA	NA					NA	NA	NA		1
Vesta			NA	NA	NA	NA					NA	NA	NA		1
Pallas			NA	NA	NA	NA					NA	NA	NA		0
Hygiea			NA	NA	NA	NA					NA	NA	NA		0
951 Gaspra			NA	NA	NA	NA					NA	NA	NA		1
243 Ida			NA	NA	NA	NA					NA	NA	NA		1
(243) Ida Dactyl			NA	NA	NA	NA					NA	NA	NA		1
132524 APL			NA	NA	NA	NA					NA	NA	NA		1
253 Mathilde			NA	NA	NA	NA					NA	NA	NA		1
5535 Annefrank			NA	NA	NA	NA					NA	NA	NA		1
2685 Masursky			NA	NA	NA	NA					NA	NA	NA		1
Asteroid			NA	NA	NA	NA					NA	NA	NA		0
Jupiter											NA	NA	NA	NA	15
Io			NA	NA	NA	NA					NA	NA	NA		5
Europa			NA	NA	NA	NA					NA	NA	NA		9
Ganymede			NA	NA	NA	NA					NA	NA	NA		3
Callisto			NA	NA	NA	NA					NA	NA	NA		2
Amalthea			NA	NA	NA	NA					NA	NA	NA		2
624 Hektor			NA	NA	NA	NA					NA	NA	NA		0
9P/Tempel			NA	NA	NA	NA					NA	NA	NA		3
d'Arrest			NA	NA	NA	NA					NA	NA	NA		0
Trojan			NA	NA	NA	NA					NA	NA	NA		5
103P/Hartley			NA	NA	NA	NA					NA	NA	NA		1
Saturn											NA	NA	NA	NA	20
Mimas			NA	NA	NA	NA					NA	NA	NA		1
Enceladus			NA	NA	NA	NA					NA	NA	NA		16
Tethys			NA	NA	NA	NA					NA	NA	NA		3
Dione			NA	NA	NA	NA					NA	NA	NA		4
Rhea			NA	NA	NA	NA					NA	NA	NA		4
Titan											NA	NA	NA		25
Iapetus			NA	NA	NA	NA					NA	NA	NA		2
Phoebe			NA	NA	NA	NA					NA	NA	NA		1
Hyperion			NA	NA	NA	NA					NA	NA	NA		2
Centaur			NA	NA	NA	NA					NA	NA	NA		3
Chariklo			NA	NA	NA	NA					NA	NA	NA		0
Pholus			NA	NA	NA	NA					NA	NA	NA		0
2060-Chiron			NA	NA	NA	NA					NA	NA	NA		1
Hidalgo			NA	NA	NA	NA					NA	NA	NA		0
Uranus											NA	NA	NA	NA	10
Miranda			NA	NA	NA	NA					NA	NA	NA		1
Ariel			NA	NA	NA	NA					NA	NA	NA		0
Umbriel			NA	NA	NA	NA					NA	NA	NA		0
Titania			NA	NA	NA	NA					NA	NA	NA		0
Oberon			NA	NA	NA	NA					NA	NA	NA		0
Neptune											NA	NA	NA	NA	10
Triton			NA	NA	NA	NA					NA	NA	NA		6
Kuiper Belt			NA	NA	NA	NA					NA	NA	NA		3
Pluto			NA	NA	NA	NA					NA	NA	NA		3
Charon			NA	NA	NA	NA					NA	NA	NA		1
Haumea			NA	NA	NA	NA					NA	NA	NA		0
Makemake			NA	NA	NA	NA					NA	NA	NA		0
2014 MU69			NA	NA	NA	NA					NA	NA	NA		1
Schwassmann-			NA	NA	NA	NA					NA	NA	NA		0
Borely			NA	NA	NA	NA					NA	NA	NA		1
81P/Wild			NA	NA	NA	NA					NA	NA	NA		1
21P/Giacobini-Zinner			NA	NA	NA	NA					NA	NA	NA		1
2P/Encke			NA	NA	NA	NA					NA	NA	NA		0
Comet			NA	NA	NA	NA					NA	NA	NA		3
	102	72	10	3	1	0	10	31	10	3	1	0	0	6	249
	Table Color Codes (Columns F-S)						Destination Categories (Column A)								
	Low number (1-4) of missions planned for destination						Ocean World								
	Medium number (4-6) of missions planned for destination						Possible Ocean World								
	Max number of missions planned for destination						Gas Giant								
	NA Not available						Icy Giant								
	New Mission Opportunities														

Table L-2. Intensity table: number of missions per destinations and per mission type studied missions.

Destination	FLYBY	ORBITER	ATM PROBE	AERIAL			SURFACE			SUBSURFACE			SAMPLE RETURN	Sum		
				BALLOON	FIXED WING	HELICOPTER	IMPACT	LANDER	ROVER	BOAT	LIQUID	SOIL			ICE	
Sun			NA	NA	NA	NA				NA	NA	NA		0		
Mercury			NA	NA	NA	NA				NA	NA	NA		1		
Venus										NA	NA	NA		2		
Lagrange Point 1			NA	NA	NA	NA	NA	NA	NA	NA	NA	NA		0		
Earth										NA	NA	NA		0		
Moon			NA	NA	NA	NA				NA	NA	NA		6		
Near Earth Object (NEO)			NA	NA	NA	NA				NA	NA	NA		1		
433 Eros			NA	NA	NA	NA				NA	NA	NA		0		
Mars										NA	NA	NA		4		
9969 Braille			NA	NA	NA	NA				NA	NA	NA		0		
Main Asteroid Belt			NA	NA	NA	NA				NA	NA	NA		0		
Ceres			NA	NA	NA	NA				NA	NA	NA		0		
Vesta			NA	NA	NA	NA				NA	NA	NA		0		
Pallas			NA	NA	NA	NA				NA	NA	NA		0		
Hygiea			NA	NA	NA	NA				NA	NA	NA		0		
951 Gaspra			NA	NA	NA	NA				NA	NA	NA		0		
243 Ida			NA	NA	NA	NA				NA	NA	NA		0		
(243) Ida Dactyl			NA	NA	NA	NA				NA	NA	NA		0		
132524 APL			NA	NA	NA	NA				NA	NA	NA		0		
253 Mathilde			NA	NA	NA	NA				NA	NA	NA		0		
5535 Annefrank			NA	NA	NA	NA				NA	NA	NA		0		
2685 Masursky			NA	NA	NA	NA				NA	NA	NA		0		
Asteroid			NA	NA	NA	NA				NA	NA	NA		0		
Jupiter								NA	NA	NA	NA	NA		5		
Io			NA	NA	NA	NA				NA	NA	NA		3		
Europa			NA	NA	NA	NA				NA	NA	NA		7		
Ganymede			NA	NA	NA	NA				NA	NA	NA		1		
Callisto			NA	NA	NA	NA				NA	NA	NA		1		
Amalthea			NA	NA	NA	NA				NA	NA	NA		0		
624 Hektor			NA	NA	NA	NA				NA	NA	NA		0		
9P/Tempel			NA	NA	NA	NA				NA	NA	NA		0		
d'Arrest			NA	NA	NA	NA				NA	NA	NA		0		
Trojan			NA	NA	NA	NA				NA	NA	NA		5		
103P/Hartley			NA	NA	NA	NA				NA	NA	NA		0		
Saturn								NA	NA	NA	NA	NA		15		
Mimas			NA	NA	NA	NA				NA	NA	NA		0		
Enceladus			NA	NA	NA	NA				NA	NA	NA		14		
Tethys			NA	NA	NA	NA				NA	NA	NA		2		
Dione			NA	NA	NA	NA				NA	NA	NA		2		
Rhea			NA	NA	NA	NA				NA	NA	NA		2		
Titan										NA	NA	NA		21		
Iapetus			NA	NA	NA	NA				NA	NA	NA		0		
Phoebe			NA	NA	NA	NA				NA	NA	NA		0		
Hyperion			NA	NA	NA	NA				NA	NA	NA		0		
Centaur			NA	NA	NA	NA				NA	NA	NA		3		
Chariklo			NA	NA	NA	NA				NA	NA	NA		0		
Pholus			NA	NA	NA	NA				NA	NA	NA		0		
2060-Chiron			NA	NA	NA	NA				NA	NA	NA		1		
Hidalgo			NA	NA	NA	NA				NA	NA	NA		0		
Uranus								NA	NA	NA	NA	NA		9		
Miranda			NA	NA	NA	NA				NA	NA	NA		0		
Ariel			NA	NA	NA	NA				NA	NA	NA		0		
Umbriel			NA	NA	NA	NA				NA	NA	NA		0		
Titania			NA	NA	NA	NA				NA	NA	NA		0		
Oberon			NA	NA	NA	NA				NA	NA	NA		0		
Neptune								NA	NA	NA	NA	NA		9		
Triton			NA	NA	NA	NA				NA	NA	NA		5		
Kuiper Belt			NA	NA	NA	NA				NA	NA	NA		3		
Pluto			NA	NA	NA	NA				NA	NA	NA		0		
Charon			NA	NA	NA	NA				NA	NA	NA		0		
Haumea			NA	NA	NA	NA				NA	NA	NA		0		
Makemake			NA	NA	NA	NA				NA	NA	NA		0		
2014 MU69			NA	NA	NA	NA				NA	NA	NA		0		
Schwassmann-Wachmann-3			NA	NA	NA	NA				NA	NA	NA		0		
Borely			NA	NA	NA	NA				NA	NA	NA		0		
81P/Wild			NA	NA	NA	NA				NA	NA	NA		0		
21P/Giacobini-Zinner			NA	NA	NA	NA				NA	NA	NA		0		
2P/Encke			NA	NA	NA	NA				NA	NA	NA		0		
Comet			NA	NA	NA	NA				NA	NA	NA		3		
	35	45	8	3	1	0	0	0	20	6	3	1	0	0	3	125

Table Color Codes (Columns F-S)				Destination Categories (Column A)			
	Low number (1-4) of missions planned for destination		Medium number (4-6) of missions planned for destination		Ocean World		Possible Ocean World
	Max number of missions planned for destination		NA		Gas Giant		Icy Giant
	Not available						
	New Mission Opportunities						

M Destination Table

Knut Oxnevad

NASA Jet Propulsion Laboratory, 4800 Oak Grove Dr, Pasadena, CA 91109

Destination	Location	Association	Type	Sphere	Surf. gravity - g (m/s ²)	Ice Thickness (km)	Ocean Depth (km)	Radius - r (km)	Semimajor Axis (km)	Surface pressure (Pa)	Temp at surface (K)	Atmosphere ⁽¹⁾
Sun	Sun	Sun	Star	Y	2.79E+01			695700	0.01		5772	
Mercury	Mercury	Mercury	Planet	Y	3.70E+00			2439	0.39	5.00E+09	340	N
Venus	Venus	Venus	Planet	Y	8.87E+00			6051.8	0.72	9.20E+06	737	Y
Lagrange Point 1	Lagrange Point 1	Earth	L1						0.99			
Earth	Earth	Earth	Planet	Y	9.81E+00			6371	1	1.01E+05	288	Y
Moon	Earth	Moon	Moon		1.62E+00			1737	1	1.00E-07	220	N
Near Earth Object (NEO)									1.3			
433 Eros	Near Earth Asteroid	Near Earth Asteroid	Asteroid	N	5.90E-02			16.84	1.458	0.00E+00		N
Mars	Mars	Mars	Planet	Y	3.71E+00			3389	1.52	6.36E+02	210	Y
9969 Braille	Mars Crossing Asteroid	Mars Crossing Asteroid	Asteroid					1	2.34	0.00E+00		N
Main Asteroid Belt										0.00E+00		N
Ceres	Main Asteroid Belt	Ceres	Dwarf Planet	Y	2.80E-01	80		473	2.77	0.00E+00	168	N
Vesta	Main Asteroid Belt	Vesta	Minor Planet	N	2.50E-01			525	2.36	0.00E+00	85	N
Pallas	Main Asteroid Belt	Main Asteroid Belt	Minor Planet	N	2.10E-01			512	2.77	0.00E+00	164	N
Hygiea	Main Asteroid Belt	Main Asteroid Belt	Minor Planet	N	9.10E-02			431	3.14	0.00E+00	164	N
951 Gaspra	Main Asteroid Belt	Main Asteroid Belt	Asteroid	N	2.00E-03			6.1	2.2	0.00E+00	181	N
243 Ida	Main Asteroid Belt	Main Asteroid Belt	Asteroid	N	7.00E-03			15.7	2.861	0.00E+00	200	N
(243) Ida Dactyl	Main Asteroid Belt	243 Ida	Moon	N				0.7	2.861	0.00E+00	200	N
132524 APL	Main Asteroid Belt	Main Asteroid Belt	Asteroid	N				1.15	2.6025	0.00E+00		N
253 Mathilde	Main Asteroid Belt	Main Asteroid Belt	Asteroid	N	9.89E-03			25	2.6484	0.00E+00	174	N
5535 Annefrank	Main Asteroid Belt	Main Asteroid Belt	Asteroid	N				2.4	2.2127	0.00E+00		N
2685 Masursky	Main Asteroid Belt	Main Asteroid Belt	Asteroid	N				10	2.57	0.00E+00		N
Asteroid	Main Asteroid Belt	Main Asteroid Belt	Asteroid	N					2.6	0.00E+00		N
Jupiter	Jupiter	Jupiter	Planet	Y	2.48E+01			69911	5.2	2.00E+05	165	Y
Io	Jupiter	Io	Moon	Y	1.80E+00			1821	5.2	0.00E+00	110	N
Europa	Jupiter	Europa	Moon	Y	1.31E+00	30	135	1560	5.2	1.00E-07	102	N
Ganymede	Jupiter	Ganymede	Moon	Y	1.43E+00	144	800	2634	5.2	0.00E+00	110	N
Callisto	Jupiter	Callisto	Moon	Y	1.24E+00	100	315	2410	5.2	7.50E-10	134	N
Amalthea	Jupiter	Amalthea	Moon	N	2.00E-02			83.5	5.2	0.00E+00	120	N
624 Hektor	Jupiter Trojan	Jupiter Trojan	Asteroid	N	6.70E-02			226	5.2	0.00E+00	122	N
9P/Tempel	Jupiter Family Comet	Jupiter Family Comet	Comet					3.8	3.124	0.00E+00		N
d'Arrest	Jupiter Family Comet	Jupiter Family Comet	Comet					1.6	3.5	0.00E+00		N
Trojan	Jupiter Trojan	Jupiter	Asteroid						5.2	0.00E+00		N
103P/Hartley	Jupiter Family Comet	Jupiter Family Comet	Comet				0	0.57	3.46	0.00E+00		N
Saturn	Saturn	Saturn	Planet	Y	1.04E+01			58232	9.5549	2.00E+05	134	Y
Mimas	Saturn	Mimas	Moon	Y	6.40E-02	100		198	9.5549	0.00E+00	64	N
Enceladus	Saturn	Enceladus	Moon	Y	1.13E-01	20	54	252	9.5549	0.00E+00	75	N
Tethys	Saturn	Tethys	Moon	Y	1.46E-01			531	9.5549	0.00E+00	86	N
Dione	Saturn	Dione	Moon	Y	2.32E-01			561	9.5549	0.00E+00	87	N
Rhea	Saturn	Rhea	Moon	Y	2.64E-01			763	9.5549	0.00E+00	75	N
Titan	Saturn	Titan	Moon	Y	1.35E+00	100	300	2575	9.5549	1.47E+05	94	Y
Iapetus	Saturn	Iapetus	Moon	Y	2.23E-01			734	9.5549	0.00E+00	110	N
Phoebe	Saturn	Phoebe	Moon		4.40E-02			106	9.5549	0.00E+00	73	N
Hyperion	Saturn	Hyperion	Moon		1.90E-01			135	9.5549	0.00E+00	93	N
Centaur	Centaur (Jupiter - Neptune)	Centaur	Centaur						12.5	0.00E+00		N
Chariklo	Centaur (Jupiter - Neptune)	Centaur (Jupiter - Neptune)	Centaur	N				151	15.8	0.00E+00		N
Pholus	Centaur (Jupiter - Neptune)	Centaur (Jupiter - Neptune)	Centaur	N				95	20.4	0.00E+00	62	N
2060-Chiron	Centaur (Jupiter - Neptune)	Centaur (Jupiter - Neptune)	Centaur	Y				109	13.63	0.00E+00	75	N
Hidalgo	Centaur (Jupiter - Neptune)	Centaur (Jupiter - Neptune)	Centaur	N				19	5.73	0.00E+00	116	N
Uranus	Uranus	Uranus	Planet	Y	8.69E+00			25362	19.23	1.00E+05	76	Y
Miranda	Uranus	Miranda	Moon	Y	7.90E-02			235	19.23	0.00E+00	60	N
Ariel	Uranus	Ariel	Moon	Y	2.69E-01			578	19.23	0.00E+00	60	N
Umbriel	Uranus	Umbriel	Moon	Y	2.00E-01			584	19.23	0.00E+00	75	N
Titania	Uranus	Titania	Moon	Y	3.79E-01			788	19.23	1.50E-06	70	N
Oberon	Uranus	Oberon	Moon	Y	3.46E-01			761	19.23	0.00E+00	75	N
Neptune	Neptune	Neptune	Planet	Y	1.12E+01			24662	30.1	1.00E+05	72	Y
Triton	Neptune	Triton	Moon	Y	7.79E-01	200		1353	30.1	1.65E+00	38	Y
Kuiper Belt									40	0.00E+00		N
Pluto	Kuiper Belt	Pluto	Dwarf Planet	Y	6.20E-01	260	0	1187	39.5	1.00E+00	44	Y
Charon	Kuiper Belt	Pluto	Moon	Y	2.88E-01			606	39.5	0.00E+00	53	N
Haumea	Kuiper Belt	Kuiper Belt	Dwarf Planet		6.30E-01			575	43.2	0.00E+00	50	N
Makemake	Kuiper Belt	Kuiper Belt	Dwarf Planet					715	45.7	8.00E-04	34	Y
2014 MU69	Kuiper Belt	Kuiper Belt	Kuiper Belt Obj	N				17.5	44.21	0.00E+00		N
Schwassmann-Wachmann-3	Periodic Comet	Periodic Comet	Comet						3.063	0.00E+00		N
Borely	Periodic Comet	Periodic Comet	Comet	N				2.4	3.59	0.00E+00		N
81P/Wild	Periodic Comet	Periodic Comet	Comet	N				2	3.45	0.00E+00		N
21P/Giacobini-Zinner	Periodic Comet	Periodic Comet	Comet					1	3.526			
2P/Encke	Periodic Comet	Periodic Comet	Comet	N				2.4	2.2178	0.00E+00	136	N
Comet	Periodic Comet	Periodic Comet	Comet						3.5			

69

Ocean World Possible Ocean World Gas Giant Icy Giant

N Reference RTGs: GPHS-RTG, MMRTG, and eMMRTG

David Woerner

NASA Jet Propulsion Laboratory, 4800 Oak Grove Drive, Pasadena, CA 91109

The following radioisotope thermoelectric generators (RTGs) were used as references throughout this study. They were a source of design details useful for sanity checks to indicate the new RTG concepts were at least rational.

N.1 GPHS-RTG

The General-Purpose Heat Source (GPHS) RTG was first flown on NASA’s Galileo mission, launched in October 1989 [1]. The last was flown on the Pluto New Horizon mission, launched January 2006 [2]. This type of RTG has been flown on many successful missions—it remains the most powerful RTG launched on a NASA mission. Some useful design details are in Table N-1.

Table N-1. The GPHS-RTG in numbers.

	Value	Comments
P_{BOL} , W	290	Beginning Of Mission
Mass, kg	57	
Number of GPHS	18	Step 0 & 1 GPHS, now obsolete
T_h , °C	1000	
Date first launched	October 18, 1989	Galileo
Date last launched	January 19, 2006	Pluto-New Horizons

These RTGs were designed so the thermoelectric convertor and the heat source shared the same volume, with no barrier between them [3]. The thermoelectric couples were cantilevers in this configuration; the RTG did not contain a surface on which to rest the hot side of the TECs; the cold end of the TECs was bolted to the RTG housing. This choice had a strong influence on lowering the generator’s mass. However, that design meant the housing contained bolt holes and hence gases and vapors could leak into the housing as well as out of the housing. During ground operations, this was managed by filling the housing with an inert gas to prevent damaging gases entering the housing and “topping-off” the cover gas occasionally. In flight, the cover gas was vented and the generators were never again put into a gaseous environment.

N.2 Multi-Mission RTG

The Multi-Mission RTG (MMRTG) was introduced here as a second reference RTG. The Multi-Mission RTG was conceived because missions to Mars and other bodies with atmosphere were left with no radioisotope power system (RPS) late in the twentieth century; hermetically sealed generators had not been built for NASA’s use since the 1970s. The first MMRTG was launched on the Mars Science Laboratory mission in November 2011 [4]. Some useful design details are in Table N-2.

Table N-2. The MMRTG in numbers.

	Value	Comments
P_{BOL} , W	110	Beginning Of Mission, required
Mass, kg	45.4	Includes cooling tubes
Number of GPHS	8	Step 2 GPHS
T_h , °C	530	
Date first launched	November 26, 2011	Mars Science Laboratory
Date last launched	Not applicable	

The MMRTG design isolates the thermoelectric couples from the heat source using an isolation liner [5] unlike the GPHS-RTG. This serves two significant functions. It completes the hermetically sealed housing that protects the TECs from harmful gases and provides a vessel that can be backed-filled

with an inert gas used to aid sublimation suppression of the TECs. These design features increase the mass of the generator.

N.3 enhanced MMRTG

The enhanced Multi-Mission RTG (eMMRTG) was introduced here as a reference RTG. The eMMRTG builds upon the MMRTG to boost end-of-design life (EODL) performance by ~50% over the MMRTG. This is possible by replacing the MMRTG TECs with ones built using skutterudite (SKD) thermoelectric (TE) material. The eMMRTG design concept preserves the hermetically sealed convertor [6] of the MMRTG design. Some useful design details are in Table N-3.

Table N-3. The eMMRTG in numbers.

	Value	Comments
P_{BOL} , W	145	Beginning Of Mission
Mass, kg	45.4	Includes cooling tubes
Number of GPHS	8	Step 2 GPHS
T_h , °C	600	
Date first launched	In development	
Date last launched	Not applicable	

As a great many design features of the MMRTG are preserved in the eMMRTG, many system parameters remain similar, mass, optical coating, cooling tubes (optional), 4-bolt-mounting interface, number of GPHS, number of TECs, and so on. While it has not been flown, it serves as a useful reference for this report.

N.4 References

- [1] Bennett, G.L. 1995. “Space Applications,” *CRC Handbook of Thermoelectrics*, Boise, ID: CRC Press LLC, pp. 515–537.
- [2] Johns Hopkins University Applied Physics Laboratory. January 19, 2006. “New Horizons, NASA’s Mission to Pluto,” web site, accessed April 18, 2017. <http://pluto.jhuapl.edu/Mission/index.php>.
- [3] Lockheed Martin. 1998. GPHS-RTGs In Support of the Cassini RTG Program, Final Technical Report, Lockheed Martin Astronautics, Philadelphia, PA.
- [4] Jet Propulsion Laboratory, California Institute of Technology. November 26, 2011. “Curiosity Mission Overview,” web site, accessed April 18, 2017. <https://mars.nasa.gov/msl/mission/overview/>.
- [5] “Multi-Mission Radioisotope Thermoelectric Generator,” *Wikipedia*, accessed April 18, 2017. https://en.wikipedia.org/wiki/Multi-Mission_Radioisotope_Thermoelectric_Generator.
- [6] Woerner, D. 2016. “A Progress Report on the eMMRTG,” *Journal of Electronic Materials*, Vol. 45, No. 3, pp. 1278–1283.

O Calculating RTG Fin Size and Mass

David Neff, Fivos Drymiotis, Sevan Chanakian, Kevin Yu

NASA Jet Propulsion Laboratory, 4800 Oak Grove Drive, Pasadena, CA 91109

O.1 Introduction

This appendix describes the method used for calculating fin size and mass for radioisotope thermoelectric generators (RTGs) built to use 2 to 16 General-Purpose Heat Sources (GPHS), operating at fin root temperature (T_{fr}) of 328 K and 430 K, using the thermoelectric couples (TECs) selected for this study.

O.2 Approach

A parametric 3D model of a generic generator was created using SOLIDWORKS® to estimate generator dimensions and mass. For each proposed generator length and efficiency, fin dimensions were varied until thermal modeling results yielded the goal T_{fr} .

O.3 Assumptions, Boundary Conditions, and Simplifications

O.3.1 Behavior of Common RTG Components When Scaled

Procedurally, we first determined mass for the set of components in similarly configured generators that are independent of fin size [1, 2]. We assumed that some component masses had a static relationship to the type of RTG being modeled and were applied to each generator regardless of generator length. We then assumed the masses of some category of components scaled linearly with the number of Step 2 GPHS and their dimensions [3] in an RTG. Baseline estimates for a 2-GPHS length RTG are presented in Table O-1.

Table O-1. Baseline RTG mass constants.

Type of Component	2-GPHS Length Mass Constants		
	Description	Behavior	Mass, kg
Nonfinned housing	Portion of housing that extends beyond fins ^a	Static	0.37
Converter	Thermoelectric elements and heat spreader	Scaling	1.08
Loading End Support Assembly	Cover and miscellaneous supports at fueling end	Static	0.99
Mounting End Support Assembly	Cover and miscellaneous supports at mounting end	Static	0.89
Mispan Support Assembly	Structural support for generators longer than 8-GPHS	Scaling	0.00
Electrical Misc	Output wiring and connectors	Static	2.41
Heat Source	GPHS Modules ^b	Scaling	3.22

^a Doesn't scale with the rest of the housing
^b Dimensions and masses for Step-2 GPHS [3]

O.3.2 Housing and Fin Dimensions

- A fixed relationship between fin length and its cross-sectional area was built into the model so fin base and tip, Fig. O-1, are driven by its length. This relationship was determined experimentally and the results were then compared with dimensions of GPHS-RTG, Multi-Mission Radioisotope Thermoelectric Generator (MMRTG) [1, 2, 4].
- The interior diameter of the housings was kept constant across all types and variants and is based on converter dimensions, insulation, and GPHS stack dimensions [1, 3].
- Housing and fin masses were estimated by SOLIDWORKS® using material properties of aluminum grades 6063 and 2219 for fin and housing, respectively [2, 4].

O.3.3 *Assumptions and Simplifications Used in Thermal Modeling*

These assumptions were made to shorten simulation processing time given the number of simulations required for this study.

- Fin relief slots, Fig. O-2, were considered during model validation only. They changed T_{fr} less than one percent but added considerable complexity to the modeling mesh, so they were not included during thermal simulation. However, mass estimates for the fins considered Relief Slots during mass calculations.
- Wall thickness of SMRTG housings was based on previous designs [1, 4]. This resulted in a simulation mesh that imposed a considerable processing time. It was observed that the 0.6-cm difference in housing diameter between SMRTG and HSMRTG resulted in a T_{fr} change of less than one percent, so these generators were assumed to have the same fin dimensions. However, the difference in mass between the housing wall thicknesses was considered during mass calculations.
- Generalized support assemblies listed in Table O-1 were not included in the thermal simulations. A constant loss of thermal power through the loading and mounting end covers was applied across all generators rather than including these features in the mesh and parametrization function.
- The thermal properties of aluminum grades 6063 and 2219 were used for the fins and housings, respectively [2, 4].
- The generator housing and fins were modeled with an emissivity of 0.9 and radiated into a 4 K sink. SOLIDWORKS® included a surface-to-surface view factor calculation in the radiation calculations.
- T_{fr} goals were 328 K and 430 K.

O.3.4 *Thermal Power Equations*

The thermal simulations estimated a unique thermal power at its inside diameter of each housing and this was distributed uniformly across that surface. That thermal power was dependent on the number of GPHS, N , and the efficiency of the TECs, η . The calculation of the thermal power at an RTG housing began with a BOL GPHS power of 250 W_{TH} per module, $P_0 = N \times 250$. A constant end cover loss, P_l was subtracted to create $P_{in} = P_0 - P_l$, the input power to thermoelectric converter. Converted power $P_c = \eta \times P_{in}$ was removed and the remainder was applied to the housing.

$$P_0 - P_l - P_c = P_{housing} \quad (O-1)$$

O.4 *Using the Model*

O.4.1 *Method*

For each identified TEC, see Section O.3, a thermal power was calculated for generators using between 2 and 16 GPHS, in increments of two GPHS. The results yielded T_{fr} for the many variants. If a simulation met the temperature goal, housing and fin masses were recorded. Otherwise, fin length was adjusted and the simulation repeated until the goal was met.

O.4.2 *Validation*

The model was validated using GPHS-RTG and MMRTG dimensions, sink environment, efficiency, and T_{fr} [1, 4]. Reference [4] was used to determine $P_{housing}$ for the MMRTG design as many of the assumptions did not apply given the significant differences between the internal configuration and parts of the MMRTG as contrasted with the GPHS-RTG design and the generator concepts proposed in this study. Using the specific dimensions of the reference generators, T_{fr} was found to agree within 3% of the

temperatures in the references [1, 4] Fig. O-3 provides an illustration of simulation results for a GPHS-RTG and an MMRTG.

O.4.3 *Determining Total Mass*

Finally, fin and housing masses were calculated using SOLIDWORKS® based on volume and material properties of each model. The results were added to baseline mass constants, which were scaled to the length of each generator. This provided the total mass estimate for each generator.

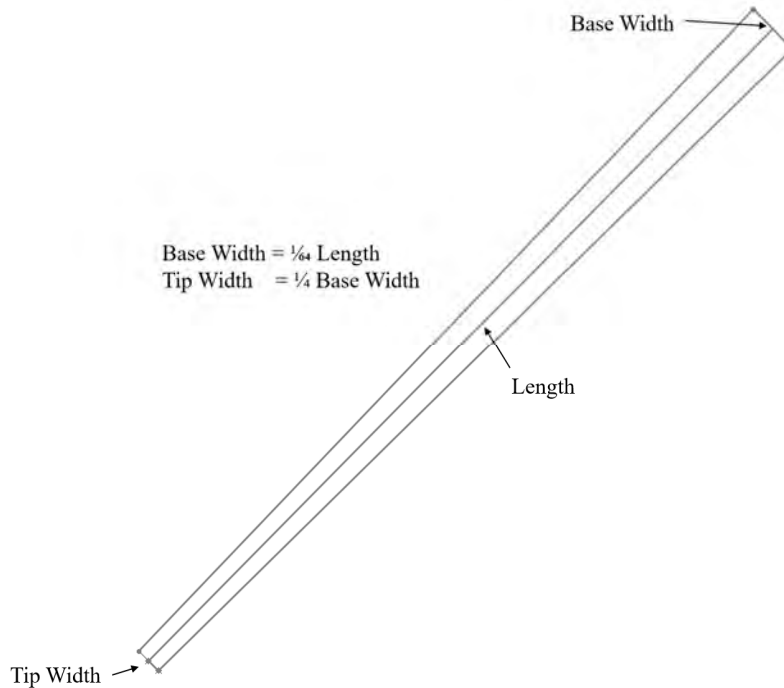


Fig. O-1. The relationship between fin length, fin base, and fin tip used in the RTG models described herein. Fin length was varied in the parametric models and this relationship drove the cross-sectional area of the fins.

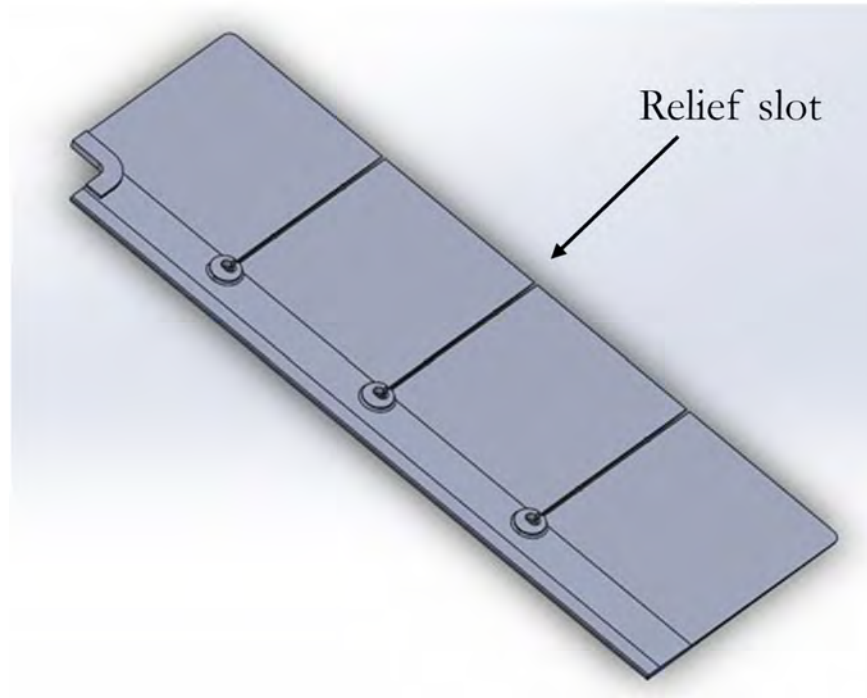


Fig. O-2. Relief slots, depicted here, were subtracted from the mass of each fin, but the feature was excluded from the thermal simulations.

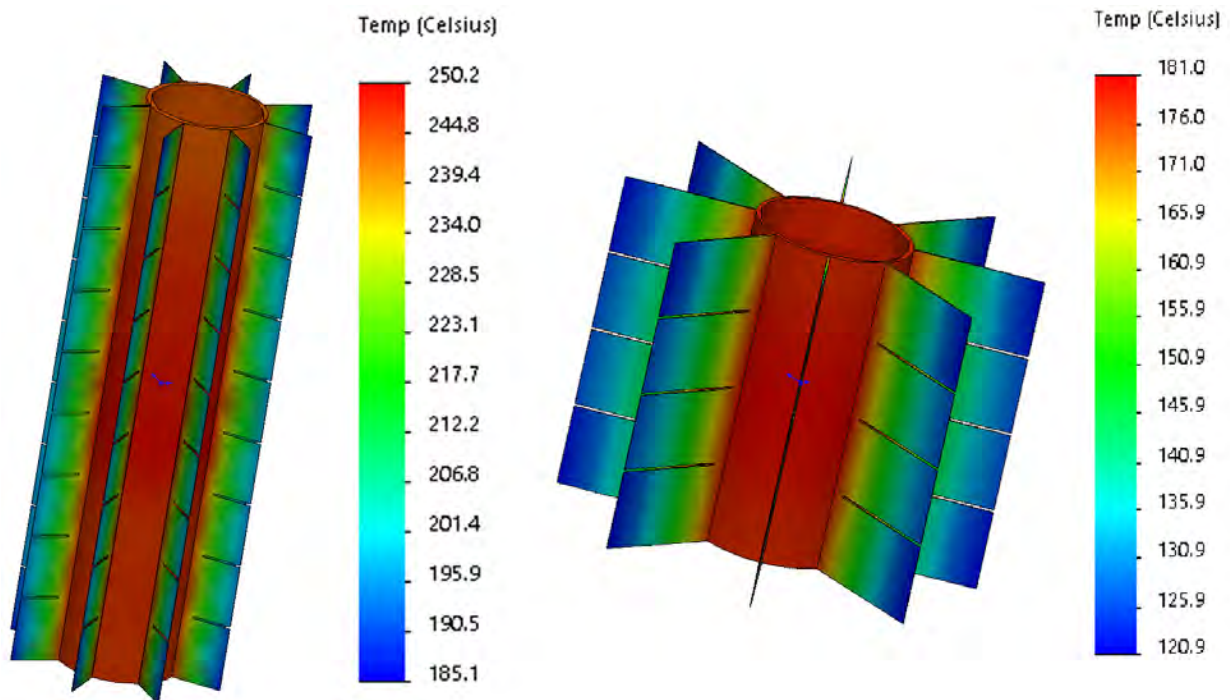


Fig. O-3. Validation of housing heat power based thermal simulation of simplified generators using GPHS-RTG and MMRTG parameters. T_{fr} is considered maximum housing temperature determined by SOLIDWORKS® and indicated here as the portion on the housing thermal simulation colored red.

O.5 References

- [1] Lange, R.G. and W.P. Carroll. March 2008. “Review of recent advances of radioisotope power systems,” *Energy Conversion and Management*, Vol. 49, Issue 3, pp. 393–401, ISSN 0196-8904. <http://doi.org/10.1016/j.enconman.2007.10.028>.
- [2] Bennett, G.L. March 2008. “Mission interplanetary: Using radioisotope power to explore the solar system,” *Energy Conversion and Management*, Vol. 49, Issue 3, pp. 382–392, ISSN 0196-8904. <http://doi.org/10.1016/j.enconman.2007.06.051>.
- [3] Lipinski, R.J. and D.L. Hensen. 2008. “Criticality Calculations for Step-2 GPHS Modules,” *AIP Conference Proceedings* 969, 452. doi: <http://dx.doi.org/10.1063/1.2845002>.
- [4] Hammel, T.E, R. Bennett, W. Otting and S. Fanale. 2008. “Multi-Mission Radioisotope Thermoelectric Generator (MMRTG) and Performance Prediction Model,” *7th International Energy Conversion Engineering Conference*, Denver, CO. doi: <http://dx.doi.org/10.2514/6.2009-4576>.

P Modeling Results for RTG Concepts

Knut I. Oxnevad

NASA Jet Propulsion Laboratory, 4800 Oak Grove Dr., Pasadena, CA 91109

P.1 Introduction

Key physical and performance parameters for the models of the radioisotope thermoelectric generator (RTG) concepts that resulted from this study are provided in the tables of this appendix (see also Section 4, RTG Concepts). The parameters herein are for the RTG concepts: SMRTG, CSMRTG, HSMRTG, CHSMRTG, SRTG, and CSRTG.

A table is provided for each of the selected eight segmented thermoelectric couples (TECs): configurations 1, 2, 3, 4, 10, 11, 14, and 21 (see Section P.3 and Appendix L for further details). One table is provided for a TEC composed of skutterudite for reference.

The third section of this appendix provides descriptions of the headers in Section P.2.

P.2 Tables

Table P-1. Types of rtg power system considered for this study: TC-1.

RTG Type	P ₀ (We, BOL)	P ₀ /Q ₀ (% , BOL): Efficiency	P ₀ /m _{rtg} (We/kg): Specific Power	P (We, BOM)	P (We,	Mass - m _{rtg} (kg)	Q ₀ (Wth)	Length (m)	Diameter w/fins (m)
SMRTG - 2 (TC-1)	55	11.00%	5.07	52	40	10.84	500	0.224	0.4096
SMRTG - 4 (TC-1)	128	12.77%	7.13	121	93	17.91	1000	0.3388	0.5147
SMRTG - 6 (TC-1)	205	13.69%	8.01	194	150	25.63	1500	0.4552	0.5690
SMRTG - 8 (TC-1)	283	14.15%	8.38	268	206	33.77	2000	0.5716	0.6045
SMRTG-10 (TC-1)	357	14.29%	8.79	338	260	40.66	2500	0.688	0.6428
SMRTG-12 (TC-1)	435	14.50%	9.20	411	317	47.27	3000	0.8044	0.6488
SMRTG -14 (TC-1)	513	14.65%	9.17	485	374	55.90	3500	0.9208	0.6901
SMRTG -16 (TC-1)	590	14.76%	9.47	558	430	62.31	4000	1.0372	0.6960
CSMRTG - 2 (TC-1)	63	12.52%	3.62	59	46	17.27	500	0.2224	0.9558
CSMRTG - 4 (TC-1)	145	14.53%	3.18	137	106	45.67	1000	0.3388	1.2952
CSMRTG - 6 (TC-1)	234	15.58%	3.04	221	170	77.00	1500	0.4552	1.4576
CSMRTG - 8 (TC-1)	322	16.10%	2.71	305	235	118.99	2000	0.5716	1.6200
CSMRTG-10 (TC-1)	407	16.27%	2.62	385	296	155.29	2500	0.688	1.6790
CSMRTG-12 (TC-1)	495	16.50%	2.28	468	361	217.08	3000	0.8044	1.8266
CSMRTG -14 (TC-1)	583	16.67%	2.19	552	425	266.94	3500	0.9208	1.8856
CSMRTG -16 (TC-1)	672	16.79%	2.09	635	490	322.10	4000	1.0372	1.9447
HSMRTG - 2 (TC-1)	55	11.00%	4.57	52	40	12.05	500	0.2224	0.4156
HSMRTG - 4 (TC-1)	128	12.77%	6.47	121	93	19.75	1000	0.3388	0.5207
HSMRTG - 6 (TC-1)	205	13.69%	7.30	194	150	28.12	1500	0.4552	0.5750
HSMRTG - 8 (TC-1)	283	14.15%	7.67	268	206	36.90	2000	0.5716	0.6105
HSMRTG-10 (TC-1)	357	14.29%	8.04	338	260	44.44	2500	0.688	0.6488
HSMRTG-12 (TC-1)	435	14.50%	8.42	411	317	51.68	3000	0.8044	0.6548
HSMRTG -14 (TC-1)	513	14.65%	8.41	485	374	60.95	3500	0.9208	0.6961
HSMRTG -16 (TC-1)	590	14.76%	8.68	558	430	68.01	4000	1.0372	0.7167
CHSMRTG - 2 (TC-1)	63	12.52%	3.39	59	46	18.48	500	0.2224	0.9618
CHSMRTG - 4 (TC-1)	145	14.53%	3.14	137	106	46.23	1000	0.3388	1.3012
CHSMRTG - 6 (TC-1)	234	15.58%	2.92	221	170	80.04	1500	0.4552	1.4636
CHSMRTG - 8 (TC-1)	322	16.10%	2.57	305	235	125.43	2000	0.5716	1.6260
CHSMRTG-10 (TC-1)	407	16.27%	2.49	385	296	163.19	2500	0.688	1.6850
CHSMRTG-12 (TC-1)	495	16.50%	2.19	468	361	226.45	3000	0.8044	1.8326
CHSMRTG -14 (TC-1)	583	16.67%	2.10	552	425	277.77	3500	0.9208	1.8916
CHSMRTG -16 (TC-1)	672	16.79%	2.01	635	490	334.40	4000	1.0372	1.9507
SRTG -16 (TC-1)	590	14.76%	9.26	558	430	63.72	4000	1.0372	0.7107
CSRTG - 16 (TC-1)	672	16.79%	2.09	635	490	322.10	4000	1.0372	1.9447

Table P-2. Types of rtg power system considered for this study: TC-2.

RTG Type	P ₀ (We, BOL)	P ₀ /Q ₀ (% , BOL): Efficiency	P ₀ /m _{rtg} (We/kg): Specific Power	P (We, BOM)	P (We, EODL)	Mass - m _{rtg} (kg)	Q ₀ (Wth)	Length (m)	Diameter w/fins (m)
SMRTG - 2 (TC-2)	51	10.15%	4.69	48	37	10.81	500	0.224	0.4037
SMRTG - 4 (TC-2)	118	11.78%	6.47	111	86	18.20	1000	0.3388	0.5336
SMRTG - 6 (TC-2)	189	12.62%	7.25	179	138	26.11	1500	0.4552	0.5868
SMRTG - 8 (TC-2)	261	13.05%	7.62	247	190	34.24	2000	0.5716	0.6163
SMRTG-10 (TC-2)	329	13.18%	7.76	312	240	42.44	2500	0.688	0.6753
SMRTG-12 (TC-2)	401	13.37%	8.01	379	292	50.03	3000	0.8044	0.6901
SMRTG -14 (TC-2)	473	13.50%	8.18	447	344	57.74	3500	0.9208	0.7122
SMRTG -16 (TC-2)	544	13.60%	8.09	515	397	67.28	4000	1.0372	0.7462
CSMRTG - 2 (TC-2)	58	11.60%	3.20	55	42	18.12	500	0.2224	1.0000
CSMRTG - 4 (TC-2)	135	13.46%	2.93	127	98	45.97	1000	0.3388	1.3246
CSMRTG - 6 (TC-2)	216	14.43%	2.72	205	158	79.71	1500	0.4552	1.4812
CSMRTG - 8 (TC-2)	298	14.91%	2.44	282	217	122.31	2000	0.5716	1.6200
CSMRTG-10 (TC-2)	377	15.06%	2.25	356	275	167.35	2500	0.688	1.7233
CSMRTG-12 (TC-2)	458	15.28%	2.06	434	334	222.04	3000	0.8044	1.8266
CSMRTG -14 (TC-2)	540	15.44%	1.87	511	394	289.61	3500	0.9208	1.9447
CSMRTG -16 (TC-2)	622	15.55%	1.89	588	453	328.70	4000	1.0372	1.9447
HSMRTG - 2 (TC-2)	51	10.15%	4.22	48	37	12.02	500	0.2224	0.4097
HSMRTG - 4 (TC-2)	118	11.78%	5.87	111	86	20.05	1000	0.3388	0.5396
HSMRTG - 6 (TC-2)	189	12.62%	6.62	179	138	28.60	1500	0.4552	0.5928
HSMRTG - 8 (TC-2)	261	13.05%	6.98	247	190	37.37	2000	0.5716	0.6223
HSMRTG-10 (TC-2)	329	13.18%	7.13	312	240	46.21	2500	0.688	0.6813
HSMRTG-12 (TC-2)	401	13.37%	7.36	379	292	54.45	3000	0.8044	0.6961
HSMRTG -14 (TC-2)	473	13.50%	7.53	447	344	62.79	3500	0.9208	0.7182
HSMRTG -16 (TC-2)	544	13.60%	7.46	515	397	72.98	4000	1.0372	0.7522
CHSMRTG - 2 (TC-2)	58	11.60%	3.00	55	42	19.32	500	0.2224	1.0060
CHSMRTG - 4 (TC-2)	135	13.46%	2.82	127	98	47.81	1000	0.3388	1.3306
CHSMRTG - 6 (TC-2)	216	14.43%	2.63	205	158	82.20	1500	0.4552	1.4872
CHSMRTG - 8 (TC-2)	298	14.91%	2.38	282	217	125.44	2000	0.5716	1.6260
CHSMRTG-10 (TC-2)	377	15.06%	2.20	356	275	171.13	2500	0.688	1.7293
CHSMRTG-12 (TC-2)	458	15.28%	2.02	434	334	226.45	3000	0.8044	1.8326
CHSMRTG -14 (TC-2)	540	15.44%	1.83	511	394	294.67	3500	0.9208	1.9507
CHSMRTG -16 (TC-2)	622	15.55%	1.86	588	453	334.40	4000	1.0372	1.9507
SRTG -16 (TC-2)	544	13.60%	8.09	515	397	67.28	4000	1.0372	0.7462
CSRTG - 16 (TC-2)	622	15.55%	1.89	588	453	328.70	4000	1.0372	1.9447

Table P-3. Types of rtg power system considered for this study: TC-3.

RTG Type	P ₀ (We, BOL)	P ₀ /Q ₀ (% , BOL): Efficiency	P ₀ /m _{rtg} (We/kg): Specific Power	P (We, BOM)	P (We, EODL)	Mass - m _{rtg} (kg)	Q ₀ (Wth)	Length (m)	Diameter w/fins (m)
SMRTG - 2 (TC-3)	52	10.44%	4.84	49	38	10.78	500	0.224	0.3978
SMRTG - 4 (TC-3)	121	12.11%	6.74	115	88	17.97	1000	0.3388	0.5189
SMRTG - 6 (TC-3)	195	12.98%	7.62	184	142	25.55	1500	0.4552	0.5660
SMRTG - 8 (TC-3)	268	13.42%	7.89	254	196	34.00	2000	0.5716	0.6104
SMRTG-10 (TC-3)	339	13.55%	8.14	320	247	41.62	2500	0.688	0.6606
SMRTG-12 (TC-3)	412	13.75%	8.24	390	301	50.03	3000	0.8044	0.6901
SMRTG -14 (TC-3)	486	13.89%	8.33	460	354	58.37	3500	0.9208	0.7196
SMRTG -16 (TC-3)	560	13.99%	8.36	529	408	66.97	4000	1.0372	0.7432
CSMRTG - 2 (TC-3)	61	12.13%	3.45	57	44	17.55	500	0.2224	0.9705
CSMRTG - 4 (TC-3)	141	14.08%	3.12	133	103	45.17	1000	0.3388	1.3100
CSMRTG - 6 (TC-3)	226	15.09%	2.87	214	165	78.90	1500	0.4552	1.4724
CSMRTG - 8 (TC-3)	312	15.59%	2.55	295	227	122.30	2000	0.5716	1.6200
CSMRTG-10 (TC-3)	394	15.75%	2.43	372	287	162.04	2500	0.688	1.6938
CSMRTG-12 (TC-3)	479	15.98%	2.10	453	349	228.49	3000	0.8044	1.8414
CSMRTG -14 (TC-3)	565	16.14%	2.01	534	412	281.09	3500	0.9208	1.9152
CSMRTG -16 (TC-3)	650	16.26%	1.98	615	474	328.71	4000	1.0372	1.9447
HSMRTG - 2 (TC-3)	52	10.44%	4.35	49	38	11.99	500	0.2224	0.4038
HSMRTG - 4 (TC-3)	121	12.11%	6.11	115	88	19.81	1000	0.3388	0.5249
HSMRTG - 6 (TC-3)	195	12.98%	6.95	184	142	28.04	1500	0.4552	0.5720
HSMRTG - 8 (TC-3)	268	13.42%	7.23	254	196	37.13	2000	0.5716	0.6164
HSMRTG-10 (TC-3)	339	13.55%	7.47	320	247	45.39	2500	0.688	0.6666
HSMRTG-12 (TC-3)	412	13.75%	7.58	390	301	54.45	3000	0.8044	0.6961
HSMRTG -14 (TC-3)	486	13.89%	7.66	460	354	63.43	3500	0.9208	0.7256
HSMRTG -16 (TC-3)	560	13.99%	7.70	529	408	72.67	4000	1.0372	0.7492
CHSMRTG - 2 (TC-3)	61	12.13%	3.23	57	44	18.75	500	0.2224	0.9765
CHSMRTG - 4 (TC-3)	141	14.08%	2.99	133	103	47.02	1000	0.3388	1.3160
CHSMRTG - 6 (TC-3)	226	15.09%	2.78	214	165	81.38	1500	0.4552	1.4784
CHSMRTG - 8 (TC-3)	312	15.59%	2.49	295	227	125.43	2000	0.5716	1.6260
CHSMRTG-10 (TC-3)	394	15.75%	2.37	372	287	165.81	2500	0.688	1.6998
CHSMRTG-12 (TC-3)	479	15.98%	2.06	453	349	232.90	3000	0.8044	1.8474
CHSMRTG -14 (TC-3)	565	16.14%	1.97	534	412	286.15	3500	0.9208	1.9212
CHSMRTG -16 (TC-3)	650	16.26%	1.95	615	474	334.40	4000	1.0372	1.9507
SRTG -16 (TC-3)	560	13.99%	8.36	529	408	66.97	4000	1.0372	0.7432
CSRTG - 16 (TC-3)	650	16.26%	1.98	615	474	328.71	4000	1.0372	1.9447

Table P-4. Types of rtg power system considered for this study: TC-4.

RTG Type	P ₀ (We, BOL)	P ₀ /Q ₀ (% , BOL): Efficiency	P ₀ /m _{rtg} (We/kg): Specific Power	P (We, BOM)	P (We, EODL)	Mass - m _{rtg} (kg)	Q ₀ (Wth)	Length (m)	Diameter w/fins (m)
SMRTG - 2 (TC-4)	47	9.49%	4.36	45	35	10.89	500	0.224	0.4185
SMRTG - 4 (TC-4)	110	11.01%	6.08	104	80	18.11	1000	0.3388	0.5295
SMRTG - 6 (TC-4)	177	11.80%	6.80	167	129	26.03	1500	0.4552	0.5838
SMRTG - 8 (TC-4)	244	12.20%	7.05	231	178	34.59	2000	0.5716	0.6251
SMRTG-10 (TC-4)	308	12.32%	7.40	291	224	41.62	2500	0.688	0.6606
SMRTG-12 (TC-4)	375	12.50%	7.65	355	273	49.02	3000	0.8044	0.6753
SMRTG -14 (TC-4)	442	12.62%	7.87	418	322	56.14	3500	0.9208	0.6930
SMRTG -16 (TC-4)	509	12.72%	7.98	481	371	63.72	4000	1.0372	0.7107
CSMRTG - 2 (TC-4)	56	11.14%	3.02	53	41	18.41	500	0.2224	1.0148
CSMRTG - 4 (TC-4)	129	12.93%	2.78	122	94	46.57	1000	0.3388	1.3321
CSMRTG - 6 (TC-4)	208	13.85%	2.50	197	151	83.02	1500	0.4552	1.5166
CSMRTG - 8 (TC-4)	286	14.32%	2.27	271	209	126.35	2000	0.5716	1.6495
CSMRTG-10 (TC-4)	362	14.46%	2.13	342	264	170.05	2500	0.688	1.7380
CSMRTG-12 (TC-4)	440	14.67%	1.91	416	321	230.37	3000	0.8044	1.8620
CSMRTG -14 (TC-4)	519	14.82%	1.74	491	378	298.28	3500	0.9208	1.9742
CSMRTG -16 (TC-4)	597	14.93%	1.76	565	435	338.60	4000	1.0372	1.9742
HSMRTG - 2 (TC-4)	47	9.49%	3.92	45	35	12.09	500	0.2224	0.4245
HSMRTG - 4 (TC-4)	110	11.01%	5.52	104	80	19.95	1000	0.3388	0.5355
HSMRTG - 6 (TC-4)	177	11.80%	6.21	167	129	28.52	1500	0.4552	0.5898
HSMRTG - 8 (TC-4)	244	12.20%	6.47	231	178	37.72	2000	0.5716	0.6311
HSMRTG-10 (TC-4)	308	12.32%	6.79	291	224	45.39	2500	0.688	0.6666
HSMRTG-12 (TC-4)	375	12.50%	7.02	355	273	53.43	3000	0.8044	0.6813
HSMRTG -14 (TC-4)	442	12.62%	7.22	418	322	61.19	3500	0.9208	0.6990
HSMRTG -16 (TC-4)	509	12.72%	7.33	481	371	69.42	4000	1.0372	0.7167
CHSMRTG - 2 (TC-4)	56	11.14%	2.84	53	41	19.61	500	0.2224	1.0208
CHSMRTG - 4 (TC-4)	129	12.93%	2.67	122	94	48.41	1000	0.3388	1.3381
CHSMRTG - 6 (TC-4)	208	13.85%	2.43	197	151	85.51	1500	0.4552	1.5226
CHSMRTG - 8 (TC-4)	286	14.32%	2.21	271	209	129.48	2000	0.5716	1.6555
CHSMRTG-10 (TC-4)	362	14.46%	2.08	342	264	173.82	2500	0.688	1.7440
CHSMRTG-12 (TC-4)	440	14.67%	1.87	416	321	234.79	3000	0.8044	1.8680
CHSMRTG -14 (TC-4)	519	14.82%	1.71	491	378	303.33	3500	0.9208	1.9802
CHSMRTG -16 (TC-4)	597	14.93%	1.73	565	435	344.30	4000	1.0372	1.9802
SRTG -16 (TC-4)	509	12.72%	7.46	481	371	68.20	4000	1.0372	0.7550
CSRTG - 16 (TC-4)	597	14.93%	1.76	565	435	338.60	4000	1.0372	1.9742

Table P-5. Types of rtg power system considered for this study: TC-10.

RTG Type	P ₀ (We, BOL)	P ₀ /Q ₀ (% ,BOL): Efficiency	P ₀ /m _{rtg} (We/kg): Specific Power	P (We, BOM)	P (We, EODL)	Mass - m _{rtg} (kg)	Q ₀ (Wth)	Length (m)	Diameter w/fins (m)
SMRTG - 2 (TC-10)	45	9.02%	4.12	43	33	10.94	500	0.224	0.4274
SMRTG - 4 (TC-10)	105	10.47%	5.69	99	76	18.39	1000	0.3388	0.5454
SMRTG - 6 (TC-10)	168	11.22%	6.34	159	123	26.53	1500	0.4552	0.6014
SMRTG - 8 (TC-10)	232	11.59%	6.49	219	169	35.70	2000	0.5716	0.6517
SMRTG-10 (TC-10)	293	11.71%	6.90	277	213	42.44	2500	0.688	0.6753
SMRTG-12 (TC-10)	356	11.88%	7.01	337	260	50.87	3000	0.8044	0.7018
SMRTG -14 (TC-10)	420	12.00%	6.95	397	306	60.46	3500	0.9208	0.7432
SMRTG -16 (TC-10)	484	12.09%	7.11	457	352	68.00	4000	1.0372	0.7521
CSMRTG - 2 (TC-10)	48	9.51%	2.50	45	35	19.01	500	0.2224	1.0043
CSMRTG - 4 (TC-10)	110	11.03%	2.23	104	80	49.48	1000	0.3388	1.3838
CSMRTG - 6 (TC-10)	177	11.83%	2.03	168	129	87.28	1500	0.4552	1.5609
CSMRTG - 8 (TC-10)	244	12.22%	1.81	231	178	134.70	2000	0.5716	1.7085
CSMRTG-10 (TC-10)	309	12.34%	1.65	292	225	186.78	2500	0.688	1.8266
CSMRTG-12 (TC-10)	376	12.52%	1.73	355	274	216.93	3000	0.8044	1.9152
CSMRTG -14 (TC-10)	443	12.65%	1.40	419	323	316.04	3500	0.9208	2.0332
CSMRTG -16 (TC-10)	510	12.74%	1.42	482	372	358.89	4000	1.0372	2.0332
HSMRTG - 2 (TC-10)	45	9.02%	3.71	43	33	12.14	500	0.2224	0.4334
HSMRTG - 4 (TC-10)	105	10.47%	5.17	99	76	20.24	1000	0.3388	0.5514
HSMRTG - 6 (TC-10)	168	11.22%	5.80	159	123	29.02	1500	0.4552	0.6074
HSMRTG - 8 (TC-10)	232	11.59%	5.97	219	169	38.83	2000	0.5716	0.6577
HSMRTG-10 (TC-10)	293	11.71%	6.34	277	213	46.21	2500	0.688	0.6813
HSMRTG-12 (TC-10)	356	11.88%	6.45	337	260	55.28	3000	0.8044	0.7078
HSMRTG -14 (TC-10)	420	12.00%	6.41	397	306	65.52	3500	0.9208	0.7492
HSMRTG -16 (TC-10)	484	12.09%	6.56	457	352	73.70	4000	1.0372	0.7581
CHSMRTG - 2 (TC-10)	48	9.51%	2.35	45	35	20.21	500	0.2224	1.0103
CHSMRTG - 4 (TC-10)	110	11.03%	2.15	104	80	51.33	1000	0.3388	1.3898
CHSMRTG - 6 (TC-10)	177	11.83%	1.98	168	129	89.77	1500	0.4552	1.5669
CHSMRTG - 8 (TC-10)	244	12.22%	1.77	231	178	137.83	2000	0.5716	1.7145
CHSMRTG-10 (TC-10)	309	12.34%	1.62	292	225	190.55	2500	0.688	1.8326
CHSMRTG-12 (TC-10)	376	12.52%	1.70	355	274	221.35	3000	0.8044	1.9212
CHSMRTG -14 (TC-10)	443	12.65%	1.38	419	323	321.10	3500	0.9208	2.0392
CHSMRTG -16 (TC-10)	510	12.74%	1.40	482	372	364.59	4000	1.0372	2.0392
SRTG -16 (TC-10)	484	12.09%	7.11	457	352	68.00	4000	1.0372	0.7521
CSRTG - 16 (TC-10)	510	12.74%	1.42	482	372	358.89	4000	1.0372	2.0332

Table P-6. Types of rtg power system considered for this study: TC-11.

RTG Type	P ₀ (We, BOL)	P ₀ /Q ₀ (% , BOL): Efficiency	P ₀ /m _{rtg} (We/kg): Specific Power	P (We, BOM)	P (We, EODL)	Mass - m _{rtg} (kg)	Q ₀ (Wth)	Length (m)	Diameter w/fins (m)
SMRTG - 2 (TC-11)	37	7.47%	3.12	35	27	11.99	500	0.224	0.4038
SMRTG - 4 (TC-11)	87	8.67%	4.38	82	63	19.81	1000	0.3388	0.5249
SMRTG - 6 (TC-11)	139	9.29%	4.97	132	102	28.04	1500	0.4552	0.5720
SMRTG - 8 (TC-11)	192	9.61%	5.17	182	140	37.13	2000	0.5716	0.6164
SMRTG-10 (TC-11)	243	9.70%	5.34	229	177	45.39	2500	0.688	0.6666
SMRTG-12 (TC-11)	295	9.84%	5.42	279	215	54.45	3000	0.8044	0.6961
SMRTG -14 (TC-11)	348	9.94%	5.49	329	254	63.43	3500	0.9208	0.7256
SMRTG -16 (TC-11)	401	10.02%	5.51	379	292	72.67	4000	1.0372	0.7492
CSMRTG - 2 (TC-11)	39	7.83%	2.02	37	29	19.38	500	0.2224	1.0620
CSMRTG - 4 (TC-11)	91	9.09%	1.77	86	66	51.20	1000	0.3388	1.4133
CSMRTG - 6 (TC-11)	146	9.74%	1.60	138	106	91.39	1500	0.4552	1.6022
CSMRTG - 8 (TC-11)	201	10.06%	1.40	190	147	143.39	2000	0.5716	1.7676
CSMRTG-10 (TC-11)	254	10.17%	1.28	240	185	198.45	2500	0.688	1.8856
CSMRTG-12 (TC-11)	309	10.31%	1.37	293	225	226.57	3000	0.8044	1.9594
CSMRTG -14 (TC-11)	365	10.42%	1.09	345	266	334.39	3500	0.9208	2.0922
CSMRTG -16 (TC-11)	420	10.49%	1.11	397	306	379.85	4000	1.0372	2.0922
HSMRTG - 2 (TC-11)	37	7.47%	3.06	35	27	12.21	500	0.2224	0.4452
HSMRTG - 4 (TC-11)	87	8.67%	4.19	82	63	20.69	1000	0.3388	0.5780
HSMRTG - 6 (TC-11)	139	9.29%	4.73	132	102	29.45	1500	0.4552	0.6223
HSMRTG - 8 (TC-11)	192	9.61%	4.90	182	140	39.21	2000	0.5716	0.6666
HSMRTG-10 (TC-11)	243	9.70%	5.15	229	177	47.06	2500	0.688	0.6961
HSMRTG-12 (TC-11)	295	9.84%	5.32	279	215	55.50	3000	0.8044	0.7108
HSMRTG -14 (TC-11)	348	9.94%	5.31	329	254	65.52	3500	0.9208	0.7492
HSMRTG -16 (TC-11)	401	10.02%	5.29	379	292	75.80	4000	1.0372	0.7787
CHSMRTG - 2 (TC-11)	39	7.83%	1.90	37	29	20.58	500	0.2224	1.0680
CHSMRTG - 4 (TC-11)	91	9.09%	1.71	86	66	53.05	1000	0.3388	1.4193
CHSMRTG - 6 (TC-11)	146	9.74%	1.56	138	106	93.88	1500	0.4552	1.6082
CHSMRTG - 8 (TC-11)	201	10.06%	1.37	190	147	146.52	2000	0.5716	1.7736
CHSMRTG-10 (TC-11)	254	10.17%	1.26	240	185	202.22	2500	0.688	1.8916
CHSMRTG-12 (TC-11)	309	10.31%	1.34	293	225	230.98	3000	0.8044	1.9654
CHSMRTG -14 (TC-11)	365	10.42%	1.07	345	266	339.45	3500	0.9208	2.0982
CHSMRTG -16 (TC-11)	420	10.49%	1.09	397	306	385.55	4000	1.0372	2.0982
SRTG -16 (TC-11)	401	10.02%	5.51	379	292	72.67	4000	1.0372	0.7492
CSRTG - 16 (TC-11)	420	10.49%	1.11	397	306	379.85	4000	1.0372	2.0922

Table P-7. Types of rtg power system considered for this study: TC-14.

RTG Type	P ₀ (We, BOL)	P ₀ /Q ₀ (% BOL): Efficiency	P ₀ /m _{rtg} (We/kg): Specific Power	P (We, BOM)	P (We, EODL)	Mass - m _{rtg} (kg)	Q ₀ (Wth)	Length (m)	Diameter w/fins (m)
SMRTG - 2 (TC-14)	47	9.40%	4.32	44	34	10.88	500	0.224	0.4161
SMRTG - 4 (TC-14)	109	10.91%	6.01	103	80	18.15	1000	0.3388	0.5307
SMRTG - 6 (TC-14)	175	11.69%	6.72	166	128	26.11	1500	0.4552	0.5868
SMRTG - 8 (TC-14)	242	12.09%	6.94	229	176	34.83	2000	0.5716	0.6310
SMRTG-10 (TC-14)	305	12.21%	7.33	289	222	41.62	2500	0.688	0.6606
SMRTG-12 (TC-14)	371	12.38%	7.64	351	271	48.62	3000	0.8044	0.6694
SMRTG -14 (TC-14)	438	12.51%	7.80	414	319	56.14	3500	0.9208	0.6930
SMRTG -16 (TC-14)	504	12.60%	7.84	477	367	64.30	4000	1.0372	0.7166
CSMRTG - 2 (TC-14)	55	11.10%	3.11	52	40	17.83	500	0.2224	0.9858
CSMRTG - 4 (TC-14)	129	12.88%	2.77	122	94	46.45	1000	0.3388	1.3248
CSMRTG - 6 (TC-14)	207	13.81%	2.51	196	151	82.46	1500	0.4552	1.5107
CSMRTG - 8 (TC-14)	285	14.27%	2.27	270	208	125.53	2000	0.5716	1.6436
CSMRTG-10 (TC-14)	360	14.41%	2.12	341	263	169.94	2500	0.688	1.7375
CSMRTG-12 (TC-14)	439	14.62%	1.95	415	320	225.49	3000	0.8044	1.8414
CSMRTG -14 (TC-14)	517	14.77%	1.76	489	377	293.06	3500	0.9208	1.9565
CSMRTG -16 (TC-14)	595	14.88%	1.78	563	434	333.63	4000	1.0372	1.9594
HSMRTG - 2 (TC-14)	47	9.40%	3.89	44	34	12.08	500	0.2224	0.4221
HSMRTG - 4 (TC-14)	109	10.91%	5.46	103	80	20.00	1000	0.3388	0.5367
HSMRTG - 6 (TC-14)	175	11.69%	6.13	166	128	28.60	1500	0.4552	0.5928
HSMRTG - 8 (TC-14)	242	12.09%	6.37	229	176	37.96	2000	0.5716	0.6370
HSMRTG-10 (TC-14)	305	12.21%	6.72	289	222	45.39	2500	0.688	0.6666
HSMRTG-12 (TC-14)	371	12.38%	7.00	351	271	53.04	3000	0.8044	0.6754
HSMRTG -14 (TC-14)	438	12.51%	7.15	414	319	61.19	3500	0.9208	0.6990
HSMRTG -16 (TC-14)	504	12.60%	7.20	477	367	70.00	4000	1.0372	0.7226
CHSMRTG - 2 (TC-14)	55	11.10%	2.91	52	40	19.03	500	0.2224	0.9918
CHSMRTG - 4 (TC-14)	129	12.88%	2.67	122	94	48.29	1000	0.3388	1.3308
CHSMRTG - 6 (TC-14)	207	13.81%	2.44	196	151	84.95	1500	0.4552	1.5167
CHSMRTG - 8 (TC-14)	285	14.27%	2.22	270	208	128.66	2000	0.5716	1.6496
CHSMRTG-10 (TC-14)	360	14.41%	2.07	341	263	173.72	2500	0.688	1.7435
CHSMRTG-12 (TC-14)	439	14.62%	1.91	415	320	229.90	3000	0.8044	1.8474
CHSMRTG -14 (TC-14)	517	14.77%	1.73	489	377	298.12	3500	0.9208	1.9625
CHSMRTG -16 (TC-14)	595	14.88%	1.75	563	434	339.33	4000	1.0372	1.9654
SRTG -16 (TC-14)	504	12.60%	7.84	477	367	64.30	4000	1.0372	0.7166
CSRTG - 16 (TC-14)	595	14.88%	1.78	563	434	333.63	4000	1.0372	1.9594

Table P-8. Types of rtg power system considered for this study: TC-21.

RTG Type	P ₀ (We, BOL)	P ₀ /Q ₀ (% BOL): Efficiency	P ₀ /m _{rtg} (We/kg): Specific Power	P (We, BOM)	P (We, EODL)	Mass - m _{rtg} (kg)	Q ₀ (Wth)	Length (m)	Diameter w/fins (m)
SMRTG - 2 (TC-21)	40	7.96%	3.64	38	29	10.95	500	0.224	0.4297
SMRTG - 4 (TC-21)	92	9.24%	5.04	87	67	18.34	1000	0.3388	0.5425
SMRTG - 6 (TC-21)	149	9.90%	5.58	140	108	26.61	1500	0.4552	0.6045
SMRTG - 8 (TC-21)	205	10.23%	5.81	194	149	35.20	2000	0.5716	0.6399
SMRTG-10 (TC-21)	258	10.34%	5.99	244	188	43.11	2500	0.688	0.6871
SMRTG-12 (TC-21)	315	10.49%	6.29	298	229	50.04	3000	0.8044	0.6901
SMRTG -14 (TC-21)	371	10.59%	6.38	351	270	58.12	3500	0.9208	0.7166
SMRTG -16 (TC-21)	427	10.67%	6.37	404	311	66.97	4000	1.0372	0.7432
CSMRTG - 2 (TC-21)	48	9.55%	2.55	45	35	18.71	500	0.2224	1.0296
CSMRTG - 4 (TC-21)	111	11.09%	2.25	105	81	49.31	1000	0.3388	1.3808
CSMRTG - 6 (TC-21)	178	11.88%	2.00	169	130	89.32	1500	0.4552	1.5816
CSMRTG - 8 (TC-21)	246	12.28%	1.82	232	179	134.70	2000	0.5716	1.7085
CSMRTG-10 (TC-21)	310	12.40%	1.66	293	226	186.83	2500	0.688	1.8266
CSMRTG-12 (TC-21)	378	12.58%	1.55	357	275	243.21	3000	0.8044	1.9152
CSMRTG -14 (TC-21)	445	12.71%	1.41	421	324	316.04	3500	0.9208	2.0332
CSMRTG -16 (TC-21)	512	12.81%	1.43	484	373	358.89	4000	1.0372	2.0332
HSMRTG - 2 (TC-21)	40	7.96%	3.28	38	29	12.15	500	0.2224	0.4357
HSMRTG - 4 (TC-21)	92	9.24%	4.58	87	67	20.19	1000	0.3388	0.5485
HSMRTG - 6 (TC-21)	149	9.90%	5.10	140	108	29.10	1500	0.4552	0.6105
HSMRTG - 8 (TC-21)	205	10.23%	5.34	194	149	38.33	2000	0.5716	0.6459
HSMRTG-10 (TC-21)	258	10.34%	5.51	244	188	46.89	2500	0.688	0.6931
HSMRTG-12 (TC-21)	315	10.49%	5.78	298	229	54.45	3000	0.8044	0.6961
HSMRTG -14 (TC-21)	371	10.59%	5.87	351	270	63.18	3500	0.9208	0.7226
HSMRTG -16 (TC-21)	427	10.67%	5.87	404	311	72.67	4000	1.0372	0.7492
CHSMRTG - 2 (TC-21)	48	9.55%	2.40	45	35	19.91	500	0.2224	1.0356
CHSMRTG - 4 (TC-21)	111	11.09%	2.17	105	81	51.16	1000	0.3388	1.3868
CHSMRTG - 6 (TC-21)	178	11.88%	1.94	169	130	91.81	1500	0.4552	1.5876
CHSMRTG - 8 (TC-21)	246	12.28%	1.78	232	179	137.83	2000	0.5716	1.7145
CHSMRTG-10 (TC-21)	310	12.40%	1.63	293	226	190.60	2500	0.688	1.8326
CHSMRTG-12 (TC-21)	378	12.58%	1.52	357	275	247.63	3000	0.8044	1.9212
CHSMRTG -14 (TC-21)	445	12.71%	1.39	421	324	321.10	3500	0.9208	2.0392
CHSMRTG -16 (TC-21)	512	12.81%	1.41	484	373	364.59	4000	1.0372	2.0392
SRTG -16 (TC-21)	427	10.67%	6.35	404	311	67.21	4000	1.0372	0.8229
CSRTG - 16 (TC-21)	512	12.81%	1.43	484	373	358.89	4000	1.0372	2.0332

Table P-9. Types of rtg power system considered for this study: SKD.

RTG Type	P ₀ (We, BOL)	P ₀ /Q ₀ (% , BOL): Efficiency	P ₀ /m _{rtg} (We/kg): Specific Power	P (We, BOM)	P (We, EODL)	Mass - m _{rtg} (kg)	Q ₀ (Wth)	Length (m)	Diameter w/fins (m)
SMRTG - 2 (SKD)	33	6.58%	3.01	31	24	10.93	500	0.224	0.4333
SMRTG - 4 (SKD)	76	7.64%	4.13	72	56	18.49	1000	0.3388	0.5513
SMRTG - 6 (SKD)	123	8.19%	4.52	116	89	27.14	1500	0.4552	0.6222
SMRTG - 8 (SKD)	169	8.46%	4.68	160	123	36.15	2000	0.5716	0.6620
SMRTG-10 (SKD)	214	8.54%	4.86	202	156	43.98	2500	0.688	0.7018
SMRTG-12 (SKD)	260	8.67%	5.03	246	190	51.73	3000	0.8044	0.7137
SMRTG -14 (SKD)	306	8.75%	5.06	290	223	60.60	3500	0.9208	0.7447
SMRTG -16 (SKD)	353	8.82%	5.17	334	257	68.21	4000	1.0372	0.7550
HSMRTG - 2 (SKD)	33	6.58%	2.71	31	24	12.13	500	0.2224	0.4393
HSMRTG - 4 (SKD)	76	7.64%	3.76	72	56	20.34	1000	0.3388	0.5573
HSMRTG - 6 (SKD)	123	8.19%	4.14	116	89	29.63	1500	0.4552	0.6282
HSMRTG - 8 (SKD)	169	8.46%	4.31	160	123	39.28	2000	0.5716	0.6680
HSMRTG-10 (SKD)	214	8.54%	4.47	202	156	47.76	2500	0.688	0.7078
HSMRTG-12 (SKD)	260	8.67%	4.63	246	190	56.14	3000	0.8044	0.7970
HSMRTG -14 (SKD)	306	8.75%	4.67	290	223	65.65	3500	0.9208	0.7507
HSMRTG -16 (SKD)	353	8.82%	4.77	334	257	73.90	4000	1.0372	0.7610
SRTG -16 (SKD)	353	8.82%	5.17	334	257	68.21	4000	1.0372	0.7550

P.3 Table Column Descriptions

P_0 (We, BOL)

Beginning-of-life electric power, BOL, also called P_0 . Here calculated as thermal inventory, Q_0 , multiplied by generator efficiency. Generator efficiency is unique to each TC and increases with an increasing number of General-Purpose Heat Sources (GPHS).

P_0/Q_0 (% , BOL)

Generator efficiency at BOL.

P_0/m_{rtg} (We/kg)

Specific power at BOL, where m_{rtg} is the mass of an RTG.

P (We, BOM)

Beginning of mission (BOM), at launch, electric power. The terrestrial storage period, t_s , before launch is assumed to be 3 years. Degradation, r , rate is set to 1.86%, the same as post-launch. Power, P , was estimated using $P=P_0 \times e^{-t_s * r}$.

P (We, EODL)

End-of-design life power, EODL. Design life is required to be 17 years and is allocated as storage, t_s , plus flight time, t_f , 3 + 14 years. $P=P_0 \times e^{-(t_s+t_f)*r}$.

m_{rtg} (kg)

Mass of RTG. Details of how m_{rtg} was calculated are provided in Appendix O.

Q_0 (Wth)

Thermal inventory at beginning at BOL.

Length (m)

Length, including, caps, of RTG.

Diameter w/fins (m)

Diameter of RTG with fins. Details of how RTG diameter was calculated is provided in Appendix O.

Q Factors of Safety – GPHS-RTG and MMRTG

Knut I. Oxnevad,
 NASA Jet Propulsion Laboratory, 4800 Oak Grove Dr., Pasadena, CA 91109

Q.1 Introduction

Structural integrity of the primary and secondary load carrying members of power system is achieved by showing positive margins of safety for yield and ultimate stress for all critical loading events. The Factors of Safety tables shown in this appendix are used for calculating the yield margin of safety and the ultimate margin of safety shown here:

$$a, MS_y = (\text{Allowable Yield Load or Stress} / (\text{Limit Load or Stress}) * FS_y) - 1 \quad [1]$$

Where MS_y is the yield margin of safety and FS_y is the yield factor of safety.

$$b, MS_u = (\text{Allowable Ultimate Load or Stress} / (\text{Limit Load or Stress}) * FS_u) - 1 \quad [1]$$

Where MS_u is the ultimate margin of safety FS_y is the yield factor of safety.

Factors of safety for the GPHS-RTG are provided in Table Q-1, and factors of safety for the MMRTG are provided in Table Q-2.

Q.2 Tables

Table Q-1. Factors of safety: GPHS-RTG [1].

	Yield	Ultimate
Structural elements, verified by testing	1	1.4
Structural elements, not verified by testing	2.32	2.6
Mission critical springs	1.5	1.68

Table Q-2. Factors of safety: MMRTG [2].

Metallic or Composite Structures	Yield	Ultimate
Structure qualified by testing on a flight or flight spare (Protoflight).	1.25	1.40
Structure qualified by testing on a test dedicated article (Prototype).	1	1.40
Composite, Non-metallic structure with test verified "B" basis allowables for composite and bonds	N/A	1.50
Metallic structure not qualified by testing.	1.6	2

Pressure Vessels and Springs	Yield	Ultimate	Fracture Mechanics (FMFS)
All pneumatic lines, and hydraulic lines, hoses, and	1.6	4	N/A
Safety critical preloaded springs.	1.65	2	1.35 and 1 Life; 1.00 and 4 Lives
Mission critical preloaded springs.	1.5	1.68	1.15 and 1 Life

Q.3 References

- [1] Lockheed Martin. 1996. Product Specification GPHS-RTG for Cassini, PS 23009148, Rev. F and Addendum I, 11,23.
- [2] Jet Propulsion Laboratory. May 27, 2011. Mars Science Laboratory Multi-Mission Radioisotope Thermoelectric Generator (MMRTG) Interface Control Document, MSL -322-0107, JPL D-27138 (Rev. A).

R Next-Generation RTG: Factors of Safety, Acoustics, and Random Vibrations

Knut I. Oxnevad,
NASA Jet Propulsion Laboratory, 4800 Oak Grove Dr., Pasadena, CA 91109

R.1 Introduction

A careful evaluation of the factors of safety, acoustic sound pressure level, and random vibration requirements provided in the GPHS-RTG and MMRTG requirement documents was done to determine which of those should be used for the Next-Generation RTG. These requirements were also evaluated against the demands of destinations, missions, and launchers. Based on this evaluation, the following determinations were made: use the latest factors of safety provided in the MMRTG interface control document requirements document [1], and use the acoustic sound pressure level and the random vibration requirements provided in the GPHS-RTG [2] requirements document. Random vibrations are induced by the acoustic sound pressure levels and the two are intrinsically linked.

R.2 Factors of Safety

Structural integrity of the primary and secondary load carrying members of power system is achieved by showing positive margins of safety for yield and ultimate stress for all critical loading events. The factors of safety tables shown in this appendix are used for calculating the yield margin of safety and the ultimate margin of safety shown here:

$$a, MS_y = (\text{Allowable Yield Load or Stress} / (\text{Limit Load or Stress}) * FS_y) - 1 \quad [1]$$

Where MS_y is the yield margin of safety and FS_y is the yield factor of safety.

$$b, MS_u = (\text{Allowable Ultimate Load or Stress} / (\text{Limit Load or Stress}) * FS_u) - 1 \quad [1]$$

Where MS_u is the ultimate margin of safety FS_y is the yield factor of safety.

Table R-1. Factors of safety [1].

Metallic or Composite Structures	Yield	Ultimate
Structure qualified by testing on a flight or flight spare (Protoflight).	1.25	1.40
Structure qualified by testing on a test dedicated article (Prototype).	1	1.40
Composite, Non-metallic structure with test verified "B" basis allowables for composite and bonds	N/A	1.50
Metallic structure not qualified by testing.	1.6	2

Pressure Vessels and Springs	Yield	Ultimate	Fracture Mechanics (FMFS)
All pneumatic lines, and hydraulic lines, hoses, and	1.6	4	N/A
Safety critical preloaded springs.	1.65	2	1.35 and 1 Life; 1.00 and 4 Lives
Mission critical preloaded springs.	1.5	1.68	1.15 and 1 Life

R.3 Acoustic Sound Pressure Levels

The Next-Generation RTG power system will be designed for a max flight acceptance (FA) overall sound pressure level (OASPL) of 143.0 dB with 1/3 octave band sound pressure levels. The Qual/Pre Flight (PF) level will be set 4 dB higher than this. See Table R-2.

Table R-2. Acoustic sound pressure levels [2].

1/3 Octave Band Center Frequency (Hz)	Qual/Pre Flight (PF) Level (dB)	Flight Acceptance (FA) Level (dB)
20	126	122
25	128	124
31.5	130	126
40	132	128
50	133.5	129.5
63	135	131
80	136	132
100	137	133
125	137.5	133.5
160	137.5	133.5
200	137.5	133.5
250	136.5	132.5
315	136	132
400	134.5	130.5
500	132	128
630	130	126
800	128	124
1000	126	122
1250	124	120
1600	122	118
2000	120	116
2500	118	114
3150	116	112
4000	114	110
5000	112	108
6300	110	106
8000	108	104
10000	106	102
Overall SPL (db)	147	143

The Qual/PF level is set 4 dB higher than the FA level [2].

R.4 Random Vibrations

Random vibrations are induced primarily by acoustic excitation of the local spacecraft structure during liftoff and transonic events. Table R-3 shows Qual/PF and FA levels. The lateral acceleration numbers for Q/PF and FA GRMS levels were used for reference in the requirements Tables 2-12 through 2-14 in Section 2.6.6.

R.5 Explanation of Terms

F: Frequency of vibration (Hz). F_l : The low frequency in an interval; F_h : The high frequency in an interval.

ASD: Acceleration Spectral density (g^2/Hz)

dB: $10 \cdot \text{LOG}(ASD_h/ASD_l)$

OCT: Octave. $\text{LOG}(F_h/F_l)/\text{LOG}(2)$

Slope: db/OCT

A: Area

GRMS: Root mean square acceleration. GRMS is the square root of the area (A) under the ASD curve in the frequency domain. The GRMS value is often used to express the overall energy of a particular random vibration event. It is a statistical value used for structural design and analysis purposes.

Table R-3. Random vibrations [2].

GPHS-RTG						
Longit. - Qual						
Freq - F (Hz)	ASD (g ² /Hz)	dB	OCT	Slope - m dB/OCT	Area A	Acceleration GRMS
20	0.01	*	*	*	*	*
51	0.04	8.10	1.35	6.00	0.64	0.80
176	0.04	0.00	1.79	0.00	5.64	2.37
192	0.008	-6.99	0.13	-55.68	5.95	2.44
240	0.008	0.00	0.32	0.00	6.34	2.52
256	0.025	4.95	0.09	53.15	6.58	2.56
352	0.025	0.00	0.46	0.00	8.98	3.00
380	0.08	5.05	0.11	45.75	10.31	3.21
450	0.08	0.00	0.24	0.00	15.91	3.99
2000	0.0041	-12.91	2.15	-6.00	43.92	6.63
Longit. - FA						
Freq - F (Hz)	ASD (g ² /Hz)	dB	OCT	Slope - m dB/OCT	Area A	Acceleration GRMS
20	0.00	*	*	*	*	*
51	0.016	8.10	1.35	6.00	0.26	0.51
176	0.016	0.00	1.79	0.00	2.26	1.50
192	0.008	-3.01	0.13	-23.98	2.44	1.56
240	0.008	0.00	0.32	0.00	2.82	1.68
256	0.01	0.97	0.09	10.41	2.97	1.72
352	0.01	0.00	0.46	0.00	3.93	1.98
380	0.032	5.05	0.11	45.75	4.46	2.11
450	0.032	0.00	0.24	0.00	6.70	2.59
2000	0.0016	-12.91	2.15	-6.00	17.90	4.23
Later. - Qual						
Freq - F (Hz)	ASD (g ² /Hz)	dB	OCT	Slope - m dB/OCT	Area A	Acceleration GRMS
20	0.01	*	*	*	*	*
72	0.08	11.09	1.85	6.00	1.88	1.37
180	0.08	0.00	1.32	0.00	10.52	3.24
205	0.016	-6.99	0.19	-37.25	11.50	3.39
245	0.016	0.00	0.26	0.00	12.14	3.48
275	0.08	6.99	0.17	41.94	13.35	3.65
450	0.08	0.00	0.71	0.00	27.35	5.23
2000	0.0041	-12.91	2.15	-6.00	55.36	7.44
Later. - FA						
Freq - F (Hz)	ASD (g ² /Hz)	dB	OCT	Slope - m dB/OCT	Area A	Acceleration GRMS
20	0.00	*	*	*	*	*
72	0.032	11.09	1.85	6.00	0.75	0.87
180	0.032	0.00	1.32	0.00	4.21	2.05
205	0.016	-3.01	0.19	-16.04	4.78	2.19
245	0.016	0.00	0.26	0.00	5.42	2.33
275	0.032	3.01	0.17	18.06	6.12	2.47
450	0.032	0.00	0.71	0.00	11.72	3.42
2000	0.0016	-12.91	2.15	-6.00	22.92	4.79

R.6 References

- [1] Jet Propulsion Laboratory. May 27, 2011. Mars Science Laboratory Multi-Mission Radioisotope Thermoelectric Generator (MMRTG) Interface Control Document, MSL -322-0107, JPL D-27138 (Rev. A).
- [2] Lockheed Martin. 1995–1996. Environmental Criteria and Test Requirements, 23009150 Rev., 9, 11, 12.